Enhanced Spectral Modeling of Sparse Aperture Imaging Systems

by

Robert E. Introne

B.S., Massachusetts Institute of Technology, 1989
M.S., Georgia Institute of Technology, 1990

A dissertation submitted in partial fulfillment of the
requirements for the degree of Doctor of Philosophy
in the Chester F. Carlson Center for Imaging Science

College of Science

Rochester Institute of Technology

2004

Signature of the Author _____ // Original Signed // _____

Accepted by _____ // Original Signed // _____
Coordinator, Ph.D. Degree Program

Report Documentation Page		*Form Approved* *OMB No. 0704-0188*

Public reporting burden for the collection of information is estimated to average 1 hour per response, including the time for reviewing instructions, searching existing data sources, gathering and maintaining the data needed, and completing and reviewing the collection of information. Send comments regarding this burden estimate or any other aspect of this collection of information, including suggestions for reducing this burden, to Washington Headquarters Services, Directorate for Information Operations and Reports, 1215 Jefferson Davis Highway, Suite 1204, Arlington VA 22202-4302. Respondents should be aware that notwithstanding any other provision of law, no person shall be subject to a penalty for failing to comply with a collection of information if it does not display a currently valid OMB control number.

1. REPORT DATE **25 JAN 2005**	2. REPORT TYPE **N/A**	3. DATES COVERED **-**

4. TITLE AND SUBTITLE **Enhanced Spectral Modeling of Sparse Aperture Imaging Systems**	5a. CONTRACT NUMBER
	5b. GRANT NUMBER
	5c. PROGRAM ELEMENT NUMBER
6. AUTHOR(S)	5d. PROJECT NUMBER
	5e. TASK NUMBER
	5f. WORK UNIT NUMBER
7. PERFORMING ORGANIZATION NAME(S) AND ADDRESS(ES) **Rochester Institute of Technology**	8. PERFORMING ORGANIZATION REPORT NUMBER
9. SPONSORING/MONITORING AGENCY NAME(S) AND ADDRESS(ES)	10. SPONSOR/MONITOR'S ACRONYM(S)
	11. SPONSOR/MONITOR'S REPORT NUMBER(S)

12. DISTRIBUTION/AVAILABILITY STATEMENT **Approved for public release, distribution unlimited**

13. SUPPLEMENTARY NOTES **The original document contains color images.**

14. ABSTRACT

15. SUBJECT TERMS

16. SECURITY CLASSIFICATION OF:			17. LIMITATION OF ABSTRACT **UU**	18. NUMBER OF PAGES **338**	19a. NAME OF RESPONSIBLE PERSON
a. REPORT **unclassified**	b. ABSTRACT **unclassified**	c. THIS PAGE **unclassified**			

Standard Form 298 (Rev. 8-98)
Prescribed by ANSI Std Z39-18

CHESTER F. CARLSON
CENTER FOR IMAGING SCIENCE
COLLEGE OF SCIENCE
ROCHESTER INSTITUTE OF TECHNOLOGY
ROCHESTER, NEW YORK

CERTIFICATE OF APPROVAL

Ph.D. DEGREE DISSERTATION

The Ph.D. Degree Dissertation of Robert E. Introne
has been examined and approved by the dissertation
committee as satisfactory for the dissertation
requirement for the Ph.D. degree in Imaging Science

// Original Signed //
Dr. John R. Schott, Dissertation Advisor

// Original Signed //
Dr. Roger L. Easton

// Original Signed //
Dr. Robert D. Fiete

// Original Signed //
Dr. Michael W. Richmond

1 Sep 04
Date

DISSERTATION RELEASE PERMISSION
ROCHESTER INSTITUTE OF TECHNOLOGY
COLLEGE OF SCIENCE
CHESTER F. CARLSON CENTER FOR IMAGING SCIENCE

Title of Dissertation:

Enhanced Spectral Modeling of Sparse Aperture Imaging Systems

I, Robert E. Introne, hereby grant permission to the Wallace Memorial Library of the
Rochester Institute of Technology to reproduce my thesis in whole or in part. Any
reproduction will not be for commercial use or profit.

Signature _____ // Original Signed // _____

Date _____ 1 Sep 04 _____

Enhanced Spectral Modeling of
Sparse Aperture Imaging Systems

by

Robert E. Introne

Chester F. Carlson Center for Imaging Science
Rochester Institute of Technology

Abstract

The remote sensing community continues to pursue advanced sensor designs and post-processing techniques that improve upon the spatial quality of collected overhead imagery. Unfortunately, spaceborne applications frequently encounter launch vehicle fairing and weight constraints that limit the size of the primary aperture that can be utilized for a given application. Sparse aperture telescopes provide a potential avenue for overcoming some of the size and weight issues associated with deploying a large monolithic mirror system. These telescope systems are constructed of smaller subapertures which are phased to form a common image field and thereby synthesize a larger effective primary diameter to obtain higher spatial resolution than that achievable with a single subaperture.

Much of the research conducted to date in this sparse aperture arena has focused on the panchromatic image quality performance of various optical configurations through approaches that make use of resampled, gray-scale imagery products. The research effort performed in conjunction with this dissertation focused on laying the groundwork for synthetic model-based approaches for evaluating the optical performance of sparse aperture collection systems with enhanced spectral fidelity and a polychromatic object scene. It entailed a fundamental investigation and demonstration of the first-principles physics required to model such imaging systems. This theoretical development ultimately led to the generation of a modeling concept that more rigorously addresses the spectral characteristics of classic sparse aperture optical configurations used in remote sensing applications. To demonstrate the proposed theoretical foundation, a proof-of-concept digital model was

implemented that incorporates essential components of the fundamental physical processes involved with typical sparse aperture collection systems, including any potential spectral effects unique to these design configurations.

In addition to modeling the detected imagery derived from the collection system, there was also an interest in exploring the quality implications of image restoration techniques typically required for sparse aperture imaging systems. Several variations of the classic Wiener-Helstrom filter were implemented and investigated in response to this research objective. The basic restoration methodologies pursued in this effort provide a foundation for research into more advanced techniques in the future. Finally, a top-level sensitivity study of the image quality performance of various sparse aperture pupil configurations subjected to varying levels of subaperture dephasing and/or aberrations was performed. This exploration of the trade space focused on a panchromatic detection scenario and attempted to bound the performance region where unique spectral quality issues are observed for the unconventional collection telescopes targeted through this research effort.

Contents

List of Figures

List of Tables

Nomenclature

Symbol	Definition
A_{det}	Detector Area
A_{eff}	Equivalent filled aperture area
α	Tobin coefficient for photodiode dark current 1/f noise
$\alpha(\lambda)$	Photon absorption coefficient (wavelength dependent)
c	Speed of light
$C_n^2[h]$	Refractive index structure constant (height dependent)
D	Optical system primary aperture diameter (exit pupil)
D_{eff}	Effective synthesized aperture diameter
D_{enc}	Physical diameter of an equivalent filled aperture
D_{obs}	Primary mirror linear obscuration (hole)
$D_{\mathrm{sub,obs}}$	Subaperture primary mirror linear obscuration (hole)
D_{sub}	Subaperture primary diameter (exit pupil)
$E_{\mathrm{de}}(\lambda)$	Emissive downwelled irradiance
$E_{\mathrm{ds}}(\lambda)$	Reflected downwelled irradiance
$E_{\mathrm{inc}}(\lambda)$	Spectral irradiance incident at the entrance pupil
$E_{\mathrm{s,exo}}(\lambda)$	Exoatmospheric direct solar irradiance
$\varepsilon(\lambda)$	Target emissivity
f	Optical system effective focal length
$f\#$	Optical system f-number (f/D)
$f[m,n]$	Digitally sampled object image intensity
$\hat{f}[m,n]$	Digitally sampled estimate of object image intensity
$f[x,y]$	Object image amplitude
$f_{\mathrm{obj}}[x,y]$	Object image intensity
$\hat{f}_{\mathrm{obj}}[x,y]$	Estimate of object image intensity
F	Hemispherical open sky fraction

Symbol	Definition
F_{fill}	Optical system fill factor
$F[k,l]$	Digitally sampled Fourier spectrum of the object intensity
$F[\xi,\eta]$	Fourier spectrum of the object image amplitude
$F_{\text{obj}}[\xi,\eta]$	Fourier spectrum of the object image intensity
$\hat{F}_{\text{obj}}[\xi,\eta]$	Estimate of object image intensity Fourier spectrum
$F_{\text{obj,gray}}[\xi,\eta]$	Fourier spectrum of the gray-world object image intensity
$g[m,n]$	Digitally sampled output image intensity
$g[x,y]$	Output image amplitude
$G\#$	Ratio of radiance to irradiance onto a detector
G_{conv}	Detector conversion gain [volts/electron]
G_{elec}	Analog signal chain electronic gain [unitless]
$G[\xi,\eta]$	Fourier spectrum of the output image amplitude
$G_{\text{incoh}}[\xi,\eta]$	Fourier spectrum of the incoherent output image intensity
GSD_{GM}	Ground Sample Distance (geometric mean)
h	Planck's constant
$\mathscr{h}[m,n]$	Digitally sampled Point Spread function
$\mathscr{h}[x,y]$	Incoherent Point Spread function (PSF)
$h[x,y]$	Coherent Point Spread Function
$\mathscr{H}[k,l]$	Digitally sampled Optical Transfer Function
$\mathscr{H}[\xi,\eta]$	Incoherent Optical Transfer Function (OTF)
$\lvert\mathscr{H}[\xi,\eta]\rvert$	Modulation Transfer Function (MTF)
$H[\xi,\eta]$	Coherent transfer function
$I[x,y;\ z=0]$	Object image intensity
$I[x,y;z_1,z_2]$	Output image intensity
$J_{\text{DC}}[T]$	Temperature-dependent dark current density [nA/cm^2]
k	Boltzmann's constant
K	Electron-to-count conversion factor
K_{ap}	Constant relating sparse aperture MTF to fill factor
(k,l)	Discrete frequency coordinates for a digital image spectrum

Symbol	Definition
$L_{be}(\lambda)$	Emissive background radiance
$L_{bgnd}(\lambda)$	Total background radiance reaching a sensor
$L_{bs}(\lambda)$	Reflected background radiance
L_{dep}	Detector depletion depth
L_{diff}	Electron diffusion length
$L_{emis}(\lambda, T)$	Self-emitted radiance of a blackbody at temperature T
$L_{e,tot}(\lambda)$	Total emissive radiance reaching a sensor
$L_{r,tot}(\lambda)$	Total reflective radiance reaching a sensor
$L_{source}(\lambda)$	Total source radiance reaching a sensor
$L_{source,FT}(\xi, \eta, \lambda)$	Fourier Transform of the source radiance reaching a sensor
$L_{target}(\lambda)$	Total target radiance reaching a sensor
$L_{ue}(\lambda)$	Emissive upwelled radiance
$L_{us}(\lambda)$	Reflected upwelled radiance
λ	Central detected wavelength
λ_{max}	Maximum detected wavelength
λ_{min}	Minimum detected wavelength
$m_{obj}[m,n]$	Local mean for $(2M+1)^2$ region of a digital image
$\hat{m}_{obj}[m,n]$	Estimate of digital image local mean
MTF_{aber}	Aberrated optics MTF
MTF_{ap}	Unaberrated aperture MTF (real-valued OTF)
MTF_{det}	Detector aperture MTF
MTF_{diff}	Detector carrier diffusion MTF
MTF_{jitter}	Image jitter (random line-of-sight motion) MTF
MTF_{poly}	Effective polychromatic system MTF
MTF_{smear}	Image smear (linear line-of-sight motion) MTF
MTF_{sys}	Total imaging system MTF
$\mu[\xi, \eta]$	Normalized scene spectrum
$\mu_{gray}[\xi, \eta]$	Normalized gray-world scene spectrum
(m,n)	Discrete spatial coordinates for a digital image

Symbol	Definition
n	Number of binary digits associated with the sensor A/D
n_{sub}	Number of subapertures on an arm of a Tri-arm system
n_{TDI}	Number of TDI stages for a scanning sensor
n_{tot}	Total noise amplitude in a pixel [counts]
$n_{tot}[m,n]$	Digitally sampled total white Gaussian noise
$n[x,y]$	Total additive noise
$n_i[x,y]$	Normally distributed i^{th} noise source (zero mean, unit variance)
$n_{tot}[m,n]$	Digitally sampled total noise profile
$N[\xi,\eta]$	Total noise spectrum (Fourier Transform of the noise)
$N_i[\xi,\eta]$	Frequency spectrum of the normally distributed i^{th} noise source
$\eta(\lambda)$	Spectral quantum efficiency of the detector
OTF_{ap}	Aberrated aperture OTF (complex valued)
p	Detector pixel pitch
$p[x,y]$	Optical system pupil function
$\mathcal{P}[x,y]$	Aberrated optical system pupil function (complex-valued)
$p_i[x-x_i,y-y_i]$	Pupil function for the ith subaperture
$P[\xi,\eta]$	Fourier Transform of the pupil function
P_{target}	Total target signal count in a M x M digital image
P_{bgnd}	Total background signal count in a M x M digital image
$\Phi(\lambda)$	Spectral flux incident at the entrance pupil
$\Phi_p(\lambda)$	Photon spectral flux incident at the entrance pupil
Φ_{phot}	Target photon arrival rate at the entrance pupil
$\Phi_{phot,bgnd}$	Background photon arrival rate at the entrance pupil
q	Electron charge; energy per photon
QSE	Quantum Step Equivalence
θ_{el}	Target elevation angle
r	Exit pupil plane radial spatial coordinate
$r(\lambda)$	Target diffuse reflectance (for radiance calculations)
r_0	Atmospheric coherence diameter

Symbol	Definition
R	Target-to-sensor range
$R(\lambda)$	Detector spectral response function
R_{dc}	Total effective dark current generation rate
$r_{ff}[m,n]$	Auto-correlation of the sampled object image intensity $f[m,n]$
$r_{fg}[m,n]$	Cross-correlation between $f[m,n]$ and $g[m,n]$
$r_{gg}[m,n]$	Auto-correlation of the sampled output image $g[m,n]$
ρ	Exit pupil plane radial spatial frequency coordinate
ρ_{co}	Optical system cutoff frequency
$\rho(\lambda)$	Target bidirectional reflectance (for radiance calculations)
R_0A	Photodiode resistance-area product
s	Scale factor between ground plane and focal plane
$s[m,n]$	Sampled detected output signal (including PSF effects)
$\hat{s}[m,n]$	Estimate of digital output signal $s[m,n]$
$S[k,l]$	Fourier Transform of sampled output signal $s[m,n]$
S_{ADC}	Sensor A/D input voltage range (max output voltage)
S_{bgnd}	Detected background signal in a pixel [electrons]
$S_{counts}[x,y]$	Two-dimensional object image signal [counts]
$S_e[x,y]$	Two-dimensional object image signal [electrons]
$S_f[k,l]$	Digitally sampled object image power spectrum
$S_f[\xi,\eta]$	Object image power spectrum
$S_g[k,l]$	Digitally sampled output image power spectrum
$S_g[\xi,\eta]$	Output image power spectrum
S_{LSB}	Voltage range of the least significant bit in the sensor A/D
$S_n[k,l]$	Digitally sampled noise power spectrum
$S_n[\xi,\eta]$	Noise power spectrum
$S_{obj}[k,l]$	Digitally sampled signal power spectrum
S_{freq}^{out}	Spectrum of detected output signal (including OTF effects)
S_{space}^{out}	Detected output signal (including PSF effects) [counts]
S_{counts}^{pix}	Object image signal in a pixel [counts]

Symbol	Definition
S_{sig}	Detected signal in a pixel [electrons]
S_{target}	Detected target signal in a pixel [electrons]
S_{freq}^{target}	Spectrum of detected target signal (including OTF effects)
S_{volt}	Detected signal in a pixel [volts]
SNR_{pix}	Output signal-to-noise ratio in the spatial domain
$SNR_{out}[\xi,\eta]$	Frequency spectrum of the output signal-to-noise ratio
SNR_{thresh}	Threshold signal-to-noise ratio for minimum acceptable quality
σ'	Solar declination angle
σ_{bgnd}	Background photon (shot) noise [electrons e$^-$]
σ_{dc}	Dark current shot noise [e$^-$]
$\sigma_{dc,therm}$	Dark current thermal noise (photodiode detector) [e$^-$]
$\sigma_{dc,1/f}$	Dark current 1/f noise (photodiode detector) [e$^-$]
σ_{elec}	Signal chain electronics noise [e$^-$]
$\sigma_g^2[m,n]$	Local variance of a digital output image
$\hat{\sigma}_g^2[m,n]$	Estimate of the local variance of a digital output image
σ_K^2	Noise power spectrum to object power spectrum constant
σ_n^2	Variance of a zero-mean white Gaussian noise source
$\sigma_{obj}[m,n]$	Local standard deviation for $(2M+1)^2$ region of a digital image
σ_{phot}	Target photon (shot) noise [e$^-$]
σ_{quan}	Quantization noise [e$^-$]
σ_{read}	Detector readout noise [e$^-$]
σ_{tot}	Total image noise (standard deviation in the signal) [rms e$^-$]
σ_{photon}^{total}	Total photon noise (target + background) [e$^-$]
$\sigma_{volts,sc}$	Signal chain electronics noise [volts]
$\sigma_{volt,read}$	Detector readout noise [volts]
T	Temperature
T_d	Dark current doubling temperature
T_{int}	Detector integration time
T_{recal}	Time period from that last dark current calibration

Symbol	Definition
T_{ref}	Dark current reference temperature
τ_1	Sun-to-target atmospheric transmission
τ_2	Target-to-sensor atmospheric transmission
τ_{opt}	Optical system transmittance
V_b	Detector voltage bias
ΔV_x	Imaging platform velocity error in the x-direction
ΔV_y	Imaging platform velocity error in the y-direction
$w[m,n]$	Digitally sampled spatial-domain Wiener filter
$w[x,y]$	Effective optical path difference (OPD)
$w_i[x-x_i,y-y_i]$	Effective optical path difference (OPD) of the ith subaperture
$w_{FIR}[m,n]$	Finite Impulse Response (FIR) Wiener filter
$w_{loc}[m,n]$	Localized digital spatial-domain Wiener filter
$w_{WF}[x,y]$	Spatial-domain Wiener filter
$W[k,l]$	Digitally sampled frequency-domain Wiener filter
$W[\xi,\eta]$	Frequency-domain Wiener filter
$W_{loc}[k,l]$	Localized digital frequency-domain Wiener filter
$W_{PI}[k,l]$	Digitally sampled frequency-domain pseudo-inverse filter
WFE_{rms}	rms wavefront error
(x,y)	Exit pupil plane rectangular coordinates
(x_0,y_0)	Detector plane rectangular coordinates
(ξ,η)	Exit pupil plane spatial frequency coordinates
(ξ_{mid},η_{mid})	Exit pupil plane mid-spatial frequency range coordinates
x_p	Detector width in the x-dimension
y_p	Detector width in the y-dimension
Δx_{GP}	Ground (object) plane incremental distance
Δx_{FPA}	Focal plane (image) plane incremental distance
z_1	Distance from object plane to entrance pupil
z_2	Distance from exit pupil to focal plane

Chapter 1

Introduction

The remote sensing community is constantly searching for new sensor implementations and post-processing techniques that improve upon the spatial resolution of collected imagery. In the last decade or so, the community has also witnessed a burgeoning interest in developing system designs for spectral applications. In an attempt to pursue both high spatial and spectral resolution simultaneously, one often finds that significant design compromises are required in one mission area or the other, with system signal-to-noise ratio (SNR) constituting one of the principal design drivers. This design tradeoff becomes particularly prominent in spaceborne applications, where launch vehicle fairing and general weight constraints often limit the size of the primary aperture that can be incorporated into the collection system design. Sparse aperture telescopes provide one means for skirting some of the size and weight issues associated with deploying a large monolithic mirror system to achieve high spatial resolution in a space-based imagery collection application.

In general, a sparse aperture system involves the synthesis of a larger effective primary aperture through the combination of separate, smaller optical systems (or subapertures) which are phased to form a common image field. Obviously, the objective of phasing smaller individual optical systems is to achieve spatial resolution comparable to a single larger effective aperture while reducing size, weight, mirror complexity and cost. Much of the research conducted to date in the sparse aperture arena has focused on the image quality of these optical configurations in panchromatic applications. A significant portion of the latter has emphasized modeling diffraction effects and system noise for various sparse aperture pupil functions with resampled panchromatic imagery from an actual aerial sensor. The research effort proposed here focuses on laying the groundwork for synthetic model-based evaluation of the optical performance of sparse aperture collection systems designed for both panchromatic and multispectral applications. It will entail a fundamental investigation and demonstration of the physics required to model such a collection system, including the incorporation of appropriate spectral effects.

The theoretical development proposed for this research activity will ultimately lead to the generation of a modeling concept for some of the classic sparse aperture optical configurations, including the annulus, Golay-6, and tri-arm system designs. The emphasis for the theoretical modeling effort will be placed on reasonably wide-field-of-view, extended scene remote sensing scenarios. Issues associated with a polychromatic system Modulation Transfer Function (MTF), spectrally diverse noise spectrum, pupil phase errors introduced at the subaperture-level, and radiometrically accurate scene generation will be addressed. To demonstrate the overall integrity of the proposed theoretical foundation for spectrally diverse sparse aperture system modeling, a strawman digital model will be implemented that incorporates key components of the fundamental physical processes explored above. Where possible, the general results of this computer model will be verified through appropriate comparisons with open-literature theory, existing panchromatic simulations, and available experimental data.

Although sparse aperture telescopes offer an opportunity to attack the problem of higher spatial resolution in spaceborne collection systems, spectral quality issues (especially those related to SNR) are likely to become even more problematic for these design configurations. The latter observation is based on the fact that sparse aperture systems generally manifest a lower inherent collection SNR than that exhibited by equivalent monolithic aperture systems, and attempts to recover MTF performance at comparable SNR tends to introduce correlated noise artifacts into the imagery. In addition, although preliminary research efforts have addressed certain issues associated with optimal Wiener filtering techniques for sparse aperture panchromatic imagery reconstruction, there has not been a dedicated effort to explore optimal filtering techniques that address the spectral implications of sparse aperture derived imagery.

The issues alluded to above drive the interest in investigating various post-processing and image restoration techniques for sparse aperture system collection data as a prominent goal of this research endeavor. Study efforts of interest in this arena include optimal conventional and adaptive Wiener filter implementations based on scene content and pupil configuration

under investigation. For this goal-level task, various image reconstruction methodologies will be evaluated on the basis of the strawman prediction implementation discussed above to address resulting data quality performance for both panchromatic and multispectral imagery. Completion of this research goal will help demonstrate the power of computer modeling for conducting system design trades and the development of post-processing algorithms for general sparse aperture configurations.

Chapter 2

Objectives

This chapter provides a general overview of the objectives associated with this research effort. As alluded to previously, the overall objective of this scientific endeavor is to advance the current state of knowledge associated with sparse aperture telescope system quality, especially as it relates to potential spectral applications. In pursuit of this overarching objective, there are certain requirements that must be satisfied and additional value-added tasks that can be categorized as goals which are not required. Section 2.1 outlines specific success criteria deemed necessary for completion of dissertation requirements. General research goals that are being targeted above and beyond the stated requirements appear in Section 2.2.

2.1 Success Criteria

The specific objectives associated with this research effort are itemized below:

- Develop a firm understanding of the underlying physics and first-principles phenomenology related to sparse aperture telescope configurations utilized for imaging applications involving extended scenes. Specific technical areas of interest include the following:
  - System-level diffraction effects associated with specific pupil configurations and characterized in terms of the system Modulation Transfer Function (MTF) and Point Spread Function (PSF).
  - Photon, dark current, and read noise effects related to certain sparse aperture system designs and their contribution to image quality performance.
  - System-level telescope phase error measurement, evaluation, modeling and tolerancing relative to certain sparse aperture configurations.
  - Various image restoration techniques required to recover image quality performance commensurate with equivalent monolithic mirror systems.

- Specific spectral considerations related to the issues enumerated above and the overall quality of data collection for potential panchromatic and multispectral sparse aperture imaging system applications.

- Develop the overarching theoretical and mathematical basis for computer modeling of the system performance associated with typical sparse aperture telescope designs emphasizing remotely sensed, extended scenes with appropriate spectral content. Specific items to be addressed in this theoretical development include the following:
  - Scene spectral radiance incident at the entrance pupil plane, including source spectral radiometry, atmospheric propagation, and imaging sensor interactions.
  - Wavefront propagation from the entrance pupil of the sparse aperture telescope to the detection sensor, including the accommodation of pupil phase errors.
  - Polychromatic system MTF characterization, including the effects of aperture configuration, system aberrations, and phase errors.
  - Spectrally diverse noise characterization, including the effects of photon, dark current, and read noise sources.

- Implement a proof-of-concept digital model demonstrating application of the theoretical development proposed above for typical sparse aperture collection systems. Specific objectives of this proof-of-concept digital implementation are enumerated below:
  - Derive synthetic extended scene radiance field images which exhibit high spatial resolution, radiometric accuracy, and appropriate spectral diversity for use as object imagery within a larger sparse aperture system simulation. Scenes of interest include a spectrally diverse United States Air Force (USAF) three-bar resolution chart displaying a variety of spatial frequencies, as well as a more complicated synthetically derived scene utilizing the DIRSIG and MODTRAN computer models.
  - Develop polychromatic system MTF algorithms that appropriately model various sparse aperture configurations and their action on the pristine object radiance images discussed above. Physical phenomena to be addressed in this

6

MTF evaluation include pupil function, focal plane, optical design aberrations, line of sight errors (jitter and smear), and system phase errors.

– Develop spectrally diverse noise models that capture the principal photon (source and background), dark current and read noise source physics under the assumption individual contributors are statistically independent.

– Demonstrate implementation of an approach for accommodating optical wavefront phase errors from individual sparse aperture telescope subapertures into the MTF analytical technique explored above.

2.2 Goals

The following goals have been identified for this research effort to help reinforce the value of the basic requirements established in the previous section:

- Implement proof-of-concept post-processing and image restoration algorithms for general sparse aperture system configurations operating in panchromatic or multispectral collection modes. Specific processing techniques and evaluations targeted in this research effort include:

    – Implementation of a basic Wiener-Helstrom filter for boosting MTF amplitudes at mid-range frequencies to recover image quality performance commensurate with equivalent monolithic apertures. This Wiener filter is designed to provide a baseline for future processing development and associated design sensitivity analyses.

    – Evaluation of the optimum noise-to-signal power spectrum term to utilize within conventional Wiener-Helstrom filters applied to source data from certain sparse aperture system configurations. This investigation will include various sensitivity analyses that address the tradeoffs between recovering MTF performance and the associated noise amplification penalty.

    – Development of advanced adaptive Wiener filter techniques that utilize combinations of scene content-derived power spectrum terms, localized statistical sampling, and spatially variant filtering operations. Results of any advanced filtering techniques pursued in conjunction with this research effort

will be compared to the baseline Wiener-Helstrom filter output described above.

- – Investigation of spectral diversity considerations associated with the various image processing and reconstruction techniques under consideration for general sparse aperture system configurations. Issues of interest include product radiometric integrity, noise amplification effects, correlated noise artifacts, MTF character implications, signal-to-noise impacts, etc. This evaluation also maintains a goal of studying the potential utilization of spectral diversity to derive improved estimates of the signal and noise power spectra within any of the Wiener filter realizations explored in the discussion above.

- Perform sensitivity analyses on critical sparse aperture system parameters and their impact on overall image and spectral quality performance. Specific performance areas of interest in the sparse aperture design trade space include the following:
  - – General sparse aperture configuration, sizing and positioning of subapertures, and the associated MTF character demonstrated by the system pupil function. This sensitivity study will address the image and spectral product quality associated with several of the classic sparse aperture configurations.
  - – Effective signal-to-noise ratio (SNR) exhibited by the system before and after the application of various image post-processing techniques. This performance study will look at the tradeoffs between SNR and correlated noise gain.
  - – Residual rms wavefront error (WFE) and/or phase errors at the subaperture level contributing an asymmetric performance profile at the system level. This sensitivity study will effectively address the image quality impact of random errors exhibited at the subaperture level.

Chapter 3

Theory

This chapter highlights the essential theoretical foundation upon which this research effort is based. The material of relevance to this investigation can essentially be categorized into five principal areas: (1) object scene radiance, (2) imaging system modulation, (3) detected image noise, (4) image restoration, and (5) miscellaneous sparse aperture system issues. Before launching into the theory associated with these individual categories, this chapter provides a brief summary of pertinent linear systems theory in Sections 3.1 and 3.2, which establish the cornerstone for the proposed system performance modeling. Section 3.3 subsequently provides detailed development of the scene radiance and associated signal equation for a typical remote sensing imaging scenario, including the potential for sparse aperture imaging system collection. The general concept of a sparse aperture system is developed and compared to conventional telescope aperture configurations in Section 3.4. Overall imaging system performance is characterized in terms of system modulation transfer function (MTF) and point spread function (PSF) in Sections 3.5 through 3.13. Section 3.14 provides background and fundamentals on system noise modeling for general overhead imaging systems, including a brief discussion on signal-to-noise ratio (SNR) as it relates to sparse aperture systems. Image restoration techniques appropriate for the degraded raw imagery anticipated from sparse aperture systems are discussed in Section 3.15. Finally, several specific performance issues unique to sparse aperture collection systems are summarized in Section 3.16.

3.1 Imaging Linear Systems Theory

Although most imaging systems are not both linear and space-invariant in the strictest mathematical sense, especially in the presence of optical aberrations, one can generally identify *isoplanatic* patches in the image field where they can be approximated as linear, shift-invariant for the purposes of modeling. Such an approximation ultimately enables one to model the action of the imaging system on an input object scene through use of a system *impulse response* to a delta function, commonly referred to as the *point spread function*

(PSF). Given the assumption of a linear, shift-invariant imaging system, the predicted output image in the absence of noise can be approximated through the following space domain expression:

$$g[x, y] = f[x, y] * h[x, y] \qquad (1)$$

where $f[x,y]$ is representative of the object plane radiance, $h[x,y]$ is the impulse response or PSF of the system, $g[x,y]$ is the acquired output image, and "$*$" is the mathematical symbol for convolution. The PSF identified in the equation above essentially quantifies the amount of "blur" the imaging system introduces for a point within the object scene. The system expressed in equation 1 can also be evaluated in the frequency domain by applying well-known properties of the Fourier transform. In general, the Fourier transform is mathematically described for continuous functions through the following operation:

$$F[\xi, \eta] = \mathscr{F}\{f[x, y]\} = \int\limits_{-\infty}^{+\infty}\int f[x, y] e^{-2\pi i(\xi x + \eta y)} dx dy \qquad (2)$$

where $f[x,y]$ is the function in the spatial domain, $F[\xi, \eta]$ is its Fourier transform pair in the frequency domain, and $\mathscr{F}\{\cdot\}$ is shorthand notation for the Fourier transform operand represented by the integral on the right hand side. One can apply the mathematical expression contained in equation 2 to each of the spatial functions in equation 1 to determine the corresponding Fourier transform pairs. This operation produces $G[\xi, \eta]$, $F[\xi, \eta]$ and $H[\xi, \eta]$ for the frequency responses of the output image $g[x,y]$, input object radiance $f[x,y]$ and point spread function $h[x,y]$, respectively. In addition, it is well established in linear systems theory through the filter theorem that convolution in the spatial domain is equivalent to multiplication in the frequency domain. Therefore, the linear, shift-invariant system described by equation 1 can be converted to the following equivalent expression in the frequency domain:

$$G[\xi, \eta] = F[\xi, \eta] \cdot H[\xi, \eta] \qquad (3)$$

The Fourier transform $H[\xi, \eta]$ of the PSF is commonly referred to as the complex system *optical transfer function* (OTF), whose normalized magnitude is the *modulation transfer function* (MTF). The transfer function magnitude is typically normalized to be unity at zero spatial frequency, which will be highlighted more extensively in the mathematical development of the OTF and MTF to follow. Frequently, system performance is easier to characterize in terms of the OTF or MTF, which has the added benefit of transforming two-dimensional convolution into simpler array multiplication. Thus, the frequency response of a noiseless imaging system is frequently characterized through equation 3, with the final spatial domain output image $g[x,y]$ generated by performing the inverse Fourier transform of the output image frequency response $G[\xi, \eta]$. For continuous functions, the inverse transform is defined by the following mathematical operation:

$$g[x,y] = \mathscr{F}^{-1}\{G[\xi,\eta]\} = \int\int_{-\infty}^{+\infty} G[\xi,\eta] e^{+2\pi i(\xi x + \eta y)} d\xi d\eta \tag{4}$$

where $\mathscr{F}^{-1}\{\cdot\}$ represents the inverse Fourier transform operator. Accordingly, one can implement a simple model for a linear, shift-invariant imaging system by computing the Fourier transforms of the object radiance "image" and the system PSF, performing array multiplication, and subsequently computing the inverse transform of the system to generate the predicted output image. Of course, the theoretical development discussed above assumed continuous functions, so one would have to implement discrete versions of equations 1-4 in order to deal with digitally sampled images and transfer functions. This is a reasonably straightforward procedure to accomplish, involving a zero-padding operation to ensure the discrete arrays have the same size and the use of Fast Fourier Transform (FFT) algorithms for discrete implementation of the continuous Fourier transform expressions found above.

Of course, the system model constructed in equations 1 and 3 is extremely oversimplified, lacking a fundamental attribute of any imaging system: *noise*. To first order, the latter can be captured in the model by including a statistically independent, additive random noise contribution to the output image:

$$g[x, y] = f[x, y] * h[x, y] + n[x, y] \tag{5}$$

where $n[x,y]$ represents the spatially varying, total additive noise present in the system. The system identified in equation 5 can be re-expressed in the frequency domain, which again takes advantage of the filter theorem and the linearity of the Fourier transform to produce:

$$G[\xi, \eta] = F[\xi, \eta] \cdot H[\xi, \eta] + N[\xi, \eta] \tag{6}$$

where $N[\xi, \eta]$ is the frequency spectrum of the additive noise component.

3.2 Incoherent Imaging System

For remote sensing applications involving sparse aperture systems, we are generally interested in the characteristics of linear systems exposed to incoherent radiation. Of course, given the unique attributes of a sparse aperture telescope, it is certainly possible that partial coherence or quasi-monochromatic conditions can arise even with an extended incoherent source, depending on the passband of the optical detector. This topic will be raised in greater detail with the interferometric considerations discussed in Chapter 4. For now the emphasis will remain with the principal physical phenomenon that will be encountered by a remote sensing collection system: that of incoherent light. As traditional optical detectors are sensitive to image intensity rather than complex amplitude, incoherent imaging systems are actually linear in *intensity*. Accordingly, if $g[x,y]$ represents the output image amplitude, the detected output image on the left side of equation 5 for incoherent systems is actually represented by the detected image intensity $I[x,y]$ or $g_{\text{incoh}}[x, y]$:

$$I[x, y] = |g[x, y]|^2 = g[x, y]g^*[x, y] = g_{\text{incoh}}[x, y] \tag{7}$$

where $g^*[x,y]$ is the complex conjugate of the complex image amplitude. Since incoherent systems are linear with intensity, one also finds that the convolution of interest in equation 5 involves the object source intensity $I[x,y; z = 0]$ or $f_{\text{obj}}[x, y]$ with the incoherent PSF ($\mathscr{A}[x,y;z_1,z_2]$). In this convention, z_1 is the object distance to the entrance pupil and z_2 is the image distance from the exit pupil to the detector plane. As a consequence of these

considerations, equation 5 is rewritten for clarity by representing an incoherent imaging system as follows:

$$
\begin{aligned}
g_{\text{incoh}}[x, y; z_1, z_2] &= |f[x, y]|^2 * |h[x, y; z_1, z_2]|^2 + n[x, y] \\
&= I[x, y; z = 0] * \mathscr{A}[x, y; z_1, z_2] + n[x, y] \\
&= f_{\text{obj}}[x, y] * \mathscr{A}[x, y] + n[x, y]
\end{aligned}
\tag{8}
$$

where $f[x,y]$ is the object complex amplitude, $h[x,y;z_1,z_2]$ is the coherent impulse response, $\mathscr{A}[x,y;z_1,z_2]$ is the complementary incoherent impulse response or PSF of interest, and $n[x,y]$ now represents noise intensity consistent with incoherent detection. From equation 8, it is readily apparent that an incoherent detection system is assumed to be linear and shift-invariant in object intensity and the incoherent PSF is the squared-magnitude of its coherent counterpart. To gain insight into the character of the impulse response, one can model a typical imaging device through a simple lens system approximation, whereby light propagates a distance z_1 from the object plane to the entrance pupil of the system in the Fresnel diffraction region, is "imaged" by a series of optics whose action on the incident field can be represented by a Gaussian lens law, and then experiences Fresnel propagation over a second distance z_2 to the detection plane. With such a model, Goodman (1968) derives the impulse response of the system assuming coherent illumination:

$$
\begin{aligned}
h[x, y; z_1, z_2] &= \frac{1}{\lambda^2 z_1 z_2} \exp\left[\frac{2\pi i(z_1 + nl + z_2)}{\lambda}\right] \exp\left[\frac{i\pi(x^2 + y^2)}{\lambda z_2}\right] \mathscr{F}\{p[x, y]\}\Big|_{\xi = \frac{x}{\lambda z_2}, \eta = \frac{y}{\lambda z_2}} \\
&= \frac{1}{\lambda^2 z_1 z_2} \exp\left[\frac{2\pi i(z_1 + nl + z_2)}{\lambda}\right] \exp\left[\frac{i\pi r^2}{\lambda z_2}\right] P\left[\frac{x}{\lambda z_2}, \frac{y}{\lambda z_2}\right]
\end{aligned}
\tag{9}
$$

where $P[\xi, \eta]$ is the Fourier transform of the optical system pupil function $p[x,y]$. From the equation above, it is apparent that the dominant term of the coherent PSF of an imaging system is the scaled Fourier transform of the optical system pupil function, which (up to an additional scale and phase factor) is the predicted Fraunhofer diffraction pattern of the system pupil function. The character of the coherent transfer function $H[\xi, \eta]$ can be evaluated by taking the Fourier transform of equation 9:

$$H[\xi,\eta] = \mathcal{F}\{h[x,y]\} \propto \mathcal{F}\left\{\frac{1}{\lambda^2 z_1 z_2} P\left[\frac{x}{\lambda z_2}, \frac{y}{\lambda z_2}\right]\right\} = \frac{z_2}{z_1} p[-\lambda z_2 \xi, -\lambda z_2 \eta] \qquad (10)$$

where the final result is achieved through application of the Fourier transform-of-a-transform property. From equation 10, one can see that the coherent transfer function essentially involves a scaled pupil function preceded by the system magnification (z_2/z_1). Although this research effort will concentrate on incoherent applications, the coherent response and transfer functions are the basic building blocks for their incoherent counterparts. This can be observed in the derivation of the incoherent PSF ($\mathscr{A}[x,y;z_1,z_2]$):

$$\mathscr{A}[x,y;z_1,z_2] = |h[x,y;z_1]|^2 = \frac{1}{\lambda^4 z_1^2 z_2^2}\left|\mathcal{F}\{p[x,y]\}\right|_{\xi=\frac{x}{\lambda z_2}, \eta=\frac{y}{\lambda z_2}}\right|^2 = \frac{1}{\lambda^4 z_1^2 z_2^2}\left|P\left[\frac{x}{\lambda z_2}, \frac{y}{\lambda z_2}\right]\right|^2 \qquad (11)$$

where it becomes apparent that the incoherent impulse response is proportional to the squared magnitude of the scaled Fourier transform of the pupil function. Similarly, one finds that the incoherent transfer function or OTF ($\mathscr{H}[\xi,\eta]$) involves the complex autocorrelation of the coherent transfer function, as observed by taking the Fourier transform of the incoherent PSF:

$$\begin{aligned}
\mathscr{H}[\xi,\eta] &= \mathcal{F}\{\mathscr{A}[x,y;z_1,z_2]\} = \mathcal{F}\left\{h[x,y;z_1,z_2]^2\right\} \\
&= \mathcal{F}\{h[x,y]\} * \mathcal{F}\{h^*[x,y]\} \\
&= H[\xi,\eta] \star H^*[\xi,\eta]
\end{aligned} \qquad (12)$$

where "$\star$" represents the mathematical symbol for correlation between two functions as defined by the expression above. If one subsequently substitutes the expression for the coherent transfer function from equation 10 into equation 12, the following relation is acquired for the complex OTF of an incoherent collection aperture:

$$\mathscr{H}[\xi,\eta] = \frac{z_2^2}{z_1^2} p[-\lambda z_2 \xi, -\lambda z_2 \eta] \star p^*[-\lambda z_2 \xi, -\lambda z_2 \eta] \qquad (13)$$

14

where the leading term is observed to be the magnification squared. For diffraction-limited pupils that are real-valued, symmetric functions, one can simplify this expression even further to develop the general proportional relation:

$$\text{OTF}[\xi,\eta] = \mathcal{H}[\xi,\eta] \propto p[\lambda z_2 \xi, \lambda z_2 \eta] \star p[\lambda z_2 \xi, \lambda z_2 \eta] \qquad (14)$$

The formulations contained in equations 13 and 14 identify the classic Fourier optical result that the OTF of an optical system in incoherent light is proportional to the autocorrelation of the scaled aperture or pupil function. As a matter of clarification, one should note that all of the OTF and PSF expressions derived so far have not been normalized, a practice which is fairly common in the field today. The intention of this section was simply to introduce the concepts in the context of the appropriate linear systems theory. Slightly more rigorous development of the normalized impulse response and transfer functions typically used in practice will appear in Sections 3.5 and 3.6.

Given the space-domain expression for the detected image intensity in equation 8, one can derive a corresponding relationship in the frequency domain by taking the Fourier transform of both sides. This leads to the equation for the frequency spectrum $G_{incoh}[\xi,\eta]$ of the detected incoherent image:

$$\begin{aligned} G_{incoh}[\xi,\eta] &= \mathcal{F}\{I[x,y;z_1,z_2]\} \\ &= \mathcal{F}\{I[x,y;z=0]\} \cdot \mathcal{F}\{\hbar[x,y]\} + \mathcal{F}\{n[x,y]\} \\ &= F_{obj}[\xi,\eta] \cdot \mathcal{H}[\xi,\eta] + N[\xi,\eta] \end{aligned} \qquad (15)$$

where $F_{obj}[\xi,\eta]$ represents the frequency spectrum of the original object intensity, i.e., the Fourier transform of $|f[x,y]|^2$. One can easily see the parallelism between the incoherent system represented by equation 15 and the system introduced in equation 6 for a generic linear, shift-invariant imaging device. Clearly, equation 15 defines the need to characterize the system in terms of its OTF ($\mathcal{H}[\xi,\eta]$) and noise spectrum ($N[\xi,\eta]$) to predict the acquired output image in the frequency domain. With such a prediction, it is a simple matter of applying the inverse Fourier transform to arrive at the detected output image intensity:

$$I[x, y] = \mathscr{F}^{-1}\{G_{\text{incoh}}[\xi, \eta]\} = g_{\text{incoh}}[x, y] \qquad (16)$$

Such an approach effectively solves the linear system defined in equation 8 making use of the power and implementation ease of the Fourier transform. Equations 8 and 15 also provide the fundamental foundation for modeling incoherent systems, and one will consequently find much of the subsequent theoretical development to follow focuses on deriving appropriate expressions for the system components in each.

3.3 Scene Radiance and Detected Signal

In accordance with the linear systems theory just discussed, one of the first critical physical components that must be properly modeled is the radiance from the imaged object scene. For the incoherent problem under consideration, it is the radiance incident at the entrance pupil of the collection aperture that is of immediate interest. Schott (1997) has shown that the governing equation for the total source radiance $L_{\text{source}}(\lambda)$ reaching a sensor in a certain spectral passband can be approximated by the following relation:

$$\begin{aligned}
L_{\text{source}}(\lambda) &= E_{\text{s,exo}}(\lambda)\cos\sigma'\tau_1(\lambda)\tau_2(\lambda)\frac{\rho(\lambda)}{\pi} + \varepsilon(\lambda)L_{\text{emis}}(\lambda, T)\tau_2(\lambda) + FE_{\text{ds}}(\lambda)\tau_2(\lambda)\frac{r(\lambda)}{\pi} \\
&+ FE_{\text{de}}(\lambda)\tau_2(\lambda)\frac{r(\lambda)}{\pi} + (1-F)[L_{\text{bs}}(\lambda) + L_{\text{be}}(\lambda)]\tau_2(\lambda)r(\lambda) + L_{\text{us}}(\lambda) + L_{\text{ue}}(\lambda)
\end{aligned} \qquad (17)$$

where $E_{\text{s,exo}}(\lambda)$ is the exoatmospheric direct solar irradiance, $L_{\text{emis}}(\lambda, T)$ is the self-emitted radiance for a blackbody at temperature T, $E_{\text{ds}}(\lambda)$ is the reflected downwelled irradiance, $E_{\text{de}}(\lambda)$ is the emissive downwelled irradiance, $L_{\text{bs}}(\lambda)$ and $L_{\text{be}}(\lambda)$ are the reflected and emissive background radiance, and $L_{\text{us}}(\lambda)$ and $L_{\text{ue}}(\lambda)$ are the reflected and emissive upwelled radiance. In addition to the radiation terms defined above, the governing equation also contains the following key expressions: atmospheric transmission (τ_1) along the sun-target path, atmospheric transmission (τ_2) along the target-sensor path, target reflectance (ρ), target reflectance (r) assuming it is diffuse, target emissivity (ε), solar declination angle (σ') to the target, and the fraction (F) of the hemisphere above the target that is sky. As written, this equation essentially captures all of the possible radiation transfer mechanisms that may contribute to any arbitrary collection scenario.

16

Frequently, it is possible to reduce the complicated expression contained in equation 17 for a particular spectral regime. For instance, in the reflective part of the electromagnetic spectrum, many of the thermal and/or self-emission terms are negligibly small and can therefore be ignored. Similarly, for collection in the emissive part of the spectrum, the reflective terms become negligible and can largely be eliminated. Given these considerations, equation 17 generally reduces to the following form for collection in the reflective region:

$$L_{r,\text{tot}} = \left[E'_{s,\text{exo}} \cos \sigma' \tau_1 \frac{\rho}{\pi} + FE_{ds} \frac{r}{\pi} + (1-F)L_{bs}r \right]\tau_2 + L_{us} \tag{18}$$

where $L_{r,\text{tot}}$ is the reflective radiance reaching the sensor and the "λ" notation has been dropped for convenience. Thus, for collection in the reflective (V/NIR) part of the spectrum, the governing equation has only direct reflected solar, downwelled radiance (skylight), reflected background radiance, and upwelled (path) radiance components. By analogy to equation 18, a similar construct applies for the relevant radiation components in the emissive part of the spectrum. In this case, where the reflective terms in equation 18 are negligibly small, the thermal radiance ($L_{e,\text{tot}}$) reaching a sensor takes the form:

$$L_{e,\text{tot}} = \left[\varepsilon L_{\text{emis}}(T) + FE_{de} \frac{r}{\pi} + (1-F)L_{be}r \right]\tau_2 + L_{ue} \tag{19}$$

where the "λ" notation has been dropped for clarity. Thus for thermal (LWIR) collection, the governing equation reduces to thermal self-emission, emissive downwelled radiance, thermal background radiance, and the self-emitted component of upwelled radiance as the dominant contributions to the radiance reaching a sensor. Obviously, if one designs a collection system that is sensitive between these two extremes, each radiation term contained in the full expression in equation 17 must be evaluated as a potential contributor to the final output image signal depending on the scenario (e.g., MWIR during daytime conditions). Given the complicated nature of the expressions above, it is fairly common practice to rely on higher fidelity atmospheric transmission and radiometry models, such as MODTRAN, to compute the source radiance reaching a sensor.

As just discussed, equation 17 constitutes the governing relation for the total radiance incident at the entrance aperture of a collection system. For the purposes of analysis, especially investigations of system signal-to-noise (SNR), it is a fairly common practice to segregate the signal from the actual target of interest and that due to non-target or background effects. Such an approach essentially re-expresses the formulation in equation 17 to the following alternative:

$$L_{\text{source}}(\lambda) = L_{\text{target}}(\lambda) + L_{\text{bgnd}}(\lambda) \tag{20}$$

where $L_{\text{target}}(\lambda)$ is the spectral radiance due to the target and $L_{\text{bgnd}}(\lambda)$ is that due to the background. Such a bookkeeping exercise ultimately results in the following terms being assigned to the expression for the target radiance:

$$
\begin{aligned}
L_{\text{target}}(\lambda) = {} & E_{s,\text{exo}}(\lambda)\cos\sigma'\tau_1(\lambda)\tau_2(\lambda)\frac{\rho(\lambda)}{\pi} + \varepsilon(\lambda)L_{\text{emis}}(\lambda)\tau_2(\lambda) \\
& + F\big[E_{ds}(\lambda) + E_{de}(\lambda)\big]\tau_2(\lambda)\frac{r(\lambda)}{\pi} + (1-F)\big[L_{bs}(\lambda) + L_{be}(\lambda)\big]\tau_2(\lambda)r(\lambda)
\end{aligned} \tag{21}
$$

Given the target radiance terms identified above and ignoring potential stray light within the optical system, the remaining terms within the "big equation" are lumped together to form the following relation for background radiance:

$$L_{\text{bgnd}}(\lambda) = L_{us}(\lambda) + L_{ue}(\lambda) \tag{22}$$

where the path radiance dominates. Other potential lower-level background signal terms that could be added to the expression above include optical system stray-light and atmospheric adjacency effect radiance contributors.

With the expressions for source radiance enumerated above, one now has the essential building blocks to address the mathematical description of the object signal required by equations 8 and 15 above. To get the signal expression in the proper form, however, one must determine the integrated flux level at the detector from the computed radiance at the

entrance pupil of the imaging system. Once again, Schott (1997) demonstrates this conversion takes the following straightforward form:

$$S_{\text{volt}} = \int_0^\infty \Phi(\lambda)R(\lambda)d\lambda = \int_0^\infty E_{\text{inc}}(\lambda)A_{\text{det}}R(\lambda)d\lambda = \int_0^\infty \frac{L_{\text{source}}(\lambda)}{G\#}A_{\text{det}}R(\lambda)d\lambda \qquad (23)$$

where S_{volt} is the detected signal in volts, $\Phi(\lambda)$ is the incident spectral flux in terms of W/µm, $E_{\text{inc}}(\lambda)$ is the incident spectral irradiance, $L_{\text{source}}(\lambda)$ is the source spectral radiance computed via equation 17, $R(\lambda)$ is the detector spectral response in units of volts/W, A_{det} is the detector area, and $G\#$ is a classic camera equation expression that relates radiance to irradiance onto the detector. Since remote sensing systems generally demonstrate negligible magnification (i.e., they are effectively focused at infinity), the factor $G\#$ in the equation above can be approximated to reasonable accuracy via:

$$G\# = \frac{L_{\text{source}}(\lambda)}{E_{\text{inc}}(\lambda)} = \frac{4(f\#)^2}{F_{\text{fill}}\tau_{\text{opt}}\pi} \qquad (24)$$

where $f\#$ is the optical system F-number (the ratio of the effective focal length to the aperture diameter), τ_{opt} is the optical system transmittance, and F_{fill} is the effective fill factor for a sparse aperture system or unobscured aperture for a more conventional telescope. Substitution of equation 24 into 23 results in the following general expression for the detected signal in volts:

$$S_{\text{volt}} = \frac{\pi A_{\text{det}}F_{\text{fill}}}{4(f\#)^2} \int_0^\infty L_{\text{source}}(\lambda)\tau_{\text{opt}}(\lambda)R(\lambda)d\lambda \qquad (25)$$

where the spectral response function limits the integration to wavelengths within the spectral passband of the sensor. One should also note that this equation essentially computes the detected "object" signal for a single pixel and ignores the effects of any spatial frequency content. The importance of this observation will become more apparent in the discussion of the final object radiance or intensity derivation to follow.

Although this theoretical development could be used as the basis for computing the object intensity or frequency spectrum in equations 8 and 15, an alternative approach is frequently cited in the literature. One should consult the papers by Fiete (2001) and Lomheim (2002) for additional detail. The objective of both approaches is the same: to quantify the object "image" intensity in terms of signal counts as a basis for modeling the final image intensity at the focal plane. Instead of quantifying the detected signal in a pixel by integrating the spectral radiance over the sensor's spectral response function, these approaches initially compute the detected signal in electrons per pixel through use of the detector's spectral quantum efficiency $\eta(\lambda)$:

$$S_{\text{sig}} = \int_0^\infty \frac{\Phi(\lambda)}{q} T_{\text{int}} \eta(\lambda) d\lambda = \int_0^\infty \frac{E_{\text{inc}}(\lambda) A_{\text{det}}}{q} T_{\text{int}} \eta(\lambda) d\lambda \tag{26}$$

where S_{sig} is the detected signal in electrons, $\Phi(\lambda)$ is again the incident spectral flux, q is the energy per photon, and T_{int} is the detector integration time. If one subsequently substitutes the classic expression for the photon energy ($q = hc/\lambda$) and evaluates the spectral flux level via the system $G\#$, the following general expression for the detected signal is obtained:

$$S_{\text{sig}} = \int_0^\infty \frac{E_{\text{inc}}(\lambda) A_{\text{det}}}{hc / \lambda} T_{\text{int}} \eta(\lambda) d\lambda = \int_0^\infty \frac{L_{\text{source}}(\lambda)}{hcG\#} A_{\text{det}} T_{\text{int}} \eta(\lambda) \lambda d\lambda \tag{27}$$

where h is Planck's constant ($6.6256 \cdot 10^{-34}$ Joules·sec) and c is the speed of light ($2.9979 \cdot 10^8$ m/sec). Finally, one can substitute the expression for $G\#$ in equation 24 into the relation above to arrive at the single-pixel signal for an electro-optical imaging system:

$$S_{\text{sig}} = \frac{\pi A_{\text{det}} T_{\text{int}} F_{\text{fill}}}{4(f\#)^2 hc} \int_0^\infty L_{\text{source}}(\lambda) \tau_{\text{opt}}(\lambda) \eta(\lambda) \lambda d\lambda \tag{28}$$

where the signal is quantified in terms of electron count through appropriate integration over the source spectral radiance $L_{\text{source}}(\lambda)$. If one employed Time Delay Integration (TDI) with a scanning Focal Plane Array (FPA) to improve the signal-to-noise ratio (SNR), an additional term quantifying the number of TDI stages must be included in the numerator of equation 28. However, since most sparse aperture systems used in remote sensing are envisioned to

involve extended-duration access at high altitude, it is highly likely that some form of staring FPA would be utilized. In this case, equation 28 is appropriate for modeling the system as written. One should also note the high degree of parallelism between equations 25 and 28, indicating that either formulation would be appropriate for a particular set of sensor data. For further theoretical development of the object intensity, we will rely upon equation 28, as it tends to be a favorite amongst detector designers.

Ultimately, the computed signal in electrons is converted by the imaging sensor to a voltage equivalent to the signal derived in equation 25 and then quantized into digital counts by an A/D Converter. Lomheim (2002) indicates that the voltage conversion can be modeled by introducing appropriate gain factors into the signal expression found in equation 28 as follows:

$$S_{\text{volt}} = G_{\text{conv}} G_{\text{elec}} S_{\text{sig}} \tag{29}$$

where S_{volt} is again the detector output signal (measured in volts), including the effects of conversion gain (G_{conv}) and electronic gain (G_{elec}) in the signal chain from the FPA to the A/D Converter. In this expression, the conversion gain is expressed in units of volts/electron and is a function of the integration capacitance and the overall efficiency of electron-to-voltage conversion. The electronic gain, on the other hand, is a dimensionless factor that quantifies the voltage efficiency of the analog signal chain to the A/D Converter. The final object image output $S_{\text{counts}}^{\text{pix}}$ in digital counts can subsequently be evaluated as the ratio of the detector output signal S_{volt} in volts to the voltage range S_{LSB} of the least significant bit (LSB) of the A/D Converter:

$$S_{\text{counts}}^{\text{pix}} = \frac{S_{\text{volt}}}{S_{\text{LSB}}} = \frac{G_{\text{conv}} G_{\text{elec}} S_{\text{sig}}}{S_{\text{ADC}} / 2^n} \tag{30}$$

where S_{ADC} is the A/D Converter input voltage range (consistent with the maximum unsaturated output voltage of the FPA) and n represents the number of binary digits associated with the A/D Converter. Substitution of equations 28 and 29 into equation 30 yields a relation for the object image in digital counts:

$$S_{\text{counts}}^{\text{pix}} = \frac{G_{\text{conv}} G_{\text{elec}} 2^n}{S_{\text{ADC}}} \frac{\pi A_{\text{det}} T_{\text{int}} F_{\text{fill}}}{4(f\#)^2 hc} \int_0^\infty L_{\text{source}}(\lambda) \tau_{\text{opt}}(\lambda) \eta(\lambda) \lambda d\lambda \tag{31}$$

This expression essentially defines the object image "intensity" for a given detector pixel. An equivalent formulation can be derived for the entire object scene if one assumes the source spectral radiance consists of a spatially varying profile $L_{\text{source}}[x,y;\lambda]$. This ultimately leads to an expression for the two-dimensional object image $S_{\text{counts}}[x,y]$ in digital counts:

$$S_{\text{counts}}[x,y] = \frac{G_{\text{conv}} G_{\text{elec}} 2^n}{S_{\text{ADC}}} \frac{\pi A_{\text{det}} T_{\text{int}} F_{\text{fill}}}{4(f\#)^2 hc} \int_0^\infty L_{\text{source}}(x,y;\lambda) \tau_{\text{opt}}(\lambda) \eta(\lambda) \lambda d\lambda \tag{32}$$

where G_{conv} and G_{elec} can exhibit some spatial variance due to sensor-unique design attributes but will be treated as constants in this discussion. If one backtracked through the digital and analog signal chains, a comparable two-dimensional expression for the object image $S_e[x,y]$ in electrons could be derived:

$$S_e[x,y] = \frac{\pi A_{\text{det}} T_{\text{int}} F_{\text{fill}}}{4(f\#)^2 hc} \int_0^\infty L_{\text{source}}(x,y;\lambda) \tau_{\text{opt}}(\lambda) \eta(\lambda) \lambda d\lambda \tag{33}$$

This is the two-dimensional, spatially variant companion to the single-pixel signal expression in equation 28. This form of the object image will come in handy when discussing photon noise signal, which typically can be modeled as the square root of the expression due to observed Poisson statistics.

The detected signal relations derived above have consistently been referred to as the "object" image required for implementation of the space- and frequency-domain system models in equations 8 and 15. The reason for this distinction is the fact that these signal expressions have been developed assuming no spatial frequency modulation due to the OTF of the imaging system. As demonstrated previously, the spatial frequency content of the detected signal can be modeled in either domain depending on the availability of an impulse response (PSF) or transfer function (OTF) that properly characterizes the optical system. In the space

domain, a new expression for the actual detected "output" signal $S_{\text{space}}^{\text{out}}$ in the absence of noise can be computed by convolving the spatially varying detected signal profile from equation 32 with the system PSF:

$$S_{\text{space}}^{\text{out}}[x, y] = f_{obj}[x, y] * \mathscr{A}[x, y] = S_{\text{counts}}[x, y] * \text{PSF}[x, y] \tag{34}$$

where $f_{\text{obj}}[x,y]$ is the object image "intensity" $I[x,y; z = 0]$. This ultimately leads to a governing expression for the output signal in the space domain (in the absence of noise):

$$S_{\text{space}}^{\text{out}}[x, y] = \frac{G_{\text{conv}} G_{\text{elec}} 2^n}{S_{\text{ADC}}} \frac{\pi A_{\text{det}} T_{\text{int}} F_{\text{fill}}}{4(f\#)^2 hc} \int_0^\infty (\text{PSF}[x, y; \lambda] * L_{\text{source}}[x, y; \lambda]) \tau_{\text{opt}}(\lambda) \eta(\lambda) \lambda d\lambda \tag{35}$$

where it is observed that one must convolve the system PSF with the source spectral radiance at each wavelength prior to integrating over the passband of interest.

A completely analogous and generally easier-to-implement system can be developed by evaluating equation 35 in the frequency domain consistent with equation 15. This approach will yield an expression for the output image signal in the frequency domain (in the absence of noise):

$$S_{\text{freq}}^{\text{out}}[\xi, \eta] = F_{\text{obj}}[\xi, \eta] \cdot \mathscr{H}[\xi, \eta] = \mathscr{F}\{S_{\text{counts}}[x, y]\} \cdot \text{OTF}[\xi, \eta] \tag{36}$$

where $F_{\text{obj}}[\xi, \eta]$ is the frequency spectrum of the object image "intensity" and $\mathscr{H}[\xi, \eta]$ is the system OTF. If one inserts the Fourier transform of equation 32 into the expression above, the expression for the frequency response of the detected "output" signal $S_{\text{freq}}^{\text{out}}$ in the absence of noise can be derived:

$$S_{\text{freq}}^{\text{out}}[\xi, \eta] = \frac{G_{\text{conv}} G_{\text{elec}} 2^n}{S_{\text{ADC}}} \frac{\pi A_{\text{det}} T_{\text{int}} F_{\text{fill}}}{4(f\#)^2 hc} \int_0^\infty \text{OTF}[\xi, \eta, \lambda] L_{\text{source,FT}}[\xi, \eta, \lambda] \tau_{\text{opt}}(\lambda) \eta(\lambda) \lambda d\lambda \tag{37}$$

where $L_{\text{source,FT}}[\xi, \eta, \lambda]$ represents the Fourier transform of the source spectral radiance profile including appropriate scale factors. This expression effectively becomes the governing

equation for the source signal in the frequency domain. Since it involves the simpler mathematical operation of multiplication of the system OTF and source spectral radiance profile within the wavelength-dependent integration, this equation is used extensively and will be the backbone for the proposed proof-of-concept modeling activity proposed in this research effort.

Fiete (2001) and Fienup (2000) suggest that the frequency-domain governing equation derived in equation 37 can be simplified for those optical systems that exhibit a real-valued system OTF. In these cases, where the MTF is comparable to the OTF, the detected output signal in the frequency domain can be approximated by:

$$
\begin{aligned}
S_{\text{freq}}^{\text{out}}[\xi,\eta] &= F_{\text{obj}}[\xi,\eta] \cdot \mathscr{H}[\xi,\eta] \\
&= S_{\text{counts}}^{\text{pix}} \frac{F_{\text{obj}}[\xi,\eta]}{F_{\text{obj}}[0,0]} \big|\mathscr{H}[\xi,\eta]\big| \\
&= S_{\text{counts}}^{\text{pix}} \mu[\xi,\eta]\text{MTF}[\xi,\eta]
\end{aligned}
\tag{38}
$$

where $S_{\text{counts}}^{\text{pix}}$ is representative of the mean count level for the final object image, $F_{\text{obj}}[\xi,\eta]$ is again the source radiance spectrum, and $F_{\text{obj}}[0,0]$ is the source spectrum evaluated at zero frequency ($\xi = 0, \eta = 0$). For simplicity the spectral dependence notation has been dropped to focus on the physical effect on the spatial frequency character. In effect, equation 38 accounts for the spatial variability within the source spectral radiance profile by introducing the normalized scene Fourier transform into the spectrum calculation. By convention, this normalized scene spectrum $\mu[\xi,\eta]$ is defined by:

$$
\mu[\xi,\eta] = \frac{F_{\text{obj}}[\xi,\eta]}{F_{\text{obj}}[0,0]}
\tag{39}
$$

and is routinely used as a means to resample high-resolution imagery for predictive image simulations. The value of this formulation can be readily seen because the source radiance spectrum term $L_{\text{source,FT}}[\xi,\eta,\lambda]$ in equation 37 can essentially be evaluated as a separable function, consisting of a two-dimensional spatial frequency component $\mu[\xi,\eta]$ and a spectral

component $L_{source}(\lambda)$. Under this construct, equation 37 can be converted to the following general approximation for the detected output signal in the frequency domain:

$$S_{freq}^{out}[\xi,\eta] = \frac{G_{conv}G_{elec}2^n}{S_{ADC}} \frac{\pi A_{det}T_{int}F_{fill}}{4(f\#)^2 hc} \int_0^\infty \frac{F_{obj}[\xi,\eta,\lambda]}{F_{obj}[0,0,\lambda]} MTF[\xi,\eta,\lambda]L_{source}(\lambda)\tau_{opt}(\lambda)\eta(\lambda)\lambda d\lambda \qquad (40)$$

where the wavelength dependence of the normalized scene spectrum and MTF have been re-introduced for clarity.

Fiete (2002) and Boucher (2000) have defined a so-called "polychromatic" MTF that spectrally weights individual MTF realizations at a given wavelength and then derives an average MTF over the spectral passband of interest. This treatment has been applied to many simulated systems, including those with sparse apertures. The general nature of this polychromatic MTF formulation will be discussed in greater detail in Section 3.13. However, the objective of defining such a transfer function is really quite simple: to make the integrand in the governing expression found in equation 37 more tractable, especially when resampling existing object scenes over a given passband. This is accomplished by effectively eliminating the spectral dependency of the MTF term in the expression and allowing it to be pulled outside the integral, as in the following approximation to the governing equation for the output signal spectrum:

$$S_{freq}^{out}[\xi,\eta] = \frac{G_{conv}G_{elec}2^n}{S_{ADC}} \frac{\pi A_{det}T_{int}F_{fill}}{4(f\#)^2 hc} MTF_{poly}[\xi,\eta] \int_0^\infty \frac{F_{obj}[\xi,\eta,\lambda]}{F_{obj}[0,0,\lambda]} L_{source}(\lambda)\tau_{opt}(\lambda)\eta(\lambda)\lambda d\lambda \qquad (41)$$

Fiete (2002) and Boucher (2000) generally perform simulations that resample high-resolution panchromatic aerial imagery. While such an approach generates good predictions of overall image quality, it also removes the true spectral character associated with the normalized scene spectrum in equation 37. As a result of resampling a gray-scale object scene (the high-resolution panchromatic image), the normalized scene spectrum ratio effectively loses its dependence on wavelength and can be pulled outside the integral for ease of computation:

$$S_{\text{freq}}^{\text{out}}[\xi,\eta] = \frac{G_{\text{conv}}G_{\text{elec}}2^n}{S_{\text{ADC}}} \frac{\pi A_{\text{det}} T_{\text{int}} F_{\text{fill}}}{4(f\#)^2 hc} \frac{F_{\text{obj,gray}}[\xi,\eta]}{F_{\text{obj,gray}}[0,0]} \text{MTF}_{\text{poly}}[\xi,\eta] \int_0^\infty L_{\text{source}}(\lambda) \tau_{\text{opt}}(\lambda) \eta(\lambda) \lambda d\lambda \qquad (42)$$

In this expression, one will note that the normalized scene spectrum for a gray scene $\mu_{\text{gray}}[\xi,\eta]$ does not depend on wavelength and is accordingly defined as follows:

$$\mu_{\text{gray}}[\xi,\eta] = \frac{F_{\text{obj,gray}}[\xi,\eta]}{F_{\text{obj,gray}}[0,0]} \qquad (43)$$

where $F_{\text{obj,gray}}[\xi,\eta]$ is the source radiance spectrum for the gray panchromatic scene used as the basis for the simulation. The resampling approach that utilizes some form of equation 42 has proven to be quite successful for conventional apertures, which generally produce a smoothly varying and circularly symmetric MTF. However, such an approximate approach may not adequately capture the spectral character of a sparse aperture system MTF, which generally exhibits non-symmetric cutoff frequencies and irregular spatial frequency modulation. This research will endeavor to investigate the potential spectral implications of a sparse aperture system by capturing more of the first-principles physics embodied by equations 35 and 37. In fact, the enhanced spectral fidelity simulations presented in the results in Chapter 5 of this dissertation rely exclusively on a digital model implementation of equations 35 and 37, with the physics in equation 42 only captured when a gray-world model comparison is performed.

With an assessment of the output signal in the frequency domain per the expressions derived thus far, we now have developed one of the key building blocks for evaluating the postulated linear system in equation 15. The remaining critical components include detailed development of the system OTF in equation 37 and the total system noise spectrum $N[\xi,\eta]$, which will occur in the following sections. With the development of the spectral radiance terms pursued above, equation 15 can be reformulated via:

$$\begin{aligned} G_{\text{incoh}}[\xi,\eta] &= F_{\text{obj}}[\xi,\eta] \cdot \mathcal{H}[\xi,\eta] + N[\xi,\eta] \\ &= S_{\text{freq}}^{\text{out}}[\xi,\eta] + N[\xi,\eta] \end{aligned} \qquad (44)$$

where $G_{incoh}[\xi, \eta]$ again represents the final incoherent image spectrum in the frequency domain. The final output image intensity is obtained by taking the inverse Fourier transform of the image spectrum expression in equation 44. This produces the general-purpose equation for the output image prediction in the space domain:

$$g_{incoh}[x,y] = \mathscr{F}^{-1}\{G_{incoh}[\xi,\eta]\} = \mathscr{F}^{-1}\{S_{freq}^{out}[\xi,\eta]\} + \mathscr{F}^{-1}\{N[\xi,\eta]\}$$
$$= S_{space}^{out}[x,y] + n[x,y] \tag{45}$$

This relationship is effectively a restatement of equation 8 with the detected scene output signal replaced by the inverse Fourier transform of the rigorous expression contained in equation 37 or the resampled approximation developed in equation 42.

3.4 System Pupil Function

From the discussion in Sections 3.1 and 3.2, it is clear that one fundamental characteristic of any imaging system is the function that describes the overall pupil geometry, commonly referred to as the *pupil function*. This is generally a "zero-one" function that defines the region over which the optical system is sensitive to incident photons and is equivalent to the exit pupil or aperture stop. From a geometric viewpoint, most conventional optical systems (e.g., Ritchey-Chrétien and Cassegrainian) with near-diffraction-limited performance can be approximated via real-valued pupil functions whose dominant character exhibits rotational symmetry. Sparse aperture systems, on the other hand, generally do not exhibit such circular symmetry, although their geometric diffraction-limited pupil functions are typically composed of arrays of conventional apertures that can be represented as real-valued pupil functions.

Of course, all real-world imaging devices have some aberrations inherent in their optical prescriptions, leading to a phase profile across the aperture that can be modeled by a complex pupil function. For sparse aperture systems, this aberration issue becomes more problematic, as even diffraction-limited subapertures can introduce detrimental "aberration-like" effects if they are not properly phased on a relative basis. As a consequence, subaperture phasing is one of the more significant technological challenges associated with sparse aperture

27

collection systems. It also drives the paramount need to represent a sparse aperture system through a complex pupil function in order to properly capture the physics of the collection problem. The following section will focus on the basic geometry considerations and the differences between conventional aperture and sparse aperture systems under investigation in this research effort. This will require a discussion of various real-valued pupil functions in order to introduce the concept of sparse aperture systems. The more fundamental problem of modeling the physics associated with subaperture aberrations and phasing physics will be captured in the complex pupil function discussion in Section 3.7.

3.4.1 Conventional Apertures

As alluded to previously, a conventional diffraction-limited aperture typically is described by a real-valued pupil function with some (frequently rotational) symmetry, although this is not a fundamental or necessary constraint. By restricting the discussion to the most common configurations, one will find that imaging systems with monolithic primary mirrors tend to have circular or rectangular pupils that can be described through classic special functions discussed in length by Gaskill (1978) and Easton (2003). As examples, some of the more common pupil functions for conventional optical system apertures are depicted in Figure 1.

| (a) Cylinder | (b) Obscured Cylinder | (c) Rectangle |
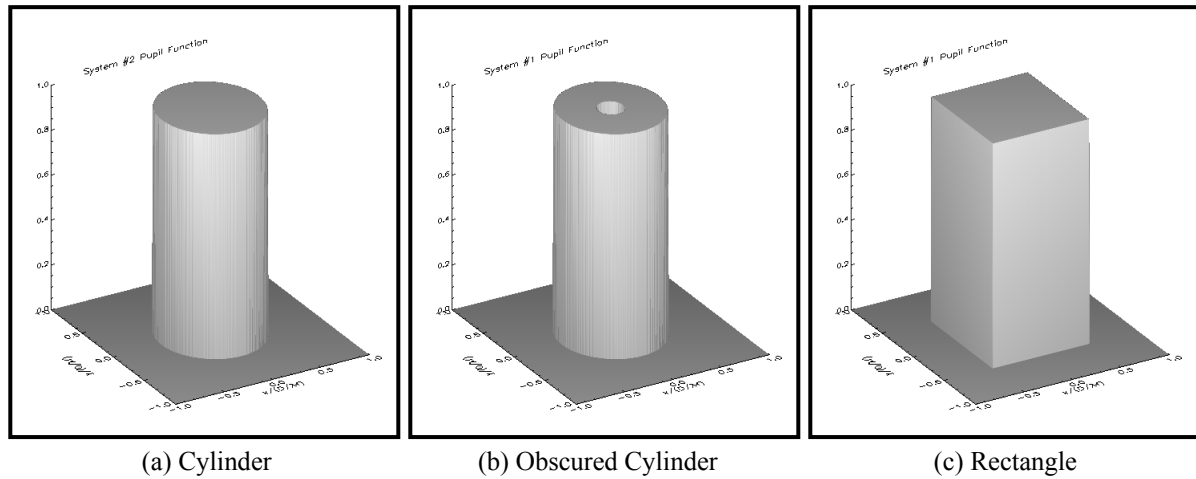
Figure 1: Special function descriptions for common optical apertures and subapertures.

Figure 1(a) shows the diffraction-limited pupil function for a filled circular aperture of diameter D, which mathematically can be represented by Gaskill's cylinder (CYL) function:

$$p[x, y] = CYL\left[\frac{r}{D}\right] = \begin{cases} 1, & 0 \le r < \frac{D}{2} \\ \frac{1}{2}, & r = \frac{D}{2} \\ 0, & r > \frac{D}{2} \end{cases} \qquad (46)$$

where r is the radial spatial coordinate:

$$r = \left(x^2 + y^2\right)^{1/2} \qquad (47)$$

In a similar fashion, the classic Cassegrainian and Ritchey-Chrétien systems use folded optics. The resulting obscuration from the secondary mirror can be modeled as the difference of two CYL functions. Accordingly, the diffraction-limited pupil function for the Cassegrainian family of apertures can be described mathematically through:

$$p[x, y] = CYL\left[\frac{r}{D}\right] - CYL\left[\frac{r}{D_{\text{obs}}}\right] \qquad (48)$$

where D is the diameter of the aperture stop or exit pupil and D_{obs} is the diameter associated with the secondary mirror linear obscuration. An example of such a configuration is depicted in Figure 1(b). Finally, a less common but still plausible optical aperture for remote sensing can be constructed using Gaskill's two-dimensional rectangle (RECT) function, shown in Figure 1(c). Systems with rectangular apertures tend to have better signal-to-noise ratios because of the larger aperture area, but at the expense of increased manufacturing difficulty. It is introduced here for completeness and as a potential subaperture building block for sparse aperture applications. Using Gaskill's convention, a square pupil function is described via:

$$p[x, y] = RECT\left[\frac{x}{b}, \frac{y}{d}\right] = RECT\left[\frac{x}{b}\right]RECT\left[\frac{y}{d}\right] \qquad (49)$$

where b is the width of the aperture in the x-dimension and d is the width in the y-dimension. By convention, the two-dimensional RECT profile is separable, being composed of several one-dimensional functions that are defined by the following relationship:

$$RECT\left[\frac{x}{b}\right] = \begin{cases} 0, & \left|\frac{x}{b}\right| > \frac{1}{2} \\ \frac{1}{2}, & \left|\frac{x}{b}\right| = \frac{1}{2} \\ 1, & \left|\frac{x}{b}\right| < \frac{1}{2} \end{cases} \qquad (50)$$

3.4.2 Sparse Aperture Configurations

We have now arrived at the point where it is appropriate to describe the general nature of sparse aperture imaging systems. In general, a sparse aperture system synthesizes a larger effective collection aperture diameter from an array of smaller subapertures. This aperture synthesis is accomplished by optically phasing separate optical systems or subapertures to form a combined image field. If phased properly, the spatial resolution of that system will exceed the performance of any individual element. The obvious objective of such a system is to obtain optical resolution commensurate with the larger synthesized aperture through the use of smaller (and less expensive) telescopes or optical elements. Such a configuration becomes especially attractive for high-altitude remote sensing applications, where the competing requirements of high spatial resolution and limited payload volume tend to severely restrict the design trade space. In satellite platforms, for example, operationally deploying a large monolithic mirrored optical system required for extended-duration access over a region of interest becomes very problematic due to launch vehicle fairing and weight-to-orbit constraints.

A sparse aperture system has the potential to overcome some of the design constraints associated with a high-altitude mission, since the phased system of subapertures will ultimately be lighter and perhaps more compact. Of course, alignment, integration, test and deployment are all likely to be more complicated compared to a monolithic optical system. In addition, the earlier discussion demonstrates that one of the most significant technological challenges associated with these systems is acquiring and maintaining the relative phasing between the subapertures, which in effect amounts to maintaining the optical path difference (OPD) between the various optical subsystems to within a small fraction of a wavelength (e.g., $1/10^{th}$ of wave). Despite these technical hurdles, however, sparse aperture systems may be feasible for certain high-altitude imaging missions that otherwise would be impossible with a conventional aperture system.

In general, there are two distinct classes of sparse aperture configurations that appear regularly in the literature. One is the class of *fixed* sparse aperture optical systems, whose OTF exhibits extensive, non-variable spatial-frequency coverage. The other is the family of telescopes or interferometers classified as *synthetic* sparse aperture configurations, which are distinguished from fixed systems in that they provide greatly reduced spatial-frequency coverage and rely upon imaging system motion to sweep out the remaining frequency plane in time. This research is specifically focused on the family of fixed sparse aperture systems.

(a) Conventional Telescope

(b) Multiple Telescope   (c) Common Secondary
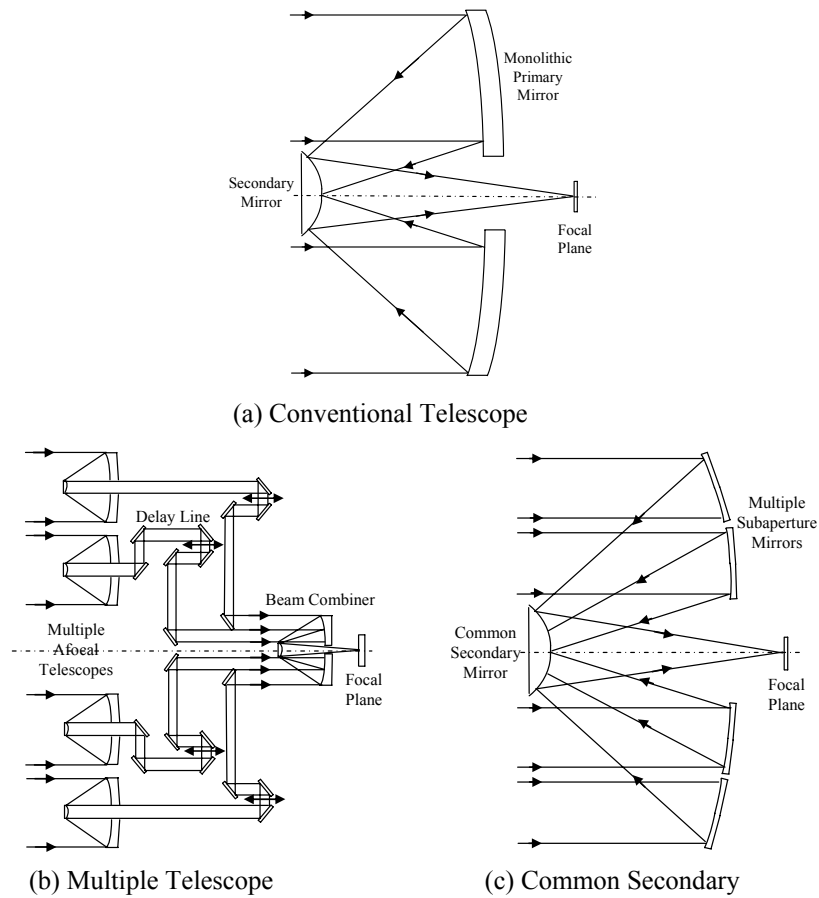
Figure 2: Conventional versus sparse aperture telescope configurations.

Within the fixed class of imaging systems, two traditional optical system configurations have been proposed: (1) multiple phased telescopes and (2) phased subapertures feeding a common secondary. Figure 2 shows perspective views of these two standard sparse aperture optical configurations, along with a more conventional monolithic system. The system in

Figure 2(a) depicts a traditional folded telescope configuration, with a monolithic primary mirror feeding a secondary (as in a Cassegrainian or Ritchey-Chretien optical system). At the bottom left, Figure 2(b) shows a planform diagram of a multiple-telescope sparse aperture system design. This system configuration typically consists of an array of afocal optical systems that transfer the incident radiance through individual delay lines into a combiner telescope to form the final image field. Given a multiple-telescope configuration, it is essential that the trombone and folding mirrors in the delay line maintain the OPD to within the necessary tolerances. At the bottom right, Figure 2(c) illustrates a standard method for packaging a phased array of optical subapertures with a common secondary mirror. In practice, the common secondary approach is typically associated with arrays of fewer subapertures due to packaging considerations. The smaller set of non-redundant array configurations originally proposed by Golay (1971) exemplifies the optical layouts for such an implementation.

Meinel (1970) demonstrated that the key to maintaining acceptable image quality in a generic sparse aperture system is ensuring that the demagnified exit pupil is a scaled copy of the entrance pupil. This effectively requires that the pupils be matched with no lateral, longitudinal, rotational, or tilt errors. Traub (1986) restated this overriding sparse aperture system requirement with crystal clarity: "… beams from separated telescopes must be recombined so that they appear to be coming directly from a single large telescope which has been masked so as to reproduce exactly the ensemble of collecting telescopes." Such a design rule is tantamount to ensuring the individual fields from each collection subaperture add constructively to achieve the higher optical performance of the synthesized telescope aperture.

As with conventional telescope apertures, the top-level optical character of sparse aperture systems can be quantified in terms of the system pupil function. For diffraction-limited performance that satisfies the subaperture phasing and pupil matching requirement (i.e., no aberrations or pupil geometry errors), one can again generally characterize the pupil in terms of real-valued special functions similar to those discussed previously for conventional

32

apertures. For the fixed sparse aperture optical configurations in Figure 2, the conventional apertures are summed to form the overall pupil function:

$$p[x,y] = \sum_{i=1}^{N} p_i[x - x_i, y - y_i]$$

(51)

where $p_i[x,y]$ represents the pupil function for the ith subaperture and the coordinate $[x_i,y_i]$ defines the displacement of each individual subaperture from the origin tied to the larger synthesized aperture. Equation 51 indicates that the pupil function of a typical diffraction-limited sparse aperture system is represented simply by the conventional aperture building blocks described in the previous section.

The construct described above enables the diffraction-limited, incoherent aperture OTF to be evaluated through an appropriate mathematical autocorrelation operation of the system geometric pupil function. This is shown in Figure 3 for several conventional and sparse aperture system configurations with the same physical encircled aperture at a given central wavelength. The conventional collection apertures on the left side of the figure (epitomized by the filled circular and Cassegrainian systems) exhibit the classic circular triangle (CTRI) function character and cutoff frequencies discussed by Goodman (1968) and Easton (2003). On the other hand, the annular, tri-arm and Golay sparse aperture systems display a dramatic reduction in modulation at mid-range frequencies and a unique character of the cutoff frequency. The ability to mathematically model various diffraction-limited pupil functions and their associated broadband, spectrally dependent, aberrated OTF constitutes a principal foundation for the proof-of-concept modeling discussed in Chapter 4. As mentioned above, the preliminary OTF calculations contained in Figure 3 are simply single-wavelength autocorrelations of the unaberrated pupil function. One must ultimately incorporate additional analysis to capture the physics associated with a real-world aperture, as will be discussed in further detail.

In addition to the great reduction in modulation exhibited by all of the sparse aperture systems, one should also take note of the rapid spatial variations in the OTF envelope and the reduced cutoff frequency (ergo reduced resolution) exhibited in particular by the tri-arm and

Golay apertures. The latter fact would imply that these systems need to be larger to achieve the same effective spatial resolution as their conventional counterparts. It also raises the concern that these systems may exhibit spectral artifacts that will be exacerbated by any subsequent restoration. This spectral issue is a principal concern of this research effort.
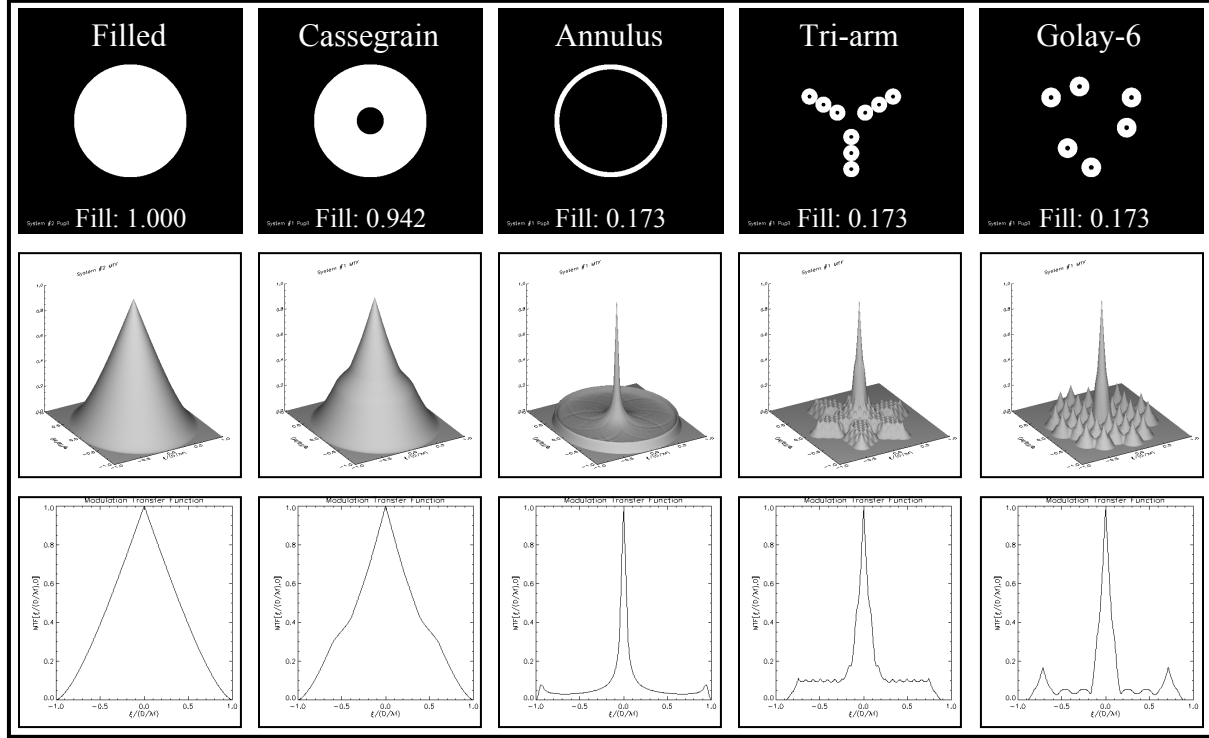
Figure 3: Sample optical system configurations and associated diffraction-limited aperture modulation transfer functions (MTF).

3.5 Optical Transfer Function

This section provides further detail on computing the normalized form of the incoherent *optical transfer function* (OTF), whose general character was originally introduced in the linear systems theory developed in Sections 3.1 and 3.2. As discussed previously, the transfer function (OTF) and impulse response (PSF) of a given imaging device are Fourier transform pairs:

$$\text{OTF}[\xi, \eta, \lambda] = \mathcal{F}\{\text{PSF}[x, y, \lambda]\} \tag{52}$$

where each representation is a function of wavelength. Goodman (1968) and Gaskill (1978) have shown that the transfer function of a coherent imaging system is a scaled replica of its pupil function:

$$H[\xi,\eta] = p[\lambda z_2 \xi, \lambda z_2 \eta] \tag{53}$$

where $H[\xi,\eta]$ is the coherent OTF, λ is the monochromatic wavelength under investigation and z_2 is the distance to the imaging plane. Such an expression shows that the coherent OTF acts like a simple low-pass filter. Through development similar to that contained in Section 3.2, Goodman and Gaskill subsequently derived expressions for the normalized OTF of an incoherent imaging system consistent with the following formulation:

$$\text{OTF} = \mathscr{H}[\xi,\eta] = \frac{p[\lambda z_2 \xi, \lambda z_2 \eta] \star p[\lambda z_2 \xi, \lambda z_2 \eta]}{\int\limits_{-\infty}^{+\infty}\int |p[x,y]|^2 dxdy} \tag{54}$$

Under this construct, it is readily apparent that the incoherent OTF of a system is effectively evaluated as the normalized autocorrelation of the coherent transfer function. Of course, the latter is simply the scaled pupil function defined by the exit pupil of the imaging system. *Accordingly, the OTF for a system used in incoherent radiation is evaluated through the normalized autocorrelation of the scaled pupil function as defined in equation 54.* As observed in the denominator of equation 54, the conventional normalization is the area of the squared magnitude of the pupil function.

The basic formulation of equation 54 can be further clarified by introducing notation for the autocorrelation operation as well as noting that the diffraction-limited pupil function is typically a zero-one function. The former clarification expands the notation to show that the autocorrelation is the convolution of the pupil function with the complex conjugate of a reversed replica. The latter (and often more useful) observation replaces the normalization factor in the denominator by an equivalent expression for the area of the exit pupil. In tandem, these two items allow equation 54 to be rewritten:

35

$$\text{OTF} = \frac{p[\lambda z_2 \xi, \lambda z_2 \eta] \star p[\lambda z_2 \xi, \lambda z_2 \eta]}{\displaystyle\int\limits_{-\infty}^{+\infty}\!\!\int p[x,y]dxdy}$$

$$= \frac{p[x,y] * p^*[-x,-y]\Big|_{x=\lambda f\xi, \, y=\lambda f\eta}}{\displaystyle\int\limits_{-\infty}^{+\infty}\!\!\int p[x,y]dxdy} \tag{55}$$

thereby providing a roadmap for computing the autocorrelation of the system pupil and simplifying the normalization process. Gaskill has shown that the revised OTF relation can be further simplified by evaluating the convolution and area integrals in the expression, noting that the area of the pupil can be computed by applying the central ordinate theory. The latter allows one to replace the area integral in the denominator with an equivalent expression involving the Fourier transform of the pupil function evaluated at zero frequency ($\xi = 0, \eta = 0$). Through these means, Gaskill ultimately derives a relation consistent with the following expression for the incoherent OTF given a zero-one pupil function:

$$\text{OTF} = \mathscr{H}[\xi,\eta] = \frac{\displaystyle\int\limits_{-\infty}^{+\infty}\!\!\int p[\alpha,\beta]p^*[\alpha - \lambda z_2 \xi, \beta - \lambda z_2 \eta]d\alpha d\beta}{\displaystyle\int\limits_{-\infty}^{+\infty}\!\!\int p[\alpha,\beta]e^{-2\pi i(0\cdot x + 0\cdot y)}d\alpha d\beta}$$

$$= \frac{p[\lambda z_2 \xi, \lambda z_2 \eta] * p^*[-\lambda z_2 \xi, -\lambda z_2 \eta]}{\mathscr{F}\{p[x,y]\}\Big|_{\xi=0, \, \eta=0}}$$

$$= \frac{p[\lambda z_2 \xi, \lambda z_2 \eta] \star p[\lambda z_2 \xi, \lambda z_2 \eta]}{P[\xi = 0, \eta = 0]} \tag{56}$$

Through a similar derivation for a real-valued, zero-one pupil function, Goodman ultimately revised equation 54 to the following integral form:

36

$$\text{OTF} = \mathscr{H}[\xi,\eta] = \frac{\int\limits_{-\infty}^{+\infty}\int p\left[x+\frac{\lambda z_2\xi}{2}, y+\frac{\lambda z_2\eta}{2}\right]p\left[x-\frac{\lambda z_2\xi}{2}, y-\frac{\lambda z_2\eta}{2}\right]dxdy}{\int\limits_{-\infty}^{+\infty}\int p[x,y]dxdy} \qquad (57)$$

where it is apparent that the OTF calculation is a ratio:

$$\text{OTF} = \frac{\text{area of overlap of two displaced pupils}}{\text{total area of the pupil}} \qquad (58)$$

Figure 4 depicts the general geometry associated with the real-valued, diffraction-limited aperture OTF calculation for a filled circular aperture. In this scheme, one can visualize the numerator of equation 57, or the autocorrelation of the scaled pupil function, as the shaded area of overlap between two displaced pupils as seen in the center of the figure. Since most diffraction-limited pupils can be represented by zero-one functions, the denominator or normalization factor in the OTF expressions found above is simply the total area of the pupil function on the left side of Figure 4. For simple geometries, such as the filled circular cylinder, one can ultimately derive analytical expressions for the OTF, making use of the basic geometry on the right side of Figure 4. The closed-form solution for this particular aperture will be discussed in greater detail shortly.
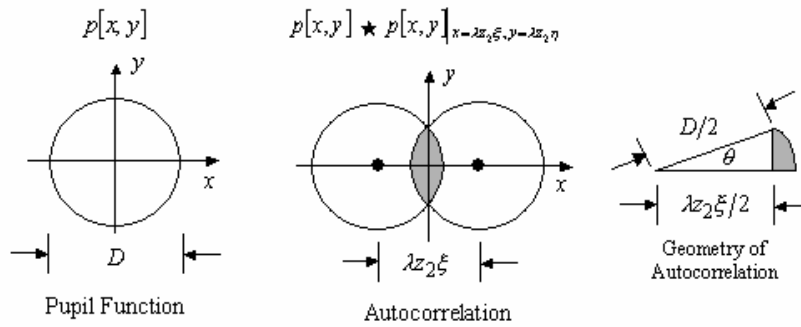
Figure 4: Geometric view of the diffraction-limited OTF calculation of a filled circular aperture performed through the mathematical autocorrelation of the exit pupil. (image based on Goodman)

Although functionally similar, the diffraction-limited aperture OTF calculation performed as the autocorrelation of the scaled pupil function is unique for a sparse aperture system configuration. This is a direct consequence of the fact that the exit pupil for a sparse aperture system contains multiple subaperture pupils which manifest both autocorrelations with themselves and cross-correlations with other paired subapertures within the array. This unique attribute of sparse aperture systems results in individual subaperture correlations that are displaced throughout the [ξ,η]-plane, providing the desired spatial frequency coverage.

To help clarify how the sparse aperture exit pupil supports the general OTF character identified previously (e.g., in Figure 3), it is instructive to expand some of the notation behind the pupil autocorrelation for these systems. For a diffraction-limited sparse aperture with identical subapertures, the overall system exit pupil can be described as the summation of N displaced subaperture pupils $s[x-x_i,y-y_i]$ centered about locations $[x_i,y_i]$. Of course, this summation can be represented as the convolution of the individual subaperture pupil $s[x,y]$ with an array of N displaced delta functions:

$$p[x,y] = s[x,y] * \sum_{i=1}^{N} \delta[x - x_i, y - y_i] = \sum_{i=1}^{N} s[x - x_i, y - y_i] \tag{59}$$

This is essentially a re-expression of equation 51 with the individual subaperture pupils $p_i[x,y]$ all defined by $s[x,y]$. As established in equation 54, the aperture transfer function for any optical system is essentially driven by the complex autocorrelation of the appropriately scaled pupil function in accordance with the following proportionality:

$$\mathscr{H}[\xi,\eta] \propto p[-\lambda z_2 \xi, -\lambda z_2 \eta] \star p^*[-\lambda z_2 \xi, -\lambda z_2 \eta] \tag{60}$$

If one substitutes the sparse aperture pupil function as defined in equation 59 into the OTF expression in equation 60 and simplifies the result, the following general proportionality is obtained for the OTF of a diffraction-limited sparse aperture with identical subapertures:

$$\mathscr{H}[\xi,\eta] \propto \left(s[-x,-y] \star s^*[-x,-y] \right) * \sum_{j=1}^{N} \sum_{k=1}^{N} \delta[x + x_j - x_k, y + y_j - y_k] \Big|_{\substack{x=\lambda z_2 \xi \\ y = \lambda z_2 \eta}} \tag{61}$$

Equation 61 provides a unique means for visualizing the implications of autocorrelating the pupil function for a distributed aperture in order to determine the system transfer function. From this expression, it becomes apparent that the fundamental building block of the sparse aperture transfer function is simply the complex autocorrelation of a pair of subapertures. The autocorrelation of a single subaperture is distributed throughout the spatial-frequency domain at points defined by the autocorrelation of the array of Dirac delta functions. As a result, one of the principal objectives of the system designer is to position subapertures in the system pupil to ensure maximum coverage in the frequency plane for the system transfer function. This makes non-redundant array designs very attractive, since cross-correlations of individual pairs generally are positioned in unique regions of support in the frequency domain if designed properly. In fact, if a particular sparse aperture system design has N individual subapertures; there will be a total of N^2 correlations within the subaperture group, of which N^2-N+1 can possibly be unique. The reduction by N-1 in frequency plane coverage is a direct result of the alignment of subaperture *auto*correlations at the origin.

The diagrams in Figure 5 illustrate the mathematical development of the sparse aperture OTF calculation for a simple Golay-4 non-redundant array. Figure 5(a) shows the exit pupil configuration for this representative system. In this diagram, the color-coded arrows represent the cross-correlations between individual subapertures. These cross-correlations effectively give rise to displaced subaperture autocorrelations positioned throughout the frequency domain, as shown in Figure 5(b). For instance, the subaperture cross-correlation represented by the green arrow in (a) results in the displaced green CTRI-function subaperture autocorrelation in the OTF depicted in (b). A similar formulation applies to the other independently supported cross-correlation pairs, some of which are color-coded for additional clarity. Figure 5(c) provides a three-dimensional surface plot of the derived aperture OTF, from which one can readily observe the independent CTRI-function subaperture autocorrelations resulting from cross-correlation pairs, as well as the "stacking" of $N = 4$ autocorrelations at the origin determined by the 4 independently supported subaperture pupils. Thus, the non-redundant Golay-4 configuration explored in this example has $N^2 = 16$ supported subaperture autocorrelations, of which $N^2-N+1 = 13$ provide unique support within the [ξ,η]-plane. With the character of this general transfer function, it is

essential to position and size the individual subapertures to provide maximum frequency domain coverage while avoiding the introduction of zeroes that eliminate spatial frequency content in the detected imagery.

| (a) Exit Pupil Autocorrelation | (b) Subaperture cross-correlations | (c) Transfer Function |
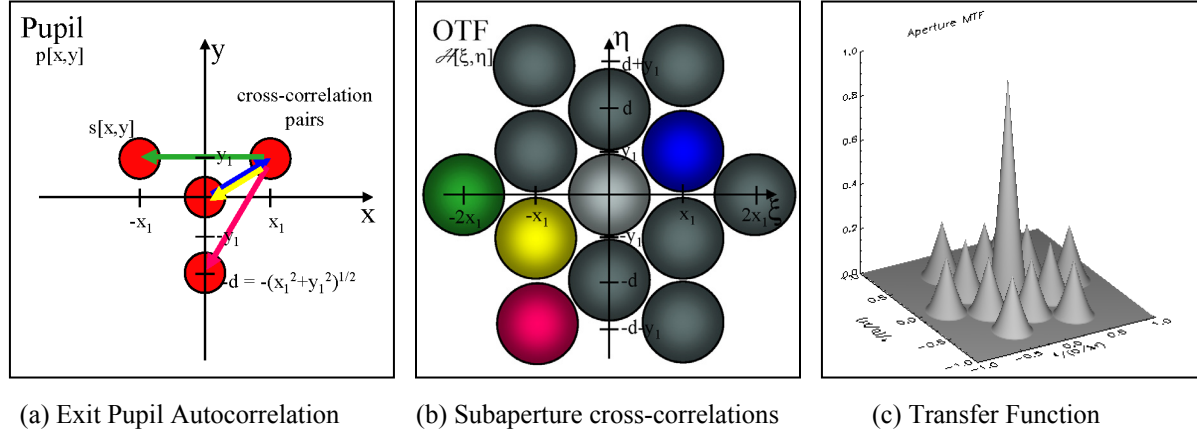
Figure 5: Geometric view of the diffraction-limited OTF calculation
of a Golay-4 sparse aperture system performed through the
mathematical autocorrelation of the exit pupil.

Although much of the preceding development would appear to involve simple mathematical wizardry, there is certainly value in exploring the various historic OTF formulations from the standpoint of having different options for mathematically deriving an estimate of the transfer function depending on the investigator's choice of numerical recipe. Ultimately, however, all of the formulations essentially entail the same general construct: the *OTF is the complex autocorrelation of the scaled pupil function normalized by the area of the exit pupil.* For more complicated pupil geometries, such as those encountered with sparse aperture systems, this mathematical operation can more effectively be modeled digitally, especially for aberrated pupils. The technique utilized in this research effort for computing the complex, aberrated transfer functions associated with the sparse aperture configurations of interest will be discussed in greater detail in Chapter 4.

The *modulation transfer function* (MTF) is simply defined as the modulus of the normalized OTF, and thus is a real-valued function that quantifies the degradation introduced by the optical system but maintains no information regarding the character of the system phase. In addition, one should note that the development has focused strictly on computing one

component of the total system OTF and MTF: that due to the optical aperture or exit pupil. Other components of the overall system transfer function will be discussed in greater detail shortly. By convention, therefore, the MTF computed as the magnitude of the OTF expression in equation 54 or any of its counterparts effectively constitutes the MTF_ap of the optical aperture as defined below:

$$\text{MTF}_\text{ap} = \text{MTF}[\xi, \eta, \lambda] = |\text{OTF}[\xi, \eta, \lambda]| \tag{62}$$

For a conventional filled circular aperture with an exit pupil diameter D, central wavelength λ and focal length f, Goodman demonstrates that the closed-form solution for the aperture MTF is:

$$\text{MTF}_\text{ap,filled} = |\mathscr{H}[\rho]| = \begin{cases} \dfrac{2}{\pi}\left[\cos^{-1}\left(\dfrac{\rho}{\rho_{co}}\right) - \dfrac{\rho}{\rho_{co}}\sqrt{1-\left(\dfrac{\rho}{\rho_{co}}\right)^2}\right] & \rho \le \rho_0 \\ 0 & \text{otherwise} \end{cases} \tag{63}$$

where ρ is the radial spatial frequency coordinate:

$$\rho = \left(\xi^2 + \eta^2\right)^{1/2} \tag{64}$$

and

$$\rho_{co} = \frac{D}{\lambda f} = \frac{1}{\lambda(f/\#)} \tag{65}$$

is the so-called cutoff frequency of the incoherent imaging system. This spatial frequency cutoff is an essential figure of merit that defines the highest spatial resolution of the optical system. As opposed to the rather simple filled aperture MTF discussed above, the sparse aperture MTF is generally not so amenable to a closed-form solution. As a result, the autocorrelation of the pupil function must typically be digitally modeled to derive the character of the MTF. Such modeling was used to implement the mathematical construct conveyed in equations 54 through 57 and derive the aperture MTF profiles contained in the figures below. For example, Figure 6 depicts the pupil function and associated aperture MTF

for a filled aperture system, which exhibits the classic circularly symmetric CTRI function character consistent with the closed-form solution identified above.
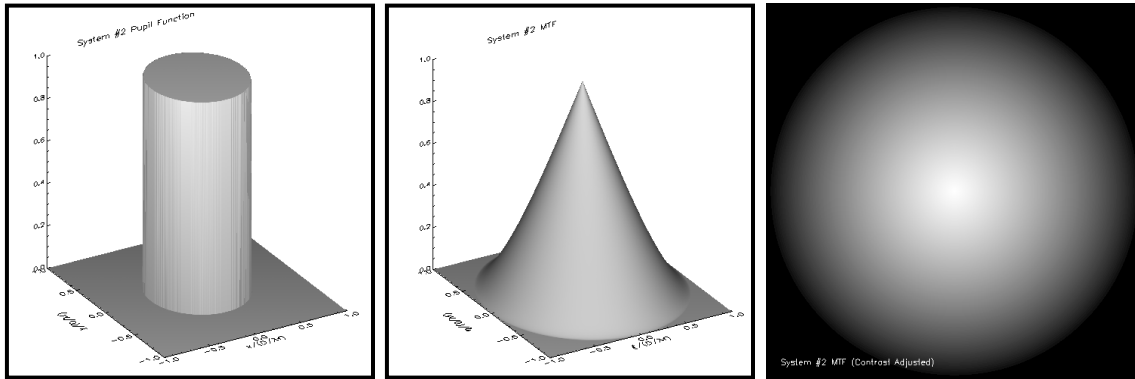
Figure 6: Filled circular aperture pupil and associated modulation transfer function.

For comparison, Figure 7 displays similar views of a tri-arm sparse aperture system pupil function and its MTF for the same encircled diameter. As with the conventional aperture analysis, the MTF profile is entirely consistent with the results cited in the literature. Comparison of the MTF profiles in figures 6 and 7 is instructive to highlight the reduced modulation and varying cutoff frequencies of the sparse aperture design relative to its filled counterpart. The MTF profile in Figure 7 also demonstrates how the subapertures of a classic sparse aperture system are arranged in a configuration to obtain good spatial frequency coverage. For these sparse aperture systems, it is highly desirable to exhibit an aperture MTF that avoids mid-frequency valleys and zeros, while maintaining expansive coverage over all those spatial frequencies that a comparable conventional aperture would image. The obvious rationale for desiring this character in the sparse aperture MTF is the overall objective of achieving comparable optical performance to a monolithic system, with minimal loss in spatial frequency content due to the introduction of zeros.

One is reminded that the development and examples cited above effectively skirt the issue of a complex-valued pupil function, which would represent aberrations and subaperture phasing. This topic will be discussed in further detail in Section 3.7.
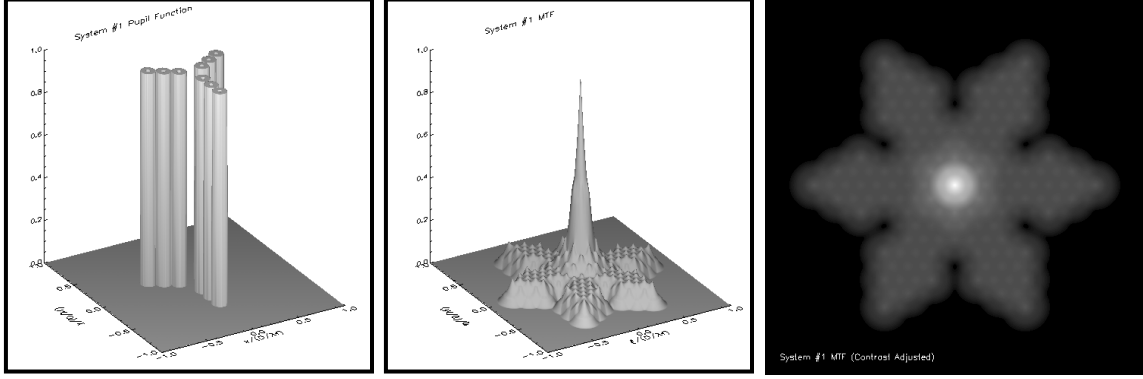
Figure 7: Tri-arm sparse aperture pupil and associated modulation transfer function.

3.6 Point Spread Function

Consistent with the discussion in Sections 3.1 and 3.2, the impulse response or *point spread function* (PSF) of an incoherent imaging system is defined to be the inverse Fourier transform of the OTF. Since the OTF is typically normalized by convention, one would intuitively conclude that the PSF (as a Fourier transform pair) should also be normalized. Unfortunately, as opposed to the almost universal acceptance of the normalized convention for the OTF, one finds a wide range of different formulations employed for the description of the aperture PSF. To maintain the integrity of the Fourier transform pair concept, Gaskill (1978) derives the following general expression for the aperture PSF:

$$
\mathrm{PSF} = \mathscr{F}^{-1}\{\mathrm{OTF}\} = \frac{\left|\mathscr{F}\{p[\lambda z_2 x, \lambda z_2 y]\}\right|^2_{\xi=x,\eta=y}}{\displaystyle\int\!\!\!\int_{-\infty}^{+\infty}\left|p[\lambda z_2\xi, \lambda z_2\eta]\right|^2 d\xi d\eta}
$$

$$
= \frac{\left|\left(\dfrac{1}{\lambda z_2}\right)^2\mathscr{F}\{p[x,y]\}\right|^2_{\xi=\frac{x}{\lambda z_2},\eta=\frac{y}{\lambda z_2}}}{\left(\dfrac{1}{\lambda z_2}\right)^2\displaystyle\int\!\!\!\int_{-\infty}^{+\infty}\left|p[x,y]\right|^2 dxdy}
\tag{66}
$$

where the normalization factor in the denominator is in effect the complex autocorrelation of the coherent transfer function evaluated at zero frequency. This convention is entirely consistent with taking the Fourier transform of equation 54 in order to evaluate the

incoherent PSF. Since the pupil function is typically a zero-one function (implying its value is comparable to its square) and the object to be imaged is typically at long range relative to the image distance for a remote sensing application (allowing z_2 to be approximated by the focal length f), one can further simplify equation 66:

$$PSF = \frac{\left(\frac{1}{\lambda f}\right)^2 \left|\mathscr{F}\{p[x,y]\}\right|^2_{\xi=\frac{x}{\lambda f},\eta=\frac{y}{\lambda f}}}{\int\limits_{-\infty}^{+\infty}\int p[x,y]dxdy} \tag{67}$$

which is the squared magnitude of the coherent impulse response normalized by the area of the exit pupil. As with the preceding discussion on OTF, there is a reasonably straightforward means for computing the incoherent PSF. To do so, one must compute the Fourier transform of the scaled pupil function, take the squared magnitude of the result, and normalize by the pupil area and a factor of $(\lambda f)^2$. Alternatively, one could also compute the normalized OTF through means described in the previous section and subsequently take the inverse Fourier transform of that result.

Some brief examples of the computational technique described above are provided in the following discussion. For instance, if one wanted to apply equation 67 in order to evaluate the incoherent PSF of a conventional diffraction-limited filled aperture with diameter D, a key step would be the computation of the Fourier transform of the CYL pupil function. The scaling property of Fourier transforms and the standard table of transform pairs leads to:

$$\left|\mathscr{F}\left\{CYL\left[\frac{r}{D}\right]\right\}\right|^2 = \left|\frac{\pi D^2}{4} SOMB[D\rho]\right|^2 \tag{68}$$

where Gaskill's sombrero (SOMB) function is defined as:

$$SOMB\left[\frac{r}{d}\right] = \frac{2J_1\left(\frac{\pi r}{d}\right)}{\left(\frac{\pi r}{d}\right)} \tag{69}$$

44

and J_1 is the first-order Bessel function of the first kind. Based on this result, it is clear that a filled circular aperture with no central obscuration will produce the classic airy pattern PSF resulting from the squared magnitude of the SOMB function. Continuing with the PSF convention identified in equation 67, one will ultimately arrive at the general equation for the normalized diffraction-limited PSF of a filled circular aperture illuminated by incoherent radiation:

$$\text{PSF}_{\text{filled}}[x, y] = \frac{\pi}{4}\left(\frac{D}{\lambda f}\right)^2 \left(\frac{2J_1[\pi r D / \lambda f]}{\pi r D / \lambda f}\right)^2 \tag{70}$$

With the normalization appropriately applied, the filled aperture MTF and PSF expressions contained in equations 63 and 70 effectively constitute Fourier transform pairs in accordance with the theoretical development explored above. Unfortunately, one will frequently find the unnormalized version of the incoherent PSF actually cited in the literature. This convention avoids the ratio of the squared magnitude of the coherent impulse response by the area of the exit pupil. With such a formulation, the unnormalized diffraction-limited PSF for a filled circular aperture with no central obscuration is:

$$\text{PSF}_{\text{filled}}[x, y] = \left(\frac{\pi D^2}{4\lambda f}\right)^2 \left(\frac{2J_1[\pi r D / \lambda f]}{\pi r D / \lambda f}\right)^2 \tag{71}$$

Although these two expressions differ only by a normalization factor, one must be careful in application if the total absolute scene power is of concern. One should also note that the relations all express the PSF in focal plane coordinates, similar to the approach taken with the OTF calculations.

Based on the closed-form analytical results, the circular filled aperture generates a classic Airy pattern PSF. This is confirmed by a digital model that essentially performs the numerical calculation. Figure 8 depicts the pupil function and associated normalized incoherent PSF for such a filled circular aperture modeled for a single central wavelength. One clearly observes the Airy pattern structure with the expected prominent central peak and

a first zero located in the wings at $1.22\lambda f/D$, consistent with theory and the Rayleigh resolution criteria.
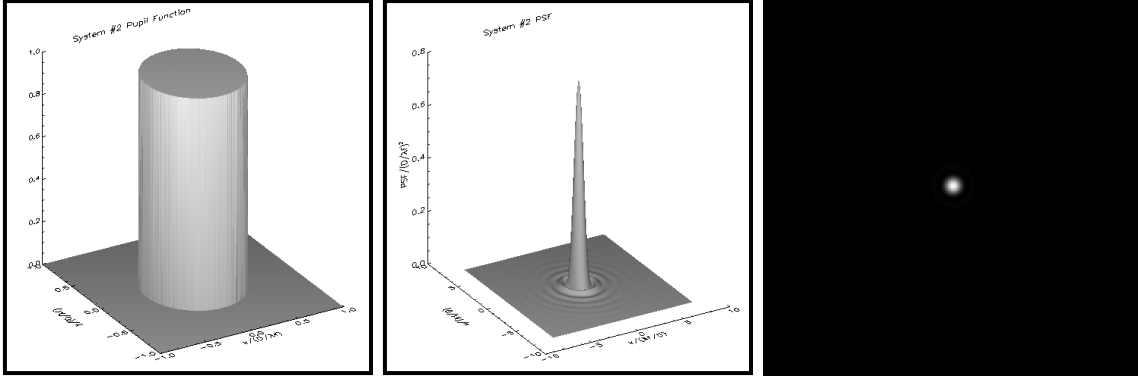
Figure 8: Filled circular aperture pupil and associated point spread function.

The next example is the evaluation of the incoherent PSF of a sparse aperture system. For this exercise, the same tri-arm configuration that was evaluated for the aperture MTF computation will be used. As discussed previously, the aperture MTF generally does not lend itself to an analytical solution simplified beyond an expression involving the normalized complex autocorrelation of the pupil function. Fortunately, in the spatial domain the diffraction-limited incoherent PSF of a sparse aperture is actually reducible to a closed-form solution of sorts. Ignoring the normalization factor in equation 67 for the time being, one can apply equation 51 for the generic description of a sparse aperture pupil to derive the general expression for the unnormalized incoherent PSF for such a collection aperture:

$$
\begin{aligned}
\text{PSF}_{\text{sparse}} &= \left(\tfrac{1}{\lambda f}\right)^2 \left|\mathscr{F}\{p[x, y]\}\right|^2 \Big|_{\xi=\frac{x}{\lambda f},\,\eta=\frac{y}{\lambda f}} \\
&= \left(\tfrac{1}{\lambda f}\right)^2 \left| P\!\left[\tfrac{x}{\lambda f}, \tfrac{y}{\lambda f}\right] \sum_{i=1}^{N} \exp\!\left[-\tfrac{2\pi i}{\lambda f}\left(x x_i + y y_i\right)\right] \right|^2
\end{aligned}
\tag{72}
$$

where the subapertures are assumed to be identical functions and use of the shift theorem accounts for the summation of phase terms within the squared magnitude. With this general formulation, one simply needs to perform the series of Fourier transform and scaling

operations for a single circular subaperture to arrive at the unnormalized relation for the diffraction-limited PSF of the sparse aperture system:

$$\text{PSF}_{\text{sparse}}[x,y] = \left(\frac{\pi D^2}{4\lambda f}\right)^2 \left(\frac{2J_1[\pi r D / \lambda f]}{\pi r D / \lambda f}\right)^2 \left|\sum_{i=1}^{N} \exp\left[-\frac{2\pi i}{\lambda f}(xx_i + yy_i)\right]\right|^2 \tag{73}$$

where N is the number of subapertures (nine in this case) within the sparse aperture system configuration. Having derived expressions for the numerator in equation 67, one simply needs to normalize both equations by the area of the exit pupil to develop the strict mathematical interpretation of the PSF proposed by Gaskill. To gain physical intuition of the general character of the closed-form expressions found above, a digital model was constructed to implement the same numerical technique used with the conventional aperture configuration. The results of this analysis are displayed in Figure 9, with the modeled tri-arm pupil function on the left and the computed incoherent PSF on the right. As anticipated by the results of the MTF evaluation for this system, the greatly reduced modulation exhibited by the sparse aperture system correlates with a degraded PSF having a reduced peak and increased energy within the wings. Such a PSF will clearly result in a degraded image product over the comparable conventional aperture prior to any image restoration attempts. Fortunately, much of the lost quality can be recovered by appropriate filtering techniques if the MTF exhibits the appropriate spatial frequency content.
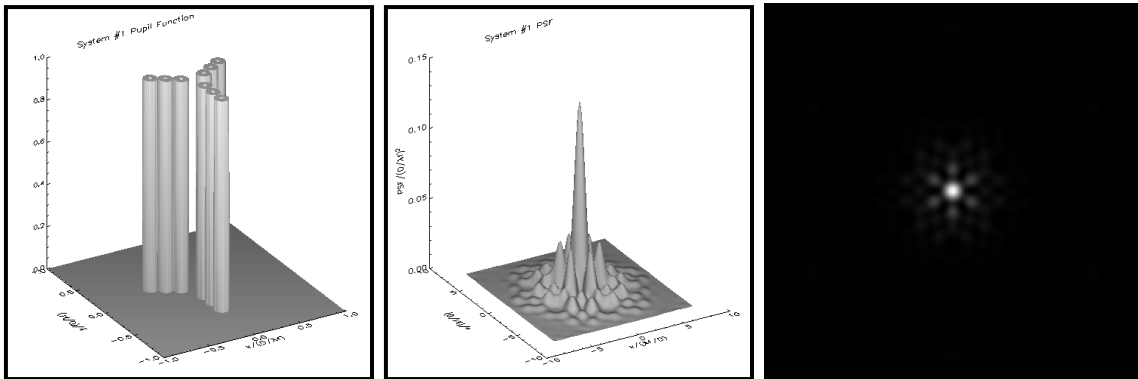
Figure 9: Tri-arm sparse aperture pupil and associated point spread function.

3.7 Aberrated Aperture MTF

The development of expressions for the pupil function, OTF and PSF have all relied upon the implicit assumption that the system is *diffraction limited*, i.e., that a point source object generates an ideal converging spherical wave at the exit pupil. Of course, real-world systems generally exhibit some form of inherent *aberration*, or wavefront departure from the ideal spherical wave model. In a sparse aperture system, the conceptual notion of an aberration takes on added meaning, as the individual subapertures could theoretically exhibit diffraction-limited performance and be inadequately phased so that the synthesized image field effectively displays an aberrant wavefront. Such errors could manifest themselves in the context of relative piston and tilt errors between subapertures, for instance. Accordingly, the development of phenomenology to deal with aberrations and phasing issues is essential to properly account for the overall physics associated with sparse aperture system imaging.

Goodman (1968) has suggested that general aberration phenomenology can be captured in a Fourier optical sense by introducing a complex pupil function, where the effect of the aberration is modeled through a phase term consistent with the optical path difference (OPD) error. Conceptually, in this formulation the pupil function can be envisioned as consisting of a real-valued term that accounts for the aperture geometry and an imaginary-valued term that effectively represents a phase screen over the aperture, thereby degrading the incident wavefront. With this model, Goodman indicates that real apertures should be represented by a complex pupil function $\wp[x,y]$ of the form:

$$\wp[x,y] = p[x,y]\exp\left(\frac{2\pi i}{\lambda} w[x,y]\right)$$ (74)

where $w[x,y]$ is a two-dimensional function that describes the effective OPD error in units consistent with the wavelength λ. The general nature of this OPD error measure can be observed in Figure 10, which depicts the imaging geometry for an aberrated wavefront with tilt error. As observed in the figure, the aberration function $w[x,y]$ simply defines the amount of OPD error present in the system relative to a converging, perfectly spherical reference wavefront at the exit pupil. It should also be noted that the measurement of path-length error

48

occurs for the two waves (reference and aberrated) which intersect the optical axis at the exit pupil or aperture stop.
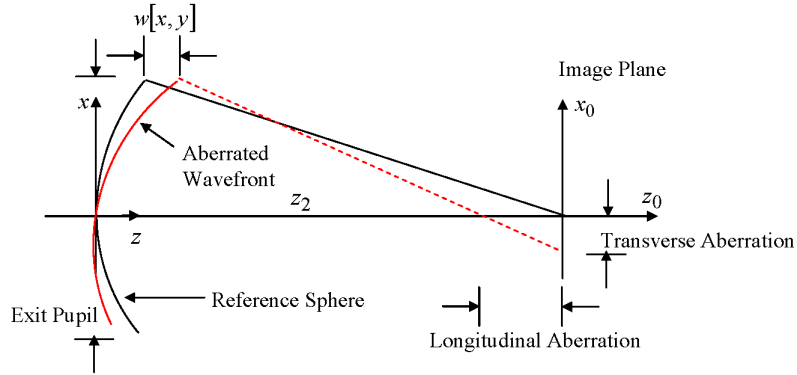
Figure 10: Geometry associated with an aberrated wavefront and the resulting aberration function $w[x,y]$, demonstrating the Optical Path Difference (OPD) from the best-fit reference sphere in the exit pupil.

For a realistic sparse aperture system with aberrations and/or phasing errors, the diffraction-limited pupil function in equation 51 is similarly revised to account for the resulting OPD errors:

$$
\rho[x,y] = \sum_{i=1}^{N} p_i[x - x_i, y - y_i] \exp\left(\frac{2\pi i}{\lambda} w_i[x - x_i, y - y_i] \right)
\tag{75}
$$

where $w_i[x,y]$ accounts for the individual path errors associated with the ith subaperture. Thus, the wavefront error associated with each subaperture can generally be addressed through similar geometric considerations as those depicted for conventional apertures in Figure 10. As will become apparent in the discussion below, one simply needs to replace the pupil function in all expressions for the transfer and impulse response with the complex expressions found above to account for any realistic aperture system with resident aberrations or pupil phase errors.

Prior to addressing the issue of an aberrated OTF or PSF, it would be useful to explore the general character of the OPD error function $w[x,y]$. Welford (1986) developed a general formulation for describing the difference between an aberrated wavefront emerging from the

exit pupil and the ideal spherical wave at the same point obtained by a power series expansion. Assuming rotational symmetry in the optical system of interest, he identifies the following expression to describe the OPD error:

$$
w[x,y] \equiv w[x,y,x_0] = a_1 \overset{\text{defocus}}{\left(x^2 + y^2\right)} + a_2 \overset{\text{tilt}}{xx_0} + a_3 \overset{\text{piston}}{x_0^2}
$$

$$
+ b_1 \overset{\text{spherical}}{\left(x^2 + y^2\right)^2} + b_2 \overset{\text{coma}}{xx_0\left(x^2 + y^2\right)} + b_3 \overset{\text{astigmatism}}{x^2 x_0^2}
$$

$$
+ b_4 \overset{\text{field curvature}}{x_0^2\left(x^2 + y^2\right)} + b_5 \overset{\text{distortion}}{xx_0^3} + b_6 x_0^4
$$

$$
+ \text{higher order terms}
$$

(76)

where $[x,y]$ are exit pupil coordinates as previously defined, $[x_0,y_0]$ are paraxial image plane coordinates, a_i are second-order OPD coefficients, and b_i are fourth-order OPD coefficients. When expressed as transverse ray departures, the b_i terms are of third order and consequently are commonly referred to as third-order aberrations. In addition, the first five third-order terms are widely known as the Seidel aberrations, with b_1 corresponding to spherical error, b_2 representing coma, b_3 indicating the presence of astigmatism, b_4 identifying field curvature, and b_5 consistent with distortion. Similar to the third-order aberration terms, the second-order OPD terms are actually first order when expressed as transverse ray aberrations. In this context, the first (a_1) term in equation 76 introduces a longitudinal shift in the center of the ideal spherical wave that is commonly referred to as defocus. The a_2 term, on the other hand, identifies a transverse shift in the center of the reference wavefront sphere, which is referred to as tilt in practice. The final first-order aberration term does not effectively change the shape of the reference wavefront, but does introduce a constant phase shift across the exit pupil known as piston error.
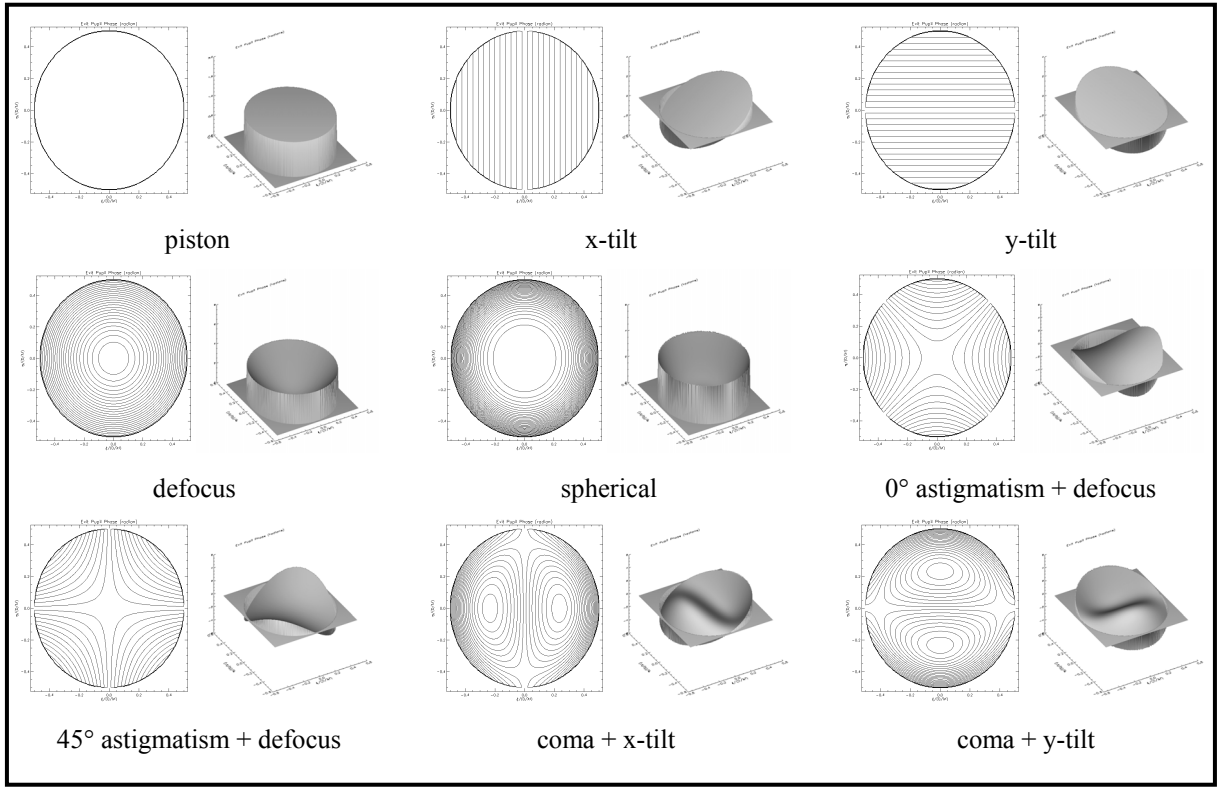
Figure 11: Contour and three-dimensional surface plots of the phase profiles
for various first-order Gaussian and third-order Seidel wavefront aberrations.

Figure 11 provides contour and surface plots of the aberrated wavefront phase profiles that arise as a result of the first- and third-order aberrations described above. These wavefront profiles are depicted in terms of either their aberration coefficient or Zernike polynomial fits, concepts which will be discussed in additional depth later. The first-order paraxial or Gaussian properties of the optical wave (piston, tip/tilt, and focus) are represented by the first four plots in the diagram through the use of aberration coefficients. These Gaussian properties will be shown to be essential parameters in the phasing of sparse aperture subapertures in later sections. The key third-order Seidel aberrations investigated in this effort appear in the remaining five diagrams, all of which were captured through Zernike wavefront analysis except spherical error, whose quartic character seemed more intuitively represented through its aberration coefficient. Naturally, the former is a matter of personal choice, and the proof-of-concept digital model developed for this research supports both Zernike and aberration coefficient definition for any number of ordered aberrations. Ultimately, one should recall that the desired wavefront would exhibit a perfectly spherical

contour. With such a reference, the various phase profiles contained in Figure 11 allow one to gain some intuitive insight into the physical nature of the various aberrations that may be present in an optical system. All of these aberrations ultimately become the nemesis of the optical designer and can have a dramatic impact on image quality depending on the severity of the error.

Wyant (1993) identifies an alternative form of equation 76 that takes advantage of the assumption of circular symmetry to introduce polar coordinates. With this approach, the pupil plane coordinates can be rewritten in polar format according to the following set of relations:

$$
\begin{aligned}
x &= r\cos\theta \\
y &= r\sin\theta
\end{aligned}
\tag{77}
$$

Introducing these polar coordinates, one will find that the expression for the OPD error found in equation 76 takes the following general form:

$$
\begin{aligned}
w[r,\theta,x_0] &= \sum_{j,m,n} W_{klm} x_0^k r^l \cos^m\theta \qquad \text{with } k = 2j+m,\, l = 2n+m \\
&= W_{020} r^2 + W_{111} x_0 r\cos\theta + W_{200} x_0^2 \\
&\quad + W_{040} r^4 + W_{131} x_0 r^3 \cos\theta + W_{222} x_0^2 r^2 \cos^2\theta \\
&\quad + W_{220} x_0^2 r^2 + W_{311} x_0^3 r\cos\theta + W_{400} x_0^4 \\
&\quad + \text{higher order terms}
\end{aligned}
\tag{78}
$$

where the W_{klm} are the so-called wavefront aberration coefficients such that k corresponds to the power of the x_0 term, l to the r coordinate term, and m to the trigonometric cosine term. Given such a convention, the relationship between the individual error terms in equation 78 and the first- and third-order aberrations can be established as observed in Table 1 below. In general, one finds that the wavefront OPD error expression found in equation 78 tends to see the most frequent use within the imaging community to address issues associated with optical aberrations.

Coefficient	Form	Aberration
W_{020}	r^2	focus
W_{111}	$x_0 r\cos\theta$	tilt
W_{200}	x_0^2	piston
W_{040}	r^4	spherical
W_{131}	$x_0 r^3\cos\theta$	coma
W_{222}	$x_0^2 r^2\cos^2\theta$	astigmatism
W_{220}	$x_0^2 r^2$	field curvature
W_{311}	$x_0^3 r\cos\theta$	distortion

Table 1: Wavefront aberration coefficients for first-order
Gaussian and third-order Seidel aberrations.

With a formulation in hand for addressing aberrations through a complex-valued pupil function driven by the wavefront OPD error expression, one can now investigate the effect of aberrations on the aperture OTF and PSF. As alluded to previously, the same numerical mechanics apply for computing these functions. One simply needs to replace the previous diffraction-limited geometric form of the pupil function with the complex function found in equations 74 and 75 in the expression of interest. For example, the functional form of the OTF for an aberrated pupil is computed by inserting the complex pupil function into equation 55 to formulate the general relation:

$$
\begin{aligned}
\mathrm{OTF} &= \frac{\mathscr{P}[\lambda z_2\xi, \lambda z_2\eta] \star \mathscr{P}[\lambda z_2\xi, \lambda z_2\eta]}{\displaystyle\int\limits_{-\infty}^{+\infty}\!\!\int p[x, y]\,dxdy} \\[2mm]
&= \frac{p[\mathrm{x,y}]\exp\!\left(\frac{2\pi i}{\lambda}w[x,y]\right)* p^*[-\mathrm{x,-y}]\exp\!\left(-\frac{2\pi i}{\lambda}w[-x,-y]\right)\Big|_{x=\lambda f\xi,\,y=\lambda f\eta}}{\displaystyle\int\limits_{-\infty}^{+\infty}\!\!\int p[x, y]\,dxdy}
\end{aligned}
\tag{79}
$$

where the OTF computation is seen to involve the complex autocorrelation of the aberrated pupil function normalized by the area of diffraction-limited exit pupil. Goodman (1968) shows that this expression can be recast into the following general form for the evaluation of the OTF when aberrations are present:

$$\text{OTF} = \frac{\int\limits_{-\infty}^{+\infty}\int p\left[x+\frac{\lambda f\xi}{2}, y+\frac{\lambda f\eta}{2}\right]p\left[x-\frac{\lambda f\xi}{2}, y-\frac{\lambda f\eta}{2}\right]\exp\left[\frac{2\pi i}{\lambda}\left(w\left[x+\frac{\lambda f\xi}{2}, y+\frac{\lambda f\eta}{2}\right]-w\left[x-\frac{\lambda f\xi}{2}, y-\frac{\lambda f\eta}{2}\right]\right)\right]dxdy}{\int\limits_{-\infty}^{+\infty}\int p[x,y]dxdy} \tag{80}$$

which allows one to directly relate the effect of OPD errors to the resulting OTF. In this expression, Goodman uses the Schwarz inequality to show that aberrations never boost the MTF and frequently lower the contrast (i.e., reduce the modulation) at certain spatial frequencies. In fact, if aberrations are severe, the modulation can be reduced enough that the *effective* cutoff frequency is significantly below the diffraction-limited metric, resulting in the apparent loss of spatial resolution in the acquired imagery. Aberrations can also reverse the phase of the OTF at certain spatial frequencies, causing the image content at those spatial frequencies to experience a reversal in perceived contrast.

As with the OTF development discussed above, the evaluation of the PSF for an aberrated optical system introduces a complex-valued pupil function. For example, the normalized PSF for an aberrated optical system can be computed through use of equation 67 and an expression for the complex pupil as follows:

$$\begin{aligned}\text{PSF} &= \frac{\left(\frac{1}{\lambda f}\right)^2\left|\mathscr{F}\{p[x,y]\}\right|^2_{\xi=\frac{x}{\lambda f}, \eta=\frac{y}{\lambda f}}}{\int\limits_{-\infty}^{+\infty}\int p[x,y]dxdy} \\[2em] &= \frac{\left(\frac{1}{\lambda f}\right)^2\left|P\left[\frac{x}{\lambda f}, \frac{y}{\lambda f}\right]*\mathscr{F}\left\{\exp\left[\frac{2\pi i}{\lambda}w[x,y]\right]\right\}\right|^2_{\xi=\frac{x}{\lambda f}, \eta=\frac{y}{\lambda f}}}{\int\limits_{-\infty}^{+\infty}\int p[x,y]dxdy}\end{aligned} \tag{81}$$

This expression cannot be simplified much further without some knowledge of the OPD error functional form. Clearly, for the first-order aberrations (i.e., piston, tilt and defocus), one can simplify the expression for the Fourier transform of the pupil phase function. Any further

reduction is completely contingent upon the physical form of the geometric diffraction-limited pupil function, which becomes quite complicated even for a simple CYL function.

As a final point on the discussion of aberrated OTF and PSF evaluation, one should note that all of the expressions discussed in this section identify a general diffraction-limited system pupil function $p[x,y]$. The latter could easily involve the summation of individual subaperture pupils in accordance with equations 51 and 75 for sparse aperture system analysis, introducing the appropriate summation and pupil shifts into the equations for the OTF and PSF. As a result, the complex nature of the expressions detailed above generally drives the need to evaluate aberrations and phasing errors through use of a digital computer model.

Due to the complexity of these expressions, Fiete (2002) suggests use of an approximation that attempts to capture the principal effects of the aberrations resident in precision optics due to manufacturing errors. Leveraging the work originally accomplished by Holst (1995), he proposes use of the following aberrated optics transfer function (MTF_{aber}) in conjunction with the diffraction-limited aperture MTF developed previously:

$$MTF_{aber} \cong 1 - \left(\frac{WFE_{rms}}{0.18}\right)^2 \left[1 - 4\left(\frac{\rho}{\rho_{co}} - \frac{1}{2}\right)^2\right] \quad \text{for } \rho \leq \rho_{co} \tag{82}$$

where ρ_{co} is the cutoff frequency of the optical system defined in equation 65 and WFE_{rms} is the total rms wavefront error of the optical system (typically budgeted on the order of 0.10 waves at the operational wavelength λ). Holst indicates that this formulation is valid for modeling precision optics with small aberrated wavefront errors (i.e., $WFE_{rms} < 0.14$). With such an expression, one can theoretically compute the autocorrelation of the real-valued geometric pupil function to derive the diffraction-limited aperture MTF and subsequently multiply the result by the aberrated optics MTF to arrive at an appropriate approximation for the normalized autocorrelation of the complex pupil function defined in equations 79 and 80 above. As an example, this analysis has been accomplished for a filled circular aperture in Figure 12 below, where one can observe the impact of various levels of rms aberration on the

diffraction-limited MTF performance of the optical system. In the context of this research effort, the development of such an aberrated optics MTF was accomplished only to verify the implementation of the more flexible wavefront polynomial approach discussed previously. In all of the results that follow in Chapter 5, a complex pupil function was constructed to capture the effect of subaperture aberrations and or dephasing.

(a) Diffraction-Limited   (b) Aberrated (0.14 waves)   (c) Comparison
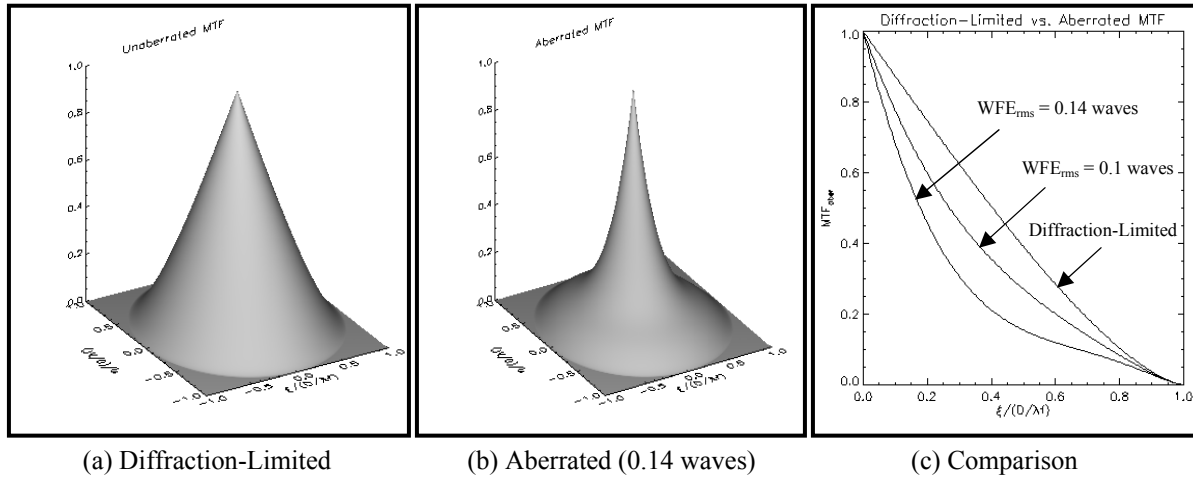
Figure 12: Comparison of diffraction-limited versus aberrated MTF
performance for various levels of rms wavefront error
using the formulation in Holst (1995).

3.8 Detector Sampling

The previously derived MTF expressions that essentially involve the complex autocorrelation of the pupil function capture the diffraction physics associated with the optical system aperture. As will be discussed later in Section 3.12, other MTF components must also be accounted for in the total system analysis. One deals with the fact that a detector has finite spatial extent rather than the infinitesimal area characteristic of a Dirac delta function. As a consequence, the non-ideal, real-world detector behaves like an averaging mechanism to further blur the object scene. Since most detectors exhibit rectangular planforms (and therefore by definition a rectangular PSF), they give rise in the frequency domain to a detector pixel aperture MTF with general character:

$$\text{MTF}_{\text{det}} = \frac{\text{SIN}[\pi\xi x_p]}{\pi\xi x_p}\frac{\text{SIN}[\pi\eta y_p]}{\pi\eta y_p} = \text{SINC}[\xi x_p]\text{SINC}[\eta y_p] \qquad (83)$$

where x_p is the width of the light-sensitive detection area in the *x*-dimension and y_p is the similar detector width in the *y*-dimension. The MTF expression defined above assumes a rectangular detection area and uniform detector response across the pixel.
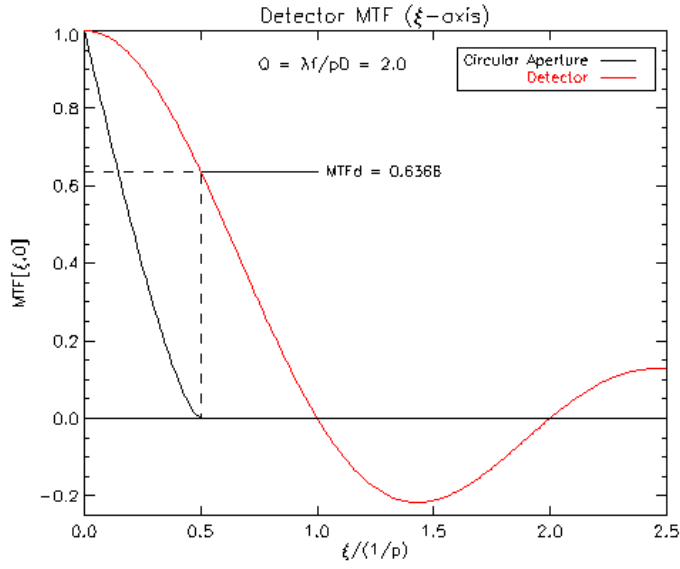
Figure 13: Comparison of the detector pixel aperture MTF (in red)
versus the MTF for a filled circular aperture given Nyquist sampling.

For visualization, the detector MTF (in red) along the ξ-axis is plotted in Figure 13. This figure illustrates that the effective detector cutoff or sampling frequency occurs at the first zero, at spatial frequency $\xi = 1/p$ where *p* is the distance between detector centers, commonly referred to as the pixel pitch. Any spatial frequency content in the imaged scene above one-half the detector cutoff or sampling frequency, i.e., above $\xi = 1/(2p)$, will be aliased back into the scene spectrum at lower frequency and therefore not be faithfully reproduced in the detected image. For comparison, a filled circular aperture MTF that is assumed to be Nyquist sampled is included in the diagram as well. One will observe that the optical cutoff frequency associated with such a system occurs at $\xi = D/\lambda f = 1/(2p)$, which establishes the highest spatial resolution that the imaging system can achieve (or highest spatial frequency

57

that can be imaged). Since the optical cutoff frequency is equivalent to one-half the sampling frequency, no aliasing occurs for such a Nyquist-sampled imaging system.

In addition to the MTF effect, the finite nature of imaging detectors also introduces quantization effects that manifest themselves in terms of pixilation in the final digital image. In the focal plane, the unit measure of sampling is again driven by the distance between detector centers or pixel pitch. For equivalent ground units, the pixel pitch must be projected to the ground plane to acquire a measure of the ground sample distance (GSD). A geometric mean evaluation of the ground sample distance (GSD_{GM}) takes the form:

$$\mathrm{GSD}_{\mathrm{GM}} = \sqrt{\mathrm{GSD_x GSD_y}} = \frac{Rp}{f}\sqrt{\frac{MN}{\sin[\theta_{el}]}} \tag{84}$$

where R represents the range to the target scene, f is the system focal length, θ_{el} defines the target elevation angle along the imaging line-of-sight, and M and N identify the number of pixels aggregated in the x- and y-dimensions, respectively. This expression essentially specifies in ground units how an object scene is sampled by the focal plane array (FPA), i.e. the spatial extent of each pixel on the ground. Conversely, one could invert the expression to determine the scale factor s that relates a given distance in the ground plane (Δx_{GP}) to that in detector plane units of distance (Δx_{FPA}):

$$\Delta x_{\mathrm{FPA}} = s \cdot \Delta x_{\mathrm{GP}} = \frac{f}{R}\sqrt{\sin[\theta_{el}]} \cdot \Delta x_{\mathrm{GP}} \tag{85}$$

With these equations, one is able to appropriately sample and scale a given object scene to ensure its frequency spectrum units are consistent with the system MTF to be applied.

3.9 Detector Carrier Diffusion

The next physical effect that can be modeled as a component of the system MTF involves carrier diffusion. Diffusion is a detector-level phenomenon that essentially involves photogenerated electrons which wander to an adjacent detector and are subsequently captured in its depletion region for read out. This results in a random number of electrons being detected in the "wrong" pixel, introducing a type of blurring effect. An anecdotal illustration of this detector-level effect can be seen on the left side of Figure 14, where an electron is generated outside the depletion region of pixel #1 and subsequently diffuses over to pixel #2 for detection. Of course, the ability of electrons to diffuse into adjacent pixels is principally driven by differences in the photon absorption length versus the depletion region depth of the detector. As a consequence, diffusion tends to be a more dominant effect for detected wavelengths greater than 0.7 μm, with more significant impact in the infrared. This can be observed on the right side of Figure 14, where the reduction in the diffusion MTF becomes substantial at wavelengths around 1000 nm. The effects of carrier diffusion can be modeled through the following MTF expression:

$$\mathrm{MTF_{diff}} = \left[1 - \frac{\exp(-\alpha L_{\mathrm{dep}})}{1 + \alpha L_{\mathrm{K}}}\right]\left[1 - \frac{\exp(-\alpha L_{\mathrm{dep}})}{1 + \alpha L_{\mathrm{diff}}}\right]^{-1} \tag{86}$$

where α is the wavelength-dependent absorption coefficient, L_{dep} is the detector depletion depth, L_{diff} is the diffusion length associated with the photogenerated electron, and L_{K} is defined by the equation below:

$$L_{\mathrm{K}} = \frac{L_{\mathrm{diff}}}{\sqrt{1 + (2\pi L_{\mathrm{diff}})^2(\xi^2 + \eta^2)}} \tag{87}$$

It should be noted that the carrier diffusion MTF described by the expressions above degrades considerably as the wavelength of the detected radiation increases. Such a result occurs because longer wavelength photons have an increased probability of being absorbed outside the depletion region, thereby increasing their opportunity to diffuse into an adjacent detector element.
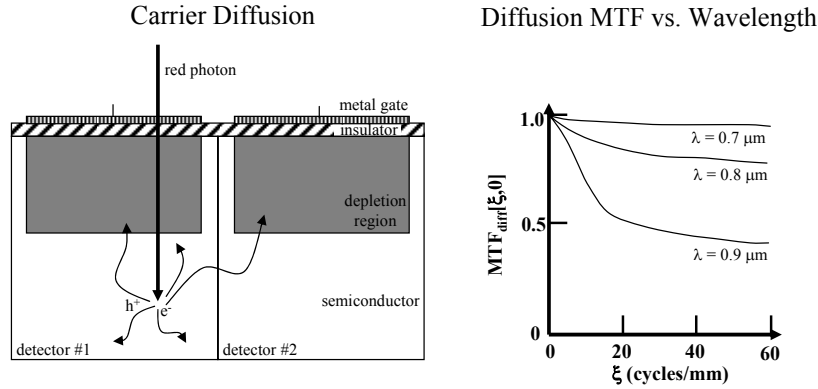
Figure 14: Depiction of the physical phenomenon involved in detector carrier diffusion and the spectral variation manifested by a typical carrier diffusion MTF.

3.10 Image Motion

Another image quality effect that must be captured in the modeling process entails the degree to which the image moves across the detector during the integration time T_{int} of the sensor. Experienced during a collection, this relative image displacement between the detector and the ground scene will introduce a blurring effect in the direction of the motion. In general, image motion can be placed into two principal categories: linear smear and random jitter. These degradation effects will be characterized through individual MTF components as described in the sections that follow.

3.10.1 Smear

Image smear, one of the most prominent motion effects, tends to be linear in nature and involves line-of-sight (LOS) fluctuation at low frequencies compared to the integration time T_{int}. Although one typically thinks about smear in the context of a scanning sensor, with along-scan and cross-scan components, it is certainly plausible to observe linear image motion or smear with a staring sensor utilized in a sparse aperture application as well. In general, one will find the means for characterizing this motion for staring sensors is somewhat simpler than that typically encountered for scanning sensors, as one does not have to worry about stages of TDI or clock phases.

For classic smear that follows the track of a ground point across the detector in a given integration period, the impulse response takes the functional form of a RECT with a base equivalent to the amount of smear or angular displacement traveled by the ground point. The Fourier transform of this PSF results in the smear transfer function (MTF$_{smear}$) for simple linear LOS motion along a cardinal access defined by the velocity mismatch vector ΔV:

$$\text{MTF}_{smear} = \frac{\text{SIN}\left[\pi\left(\xi\Delta V_x + \eta\Delta V_y\right)T_{int}\right]}{\pi\left(\xi\Delta V_x + \eta\Delta V_y\right)T_{int}} = \text{SINC}\left[\left(\xi\Delta V_x + \eta\Delta V_y\right)T_{int}\right] \tag{88}$$

where ΔV_x is the velocity error in the x-direction appropriately scaled for focal plane coordinates and ΔV_y is the velocity error in the y-direction in similar units. With the expression above, one finds that it is generally necessary to keep image smear to less than half- to quarter-pixel ($0.50p$-$0.25p$) for high-resolution remote sensing systems to avoid excessive image degradation. This can be quite problematic for a sparse aperture system, as the long integration times required to achieve adequate signal due to the reduced fill factor of the pupil introduce very stressing stability requirements for the imaging platform.

Figure 15 depicts how the ξ-axis MTF due to smear or linear motion (in red) varies as a function of the velocity error in the x-direction. Obviously, smear only impacts the transfer function along the cardinal axis in the frequency plane corresponding with the direction of the linear motion in the space domain. As observed in the figure, excessive linear motion ultimately results in negative amplitude in the transfer function, a phenomenon that induces phase reversal in detected imagery. Once again, the figure includes a plot of a Nyquist-sampled, filled circular aperture MTF for comparative purposes.
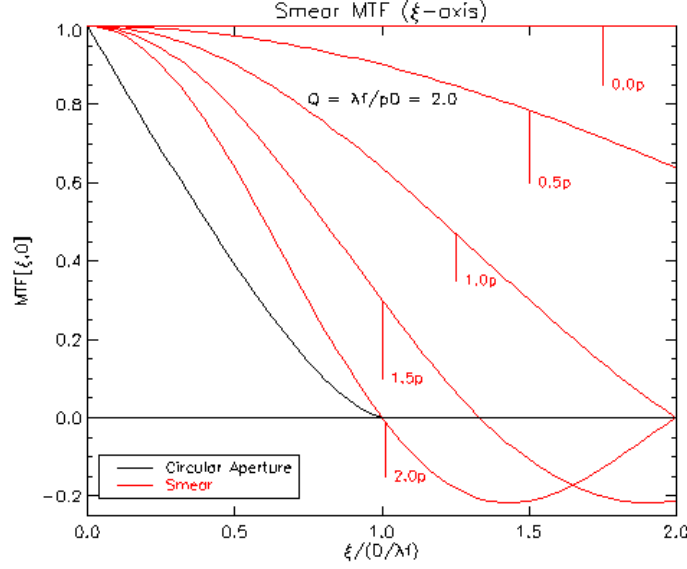
Figure 15: Variation of the smear MTF (in red) with target velocity mismatch relative to the imaging system over the integration period given Nyquist sampling. The MTF associated with a filled circular aperture is plotted for comparison.

3.10.2 Jitter

Another important physical motion parameter that must be considered in the modeling process entails imaging system jitter. Jitter effectively consists of random, high frequency line-of-sight (LOS) fluctuations that, like linear smear, can be modeled through an appropriate MTF implementation. It is typically induced by vibrations on the platform upon which the imaging sensor resides. If one assumes that the platform jitter can be described by an isotropic random variable that abides by Gaussian statistics over the detector integration time T_{int}, the following jitter transfer function (MTF$_{jitter}$) can be utilized to model the rapid LOS fluctuations:

$$\text{MTF}_{jitter} = \text{EXP}\left[-2\pi^2 \sigma_{jit}^2 \left(\xi^2 + \eta^2\right)\right] \tag{89}$$

where σ_{jit} is the standard deviation of the observed random vibration profile in mrad. It is fairly common practice to use an rms (1σ) value for modeling the jitter motion, which can be on the order of the angular displacement of linear motion or smear discussed in Section

62

3.10.1, depending on the quality of the platform stabilization approach and the nature of the collection (e.g, airborne versus spaceborne).

Figure 16 illustrates the variation of the ξ-axis MTF due to jitter or random motion (in red) as a function of the standard deviation of the random displacement. From this figure, it is apparent that random jitter constitutes a much more deleterious effect on image quality than linear motion for a given level of displacement over a detector subtense. As a consequence, one ideally desires to keep jitter down to a level of a quarter- to a tenth-pixel ($0.25p$-$0.10p$) to avoid serious quality implications. As before, a Nyquist-sampled, filled circular aperture MTF is also included in the diagram for comparison.
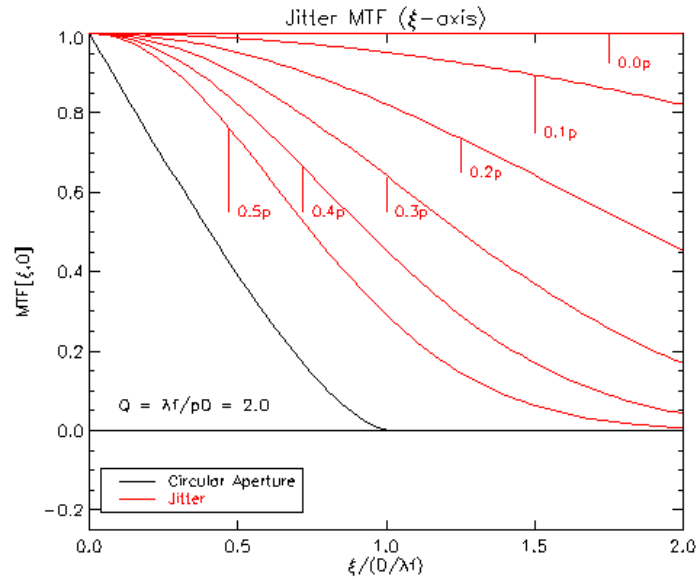
Figure 16: Variation of the jitter MTF (in red) with the standard deviation of the random Gaussian distribution for high-frequency motion given Nyquist sampling. The MTF for a filled circular aperture is plotted for comparison.

3.11 Atmospheric Turbulence

The final MTF component investigated in this research effort involved characterizing atmospheric turbulence, which essentially entails random fluctuations in the refractive index of the atmosphere. In general, turbulence arises as a result of random fluctuations in air pressure and temperature, causing small-scale modifications to the arrival angle of light

propagating through the medium. These changes in the angle-of-arrival of the incident light ultimately manifest themselves in apparent image motion and blurring. The impact of turbulence scales with altitude, with the most serious effect observed within a few meters of ground level. In addition, turbulence tends to have a more dramatic effect on image quality when it resides closer to the entrance aperture of the imaging system. Therefore, a down-looking, remote sensing application from an overhead sensor tends to be less susceptible to atmospheric turbulence than an up-looking, imaging scenario with a ground-based observer.

Obviously, the observed fluctuations due to turbulence are also highly dependent on atmospheric conditions, time of year, time of day, wind velocity, thermal convection, surface roughness, etc. Given the highly dynamic, non-stationary, statistical nature of atmospheric turbulence, it is only reasonable to model this phenomenon on a macroscale level, utilizing a time-averaged approximation originally introduced by Fried (1966) and further developed by Goodman (1985). Fortunately, for high-resolution remote sensing imaging system observing the earth under typical conditions, atmospheric turbulence tends to be a minor contributor to overall image quality so the top-level approximation and characterization through an average transfer function is entirely appropriate.

For many remote sensing applications, the atmospheric turbulence can effectively be quantified through use of the refractive index structure constant C_n^2. If one assumes turbulence can be modeled as a homogeneous random field obeying Kolmogorov statistics, its power spectral density can be shown to first order to be directly proportional to C_n^2. Accordingly, the refractive index structure constant is a good indicator of the relative strength of the fluctuations associated with the turbulence. As a measure of turbulence, the structure constant scales with altitude above ground level, varies throughout the day/year, and tends to exhibit a slowly changing, near-maximum plateau around mid-day. Although the structure constant is highly dynamic in accordance with the turbulent fluctuations it represents, several analytical expressions have been developed for vertical optical path lengths through a turbulent medium. Goodman (1985) cites one such example of an

approximation proposed by Fried to model the refractive index structure constant $C_n^2[h]$ as a function of height:

$$C_n^2[h] = 4.2 \cdot 10^{-14} \left(\frac{1}{h}\right)^{\frac{1}{3}} \exp\left[-\frac{h}{h_0}\right]$$

(90)

where h is the altitude above ground level in meters and $h_0 = 3200$ m. For low altitude scenarios (e.g., less than 25 m), scientific measurements have indicated that the structure constant generally scales with $h^{-\frac{4}{3}}$ during the daytime, consistent with the following model attributed by Holst (1995) to Tatarski:

$$C_n^2[h] = C_{n0}^2 h^{-\frac{4}{3}}$$

(91)

where C_{n0}^2 is the value of the refractive index structure constant at altitude $h = 1$m. A variant of the Hufnagel-Valley model represents another analytical approximation for the refractive index structure constant that exhibits the $h^{-\frac{4}{3}}$ dependency alluded to above. In this model, $C_n^2[h]$ assumes the following analytical form:

$$C_n^2[h] = 8.2 \cdot 10^{-26} v^2 \left(\frac{h}{1000}\right)^{10} \exp\left[-\frac{h}{1000}\right] + 2.7 \cdot 10^{-16} \exp\left[-\frac{h}{1500}\right] + C_{n0}^2 h^{-\frac{4}{3}} \exp\left[-\frac{h}{100}\right]$$

(92)

where v is the rms wind speed in m/s across an altitude range of 5-20 km and h and C_{n0}^2 have been previously defined.

For comparative purposes, the three models introduced above are displayed in Figure 17, where C_{n0}^2 was arbitrarily selected to be $4.2 \cdot 10^{-14}$ m$^{-\frac{2}{3}}$ and v defined as 20 m/s. As anticipated, the relative strength of the turbulence, as reflected in the amplitude of C_n^2, decreases substantially as altitude increases. This is a direct reflection of reduced temperature fluctuations at higher altitudes, a well established physical atmospheric phenomenon. One will also observe that the Tatarski and Hufnagel-Valley models correlate

well at heights below 20 m, where the classic daytime $h^{-\frac{4}{3}}$ dependency has been observed in empirical measurements. At higher altitudes of interest to airborne and spaceborne remote sensing scenarios, however, the Fried and Hufnagel-Valley expressions become more representative of measured C_n^2 values. With respect to the latter, Fried's formulation tends to be more conservative for a given initialization height, while the Hufnagel-Valley variant displays altitude variation structure consistent with time averages observed in empirical data. In the interest of completeness, both of these atmospheric models are supported in the proof-of-concept digital model developed in conjunction with this research effort.
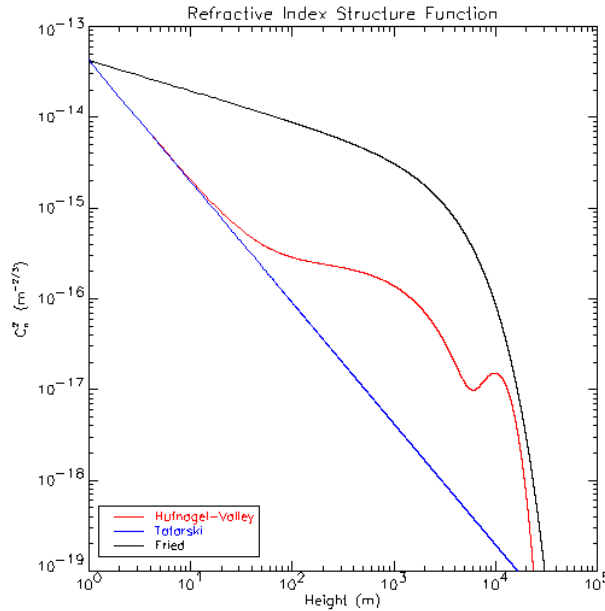
Figure 17: Comparison of various models for the refractive index structure constant C_n^2 versus height for typical daytime conditions.

In addition to the refractive index structure constant discussed above, another physical parameter used frequently to characterize atmospheric turbulence is the coherence diameter r_0, originally introduced by Fried. Fried and Goodman have shown numerically that r_0 provides a good measure of the coherence diameter of the atmosphere, whereby the resolution of a diffraction-limited imaging system under long exposure improves with aperture size until it roughly achieves r_0, beyond which point the resolution is limited by the atmosphere and remains roughly constant. For overhead remote sensing scenarios, one must

account for the spherical nature of propagated wavefronts, for which the coherence diameter assumes the following general form:

$$r_0 = 0.185\lambda^{\frac{6}{5}}\left[\int_0^R \left(\frac{h}{R}\right)^{\frac{5}{3}} C_n^2[h]dh\right]^{-\frac{3}{5}} \tag{93}$$

where R is the slant path to the target and vertical (nadir) viewing geometry has been assumed. For oblique imaging scenarios, one must include several geometric terms to accommodate the target elevation angle (θ). For oblique path lengths, Holst defines the coherence diameter according to the following expression:

$$r_0 = 0.185\lambda^{\frac{6}{5}}\left[\text{SEC}[\theta]\int_0^{R\cdot\text{COS}[\theta]} \left(\frac{h}{R\cdot\text{COS}[\theta]}\right)^{\frac{5}{3}} C_n^2[h]dh\right]^{-\frac{3}{5}} \tag{94}$$

Given the r_0 expressions identified above, one will observe that stronger turbulence (i.e., higher C_n^2) generates a smaller coherence diameter. In addition, since r_0 is a dominant function of the refractive index structure constant, it also exhibits greater sensitivity to turbulence in close proximity to the entrance aperture.

With the expressions for coherence diameter and refractive index structure constant developed above, Fried (1966) and Goodman (1985) identify closed-form, time-averaged expressions for an atmospheric turbulence transfer function. Their development focuses on several different imaging conditions, including far-field versus near-field and long- versus short-exposure times. Since this research effort emphasizes remote sensing applications, only far-field imaging conditions are of interest. The appropriate expression for exposure is essentially driven by whether the integration times are long or short relative to the characteristic fluctuation time associated with the atmospheric turbulence. Goodman suggests that integration times greater than ~10 msec correspond to long-exposure conditions while exposure times less than that enter the realm of short-exposure physics. For far-field,

long-exposure imaging scenarios, Fried identifies the following expression for the
atmospheric turbulence transfer function MTF_{atm}:

$$\text{MTF}_{atm} = \exp\left\{-3.44\left[\frac{\lambda f\rho}{r_0}\right]^{\frac{5}{3}}\right\} \tag{95}$$

where ρ is the radial spatial frequency component identified in equation 64. For far-field,
short-exposure conditions characterized by frame times considerably less than 10 msec,
Goodman indicates that the atmospheric turbulence transfer function is given by the
following expression:

$$\text{MTF}_{atm} = \exp\left\{-3.44\left[\frac{\lambda f\rho}{r_0}\right]^{\frac{5}{3}}\left[1-\alpha\left[\frac{\lambda f\rho}{D}\right]^{\frac{1}{3}}\right]\right\} \tag{96}$$

where D is the diameter of the entrance pupil and α equals 0.5 for far-field imaging
conditions. From this expression, it is apparent that the long-exposure atmospheric MTF is
simply a derivative of the short-exposure expression with $\alpha = 0$.

Figure 18 provides a comparison of the long- and short-exposure atmospheric transfer
functions relative to a filled, circular MTF for the nominal collection scenario pursued in
Chapter 4. This figure clearly illustrates that the atmospheric turbulence transfer function is
a minor contributor to overall image quality for the imaging conditions investigated in this
effort. Although many conventional remote sensing instruments capture frames in the short-
exposure regime, the longer integration period associated with the human eye effectively
leads to observations that can be characterized as long-exposure in nature. In addition, for
the overhead imaging scenarios projected for this research, i.e., involving extended duration
integration times with sparse aperture systems, the long-exposure equations for atmospheric
turbulence are definitely relevant. For completeness, however, both implementations are
available within the digital model produced for this research effort.
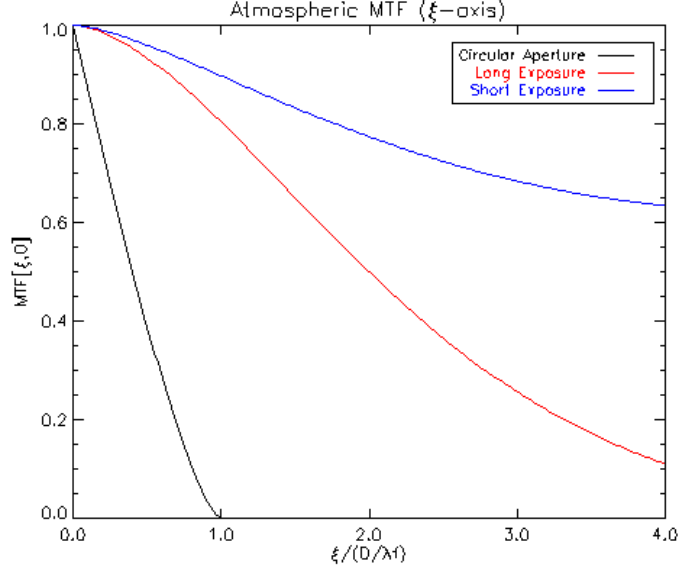
Figure 18: Comparison of the average transfer functions for
long- and short-exposure atmospheric turbulence
versus the MTF of a filled circular aperture.

3.12 System Transfer Function

The component transfer function development detailed above highlights one advantage of
evaluating the linear systems model described in Sections 3.1 and 3.2 in the frequency
domain: individual system elements and physical effects generally have functional forms that
lend themselves to analysis through appropriate modeling techniques. The other unequivocal
benefit to pursuing an MTF analysis approach is that the entire system can ultimately be
characterized by simply *multiplying* the individual components together. One should note
that this is equally true for the parallel OTF evaluation, which will be considered equivalent
to the MTF for the purposes of discussion, recognizing that it will in reality involve complex
expressions. In the spatial domain, one would tend to run into increased computational
complexity, as individual system PSF components need to be *convolved* together. Given the
frequency domain approach, the final system transfer function (MTF$_{sys}$) is formulated by
cascading the individual MTF components per the following mathematical relation:

$$\mathrm{MTF}_{sys} = \prod_{i=1}^{N} \mathrm{MTF}_i[\xi, \eta] \tag{97}$$

where N represents the total number of MTF components which characterize the imaging system. From a strict mathematical sense, one should note that the multiplication of individual MTF components in such a manner is only appropriate for a truly linear imaging system and most sensors demonstrate some form of nonlinearity. Fortunately, it has been demonstrated for most electronic imaging systems that such a cascading approach provides a reasonably accurate approximation to overall system performance. Consequently, for the components developed previously, the total system MTF can essentially be expressed as:

$$\mathrm{MTF_{sys}}[\xi,\eta,\lambda] = \mathrm{MTF_{ap}}[\xi,\eta,\lambda] \cdot \mathrm{MTF_{det}}[\xi,\eta] \cdot \mathrm{MTF_{smear}}[\xi,\eta]$$
$$\cdot \mathrm{MTF_{jitter}}[\xi,\eta] \cdot \mathrm{MTF_{diff}}[\xi,\eta,\lambda] \cdot \mathrm{MTF_{atm}}[\xi,\eta,\lambda] \tag{98}$$

where $\mathrm{MTF_{ap}}$ represents the modulus of the aberrated complex aperture OTF (or alternatively the diffraction-limited aperture MTF cascaded with the aberrated optics MTF) and the remaining terms have been previously defined. Given the emphasis on spectral considerations for this research effort, one should take note that the aperture, carrier diffusion, and atmospheric turbulence MTFs are the principal components of the overall system MTF that actually exhibit a wavelength dependency. In addition, for Nyquist-sampled systems under typically benign imaging conditions (jitter, smear, atmosphere, etc.), the aperture transfer function tends to represent the dominant effect. As a result, most attention will be placed on aberrated aperture transfer function since it alone will tend to have the sparse aperture-unique character of interest.

3.13 Polychromatic MTF

The discussion of the total system MTF appearing in Section 3.12 essentially focused on deriving a single wavelength-dependent realization that rigorously should be included within the integral of the governing equation 37, assuming an actual complex-valued aperture OTF is evaluated. This would ensure that the spectral effects of a given collection scenario are properly captured in the signal equation during the integration process. Since most evaluations of interest entail some broadband collection problem (e.g., panchromatic from 0.4 to 0.8 μm), it is fairly common practice to derive a so-called *"polychromatic MTF"* that involves developing an average equivalent transfer function through an appropriate

70

weighting scheme. The standard technique which is pursued involves computing the system MTF from equation 98 for many discrete wavelengths that span the collection passband and performing a weighted sum using some form of the incident source radiance $L_{source}(\lambda)$, the optics spectral transmittance $\tau_{opt}(\lambda)$, and the detector spectral quantum efficiency $\eta(\lambda)$. An analytical expression that captures the overall form of the polychromatic system MTF ($MTF_{poly}[\xi, \eta]$) as outlined above would be consistent with the following continuous relation:

$$
MTF_{poly}[\xi, \eta] = \frac{\int_{\lambda_{min}}^{\lambda_{max}} MTF[\xi, \eta, \lambda] L_{source}(\lambda)\tau_{opt}(\lambda)\eta(\lambda)\lambda d\lambda}{\int_{\lambda_{min}}^{\lambda_{max}} L_{source}(\lambda)\tau_{opt}(\lambda)\eta(\lambda)\lambda d\lambda}
\tag{99}
$$

where λ_{max} and λ_{min} represent the effective high and low cutoffs of the spectral passband. By inspection of equation 17 for the source spectral radiance, it becomes immediately apparent that implementing this spectral weighting function over hundreds of wavelengths constitutes a rather significant computational burden. To relieve some of the complexity, investigators tend to take advantage of the fact that the source radiance in the reflective regime of the electromagnetic spectrum is to first order principally driven by the direct reflected solar spectrum according to the following general proportionality:

$$
L_{source}(\lambda) \propto E_{s,exo}(\lambda)\tau_1(\lambda)\tau_2(\lambda)\rho(\lambda)
\tag{100}
$$

where $E_{s,exo}(\lambda)$ is the exoatmospheric solar irradiance, $\tau_1(\lambda)$ is the atmospheric transmittance from the sun to the target, $\tau_2(\lambda)$ is the transmittance from the target to the imaging sensor, and $\rho(\lambda)$ is the target spectral reflectance. If one approximates the scene radiance by the general proportionality established above, a greatly simplified expression for the polychromatic MTF can be utilized to capture some of the spectral character of the imaging system. Given such an approximation, a discrete realization of the MTF_{poly} formulation in equation 99 can be performed to arrive at the following spectrally averaged system transfer function:

$$\text{MTF}_{\text{poly}}[\xi,\eta] = \frac{\sum\limits_{i=1}^{M}\text{MTF}[\xi,\eta,\lambda_i]E_{\text{s,exo}}(\lambda_i)\tau_1(\lambda_i)\tau_2(\lambda_i)\rho(\lambda_i)\tau_{\text{opt}}(\lambda_i)\eta(\lambda_i)\lambda_i\Delta\lambda_i}{\sum\limits_{i=1}^{M}E_{\text{s,exo}}(\lambda_i)\tau_1(\lambda_i)\tau_2(\lambda_i)\rho(\lambda_i)\tau_{\text{opt}}(\lambda_i)\eta(\lambda_i)\lambda_i\Delta\lambda_i} \qquad (101)$$

where *M* defines the number of discrete wavelengths that are spectrally averaged over the passband.

The broadband MTF expression in equation 101 has seen routine use with some form of governing signal expression comparable to equation 42 to perform system-level simulations of various imaging platforms with resampled panchromatic (i.e., gray-body object) imagery. Fiete (2002) and Boucher (2000) have demonstrated that such an evaluation approach can be quite effective for evaluating the image quality associated with conventional apertures sensing broadband illumination. The latter observation makes good intuitive sense since conventional apertures tend to exhibit radially smooth MTF structure at discrete wavelengths. In addition, for well designed and manufactured optics, conventional aperture systems tend to exhibit higher order aberrations due to polishing/figuring errors which lead to transfer functions with considerably less structure as a function of wavelength when compared to mis-phased sparse apertures with first-order piston, tip/tilt errors. As a consequence of these considerations, the overall averaging effect of the broadband polychromatic MTF derived above typically represents a good approximation to the collection physics associated with conventional apertures.

For this research effort, the principal question is whether the first-order imaging physics (e.g., gray-scale world assumption) previously verified for conventional panchromatic applications continue to hold for the highly structured, demodulated OTF and lower collection SNR associated with a typical sparse aperture imaging system. For several visible wavelengths, Figure 19 illustrates the spectral variation of the diffraction-limited aperture MTFs for various sparse aperture configurations of interest. As indicated in the figure, the MTF associated with a typical sparse aperture generally exhibits spatial frequency "ripples" whose positional location in the (ξ,η)-plane vary with wavelength. This transfer function character, with alternating peaks and valleys located at different spatial frequencies as a

function of wavelength, becomes even more prominent when the sparse aperture pupil is dephased or aberrated. This will ultimately lead to certain contrast accentuation and reduction for the spectral signal content at varying spatial frequencies. Since the spectrally weighted broadband MTF approach tends to produce radially smeared versions of the single wavelength incoherent MTF, there is some concern that such an approach may not adequately capture the image quality implications of the actual spectral content one would expect in a real-world collection. In addition, since the spatial frequency ripple is a real effect at individual wavelengths, one would anticipate that the traditional approach of image restoration through use of an averaged broadband OTF characterization would introduce spectral artifacts. These issues have not been sufficiently addressed through past investigations and consequently form the principal thrust for this research effort.

(a) Annulus (b) Tri-arm (c) Golay-6
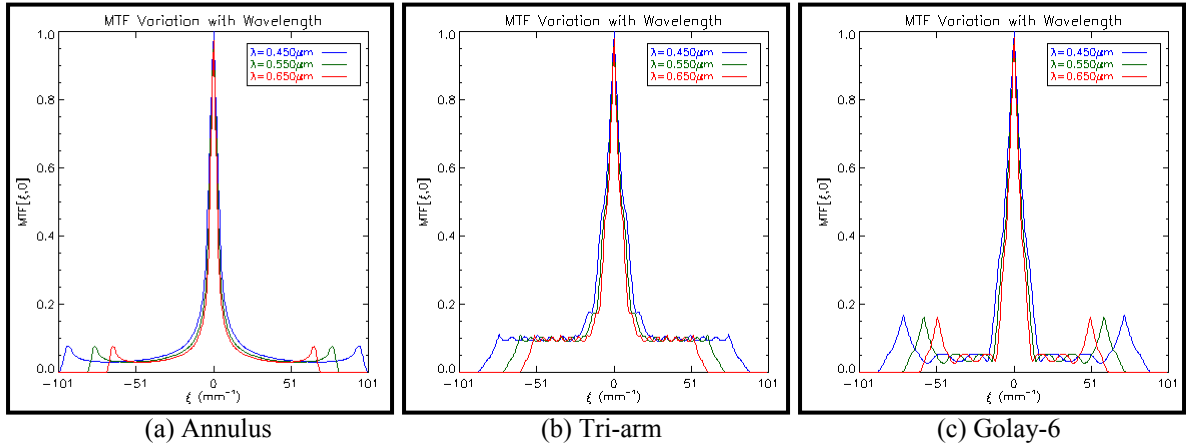
Figure 19: Variation of the diffraction-limited aperture MTF with wavelength
for several sparse aperture system configurations of interest.

3.14 System Noise

Given the derivation of appropriate theoretical expressions for the object image intensity or signal (equation 37) and the associated system MTF or OTF (equation 98 with its unit components), the final key physical effect that must be addressed in the proposed linear systems model is image noise. Clearly, one can develop a long laundry list of noise sources that can be contributors in a remote sensing application. This theoretical development will focus on the more prominent system noise sources. In general, one can quantify noise as the standard deviation (σ) of a random variable that quantifies the uncertainty associated with the signal level arising from a given scene. If individual noise components are statistically independent, which will be assumed for the purposes of this model, they will effectively add in quadrature to form an expression for the total noise σ_{tot} according to the following formulation:

$$\sigma_{tot} = \left(\sum_{i=1}^{N} \sigma_i^2 \right)^{1/2} = \left(\sigma_{phot}^2 + \sigma_{bgnd}^2 + \sigma_{dc}^2 + \sigma_{quan}^2 + \sigma_{elec}^2 + \sigma_{read}^2 \right)^{1/2} \tag{102}$$

where the N independent noise components of interest have been identified as target photon noise (σ_{phot}), background photon noise (σ_{bgnd}), dark current shot noise (σ_{dc}), quantization noise (σ_{quan}), signal chain electronics noise (σ_{elec}), and traditional detector readout noise (σ_{read}). One typically finds that the total standard deviation of the signal or system noise σ_{tot} is expressed in terms of rms electrons. With this convention, one must apply the same series of conversion and gain factors utilized with the object signal in equation 30 to derive a final expression for the total noise n_{tot} in digital image counts. This ultimately results in the following spatial domain expression for quantized image noise:

$$n_{tot} = \frac{2^n G_{conv} G_{elec}}{S_{ADC}} \sigma_{tot} = K \cdot \sigma_{tot} \tag{103}$$

where K is a proportionality factor that captures the conversion and gain process from the FPA through the A/D Converter, including any resident signal chain effects.

3.14.1 Photon Noise

For imaging scenarios that are characterized by high signal count, one finds that photon (or shot) noise is the predominant noise effect. In general, this so-called photon noise arises due to random fluctuations in the incident photon arrival rate. In addition, it tends to exhibit a distribution consistent with Poisson statistics, whereby the variance of the signal is equal to its mean. As a result of the Poisson distribution, one finds that the total photon noise σ_{photon}^{total} can simply be computed by taking the square root of the total signal S_{sig} in electrons as observed in the following relation:

$$\sigma_{photon}^{total} = \left(S_{target} + S_{bgnd}\right)^{1/2} = \left(S_{sig}\right)^{1/2} \tag{104}$$

where S_{sig} is broken up into target (S_{target}) and background (S_{bgnd}) signal components consistent with equation 20. When the photon arrival rate is large enough, one finds that the Poisson distribution essentially takes on the familiar form of a Gaussian, allowing one to model the noise through appropriate zero-mean, unit variance normal distributions. Given the list of noise contributors in equation 102 and the basic photon noise expression above, one can develop the following relation for the photon noise associated with only the target signal:

$$\sigma_{phot} = \left(S_{target}\right)^{1/2} \tag{105}$$

where the target signal is governed by a similar expression as the total signal found in equation 28. Thus, the target signal in the photon noise expression above takes the following form:

$$S_{target} = \frac{\pi A_{det} T_{int} F}{4(f\#)^2 hc} \int_0^\infty L_{target}(\lambda)\tau_{opt}(\lambda)\eta(\lambda)\lambda d\lambda \tag{106}$$

where the source radiance term L_{target} is due to the target alone. In a similar fashion, one can separately define the photon noise due to the background signal content according to the following expression:

$$\sigma_{\text{bgnd}} = \left(S_{\text{bgnd}}\right)^{1/2} \tag{107}$$

where the background source radiance is inserted into the signal equation integral found above. The reason for introducing the two separate photon noise components will become apparent later during the discussion of SNR, where one needs to separately itemize the signal due to the target and the total signal contributing to the noise in order to effect an accurate calculation.

3.14.2 Dark Current

The next noise contributor of interest involves detector dark current, a so-called fixed pattern noise source that shows spatial variability from detector to detector. Resulting from defects in the crystalline structure of a detector, dark current essentially manifests itself in the way of thermal generation of electrons which are subsequently captured in the detector depletion region and read out. In general, one typically observes that the dark current offset increases with the detector integration time T_{int} and is characterized by Lomheim (2002) according to the following general expression for silicon-based, visible detectors:

$$\sigma_{\text{dc}} = R_{\text{dc}}T_{\text{int}} = \frac{J_{\text{dc}}[T_{\text{ref}}]2^{\frac{T-T_{ref}}{T_d}}(n_{TDI}+1)A_{\text{det}}T_{\text{int}}}{q} \tag{108}$$

where R_{dc} represents the effective dark current generation rate, $J_{\text{dc}}[T]$ is the classic temperature-dependent dark current density (typically in nA/cm^2), T_{ref} is the dark current reference temperature, T_{d} is the temperature increment over which the dark current doubles, A_{det} is the area of the detector, q is an electronic charge, and n_{TDI} defines the number of TDI stages (unity for a staring sensor). For photodiode-based, infrared detectors, Lomheim indicates the dark current can be modeled through a set of two noise components, one capturing the effects of thermal noise ($\sigma_{\text{dc,therm}}$) and the other one modeling the 1/f noise ($\sigma_{\text{dc,1/f}}$). Given this convention, the following noise terms can be developed for the dark current offset associated with a typical infrared detection device:

$$\sigma_{\text{dc,therm}} = \frac{1}{q}\left[\frac{2kTA_{\text{det}}T_{\text{int}}}{R_o A}\right]^{1/2} \tag{109}$$

$$\sigma_{\text{dc,1/f}} = \frac{\alpha kTA_{\text{det}}}{R_o Aq^2}\left|\exp\left(\frac{qV_b}{kT}\right) - 1\right|\sqrt{\ln\left(\frac{T_{\text{recal}}}{2T_{\text{int}}}\right)}T_{\text{int}} \tag{110}$$

where R_0A is the photodiode resistance-area product, α is the Tobin coefficient, k is Boltzmann's constant, T is the detector temperature, V_b is the detector voltage bias, and T_{recal} is the time period from the last dark current offset calibration effort.

3.14.3 Read and Signal Chain Noise

There are several system noise sources that become prominent in low signal collection regimes and are present even when no radiation is incident on the detector. These sources include detector readout noise and signal (processing) chain noise, which essentially are borne by electronic noise effects that are typically measured within the voltage domain (e.g., detector voltage swings). Given such a test measurement, one can invert the noise factors into rms electrons by applying the appropriate conversion and gain factors introduced earlier. For instance, Lomheim (2002) formally expresses the read noise in rms electrons via the following relation:

$$\sigma_{\text{read}} = \frac{\sigma_{\text{volt,read}}}{G_{\text{conv}}} \tag{111}$$

where $\sigma_{\text{volt,read}}$ is the detector readout voltage noise and is generally driven by the dual effects of readout unit cell and amplifier noise components. For the analog signal processing chain noise, Lomheim identifies the following general expression:

$$\sigma_{\text{elec}} = \frac{\sigma_{\text{volt,sc}}}{G_{\text{conv}}G_{\text{elec}}} \tag{112}$$

where $\sigma_{\text{volt,sc}}$ represents the signal chain output noise. One should note that both of the noise sources identified above tend to be relatively constant over a given imaging scenario, essentially introducing a bias term in rms electrons to the total noise count.

3.14.4 Quantization Noise

The final source to be considered in this discussion involves quantization noise due to pixel digitization within the A/D Converter. This noise effectively arises due to the fact that a continuous input signal from the scene is quantized into discrete digital bins, creating uncertainty in the target signal level actually detected. In other words, quantization noise surfaces as a result of the A/D digitizing a range of different signal levels into the same binary digit value. From information theory, it is known that the standard deviation of a uniform distribution is simply $1/\sqrt{12}$. Thus, if one assumes the quantization is uniformly distributed, Lomheim (2002) shows that quantization noise in rms electrons can be expressed through the following equation:

$$\sigma_{\text{quan}} = \frac{S_{ADC}}{2^n \, G_{conv} G_{elec} \sqrt{12}} = \frac{\text{QSE}}{\sqrt{12}} \qquad (113)$$

where S_{ADC} is the A/D Converter input voltage range, G_{conv} is the conversion gain, G_{elec} prescribes the electronic voltage gain in the analog signal chain, n represents the number of binary digits associated with the A/D Converter and QSE is the quantum step equivalence or effective bin size of the quantization scheme in rms electrons per count.

3.14.5 Total Noise

With all the prominent system noise sources identified above, one can now utilize equation 102 to derive an appropriate expression for the total noise given a particular imaging scenario. Of course, one would anticipate that the noise profile would vary spatially within the image according to the various random processes and physical phenomena present in the collection. In addition, the total noise expressed in rms electrons must undergo the same conversion, gain and quantization processes that the target signal encountered, with proper adjustments for where in the image chain the noise is actually introduced. As could probably

be detected during their individual development, this adjustment has already been effectively accomplished in the noise terms defined above. Consequently, one needs to make use of statistical probability density functions to model the randomness associated with the various noise components cited above and combine the results with the appropriate scale factor to derive a two-dimensional functional profile of the total noise $n_{\text{tot}}[x,y]$ in digital image counts.

Jain (1989) has suggested that it is appropriate to model the two-dimensional noise profile associated with image formation according to the following general expression given the nomenclature introduced in this dissertation:

$$n[x,y] \cong \mathcal{P}\left\{f_{obj}[x,y] * \mathcal{A}[x,y]\right\} + \sigma_{\text{dc}} n_2[x,y] \\ + \sigma_{\text{quan}} n_3[x,y] + \sigma_{\text{elec}} n_4[x,y] + \sigma_{\text{read}} n_5[x,y] \tag{114}$$

where $n[x,y]$ is the total noise in rms electrons, $\mathcal{P}\{\cdot\}$ is an operator that represents a Poisson noise distribution consistent with total photon noise, and the $n_i[x,y]$ are statistically independent, additive Gaussian white noise sources with zero-mean and unit-variance. Again making appropriate modifications for the nomenclature used in this theory section, Fienup (2000) introduces a similar modeling approximation for the total noise associated with an imaging system:

$$n[x,y] \cong \sqrt{f_{obj}[x,y] * \mathcal{A}[x,y]}\, n_1[x,y] + \sigma_{\text{dc}} n_2[x,y] \\ + \sigma_{\text{quan}} n_3[x,y] + \sigma_{\text{elec}} n_4[x,y] + \sigma_{\text{read}} n_5[x,y] \tag{115}$$

whereby the photon noise is defined as the square root of the convolution of the total object signal $f_{\text{obj}}[x,y]$ with the system PSF $\mathcal{A}[x,y]$ and distributed according to Gaussian statistics. As in the previous equation, all of the noise sources are assumed to abide by a normal distribution $n_i[x,y]$ with zero mean and unit variance. In the Fourier domain, the noise spectrum associated with equation 115 is simply:

$$N[\xi,\eta] \cong \mathcal{F}\left\{\sqrt{f_{\text{obj}}[x,y] * \mathcal{A}[x,y]}\right\} * N_1[\xi,\eta] + \sigma_{\text{dc}} N_2[\xi,\eta] \\ + \sigma_{\text{quan}} N_3[\xi,\eta] + \sigma_{\text{elec}} N_4[\xi,\eta] + \sigma_{\text{read}} N_5[\xi,\eta] \tag{116}$$

where the $N_i[\xi, \eta]$ represent the frequency spectra of the individual noise source Gaussian distributions. Fienup indicates that all of the noise terms in the expression above are uniformly distributed in the frequency domain for extended remote sensed scenes, allowing one to develop the following analytical expression for the total noise spectrum including the gain, conversion, and quantization proportionality factor:

$$N_{\text{tot}}[\xi, \eta] = \frac{2^n G_{\text{conv}} G_{\text{elec}}}{S_{ADC}} \left[S_{sig} + \sigma_{\text{dc}}^2 + \sigma_{\text{quan}}^2 + \sigma_{\text{elec}}^2 + \sigma_{\text{read}}^2 \right]^{1/2} \tag{117}$$

where the noise is seen to be independent of spatial frequency by this modeling convention.

3.14.6 Signal-to-Noise Ratio

With appropriate expressions now developed for the signal and noise components of any remote sensing problem, including the one addressed by sparse aperture collection platforms, one may now investigate the general character of system signal-to-noise ratio (SNR). Numerous papers appear in the literature and a number of different conventions have been proposed to address this fundamental topic area. This section will only summarize the development presented by Fiete (2001), as it essentially captures the essence of critical features of system SNR for general remote sensing applications.

At a top level, one can obviously define the output signal-to-noise associated with a pixel (SNR_{pix}) to be the ratio of the mean detected electrons from the target (S_{target}) expressed in equation 106 to the standard deviation of the detected signal (i.e., total noise σ_{tot}) found in equation 102. This results in the following general expression for the pixel-level output SNR in the image domain:

$$\text{SNR}_{\text{pix}} = \frac{S_{\text{target}}}{\sigma_{\text{tot}}} = \frac{S_{\text{target}}}{\left[S_{\text{sig}} + \sigma_{\text{dc}}^2 + \sigma_{\text{quan}}^2 + \sigma_{\text{elec}}^2 + \sigma_{\text{read}}^2 \right]^{1/2}} \tag{118}$$

where all the quantities in the expression have been defined in previous sections. Although conventionally used to determine system SNR, the expression above does have some shortcomings, as it fails to address the general spatial frequency content of the image and the

action of the imaging system (i.e., system OTF). This introduces the concept of computing the output SNR as a function of spatial frequencies in order to account for these issues. Assuming one observes statistically independent, additive white noise and a real-valued OTF for the imaging system, the following expression for the detected signal spectrum in the frequency domain can be developed:

$$S_{\text{freq}}^{\text{target}}[\xi,\eta] = \frac{2^n G_{\text{conv}} G_{\text{elec}}}{S_{ADC}} S_{\text{target}} \frac{F_{\text{obj}}[\xi,\eta]}{F_{\text{obj}}[0,0]} \text{MTF}[\xi,\eta] \qquad (119)$$

where the first term defines the conversion factor from electrons to counts, S_{target} is the target signal in electrons per equation 106, and $F_{\text{obj}}[\xi,\eta]$ represents the target spectrum. In this development, equation 117 can essentially be used to define the corresponding noise spectrum term $N[\xi,\eta]$ required for the spatial-frequency SNR computation. With the individual signal and noise spectra separately identified through the expressions explored above, Fiete (2001) derives an analytical expression for the output SNR in the frequency domain ($\text{SNR}_{\text{out}}[\xi,\eta]$) that would take the following form given the nomenclature introduced in this dissertation:

$$\text{SNR}_{\text{out}}[\xi,\eta] = \frac{S_{\text{freq}}^{\text{target}}[\xi,\eta]}{N_{\text{tot}}[\xi,\eta]} = \frac{S_{\text{target}} \dfrac{F_{\text{obj}}[\xi,\eta]}{F_{\text{obj}}[0,0]} \text{MTF}[\xi,\eta]}{\left[S_{\text{sig}} + \sigma_{\text{dc}}^2 + \sigma_{\text{quan}}^2 + \sigma_{\text{elec}}^2 + \sigma_{\text{read}}^2\right]^{1/2}} \qquad (120)$$

$$= \text{SNR}_{\text{pix}} \frac{F_{\text{obj}}[\xi,\eta]}{F_{\text{obj}}[0,0]} \text{MTF}[\xi,\eta]$$

This expression for the output SNR spectrum provides a functional form for evaluating how SNR varies as a function of spatial frequency under the assumption of uncorrelated, white noise. Additional image-based SNR metrics utilized to evaluate the simulated imagery products generated for this research effort appear in Section 4.12.

81

3.15 Image Restoration

With a foundation now established for the basic image formation theory and modeling process, the next significant area that needs to be addressed involves image restoration. Based on the discussion in Sections 3.5 and 3.6, it is readily apparent that sparse aperture systems will generally produce imagery that displays significantly reduced contrast or sharpness compared to the equivalent conventional aperture system due to OTF or PSF effects. In order to recover some of this lost image quality, one typically applies an appropriate filtering technique to boost the reduced modulation in the MTF while accommodating the resulting system noise gain. This is the classic task of image restoration, which at a top level attempts to reconstruct an estimate of the original object from degraded imagery through use of a-priori knowledge (e.g., system MTF). Image restoration typically involves two separate mechanisms, one that deals with image sharpening (or deblurring) and one that targets system noise reduction. This section will introduce the classic restoration methodology (Wiener-Helstrom filter) that appears to be the basis for most of the previous research effort investigating sparse aperture system quality. It will then develop some of the theory associated with alternative restoration techniques that entail spatially varying (or adaptive) filtering techniques. Addressing the potential image quality improvement one can acquire through the latter techniques is a major goal of this research effort.

The conventional Wiener-Helstrom filter (commonly referred to as just the "Wiener filter") represents a classic image restoration approach, since it simultaneously attempts to address image blurring mechanisms and the statistical nature of the system noise. The fundamental method is founded on deriving an estimate $\hat{f}_{\text{obj}}[x, y]$ of the original spatial-domain object image $f_{\text{obj}}[x,y]$ by minimizing the *mean-square error* (MSE) between the two. In this context, the filter can be developed from first principles via the following optimization system equation:

$$\min \text{MSE} = \min e^2 = \min E\left\{\left(f_{\text{obj}}[x, y] - \hat{f}_{\text{obj}}[x, y]\right)^2\right\} \qquad (121)$$

where "min" represents the mathematical operation of minimization and $E\{\cdot\}$ defines the expected value of the term in the brackets. In order to perform the derivation, one must assume that the noise is an additive, statistically independent process with zero mean and that the reconstructed object image is linearly related to the degraded detected output image. These assumptions are consistent with the original linear systems model proposed in equation 15, where the frequency spectrum of the degraded output image $G_{\text{incoh}}[\xi, \eta]$ is expressed by:

$$G_{\text{incoh}}[\xi, \eta] = F_{\text{obj}}[\xi, \eta] \cdot \mathscr{H}[\xi, \eta] + N[\xi, \eta] \tag{122}$$

Such that $F_{\text{obj}}[\xi, \eta]$ represents the frequency spectrum of the original object, $\mathscr{H}[\xi, \eta]$ is the system OTF, and $N[\xi, \eta]$ constitutes the total noise spectrum. In the general modeling process described previously, all of these terms have been described in order to develop an expression for the detected output image prediction. Unfortunately, in a real-world imaging scenario, the object spectrum is generally not known a-priori and the noise spectrum is by its nature a random variable. Therefore, one must assume the former quantities are effectively unknowns that must be accommodated in the overall restoration process. In equation 122, one should note that the frequency spectrum of the output signal in the absence of noise can be separated from the general expression:

$$S_{\text{freq}}^{\text{out}}[\xi, \eta] = F_{\text{obj}}[\xi, \eta] \cdot \mathscr{H}[\xi, \eta] = F_{\text{obj}}[\xi, \eta] \cdot \text{MTF}[\xi, \eta] \tag{123}$$

which essentially defines the blurring mechanism that is present during image formation and is assumed by definition to be uncorrelated with the additive noise process. Given the imaging system convention defined above, one can show that the frequency-domain filter that minimizes MSE takes the following general form:

$$W[\xi, \eta] = \frac{1}{\mathscr{H}[\xi, \eta]} \frac{\left|S_{\text{freq}}^{\text{out}}[\xi, \eta]\right|^2}{\left|S_{\text{freq}}^{\text{out}}[\xi, \eta]\right|^2 + \left|N[\xi, \eta]\right|^2} \tag{124}$$

where the so-called Wiener filter $W[\xi, \eta]$ has both an inverse filter deblurring component represented by the inverse system OTF ($\mathscr{H}[\xi, \eta]$) term and a noise reduction component

consisting of terms for the output signal and noise power spectra. If one substitutes equation 123 into equation 124, the following alternative form of the Wiener filter implementation is obtained:

$$W[\xi,\eta] = \frac{\mathscr{H}^*[\xi,\eta]\left|F_{obj}[\xi,\eta]\right|^2}{\left|\mathscr{H}[\xi,\eta]\right|^2\left|F_{obj}[\xi,\eta]\right|^2 + \left|N[\xi,\eta]\right|^2} \tag{125}$$

where terms are introduced for the power spectrum of the original undegraded object $\left|F_{obj}[\xi,\eta]\right|^2$ and the power spectrum of the noise $\left|N[\xi,\eta]\right|^2$. Finally, by rearranging the terms in equation 125, Gonzalez and Woods (2002) develop the following convention for the Wiener filter in the frequency domain:

$$W[\xi,\eta] = \frac{\mathscr{H}^*[\xi,\eta]}{\left|\mathscr{H}[\xi,\eta]\right|^2 + \dfrac{\left|N[\xi,\eta]\right|^2}{\left|F_{obj}[\xi,\eta]\right|^2}} = \frac{\mathscr{H}^*[\xi,\eta]}{\left|\mathscr{H}[\xi,\eta]\right|^2 + \dfrac{S_n[\xi,\eta]}{S_f[\xi,\eta]}} \tag{126}$$

where $S_f[\xi,\eta]$ represents the object image power spectrum and $S_n[\xi,\eta]$ is the corresponding noise power spectrum. One should take note that the ratio of noise power spectrum to object power spectrum provides the essential mechanism for the filter to avoid "blowing up" in the presence of noise, a common malady of the simple inverse filter which addresses image deblurring alone.

Under the modeling theory developed above for the remote sensing problem, the noise spectrum was considered to be spectrally white in nature, so $S_n[\xi,\eta]$ can be considered a constant for this application. Unfortunately, the power spectrum of the original object image is seldom known a-priori, clearly will manifest some spatial frequency dependency, and is generally difficult to estimate from the degraded output image. In order to deal with this dilemma, most investigators simply treat the ratio of noise-to-object power spectra as a constant σ_K^2. With such an implementation, the reconstructed image estimate in the

frequency domain $\hat{F}_{\text{obj}}[\xi,\eta]$ is acquired through application of the Wiener filter according to the following general expression:

$$\hat{F}_{\text{obj}}[\xi,\eta] = W[\xi,\eta] \cdot G_{\text{incoh}}[\xi,\eta] = \frac{\mathcal{H}^*[\xi,\eta]}{\left|\mathcal{H}[\xi,\eta]\right|^2 + \sigma_{\text{K}}^2} G_{\text{incoh}}[\xi,\eta] \qquad (127)$$

where σ_{K}^2 is treated as a knob that is tweaked through psychoanalytical sensitivity studies that attempt to ascertain when the human perception system determines the optimum image quality is achieved.

Despite the obvious limitations associated with determining the individual constituents within the filter, the overall Wiener restoration technique has proven to be very effective in restoring the quality of highly degraded imagery products, properly balancing the need to boost the MTF for increased sharpness without unduly boosting the noise to an unacceptable level. Figure 20 graphically illustrates why the Wiener filter tends to be the optimal restoration technique, at least from a mean-square error perspective across the entire image. In Figure 20(a), a typical real-valued optical transfer function is depicted, demonstrating the traditional modulation roll-off to the optical cutoff frequency ρ_{co} one will observe with any electro-optical imaging system. Based on equations 1 and 3, one could in theory exactly recover the original object from the detected image spectrum in the absence of noise by applying such an inverse filter. Of course, digitally one would have to apply a boost threshold to ensure the inverse filter did not become undefined as the result of zeros in the system transfer function used in the denominator to develop it. This gives rise to the practical pseudo-inverse filter implementation (in green) illustrated in Figure 20(b), which avoids the infinite boosting associated with the functional inverse filter (in red) for spatial frequencies beyond the optical cutoff. In the absence of noise, one can establish a reasonably high boost threshold with near-zero values from the system transfer function included in the restoration filter. Therefore, in the absence of noise, one can almost exactly recover the original object if the system transfer function is precisely known. Unfortunately, real-world imaging systems suffer degradation due to image noise power, which the inverse filter significantly over-boosts for any reasonable level of potential sharpening. As observed in

Figure 20(c), the Wiener filter balances the competing requirements for sharpening and noise reduction through inclusion of the noise-to-object power spectrum term. This filter enables a tailored reduction of the boost of high spatial-frequency content and thereby marginalizes on a mean-square error basis the amount of destructive, high-frequency noise boost that occurs through the restoration process relative to other filter implementations.

(a) Transfer Function   (b) Inverse Filter   (c) Wiener Filter
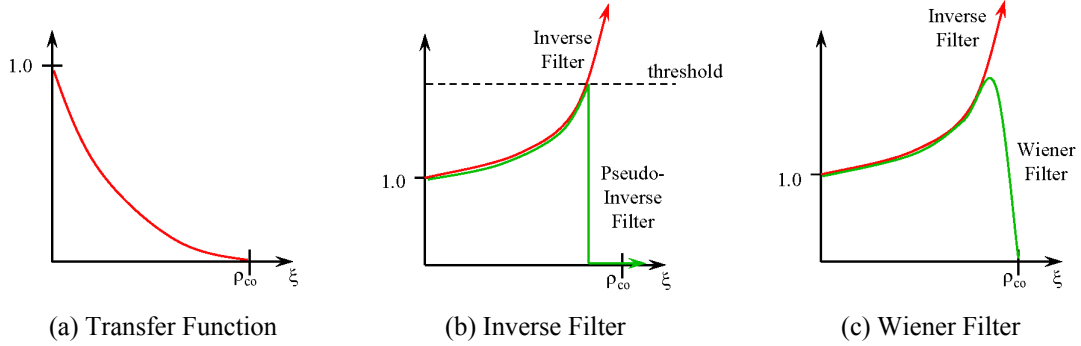
Figure 20: Typical optical system transfer function and the frequency response characteristics of derived filters utilized in post-processing to restore image quality.

3.16 Sparse Aperture System Issues

The final theoretical section contained in this dissertation addresses some of the system issues that are unique to a sparse aperture imaging system and have not yet been covered in a previous discussion. These miscellaneous topic areas include description of the effective collection aperture diameter (a hotly disputed topic), the determination of system fill factor, and finally the impact of fill factor on the system collection time required to achieve adequate SNR. These general topics areas will receive summary attention in the development contained below. One is encouraged to consult the references at the back of this dissertation if further detail is desired.

3.16.1 Effective Collection Aperture

One of the principal design issues associated with sparse aperture systems is how large to size the physical dimensions of the overall optical system in order to achieve image quality that is commensurate with comparable conventional apertures. In effect, this amounts to

determining the *effective* aperture diameter of the sparse aperture system, which is comparable to identifying the equivalent filled aperture diameter that achieves similar image quality as the synthesized sparse aperture. The reason this issue has been so hotly contested within the community is effectively highlighted by the sparse aperture OTF discussion in Section 3.5. In this section, it was pointed out that the tri-arm system OTF exhibits a cutoff frequency that is considerably reduced from that anticipated by the physical encircled diameter of the overall exit pupil. This can be readily observed in Figure 21, where the aperture MTF for a tri-arm system configuration is depicted along with various equivalent aperture diameter figures of merit. This figure clearly illustrates that identifying the encircled diameter as the effective aperture size is overly optimistic. As a consequence, one would be overstating the performance of the system if the encircled diameter were chosen, since it would imply the system could collect spatial frequencies beyond its inherent capabilities. Similarly, if one identified the effective aperture to be consistent with that which supported the maximum cutoff frequency of the tri-arm sparse aperture system, the performance would again be overstated due to the radial reduction in the OTF cutoff frequency at various clocking angles around the spatial-frequency plane. On the other hand, selecting the minimum spatial frequency to define the effective diameter greatly understates the available performance, as such a convention completely ignores higher spatial frequency content actually supported by the tri-arm system OTF. These considerations have precipitated a fair amount of debate within the community as to the appropriate metric for identifying the effective diameter associated with a given sparse aperture configuration.
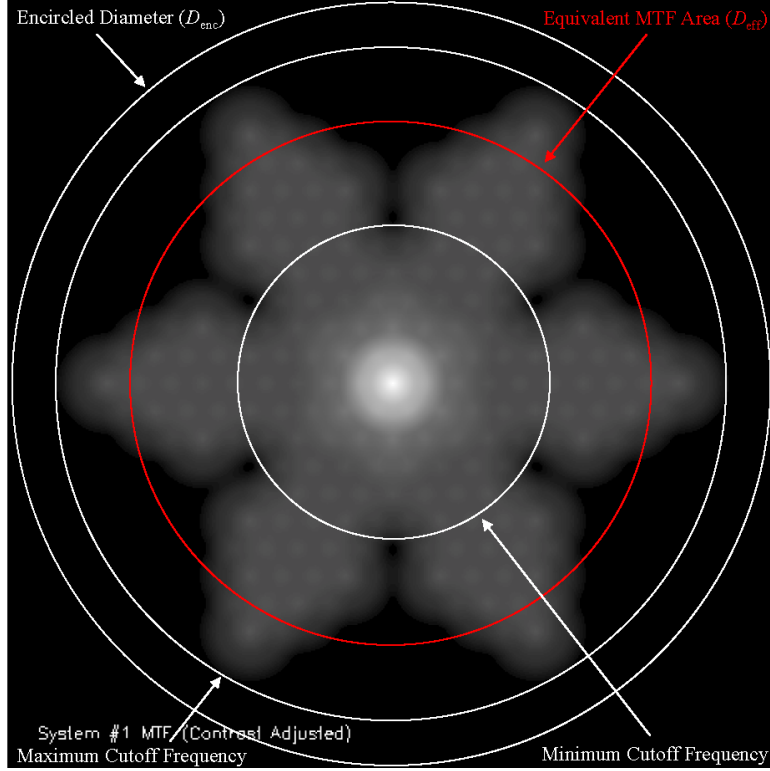
Figure 21: Representative tri-arm aperture MTF depicting various techniques for evaluating the effective diameter of a sparse aperture system.

As a result of this dilemma, Boucher (2000) and Fiete (2002) have identified a means for evaluating the effective diameter (D_{eff}) of a sparse aperture system that entails finding the equivalent filled aperture that manifests the same spatial frequency support (or area). This D_{eff} measure can be computed by evaluating the equivalent MTF area through use of a zero-one function derived from the autocorrelation of the MTF as in the following expression:

$$D_{\text{eff}} = \frac{1}{2}\left[\frac{4}{\pi}\int\limits_{-\infty}^{+\infty}\!\!\!\int \left(\text{MTF}[\xi,\eta]\bigstar\text{MTF}[\xi,\eta] > 0\right)d\xi d\eta\right]^{1/2} \tag{128}$$

where the operative function in parentheses assumes a value of one when the autocorrelation is nonzero and a value of zero otherwise. From Figure 21, it is clear that such a figure of merit for the effective collection aperture size does represent a reasonable compromise between the minimum and maximum cutoff frequencies. Acceptance of such a general formulation is certainly not universal, however, and even Fiete has used alternative

88

conventions (e.g., geometric mean of the minimum and maximum cutoff frequencies) due to the apparent lack of consensus amongst interested investigators.

3.16.2 Fill Factor

The degree of sparseness associated with a given optical system represents another classic design parameter for differentiating between sparse aperture configurations. This figure of merit is typically quantified in terms of the system fill factor F_{fill}, which is defined according to the following relationship:

$$F_{fill} = \frac{\text{sparse aperture pupil area}}{\text{equivalent filled aperture pupil area}} \qquad (129)$$

Some parties like to distinguish between what is occasionally referred to as dilute apertures (with fill factors greater than ~10% but considerably less than the conventional 80%) and sparse apertures (with fill factors below 10%). For the purposes of analysis, this research effort will not differentiate between sparse and dilute apertures, as all systems that exhibit some form of reduced fill factor will be categorized as sparse aperture imaging systems of interest.

The following discussion will summarize the general formulation for the fill factor associated with several standard sparse aperture system configurations of interest: the annulus, Golay-6 and tri-arm. For the annulus "ring aperture" design introduced in Figure 3, the fill factor (F_{annul}) is identified through the following expression:

$$F_{annul} = 1 - \frac{D_{obs}^2}{D^2} \qquad (130)$$

where D_{obs} is the diameter of the central hole and D is the physical diameter of the exit pupil. One should note that even conventional apertures manifest a fill factor, and the expression above is consistent with the optical throughput factor typically associated with a Cassegrainian system given a linear central obscuration D_{obs} due to the secondary mirror. Accordingly, the classic Cassegrainian aperture is essentially an annulus with a high fill

factor, typically greater than ~80%. Also introduced in Figure 3, the Golay-6 non-redundant array of subapertures is characterized by a fill factor (F_{Golay}) of the following form:

$$F_{Golay} = \frac{6D_{sub}^2\left(1 - D_{sub,obs}^2\big/D_{sub}^2\right)}{D_{enc}^2} \tag{131}$$

where D_{sub} is the diameter of the subapertures, $D_{sub,obs}$ is the central obscuration associated with the subapertures assuming a multiple-telescope configuration, and D_{enc} is the diameter of an equivalent filled aperture that physically encircles the synthesized sparse aperture. Given such a formulation, the maximum fill factor that a Golay-6 configuration can exhibit is 36.5%, which also assumes no central obscuration in the physically touching subapertures. The final sparse aperture system of interest in this study effort involves the tri-arm design, which essentially consists of an array of subapertures configured in a "Y" layout as depicted in Figure 3. For this sparse aperture design, assuming no central telescope in the "Y", the fill factor ($F_{tri-arm}$) assumes the following form:

$$F_{tri-arm} = \frac{D_{sub}^2\left(3n_{sub}\right)\left(1 - D_{sub,obs}^2\big/D_{sub}^2\right)}{D_{enc}^2} \tag{132}$$

where n_{sub} identifies the number of circular subapertures in an individual arm of the "Y" configuration and the remaining terms have been previously defined. For the tri-arm system depicted in Figure 3, there are three apertures on each arm (i.e., $n_{sub} = 3$) and no central subaperture, so the maximum fill factor that can be supported is ~18.4% assuming the subapertures are in physical contact and have no central obscuration. Besides the obvious design tradeoffs in weight, volume and OTF performance, one of the primary reasons the fill factor is such a critical design parameter will be highlighted in the next section.

3.16.3 Integration Time vs. Fill Factor

Naturally, it is quite intuitive that one loses signal photons as the fill factor of a sparse aperture imaging system is reduced. This will ultimately lead to poorer image quality if one does not take appropriate action to counter the loss in output SNR. For electro-optical systems, one can attempt to improve the overall collection efficiency of the imaging device

but the real lever for counteracting reduction in fill factor will be increased integration time T_{int}. This can be seen in the following expression for the total number of *detected* photons P_{target} (or equivalent rms electrons) acquired from a target source of interest:

$$P_{target} = M^2 S_{target} = \Phi_{phot} F_{fill} A_{eff} \tau_{opt} \eta_{eff} T_{int} \tag{133}$$

where the target signal S_{target} is distributed across an M x M digital image and Φ_{phot} is the incident target photon arrival rate, F_{fill} is the fill factor, A_{eff} is the effective or equivalent filled aperture area, τ_{opt} is the optical transmittance, η_{eff} is the detector quantum efficiency, and T_{int} is the sensor integration time. Although one would initially be inclined to think that the integration time should be increased by a factor of $1/F_{fill}$ to counter a reduction in the fill factor based on the expression above, Fienup (2000) has demonstrated that this is not the case for sparse aperture systems. To demonstrate the relationship between fill factor and integration time, Fienup develops an appropriate expression for system output SNR that unfolds along the lines of the following discussion.

First, one should recall that the target signal is accompanied by an appropriate background signal S_{bgnd} consistent with equation 20. The form of this background signal, which is largely dominated by path radiance, is very similar to that expressed for the target signal, as seen in the following general relation:

$$P_{bgnd} = M^2 S_{bgnd} = \Phi_{phot,bgnd} F_{fill} A_{eff} \tau_{opt} \eta_{eff} T_{int} \tag{134}$$

where $\Phi_{phot,bgnd}$ is the incident background photon arrival rate that is detected in an M x M digital image. In addition to the two signal terms identified above, Fienup also indicates that sparse aperture systems typically have an MTF structure that is directly proportional to the fill factor over an extensive, flat plateau region. This MTF characteristic generally exists over the middle spatial frequencies (ξ_{mid}, η_{mid}), allowing one to write the following approximation to the MTF:

$$\text{MTF}[\xi_{mid}, \eta_{mid}] \cong K_{ap} F_{fill} \tag{135}$$

where K_{ap} is a constant that varies with aperture type.

Similar to the functional form of the output SNR spectrum developed by Fiete (2001) in equation 120, Fienup (2000) develops a form of the output SNR in the frequency domain by determining the ratio of the mean number of total target photons (or conversely rms electrons) in an M x M digital object image to the total image noise. In this development, the following general relationship is established for the Fourier domain output SNR associated with a finite digital image:

$$\text{SNR}_{\text{out}}[\xi,\eta] = \frac{\left(\dfrac{P_{\text{target}}}{M}\right)\cdot\text{MTF}[\xi,\eta]\dfrac{F_{\text{obj}}[\xi,\eta]}{F_{\text{obj}}[0,0]}}{\left[\left(\dfrac{P_{\text{target}}}{M^2}\right)+S_{\text{bgnd}}+\sigma_{\text{dc}}^2+\sigma_{\text{quan}}^2+\sigma_{\text{elec}}^2+\sigma_{\text{read}}^2\right]^{1/2}} \tag{136}$$

where one should note that Fienup's original expression has been modified to reflect the nomenclature and standard unit conventions present in this theory section. Given the general scaling relationships established above, one can make the appropriate substitutions for P_{target}, S_{bgnd} and mid-frequency MTF in the expression for SNR_{out} found in equation 136 to arrive at the following output SNR spectrum formulation for sparse aperture remote sensing applications:

$$\text{SNR}_{\text{out}}[\xi_{\text{mid}},\eta_{\text{mid}}] = \frac{\dfrac{1}{M}\left(\Phi_{\text{phot}}F_{\text{fill}}A_{\text{eff}}\tau_{\text{opt}}\eta_{\text{eff}}T_{\text{int}}\right)\left(K_{\text{ap}}F_{\text{fill}}\right)\dfrac{F_{\text{obj}}[\xi,\eta]}{F_{\text{obj}}[0,0]}}{\left[\dfrac{1}{M^2}\left(\Phi_{\text{phot}}+\Phi_{\text{phot,bgnd}}\right)F_{\text{fill}}A_{\text{eff}}\tau_{\text{opt}}\eta_{\text{eff}}T_{\text{int}}+R_{\text{dc}}T_{\text{int}}+\sigma_{\text{quan}}^2+\sigma_{\text{elec}}^2+\sigma_{\text{read}}^2\right]^{1/2}} \tag{137}$$

which ultimately establishes the relationship between the fill factor and integration time as a principal function of the mid spatial-frequency output SNR, target object normalized frequency spectrum and incident photon arrival rates. If a threshold SNR is established for the lowest acceptable image quality, one can subsequently solve this equation for the integration time, resulting in a rather complicated quadratic expression in F_{fill} and the remaining terms. Instead of explicitly solving this quadratic expression, Fienup explores its general character in terms of its individual noise components, including photon noise, read

noise and dark current. For the case of photon noise only, Fienup derives the following expression for the integration time:

$$T_{int} = \frac{SNR_{thresh}^2}{F_{fill}^3 A_{eff} \tau_{opt} \eta_{eff} \left(K_{ap} \mu[\xi,\eta]\right)^2} \left(\frac{\Phi_{phot} + \Phi_{phot,bgnd}}{\Phi_{phot}^2}\right) \propto \frac{1}{F_{fill}^3}$$ (138)

where one observes that sparse aperture imaging scenarios that are photon-noise limited (e.g., high SNR$_{out}$ collections) will exhibit integration times that are proportional to the *cube of the inverse fill factor*.

The so-called "fill factor cubed law" introduced by Fienup through equation 138 has significant system implications, as it implies that for a given SNR$_{thresh}$ acceptable for a filled aperture image, one must increase the integration time 1000x for the equivalent sized sparse aperture with a fill factor of 10%. Such integration times put severe requirements on maintaining imaging platform stability and overall optical system phasing in order to ensure adequate image quality. For the other noise constituents, Fienup determined that the read noise drives an inverse square relationship to the fill factor and the dark current abides by an inverse fourth power of the fill factor. In this derivation, one should note that the fill factor relationships were driven by two essentially different phenomena: the loss of signal photons and the reduction in MTF. These two factors ultimately combine to require increased integration time over what intuition alone would suggest. Fiete (2002) subsequently demonstrated through a series of psycho-physical image quality studies that the integration time generally varied between $1/F_{fill}^2$ and $1/F_{fill}^3$ depending on the sparse aperture system and the particular simulation performed, essentially confirming the general integrity of Fienup's analytical results as cited above. As a result, it is clear that the sparse aperture system fill factor is a critical design parameter for remote sensing applications.

As a final note on the output SNR discussion developed above, one should again remember that the traditional analyses have been performed assuming a gray world. As mentioned previously, this has enabled high resolution aerial panchromatic imagery to be utilized in the past for the purposes of modeling and simulation, resulting in high fidelity predictions for conventional aperture types. Given its heritage, pursuit of a similar approach in the sparse

aperture arena constituted a natural progression for the modeling community. Unfortunately, sparse aperture configurations tend to manifest system characteristics that are relatively unique compared to more conventional optical systems. For instance, the spectral-spatial structure inherent in a typical sparse aperture system OTF is likely to introduce color artifacts that typically are not encountered with traditional apertures and will ultimately diminish image quality. The fundamental question at hand is whether these anticipated spectral artifacts are significant enough that some of the previously derived physical "rules of thumb" need to be revisited and/or alternative collection/processing techniques pursued to accommodate them. It is the objective of this research endeavor to provide the initial hooks for evaluating the spectral implications associated with a sparse aperture system, thereby paving the way for future investigation if the spectral issues are significant enough to merit further attention.

Chapter 4

Approach

With the basic theoretical development introduced previously, this chapter lays out the fundamental approach that was pursued to accomplish the dissertation objectives enumerated in Chapter 2. In that vein, Section 4.1 provides a brief summary of the satisfaction of phenomenological and theoretical requirements through the previously discussed imaging mathematics. Section 4.2 subsequently provides a top-level overview of the proof-of-concept modeling process developed in conjunction with this research effort, the critical piece needed to satisfy the remaining dissertation requirements. The rest of this chapter is then dedicated to detailing specific aspects of the general modeling approach. As part of that discussion, a nominal imagery collection scenario is defined for the exploration of unique sparse aperture spectral quality issues found later in Chapter 5. Given this nominal scenario, Section 4.3 identifies how the actual imagery collection geometry was determined for the proof-of-concept modeling effort. Sections 4.4 and 4.5 identify the general approach utilized to define the spectral radiance reaching the optical system entrance pupil, appropriately accounting for scene spectral radiometry as well as atmospheric propagation and losses. Following scene characterization, the specification of imagery collection system characteristics, including pupil configuration, system transfer function, impulse response, and optical aberrations, are discussed in Section 4.6. Except for addressing the system noise implementation, which is introduced as a pre-cursor to the restoration process below, the approach for modeling key components of the collection process is accordingly captured in the initial sections of this chapter.

With the foundation described above, the remaining part of the chapter is more or less dedicated to addressing various system-level evaluations pursued in this research effort, with emphasis on detected and restored imagery products. Given the described collection phenomenology on a wavelength-by-wavelength basis, Section 4.7 discusses the nature of the quasi-monochromatic imagery evaluation that preceded the integrated signal implementation. Following that discussion, the approach for evaluating the actual integrated

detected signal across the passband of the sensor is described in Section 4.8. To this point, the discussed approach has only considered object signal content; no system noise component has yet been introduced. Section 4.9 rectifies that situation by describing the noise model that is incorporated into the modeling process. With a noisy, integrated signal in hand, Section 4.10 discusses the various Wiener restoration approaches pursued to restore the detected imagery predictions for the optical configurations under investigation. This is followed in Section 4.11 by a summarization of the initial studies performed to compare the spectrally based imagery products developed through this dissertation effort with the more traditional approach based on resampling gray-scale imagery. As a result, this section ultimately introduces the crux of the research effort in determining whether sparse aperture optical systems exhibit unique attributes that drive the need to address higher spectral fidelity in performing image simulations. Finally, Section 4.12 develops the mathematical theory behind the various evaluative metrics utilized in this effort in an attempt to quantify the observed quality considerations.

4.1 Theoretical Development

As alluded to above, the discussion in the previous chapter effectively addresses the theoretical and phenomenological development requirements for modeling the key spectral issues associated with sparse aperture remote sensing collection systems. As indicated in that chapter, the basic foundation for the developed theoretical approach is the general linear systems model for incoherent imaging platforms formulated through equations 8 and 15. Given these fundamental governing relations, analytical terms were developed to capture the major constituents of the detected imagery physics, including but not limited to the object spectral signature, optical system pupil function and associated phase errors, aberrated system optical transfer function, and spectrally diverse image noise. In addition, the theory associated with standard image restoration techniques was also introduced, with heavy emphasis on the developed Wiener-Helstrom filtering methodology investigated through this research effort. To support evaluation efforts, additional analytical development of certain imagery metrics will be provided in Section 4.12 of this chapter. As a consequence of the overall theoretical effort outlined here, a basic end-to-end system construct has been introduced that captures the first-principles physics required to address fundamental spectral

considerations in generic sparse aperture system configurations. Areas that will receive some additional attention in future discussion stemming from the acquired research results include implications of modeling spectrally variant pupil phase errors, polychromatic optical transfer functions, polychromatic versus gray-world object scene content, and system transfer knowledge in the restoration process. With the basic theoretical building blocks established, the emphasis of the remaining approach section will be targeted on describing the various components of the proof-of-concept sparse aperture imaging model developed for this research effort

4.2 Modeling Approach

Given the end-to-end system modeling construct detailed in Chapter 3, this section will describe the proof-of-concept modeling effort that implemented the theoretical development in a first-principles approach. As stated previously, the objective of this engineering simulation effort was to demonstrate the feasibility of the proposed approach and to pursue general modeling results in an attempt to gain physical insight into the spectral implications unique to sparse aperture collection systems. The intent was not to develop an integrated, user friendly product for widespread use. The overall approach and general modeling capabilities that were developed for this engineering model are discussed below.

4.2.1 Modeling Overview

As indicated in previous discussion, the principal underlying assumption for this research effort is that one can identify regions in the detected object scene, referred to as *isoplanatic patches*, at given field angles where the imaging physics can to first order be approximated as linear, shift-invariant. This isoplanatic assumption is fundamental to the overall applicability of the general linear systems model developed in the previous chapter. Given this assumption, the research model implementation entailed various simulation components, some of which existed in detailed physical models with years of heritage and others which required development of prototypical engineering code as part of this effort. As anticipated, integration of the inputs and outputs from various modeling capabilities was not necessarily a trivial exercise, consuming a fair amount of time to ensure model compatibility and the

integrity of the physics. To better appreciate the implemented approach for the proof-of-concept engineering model, one should consult the general flowchart depicted in Figure 22. This figure provides an overview of the entire modeling effort, developed to be an end-to-end system model that captures the critical physical attributes of sparse aperture overhead system collection of a remotely sensed scene.
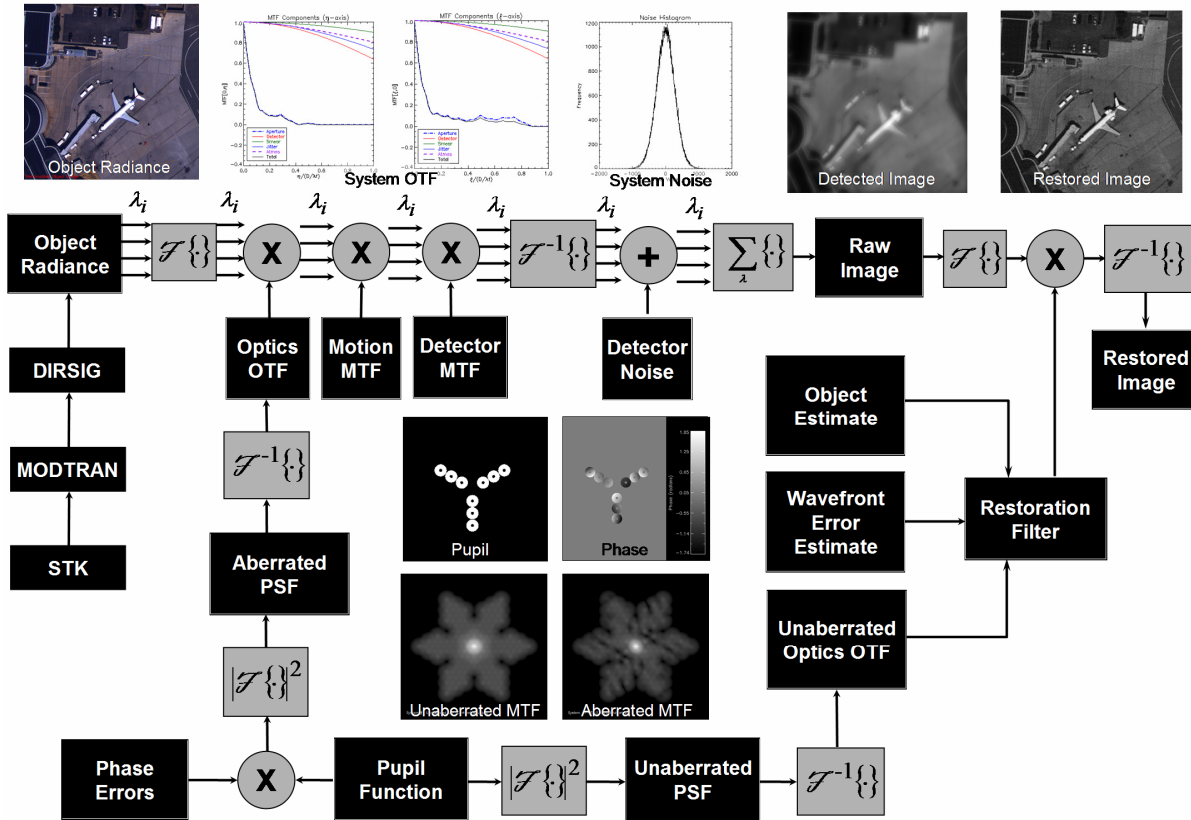
Figure 22: Overview of the implemented modeling approach.

As observed in the flowchart, the primary thrust of the approach is to create a first-principles model of each critical component specified in the governing linear systems equation on a spectral radiometric basis. For general orientation, the flow essentially goes from the object radiance "spectral cube" in the top left of the flowchart to the restored, integrated image in the top right, with various key physical modeling chains feeding up from the bottom of the figure. The gray boxes in the flowchart essentially delineate key mathematical operators utilized in the modeling process and black boxes represent significant modeling capabilities,

routines and/or outputs. The spectral radiometric aspect of the model is captured through the arrow array emerging from the object radiance box, with λ_i capturing the concept of multiple spectral "images" passing through the physical modeling process. Some exemplar outputs of this modeling implementation appear at the center of the diagram, where one will observe a representative sparse aperture pupil function, its associated MTF, the detected red-green-blue (RGB) quasi-monochromatic system prediction, and its Wiener filter restoration. Considerably more detail on the nature of these modeling products will be provided in future discussion.

Within this modeling construct, the spectral object scene or radiance profile at the entrance pupil of the sparse aperture optical system can be derived through several different means. The two principal options pursued in this research endeavor use either a simulated hyperspectral radiance cube or actual airborne multi/hyperspectral imagery. The synthetically-generated spectral object scenes were produced using the Digital Imaging and Remote Sensing Image Generation (DIRSIG) model developed at the Rochester Institute of Technology (RIT). Alternatively, the Wildfire Airborne Sensor Program (WASP) Terrapix RGB digital framing camera and the airborne Hyperspectral Mapper (HyMap) scanning sensor provided real overhead spectral imagery for resampled polychromatic object scenes. The pros and cons associated with these scene generation approaches will be addressed in Section 4.5.

As displayed in the flowchart in Figure 22, the collection geometry and timeframe for a given collection scenario are established through use of the commercially-available, orbital propagation Satellite Tool Kit (STK) v5.0 from Analytical Graphics, Inc. Regardless of the technique for producing an object scene, the spectral radiance reaching the entrance pupil of the imaging system is essentially determined by the U.S. Air Force MODTRAN 4.0 atmospheric propagation code using the temporal and geometric parameters from STK. This radiation transfer code is widely accepted as an industry standard for computing atmospheric propagation and losses at moderate resolution. The output from MODTRAN 4.0 is subsequently utilized in conjunction with DIRSIG to produce a synthetic spectral radiance cube as described previously or to provide a mean radiance level for a given collection

scenario to convert raw digital counts in real overhead imagery to units consistent with sensor-reaching spectral radiance. This process effectively establishes the spectral radiance at the entrance pupil to the optical telescope at the spectral resolution associated with the source. In accordance with the flowchart, this "spectral cube" is then transformed into the Fourier domain to allow application of various component transfer functions which model the action of the imaging system on the object scene.

Per the previous theoretical development, a Fourier optical approach has been implemented to apply the various system transfer function components developed in Sections 3.7 through 3.11 including dephased/aberrated optics, relative imaging platform motion, and focal plane detector characteristics. Most of the optical simulation process detailed in Figure 22 uses engineering software developed in the IDL^{TM} programming environment. Within this simulation, the optical transfer function associated with the aperture is evaluated through a digital implementation of the complex autocorrelation of the aberrated, spectrally scaled pupil function. Details of this implementation will be described in greater detail in sections to follow, but the flowchart in Figure 22 clearly indicates that spectrally scaled pupil function and phase error descriptions feed a set of Fourier transform operations to accomplish the appropriate autocorrelation. At this juncture, the phase error and aberration implementation relies upon the application of traditional aberration coefficient or Zernike polynomials to describe the phase profile across the pupil in the context of an analytical sensitivity evaluation of a desired rms wavefront error. This polynomial fit to the optical phase error is digitally sampled within the model to create a discrete, two-dimensional array representing the distributed phase profile. Clearly, the aberrated phase or OPD error description could be acquired through use of a detailed optical design package, such as Code V or Optics Software for Layout and Optimization (OSLO). If available, empirically measured OPD errors could also be easily captured within the current modeling construct with minimal code modifications. Once individual transfer function terms have been developed for the imaging system components of interest, they are cascaded to form a system OTF and applied to the object scene spectrum as seen on the top leg of the flowchart.

100

The inverse transform of the degraded image spectrum for each spectral radiance "line" is subsequently computed to allow incorporation of the appropriate noise effects, consistent with the theoretical development in Section 3.14. This implementation assumes that uncorrelated, statistically independent noise is added to the predicted degraded imagery acquired through the Fourier optics approach. Of course, there is no fundamental limitation that would prevent addressing spectrally correlated noise in the overall simulation architecture described by Figure 22. Following application of noise, the proof-of-concept model performs integration, resampling and quantization operations with the individual spectral radiance realizations to predict the expected detected imagery (prior to restoration) across the passband of interest. The development of this integrated signal content is represented by the summation block in the flowchart above, producing the "raw" detected imagery output.

As observed in the flowchart in Figure 22, the simulated "raw" imagery acquired through this process is designed to capture any spectral effects associated with a sparse aperture collection scenario, including appropriate wavelength-dependent scene radiance, aberrated system transfer function and noise effects. As such, this spectral radiometric model implementation provides a capability to address an area of investigation that has not been previously pursued in the body of research conducted in the sparse aperture arena. As will be demonstrated in a subsequent discussion, the proof-of-concept tool has enabled various systems to be compared in order to evaluate the spectral nature of remotely sensed collections acquired from different sparse aperture sensor types. Although the demonstrated ability to model the raw, detected imagery from a generic sparse aperture system configuration on a spectral radiometric basis constituted the original final requirement for this research endeavor, the end-to-end system model would not be complete without the inclusion of an appropriate restoration technique. As a consequence, various conventional Wiener filter restoration routines were implemented in the proof-of-concept modeling process, as depicted by the final analysis chain on the right hand side of Figure 22. Consistent with the discussion in Section 3.15, these Wiener restorations attempt to mitigate some of the effects of the blurring and additive noise operations incorporated into the strawman modeling process. As observed in the flowchart, these Frequency-domain filter implementations make use of the unaberrated pupil function

description, presumed understanding of in-situ phase errors, and potentially any noise-to-object power spectrum ratio knowledge to restore degraded detected imagery. The output of this restoration process ultimately represents a prediction of the expected derived imagery from the sparse aperture system under investigation, including the spectrally dependent effects of the system OTF, phase errors, noise, and image restoration.

Figures 23 and 24 provide additional sample output products from the proof-of-concept modeling process depicted in Figure 22. On the left side of Figure 23, one will observe a typical tri-arm sparse aperture system pupil function, with a phase profile depicting randomly distributed piston/tip-tilt. The right side of Figure 23 illustrates the nature of the aperture modulation transfer function (MTF) that is acquired by autocorrelating the aberrated pupil on the left. This diagram provides a qualitative feel for the effects of dephased subapertures, as one will note that the MTF exhibits considerably reduced modulation relative to its diffraction-limited counterpart, to the point of introducing nulls in its spatial frequency coverage. These nulls will ultimately give rise to lost spatial frequency content and reduced quality in the derived output imagery.
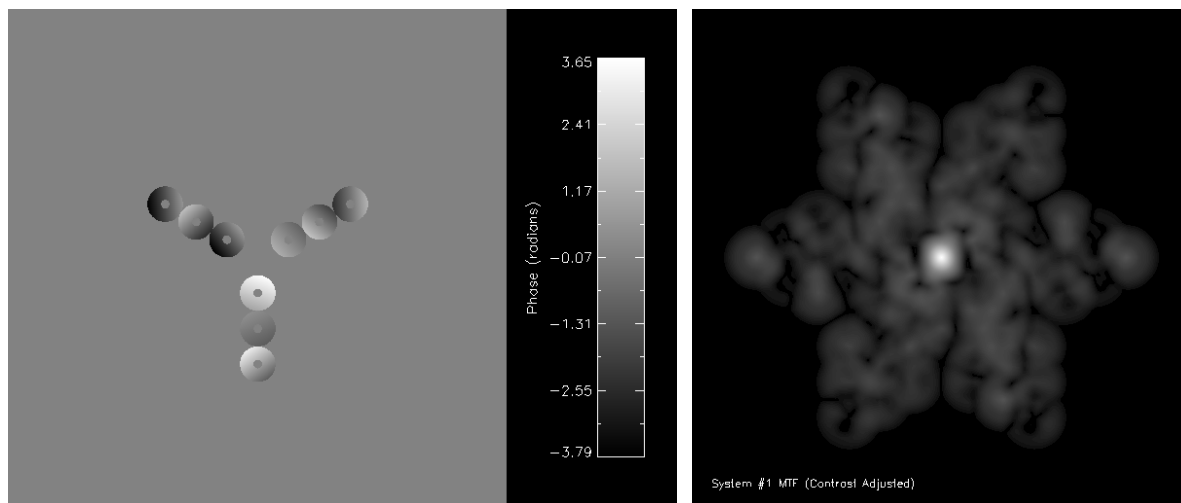
Figure 23: Sample tri-arm pupil function and associated pupil autocorrelation.

Figure 24 displays the quasi-monochromatic imagery predictions that can be acquired from the implemented spectral radiometric model. On the left side of the figure, one will observe an airborne digital RGB image whose intensities have been rescaled through use of

MODTRAN 4.0 to represent the object spectral radiance at the entrance pupil. The center of the figure depicts a prediction of the noisy, degraded RGB image acquired for the aberrated pupil in Figure 23. As anticipated, the system transfer function of the sample tri-arm system produces imagery with significantly reduced sharpness. Finally, the right side of the figure illustrates an "optimal" Wiener filter restoration one would acquire with perfect OTF and phase knowledge, as well as the ability to restore individual RGB "bands." Obviously, this set of examples typifies an optimal case, so more representative scenarios will be pursued in the sections that follow. In addition, detailed parameters from individual model runs associated with specific scenarios conducted for this research effort will be provided in later discussion.

| (a) Original Object | (b) Detected Image | (c) Wiener Filter Restoration |
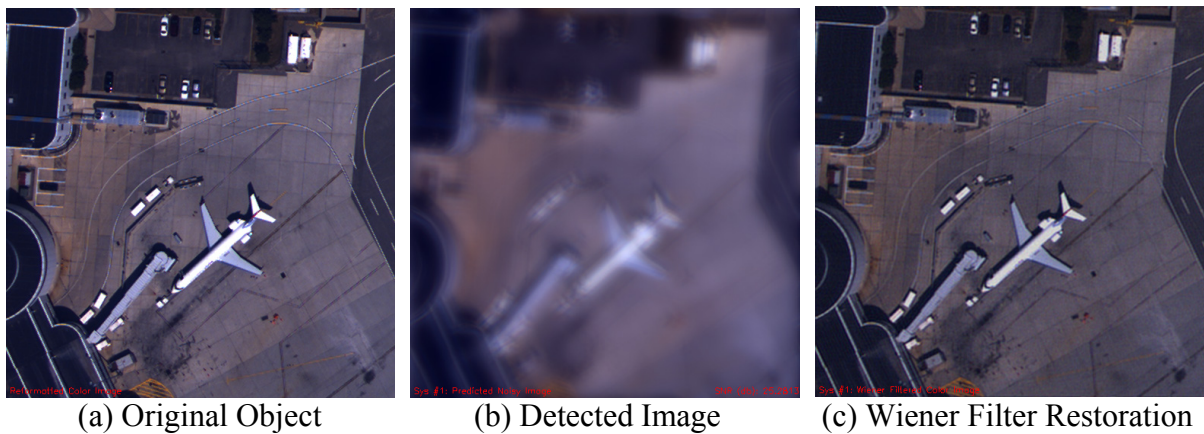
Figure 24: Sample image predictions for the tri-arm system configuration in Figure 23.

4.2.2 Nominal Collection Scenario

Although many different imaging conditions have been modeled in the course of implementing and exercising the proof-of-concept model, the nominal collection scenario pursued in this research effort appears in Table 2. As seen in the table, this research has principally focused on evaluating a panchromatic, visible/infrared (VNIR) scenario under conditions where the spectral integrity of a polychromatic object scene was preserved. Therefore, although a spectral application was not specifically considered, the required spectral radiometric physics were implemented and exercised for an imaging scenario that could manifest spectral quality issues. The objective of this panchromatic simulation focus was to gain insight into whether increased spectral fidelity in a sparse aperture imagery

prediction led to detrimental quality effects not captured by traditional gray-world resampling approaches.

Parameter	Value
Spectral Passband	0.4-0.8 μm
System f-number ($f^{\#}$)	18.0
Optical Sampling	Nyquist (or better)
Ground Sample Distance (GSD)	Variable; 18 in (nominal)
System Transmission ($\eta \cdot \tau_{opt}$)	Profile; 0.3 (average)
Secondary Obscuration (ε_{sub})	0.24
Focal Plane Array (FPA)	Staring Frame CCD
Read Noise	50 rms electrons
Dynamic Range	11 bits
Image Smear	0.5 pixel
rms Wavefront Error	Variable; 0.10 waves rms (nominal)
Atmosphere	MODTRAN 4.0 mil-latitude summer
Visibility	17.0 km
Simulation Time	~1700 GMT (~79° sun elevation angle)
Target Location	43.2° N Lat, 77.6° W Lon

Table 2: Nominal collection scenario

As seen in Table 2, the simulations executed for this research effort assumed Nyquist sampling. Although not necessarily common for conventional optical systems, Nyquist sampling has traditionally been pursued in most sparse aperture system studies. This selection of optical sampling had the added benefit of avoiding aliasing artifacts that could be misconstrued as spectrally induced. Since the collection scenario assumed extended access coverage from a space-based platform, the implemented sensor model is a staring frame charge-coupled device (CCD), thereby eliminating certain scanning sensor issues. Of course, it would be rather trivial to modify the existing model if a scanning system were of interest. In addition, as complementary metal oxide semiconductor (CMOS) devices gain maturity and start competing with CCD design concepts, one may also consider implementing a CMOS detector MTF, including an appropriate carrier diffusion term.

Table 2 also shows that a number of different system wavefront error values were investigated. The objective of modeling different aberration levels was to bound the point at

which spectrally induced effects surface. As part of this exercise, a nominal value of 0.10 waves rms was assumed to probe the validity of that traditional "rule-of-thumb" for high-quality imagery collection given the spectral radiometric model implemented for this research. Most of the remaining optical system parameters were selected rather arbitrarily but deemed satisfactory for a typical remote sensing application. Once again, any number of the modeling parameters could be modified at the discretion of the investigator without significantly altering the principal character of the spectral issues observed in this research.

In addition to the optical system characteristics, Table 2 also defines some of the key spatial, temporal, and atmospheric conditions that were modeled in the nominal collection scenario. As observed in the table, one of the default MODTRAN atmospheres (mid-latitude summer) with good overall visibility was utilized in the model. In addition, a geodetic location on the earth corresponding to Rochester, NY was selected for orbital analysis and related atmospheric propagation evaluation. The principal rationale for this selection was the fact that detailed synthetically generated DIRSIG scenes of the Rochester metropolitan area were available to support the modeling effort. As a consequence, all scenes (synthetically generated and resampled imagery approaches alike) were arbitrarily assumed to be located at the target position identified in Table 2. This selection provided representative sensor-reaching radiation transfer while minimizing the number of required MODTRAN atmospheric propagation runs. In addition to the chosen standard atmosphere, an arbitrary time of day (approximately 1:00 pm EDT) was selected for the nominal collection scenario, ensuring a high solar elevation angle and good signal-to-noise ratio (SNR). Early in the research, the investigation of different atmospheres and radiation conditions was determined to be a secondary objective relative to the demonstration of a general-purpose spectral radiometric sparse aperture model and exploration of sparse aperture-unique spectral quality issues. Clearly, however, it would be a worthwhile exercise to perform sensitivity studies on sparse aperture image quality, with atmosphere, scene contrast, radiometry, collection geometry and SNR as parameters of interest in the overall trade space.
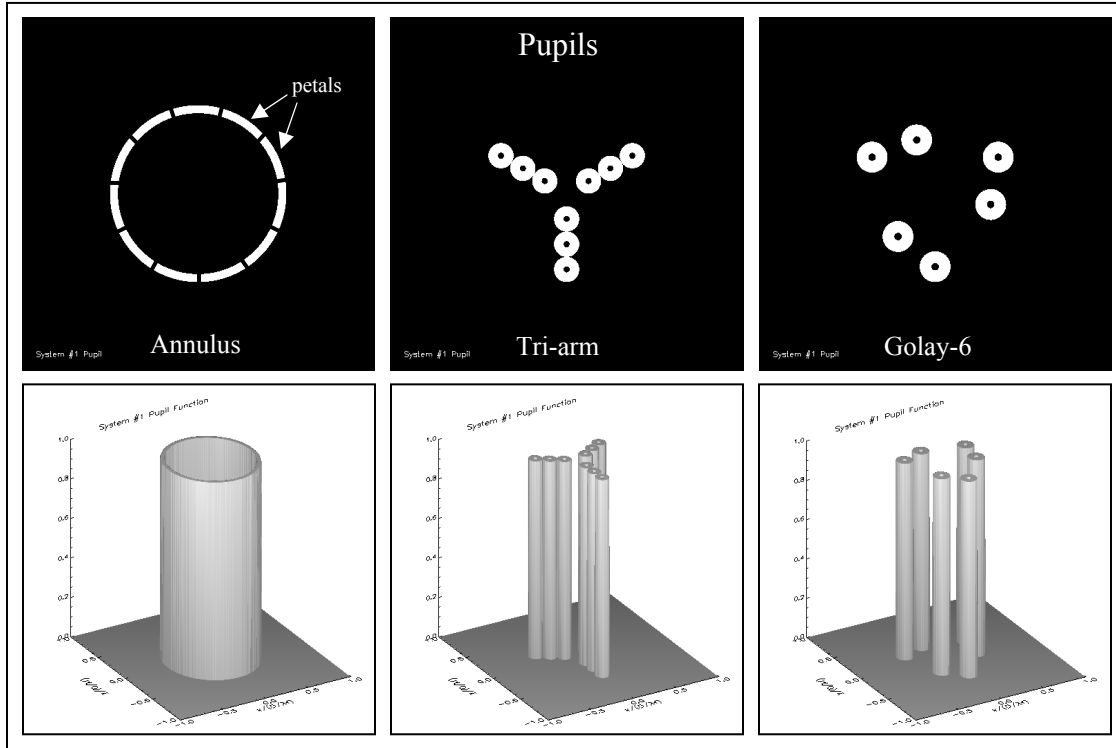
Figure 25: Baseline sparse aperture pupil configurations.

Given the general imaging system and collection parameters in Table 2, several sparse aperture exit pupil configurations were selected for evaluation under the nominal collection scenario. These sparse aperture pupil configurations appear in Figure 25. The standard "annulus" configuration is shown on the left. For this research effort, it was assumed that the annulus was designed to be a serious of adjoining optical petals or subaperture "wedges" used to form the annular configuration. Under this construct, models for evaluating configurations consisting of nine (9), eleven (11), and fifteen (15) optical wedges were constructed for comparative purposes. The center of the diagram depicts a typical tri-arm sparse aperture system consisting of nine (9) subapertures in the classic "Y" configuration. Representative of many sparse aperture systems, this configuration was selected for many of the initial trade studies performed for this research, and one will discover the preponderance of runs in the results section to follow involve this configuration. Finally, a standard Golay-6 sparse aperture pupil configuration is illustrated on the right side of Figure 25. As its name implies, this configuration is one of the myriad non-redundant arrays originally proposed by Golay (1971) and entails the appropriate positioning of six (6) subapertures to provide good coverage in the spatial frequency domain. Although these three pupil configurations were

evaluated extensively in this research, numerous other geometries were also investigated over the course of the effort. During these studies, it was determined that the three pupils in Figure 25 adequately captured the typical character of the image quality issues observed during the investigation. One should also note that the model was designed to provide relative comparisons between two aperture types. Therefore, conventional filled circular and obscured Cassegrainian configurations were also considered for comparison.

4.3 Imagery Collection Geometry

As discussed previously, MODTRAN and DIRSIG (if pursuing a synthetically-generated object simulation) both require information about collection geometry to predict the radiance profiles at the entrance pupil of the imaging system. In addition, the DIRSIG model can simulate a flight trajectory over a given target scene. Of course, this requires information on how the collection geometry changes with time. Since the application envisioned for sparse aperture systems in this research involves remote sensing of the earth from relatively high altitude, a hypothetical space mission was designed with the help of Satellite Tool Kit (STK) v5.0. With various baseline orbital propagators, including J4 Perturbation and SGP4, STK has become an industry-wide standard for calculating the position and attitude of satellite vehicles as a function of time. The overall software package includes a suite of analytical tools that allow time-dependent flight profile information, such as position, orientation, range, line-of-sight, and general sensor coverage, to be computed. In addition to essential analysis, STK also includes a toolbox of various visualization capabilities that allow an appropriate flight path to be designed for the desired collection scenario. Therefore, the commercially available orbital evaluation software was used to develop the desired mission profile and imaging platform collection geometry for the space-based collection scenario pursued in this research effort.

Since the proposed mission is genuinely hypothetical, an arbitrary orbital design was developed within STK to ensure an ascending pass over Rochester, NY, with a nadir viewing geometry. Once again, this orbital design was selected to support the nominal collection scenario described in Section 4.2.2 and enable the use of existing detailed synthetic object scenes for DIRSIG, which will be discussed in greater detail later. Figure 26 provides a

three-dimensional illustration of the selected orbital design in a geocentric inertial frame. Both the orbital path and ground track for the imaging vehicle (identified by the yellow "dot") are depicted in the diagram, with the region of the orbit within view of the Rochester object scene (identified by the yellow "x") highlighted in yellow. This geocentric inertial view shows that the designed mission profile provides a ground track that passes right over the desired target region, providing the desired nadir viewing conditions.
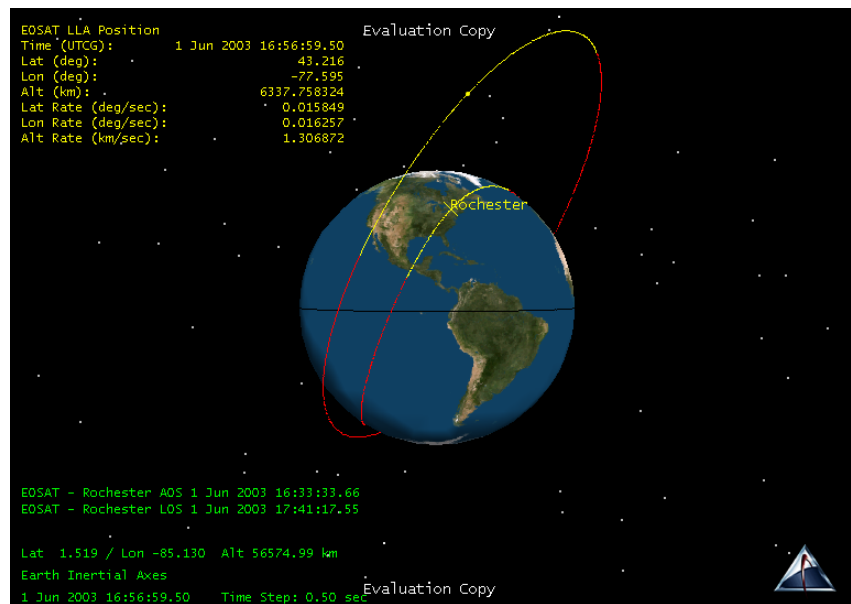
Figure 26: Three-dimensional view of the arbitrary collection orbit
from STK designed to support this research effort.

For the chosen collection scenario, the imaging vehicle has access to Rochester in its field of regard for a little over 1.12 hours (~4064 sec) during a period of time around 1:00 pm EDT, in accordance with the nominal collection scenario discussed previously. Details of the specific collection scenario appear in Table 3. In addition to the time of day for the collect (which establishes detection SNR), the only other significant detail of interest is the range (~6337 km) to the target at nadir since it establishes how much atmosphere is present over the imaged path length for the performed simulation cases. Although this parameter clearly impacts path radiance and the overall spectral radiance solution, one should not lose sight of the fact that it is not unique and any number of different orbital altitudes could have been investigated. The one selected here was simply deemed to be "representative" of one that could theoretically be used for remote sensing applications.

Parameter	Value
Date of Collection	1 June 2003
Access Start Time (GMT)	16:33:33.66
Access Stop Time (GMT)	17:41:17.55
Access Duration (sec)	4063.893
Time of Collection (GMT)	16:56:59.00
Collection Range (km)	6337.008
Collection Azimuth (deg)	133.1
Collection Elevation (deg)	89.9

Table 3: Collection scenario details for the
designed mission profile.

Figure 27 provides additional two-dimensional visualization options available through STK
that were used to help design the collection scenario for this research effort. In this figure,
the imaging vehicle's ground track is displayed on a flat map projection of the earth. Once
again, the highlighted yellow region correlates with that part of the track that is within view
of the Rochester targeted area. The diagram on the left side of the figure provides the overall
satellite ground track for the entire orbit. The right side of the figure depicts a magnified
region of the ascending pass over the Rochester area, with the satellite vehicle shown rapidly
approaching the target. Through use of the STK orbital propagation engine and associated
visualization capabilities, the classical Keplerian orbital elements (principally focused on the
right ascension of the ascending node) were slightly adjusted from the initial mission design
until the desired nadir ground track geometry over Rochester was acquired. This exercise
resulted in a set of orbital elements that produced the mission profile illustrated in Figure 27
and detailed in Table 3.
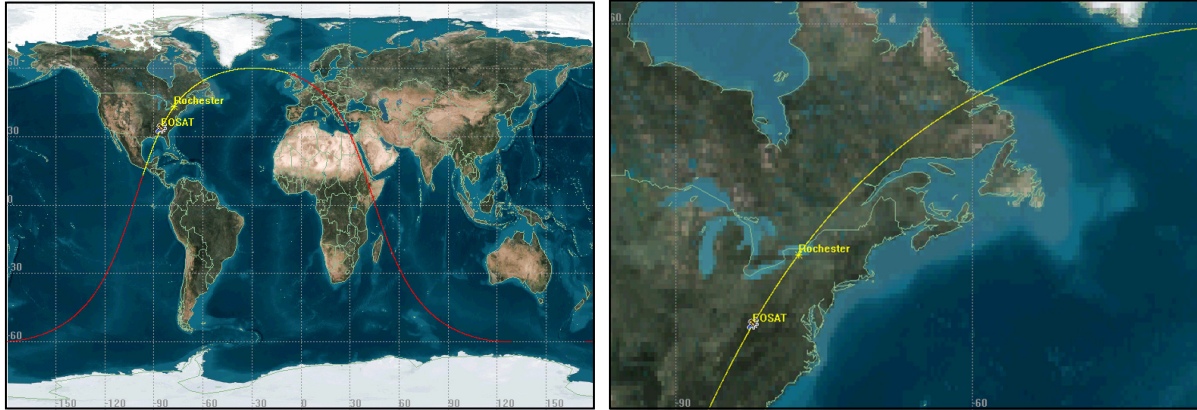
Figure 27: Orbital ground tracks for the nominal collection scenario designed in STK.

Following the mission scenario development discussed above, the final output of this orbital propagation evaluation effort was a series of line-of-sight, sensor-to-target range, and associated collection geometry information (e.g., azimuth and elevation angles) at regular time intervals required to model an imaging system passing over a targeted scene. Figure 28 displays the unique capabilities for visualizing three-dimensional collection geometry through STK's Visualization Option. This viewing option was highly beneficial during mission design in evaluating the azimuth and elevation angles associated with the telescope of the imaging vehicle at each step of the imaging encounter.
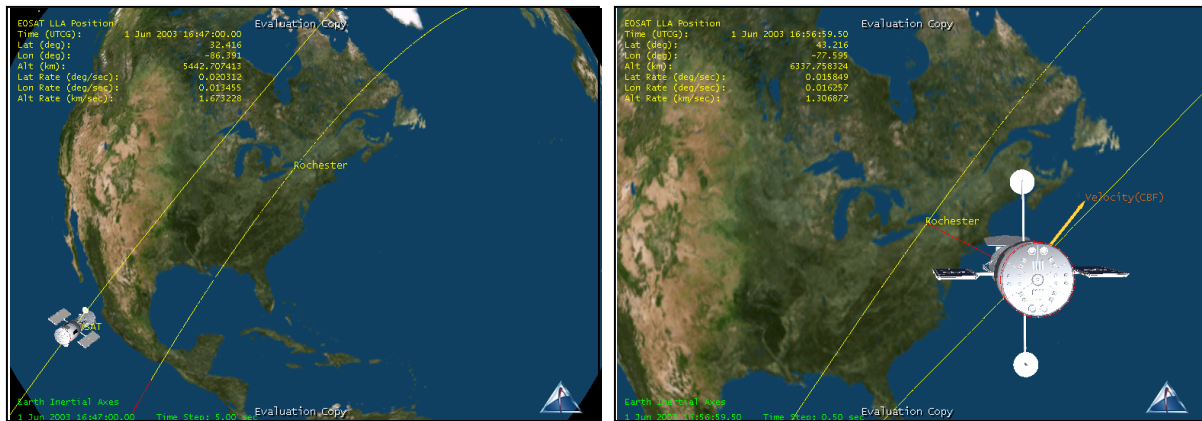
Figure 28: Three-dimensional visualization of the satellite collection geometry
for the nominal mission profile designed in STK.

110

In addition to the unique collection geometry tools discussed above, STK also provided evaluation windows that enabled evaluation of the precise collection angles and range-to-target, as depicted in Figure 29. The image on the left shows how STK can place an inertial sphere around the imaging vehicle during the orbital propagation scenario, allowing one to evaluate vehicle attitude on a temporal basis. Additionally, STK can also analyze key orbital parameters, such as the azimuth (in green), elevation (in red) and range (in blue) data that appear on the right side. Of course, this collection geometry data could also be output in raw ASCII format for use as flight trajectory data in a larger simulation such as that afforded through DIRSIG. With all of this visualization and analysis capability, it was possible to simultaneously view the satellite-to-target collection geometry (as observed in Figure 28) and the raw geometry numerical detail (as seen in Figure 29) at each time step. As a result, STK was instrumental in performing the mission analysis needed to define the overall collection geometry for the hypothetical sparse aperture scenario modeled during this research effort.
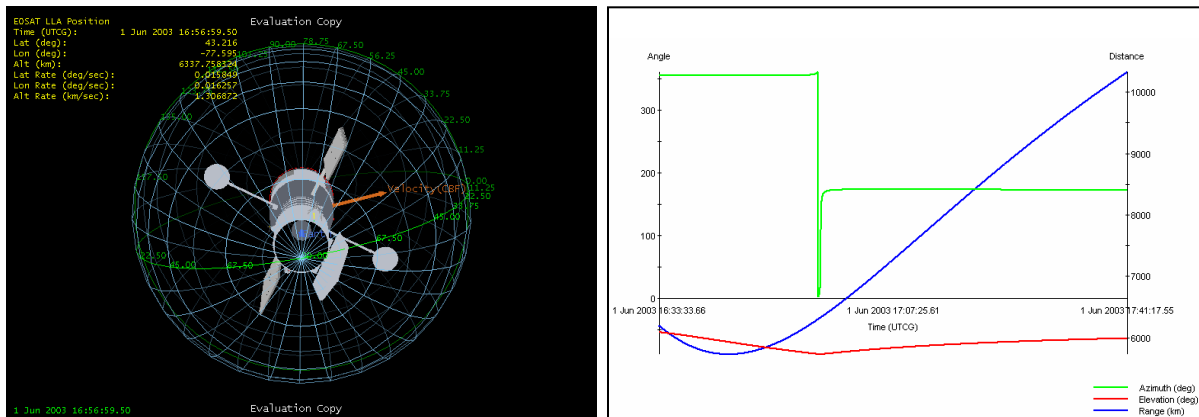
Figure 29: Visualization of the imaging satellite attitude and range-to-target
for the nominal mission profile designed in STK.

4.4 Atmospheric Modeling

As discussed previously, a critical element needed to support the evaluation of the spectral radiance reaching the collection aperture is the characterization of the atmosphere. For this requirement, it is standard practice to rely on the MODTRAN atmospheric propagation model for remote sensing applications. This model is widely used within the community to

compute radiation transfer through the atmosphere at moderate spectral resolution (limited to the highest resolution of 2 cm^{-1}). The program will compute atmospheric transmission, scattering, absorption and emission phenomena given input characterization data or defaulting to one of the standard atmospheres in its internal database. Atmospheric characterization data are input via a file called a "card deck" that contains detailed collection parameters and known atmospheric conditions. Output is in the form of several "tape" files that contain details of the radiation transfer prediction.
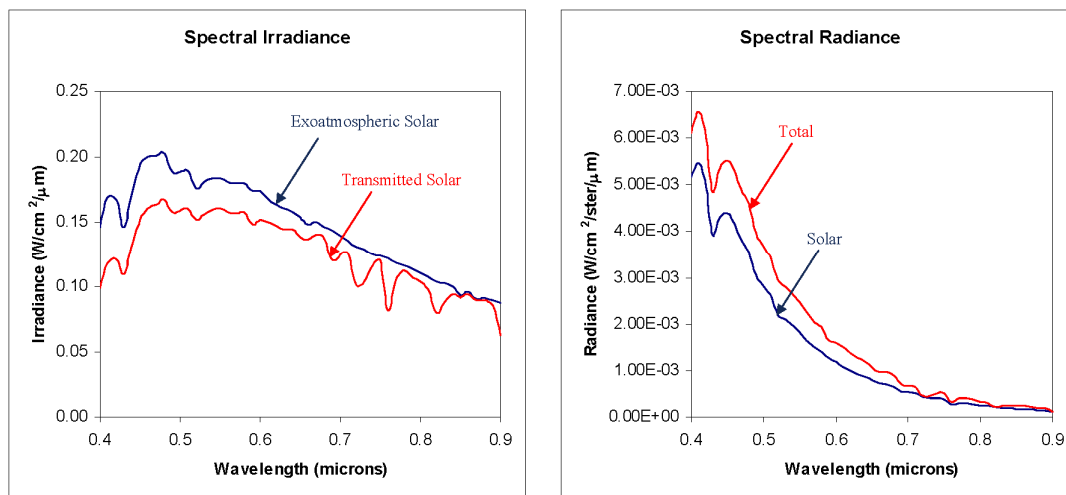
Figure 30: MODTRAN 4.0 output for the nominal collection scenario.

Figure 30 plots the spectral irradiance and radiance profiles versus detection wavelength that were acquired for the nominal collection scenario through use of this radiation propagation model. These data were generated as a result of running MODTRAN 4.0 with the previously defined geometry, a mid-latitude summer default standard atmosphere, relatively good visibility (17 km), and high sun angle (~79° elevation). The spectral irradiance plots on the left side of the figure demonstrate the classic profiles for exoatmospheric (in blue) and transmitted (in red) direct solar components over the general passband of interest. The diagram on the right contains sample plots of the direct solar (in blue) and sum total (in red) spectral radiance one would observe at the entrance pupil for the nominal scenario investigated in this research. As anticipated, these plots indicate that direct solar represents the principal source of detected radiation and transmission losses are relatively benign for the collection scenario explored in this investigation.

112

By design, DIRSIG currently has embedded hooks in its radiometry submodel that rely upon MODTRAN outputs to compute the exoatmospheric irradiance, upwelled and downwelled path radiance, and path transmission characteristics. This allows the radiometry calculations performed within DIRSIG to be based upon an industry standard radiation transfer code, ensuring its overall integrity for computing spectral radiance profiles reaching the entrance pupil of an imaging sensor. When one performs spectral simulations utilizing resampled digital imagery, the spectral radiance calculations become slightly more cumbersome, requiring some manual manipulation of MODTRAN output to rescale raw digital counts. This was somewhat marginalized for this research effort by identifying a standard nominal collection scenario for all object scenes. As a consequence of that assumed simulation approach, a single MODTRAN 4.0 run could be utilized with DIRSIG to provide the "representative" radiance amplitudes required to rescale raw imagery. At this point, it is important to remember that the overall focus of this investigation was not to precisely model different imaging scenarios, but to accurately capture the general phenomenology of the imaging physics in a proof-of-concept model that enabled unique sparse aperture system characteristics to be addressed from a spectral radiometric perspective.

There are several limitations within the overall MODTRAN modeling construct of which one should be cognizant. In addition to the constraint in spectral resolution indicated above, MODTRAN also does not have the capacity to model background reflected radiance as identified in equation 17, so that radiation mechanism is not generally captured by the program. In addition, the atmospheric propagation model does not compute downwelled radiance directly but can be manipulated to provide directional downwelled radiance. By placing a sensor on the ground looking out to space and subsequently numerically integrating values across the encapsulating hemisphere, one can acquire reasonable estimates of downwelled radiance. Fortunately, the DIRSIG model has been developed to capture these general radiation mechanisms through use of the basic industry-standard capabilities resident within MODTRAN. This ultimately enables detailed, high-accuracy spectral radiance calculations to be performed consistent with the governing target signal expression found in equation 17.

4.5 Scene Spectral Radiometry

As discussed previously, the fundamental object signal computation will be formulated through use of either a resampled, high-resolution airborne spectral image (e.g., from WASP or HyMap) or a synthetically-derived spectral radiance cube predicted by the Digital Imaging and Remote Sensing Image Generation (DIRSIG) model. From a simulation perspective, the airborne spectral products have certain appeal since they provide real-world object scene content. Unfortunately, the airborne products have fundamental constraints in the tradeoff between spatial and spectral resolution that tend to restrict their universal application. For instance, one will typically find that a spectral system with superb spatial resolution has limitations in spectral resolution (e.g., WASP). Conversely, a hyperspectral imaging system designed for good spectral resolution will frequently suffer constraints in spatial resolution (e.g., HyMap). Therefore, although providing useful object scene data for certain investigations, current state-of-the-practice airborne spectral imagery exhibits inherent resolution limitations that impact the level of fidelity that can ultimately be addressed from a simulation perspective.

Since synthetically-derived imagery products do not theoretically suffer from the same limitations (i.e., one can essentially "dial up" any spatial or spectral resolution desired), they provide a good bridge between the two extremes observed with real-world spectral imagery. Of course, synthetic products tend to suffer from a certain lack of realism, especially in the context of background clutter or texture, so they do not represent the panacea for all spectral modeling issues. As a consequence of the dilemma introduced here, this research effort pursued simulations that made use of both object imagery types, recognizing the inherent imitations of both but figuring that all could provide insight into the fundamental issue of addressing potential spectral issues with sparse aperture collection systems. Given its overall complexity, the DIRSIG simulation capability will be addressed in the initial discussion below, followed by a brief summary of the nature of the airborne imagery products utilized as object scene content in this research effort.

The basic synthetic image generation software code utilized in this effort has evolved over the years through the dedicated efforts of graduate students and staff members at the Center

for Imaging Science (CIS) at RIT. The top-level architecture associated with this detailed simulation code appears in the block diagram in Figure 31. In general, the DIRSIG modeling capability represents a first-principles based evaluation of the distributed spectral radiance reaching a remote sensing collection platform. It is designed to produce synthetic radiance field images with high spectral fidelity over the wavelength range covering 0.3 to 20.0 μm in the overall electromagnetic spectrum. The code accomplishes the required radiation transfer computations through use of a back-propagation ray trace methodology, which allows both direct and multiple-bounce radiation paths to be computed. Pristine object scenes and targets are represented in a three-dimensional faceted construct with assigned material properties that enable accurate light-matter interaction physics (i.e., target reflectance or bi-directional reflectance distribution function BRDF) to be modeled.
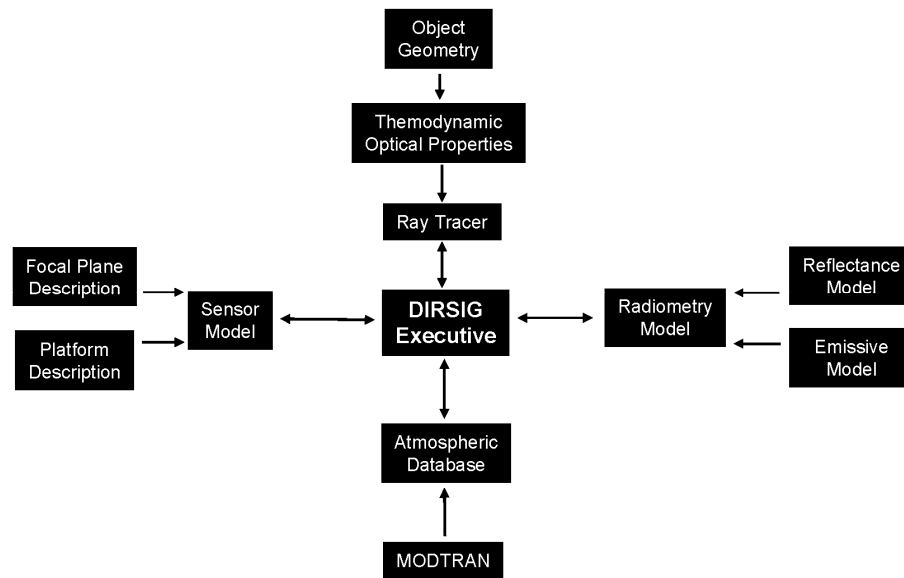
Figure 31: Top-level DIRSIG architecture.

Given its reliance on MODTRAN for performing radiation propagation, DIRSIG has the inherent capability to perform accurate spectral radiometric predictions of various collection scenarios, including the effects of direct and scattered solar, upwelled and downwelled path radiance, background shadowing, thermal emission effects and the other general radiation mechanisms captured in equation 17. With the collection geometry information provided by STK and the embedded use of MODTRAN for atmospheric propagation, numerous iterations

of the DIRSIG model were executed to provide the instantaneous spectral radiance field for a staring sensor configuration at a given collection time. This approach for deriving the object scene radiance captures the required scene-induced spectral and geometric effects that are of interest to the research effort as input to the sensor transfer function, signal integration, sampling and noise modeling process outlined previously.

For this research effort, the principal DIRSIG-generated target object involved a complex extended scene of the Rochester metropolitan area referred to as *megascene*. During algorithm development and testing, simpler monochromatic target constructs were investigated to verify the integrity of the model implementation. The results of these preliminary investigations will not be recounted here in the interest of space. The objective of the more complicated extended source was to capture the expected spectral and spatial characteristics of a real-world remotely sensed scene to determine if the predicted spectral effects manifest themselves in elaborate scenes with high spatial detail and complicated light-matter interactions. As observed in Figure 32, the chosen Rochester megascene target exhibits complex spatial attributes that are ideal for evaluating the image quality associated with an overhead collection system. As observed in this figure, the target consists of suburban scene content, with high-fidelity models of buildings, trees, swimming pools, tennis courts, roads, athletic fields, and other man-made objects. Although advertised to demonstrate spatial fidelity on the order of 1 meter (~39 inches), the underlying texture map acquired from airborne visible spectral data is sampled at 6-in GSD and certain features on the modeled scene content (e.g., buildings, automobiles, etc.) are frequently better than the resolution associated with the background clutter. The level of detail that ultimately can be supported by DIRSIG target objects is illustrated by the aircraft, vehicles and man-made structures appearing in Figure 33. Accordingly, the Rochester-area megascene representation provides an excellent object for addressing complex scene interactions through a synthetically-driven model that has the added flexibility of allowing the investigator to effectively set any spatial or spectral resolution of interest.

Figure 32: Sample DIRSIG spectral radiance image of the Rochester *megascene* object generated with RGB spectral planes.
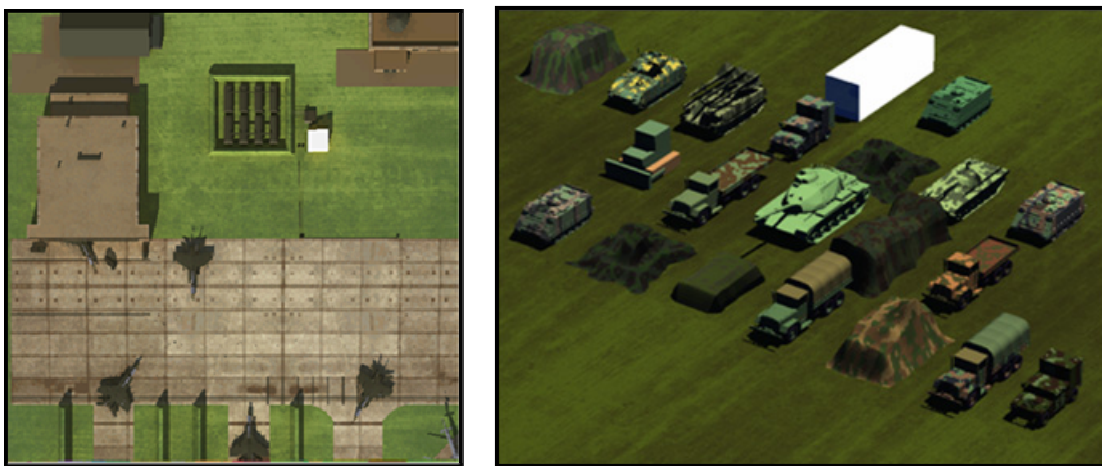
Figure 33: Sample DIRSIG target objects demonstrating supported level of detail.

As discussed previously, the baseline scenario that was modeled in this effort involved generation of spectral radiance image cubes in the reflected region of the electromagnetic spectrum, emphasizing the spectral implications associated with panchromatic collection applications. Of course, there is nothing unique with that modeling focus and certainly narrower band multispectral scenarios could be investigated with the proof-of-concept model developed for this research. With the flexibility provided by DIRSIG, the object scene was initially rendered at high spatial resolution and moderate spectral resolution to adequately capture the spatial and spectral effects of the structurally detailed object prior to resampling in the proof-of-concept sensor model. For the DIRSIG megascene object described above, the scene was spatially oversampled by 2:1 to 3:1 relative to the desired collection ground sample distance (GSD) prior to the application of the system transfer function in the Fourier optics model implementation. This implies that the megascene object was rendered at a 1:1 spatial resolution of 6-9 inches to achieve the 18 inch resampled GSD prescribed in the nominal scenario. As a result, the scene was essentially pushed to the limits of its spatial fidelity to acquire nominal 18-in GSD imagery simulations with appropriate oversampling. Within the proof-of-concept modeling tools, the spectral radiance field acquired from DIRSIG is optically sampled to be consistent with sensor characteristics and transformed to the Fourier domain for application of the various sparse aperture system OTF components addressed in Chapter 3. Following the addition of image noise, the spatial domain result of this image simulation process is subsequently integrated across the passband of interest including spectrally variant detector effects, converted to detected electrons via the governing expressions in the previous chapter, and quantized to digital counts to produce a prediction of detected image quality.

With the synthetically-derived object discussion complete, the following discussion provides insight into the real-world airborne spectral imagery that was also utilized to address the requirements of this research endeavor. The principal sources of this spectral digital imagery were the Terrapix digital frame camera from the Wildfire Airborne Sensor Program (WASP) and the Hyperspectral Mapper (HyMap) scanning sensor from Integrated Spectronics. The WASP sensor for VNIR collection entails a commercially available aerial mapping camera with an Eastman Kodak 4080x4080 pixel mosaic CCD array. Its spectral coverage spans the

reflective spectrum from 0.4-0.9 μm with three detection bands (red/NIR, green and blue). The individual spectral bands in the WASP CCD are created through use of a color filter array configured in a Bayer pattern. The source imagery used in this investigation had already been interpolated to create three fully populated spectral arrays of data prior to conversion to object scene radiance values in the digital sparse aperture model. Any artifacts induced by this interpolation scheme were assumed to represent true object radiometry and were therefore ignored in subsequent evaluation of the spectrally induced effects acquired in the sparse aperture simulations. As a consequence of this approach, color filter array interpolation issues were eliminated as a potential source of chromatic artifacting in this research effort, which was focused on isolating the inherent spectral implications of a distributed aperture. The optical configuration of the WASP camera exhibits an instantaneous field-of-view (IFOV) of 0.164 mrad, enabling a GSD of 7.85 inches at a 4000-ft collection altitude. Figure 34 provides RGB color composite examples of WASP imagery at the latter GSD that were utilized in this simulation effort. From this description, it is clear that the WASP instrument provides an excellent source of high-spatial resolution data but suffers limitations in spectral diversity that ultimately must be explored. Despite this spectral resolution concern, it was decided the WASP data would still be useful in providing insight into the spectral character of a high-resolution, panchromatic overhead collection system.
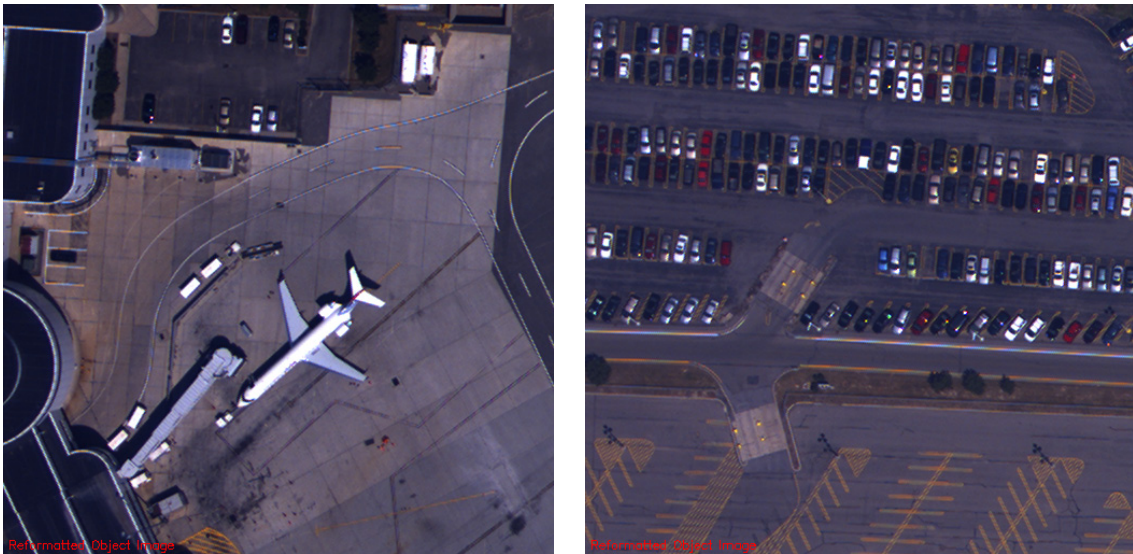
Figure 34: Sample ortho-rectified WASP airborne multispectral imagery.

Figure 35: Sample HyMap airborne hyperspectral scanner imagery.

The HyMap airborne hyperspectral sensor, on the other hand, is a commercially available scanning monochromator with 126 bands spanning the VNIR/SWIR part of the electromagnetic spectrum from 0.44-2.5 μm. The IFOV of the instrument is 2.0 mrad cross-track and 2.5 mrad in the along-track direction, providing a geometric mean GSD of 11.2 feet (3.4 meters) at a nominal 5000-ft operating altitude. The HyMap sensor consists of 512 pixels in the cross-track direction, resulting in a swath width of ~1.5 km at a 3-m IFOV. For this simulation activity, an existing HyMap aerial collection of an extensive area around Mobile, AL area at 10-15 ft GSD was utilized as a source for the spectral object data required by the proof-of-concept modeling capability. Although all 126 hyperspectral bands were available, only 33 bands spanning the spectral range from 0.4-0.9 μm were actually used to perform the panchromatic simulations in this investigation. Samples of the scene content resident in this data collection appear Figure 35, where an RGB image was formed from three of the visible hyperspectral bands for the purposes of display. Based on the discussion above, it is apparent that the HyMap sensor exhibits good spectral resolution (with bandwidths on the order of 15-20 nm) but suffers from less than nominal spatial resolution for the high-resolution applications of interest. Once again, however, the data was deemed worthy enough to provide some insight into spectral phenomenology for the collection systems of interest and was consequently included in subsequent investigation. It is interesting to note that the two real-world sensors that were discussed here suffer from

120

exactly the trade-off dilemma between spatial and spectral resolution that was introduced in a previous section, clearly demonstrating the overall utility in pursuing synthetic-based simulations as well to help bridge the limitations.

4.6 Imaging System Characterization

As alluded to in previous discussion, the principal means for characterizing an imaging system is through its impulse response or associated system transfer function. Those fundamental parameters represent the basic building blocks for the governing linear imaging expressions found in equations 8 and 15. For the imaging configurations under investigation, the dominant contributor to the system transfer function will be shown to be the complex autocorrelation of the exit pupil or aperture stop of the optical system. Accordingly, the unique aperture configurations pursued in this study must be adequately characterized, including their complex-valued nature in the presence of subaperture dephasing or optical aberrations. From a geometry perspective alone, one should recall that the individual aperture configurations are defined through a real-valued, one-zero pupil function as described in Chapter 3 and demonstrated for nominal sparse aperture configurations in Figure 25. Of course, since spectral attributes represent a primary thrust for this dissertation, the spectral character of the complex pupil configurations must also be appropriately captured. This section introduces the principal means pursued in this research effort for characterizing the various optical configurations under investigation, including the characterization of the aberrated phase profile across the aperture (Section 4.6.1), the aperture optical transfer function (Section 4.6.2), the aperture point spread function or impulse response (Section 4.6.3), and the total system transfer function definition (Section 4.6.4).

4.6.1 Pupil Phase Profile

As introduced in the theoretical development found in Chapter 3, one of the principal distinctions that set sparse aperture systems apart from conventional telescope configurations is the problem of phasing an array of smaller subapertures to achieve a common image field at the detector with the increased optical resolution of an effectively larger synthesized aperture. As conveyed in Section 3.7, this research effort addressed system aberrations and

121

phasing issues in the same general context: through use of a complex aperture function with a phase term that captures the nature of the error in terms of the optical path difference (OPD). The principal component of this phase term is traditionally referred to as the aberration function $w[x,y]$ and can be described through the use of many different polynomial fit options. The two most common approaches for capturing the pupil phase profile involve either standard aberration coefficients W_{klm} used in conjunction with a polynomial expression of the form of equation 78 or normalized Zernike polynomial coefficients Z_i which will be described in greater detail in the discussion below. This research effort developed modeling tools that enabled one to pursue either option as a matter of investigator choice.

Regardless of how the OPD or aberration function is prescribed, the ultimate objective of the modeling is to physically describe the character of the aberrated phase profile (and by extension wavefront) across the exit pupil. Figure 36 illustrates the geometric one-zero pupil functions ("white" is 1.0 and "black" is 0.0) for the nominal sparse aperture configurations investigated in this dissertation, along with single realizations of a randomly distributed piston/tip-tilt error phase profile contributing 0.20 waves rms of total wavefront error across each pupil. In the phase profiles, the background grayscale intensity correlates with zero phase, lighter than background intensity implies positive phase, and darker than background defines negative phase. Accordingly, one can observe that the individual subapertures have random amounts and orientations of constant piston and linear tip/tilt applied to each subaperture. As with all the phase profiles created during this effort, a random zero-mean, unit-variance Gaussian distribution was utilized to define the spatially variant nature of the aberrations in Figure 36. Therefore, the objective of the polynomial descriptions discussed above and in subsequent pages is to develop a functional form that mathematically describes aberrated phase profiles similar to those appearing in the figure.
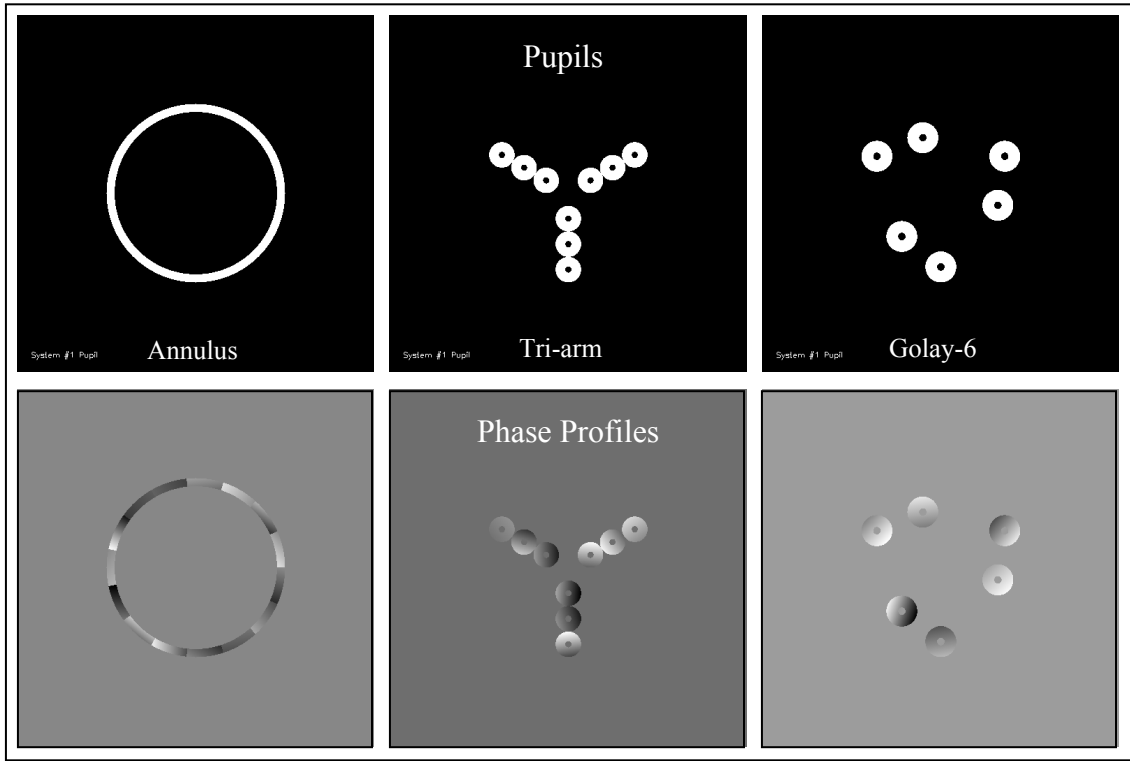
Figure 36: Baseline sparse aperture pupil configurations
(rms wavefront error: 0.20 waves).

In order to streamline the evaluation of wavefront errors in an optical system, one typically relies upon an analytical expression utilizing standard aberration or Zernike polynomial coefficients, whereby the functional forms are subsequently digitally sampled for use in a computer model for the purposes of analysis. This is exactly the approach that was pursued and implemented in this dissertation. Since the background associated with aberration coefficients was introduced in the previous chapter, the concept of representing the aberrated subaperture phase profile via Zernike polynomials will be introduced here. In general, Zernike polynomials see frequent use in similar optical wavefront analyses as they have unique orthogonality and symmetry properties that make them convenient to implement. From a top-level perspective, Zernike polynomials simply consist of three basic constituents: a normalization factor, a radial polynomial term, and a trigonometric function. These three terms can be observed in the following formulation for the ith Zernike polynomial Z_i:

$$Z_i = N_{2n-m}^m \cdot Q_n^m(r) \cdot r^m A_i \tag{139}$$

where N_{2n-m}^m is the appropriate normalization factor, $Q_n^m(r) \cdot r^m$ is the radial component of the polynomial, A_i is the trigonometric function ($\cos m\theta$ or $\sin m\theta$) associated with the polynomial, ρ is the radial exit pupil coordinate, and m and n jointly define specific characteristics of the polynomial as defined in the discussion below. Given this convention, the normalization constant typically assumes the form:

$$N_{2n-m}^m = [(2 - \delta_{m0})(n+1)]^{1/2} \tag{140}$$

where δ_{m0} is the Kronecker delta function and (m,n) are positive integers that are separately defined for each numbered Zernike polynomial. Similarly, the radial component in the Zernike polynomial expression identified above can be expressed according to the (m,n)-convention as follows:

$$Q_n^m(r) = \sum_{s=0}^{n-m} (-1)^s \frac{(2n-m-s)!}{s!(n-s)!(n-m-s)} r^{2(n-m-s)} \tag{141}$$

Given this general formulation, Wyant and Creath (1992) provide a good tabulated summary of the first 36 Zernike polynomials for use in various wavefront analyses. These basic Zernike polynomial building blocks can subsequently be utilized to re-express the wavefront aberration function appearing in equation 78:

$$\begin{aligned}
w[r,\theta] = {}& Z_0 + Z_1 r \cos\theta + Z_2 r \sin\theta + Z_3 \left(2r^2 - 1\right) \\
& + Z_4 r^2 \cos 2\theta + Z_5 r^2 \sin 2\theta + Z_6 \left(3r^2 - 2\right) r \cos\theta \\
& + Z_7 \left(3r^2 - 2\right) r \sin\theta + Z_8 \left(6r^4 - 6r^2 + 1\right) \\
& + \text{higher order terms}
\end{aligned} \tag{142}$$

where the Z_k represent aberrated wavefront coefficients for the individual Zernike polynomials that have been explicitly stated after them. In order to isolate specific first- and

third-order aberration effects as described previously, one simply needs to reorder the individual terms in the equation above consistent with the following general construct:

$$
\begin{aligned}
w[r,\theta] = Z_0 - Z_3 + Z_8 & \qquad \text{piston} \\
+ (Z_1 - 2Z_6)r\cos\theta + (Z_2 - 2Z_7)r\sin\theta & \qquad \text{tilt} \\
+ (2Z_3 - 6Z_8 + Z_4\cos 2\theta + Z_5\sin 2\theta)r^2 & \qquad \text{focus + astigmatism} \\
+ 3(Z_6\cos\theta + Z_7\sin\theta)r^3 & \qquad \text{coma} \\
+ 6Z_8 r^4 & \qquad \text{spherical} \\
+ \text{higher order terms} &
\end{aligned}
\tag{143}
$$

where key terms required for the analysis of aberrations and pupil phasing errors have been specifically identified in the margin.

To quantify the extent of optical aberrations in an imaging system, one typically specifies the number of *root-mean-square* (rms) waves of aberration present. With the developed OPD error terms expressed in waves, one can compute the rms wavefront error σ_{WFE} associated with an optical system via the following continuous and discrete formulations:

$$
\begin{aligned}
\sigma_{\text{WFE}} &= \left[\frac{1}{\pi} \int_{\theta=0}^{2\pi} \int_{r=0}^{1} \left| w[r,\theta] - \overline{w[r,\theta]} \right|^2 \rho\, d\rho\, d\theta \right]^{1/2} \\
&= \left[\frac{1}{M^2 - 1} \sum_{x=-\frac{M}{2}}^{\frac{M}{2}-1} \sum_{y=-\frac{M}{2}}^{\frac{M}{2}-1} \left| w[x,y] - \overline{w[x,y]} \right|^2 \right]^{1/2}
\end{aligned}
\tag{144}
$$

where $\overline{w[r,\theta]}$ is the mean wavefront optical path difference in waves. By convention, the rms wavefront error is typically cited for a particular wavelength to convert it to waves, with the central or mean wavelength of the collection passband a common choice. Since this research effort focused on modeling the polychromatic signal content for an imaging system, aberrations and optical phase were characterized across multiple wavelengths. Therefore, rms wavefront error could conveniently be computed utilizing any wavelength of the spectrally variant optical phase data available through the modeling process. During this research effort, an alternative convention for the rms wavefront error was also explored,

computed as the standard deviation of the OPD error (in waves) across all discretely modeled wavelengths. An investigation of how this convention compared with a more traditional mean wavelength designation of rms wavefront error seemed to show they were within 2-5% of each other for the collection scenarios under review. For the purposes of this dissertation, a conventional definition was ultimately adopted and one should consequently note that all of the rms wavefront error metrics cited in the sections to follow have been computed at the mean wavelength of the spectral passband. It should also be reinforced that the cited rms wavefront errors are specifically relevant to the nominal collection scenario described in Section 4.2.2 (i.e., for a panchromatic passband from 0.4-0.8 μm).

With the fundamental aberration coefficient and Zernike conventions to quantify the overall nature of system OPD errors, one can subsequently apply the methods formulated in Section 3.7 to describe the effects of the aberrated or improperly phased wavefront on overall image quality. From this development, it is clear that the key then becomes how to specify the wavefront error associated with the optical system under investigation. There are several potential avenues one could explore to address this modeling issue. The first simply explores the impact of a fixed acceptable rms wavefront error that is adjusted in the context of a sensitivity study. Such an approach provides valuable insight into the range of potential effects that could be observed with various wavefront errors. Alternatively, a more rigorous approach uses a detailed optical ray trace design capability such as that available through Code V or OSLO. Both of these optical design packages have the necessary analytical and visualization capabilities for evaluating the optical performance of radially symmetric optics and can be manipulated to address optical arrays similar to the sparse aperture configurations described in this dissertation. They also can provide detailed wavefront reports for a given optical layout in a transverse aberration or OPD Zernike polynomial format that could be imported directly into the engineering modeling tool developed for this effort. As with other codes proposed for use in this research endeavor, the Code V and OSLO design tools constitute industry standards that could provide high-fidelity metrics for use in a phase error study.

The significant drawback in the use of optical design software is the detailed optical prescription data required to support analysis. A considerable amount of time generally must be dedicated to developing the optical design before any wavefront analysis. Because of this issue, use of detailed optical design tools are much more amenable to developing and evaluating a specific design solution, not necessarily performing the sensitivity investigations envisioned for this dissertation. As a consequence, this research utilized an approach where the rms wavefront error was mathematically prescribed by the conventions introduced above and varied according to the scenarios of interest. Consistent with the desired end-point rms wavefront error, polynomial coefficients for individual aberration terms were adjusted for the mean wavelength of the collection passband to explore the contributions of individual error sources (e.g., piston, tip/tilt) from a sensitivity perspective. The amplitudes of these polynomial coefficients were then scaled appropriately for each discrete wavelength modeled within the simulation. Assuming the subapertures exhibit uncorrelated phase profiles, a random number generator was subsequently utilized to distribute the defined phase error amplitude across the full aperture according to a zero-mean, unit-variance Gaussian and consistent with the multiple subaperture pupil geometry. Given the digital nature of the model, these profiles are actually discrete, two-dimensional arrays formed by sampling the appropriate phase error polynomial.

Due to the random variable involved in the process, the approach pursued in this dissertation implicitly entails running a number of iterations to ultimately acquire a given wavefront error (e.g., 0.10 waves rms) with a statistically normal phase distribution. Such a modeling process is conceptually not inconsistent with what one might expect to encounter operationally with a phased sparse aperture telescope array. Of course, the implemented approach is flexible enough that a system designer could perform the detailed optical design analysis described above and simply insert the evaluated Zernike coefficients into the appropriate routines. As an example of the implemented approach, Figure 37 depicts the pupil function for a conventional filled circular aperture (on the left) and the phase profile associated with a 0.10 wave rms tip/tilt error (on the right) prescribed through the appropriate Zernike polynomial coefficient. For comparative purposes, Figure 38 displays similar information for a nine-subaperture tri-arm sparse aperture system with 0.10 waves rms of

randomly distributed piston, tip/tilt. These figures provide examples of the standard products available for characterizing the aberrated complex pupil function through techniques described above with the developed proof-of-concept simulation model.
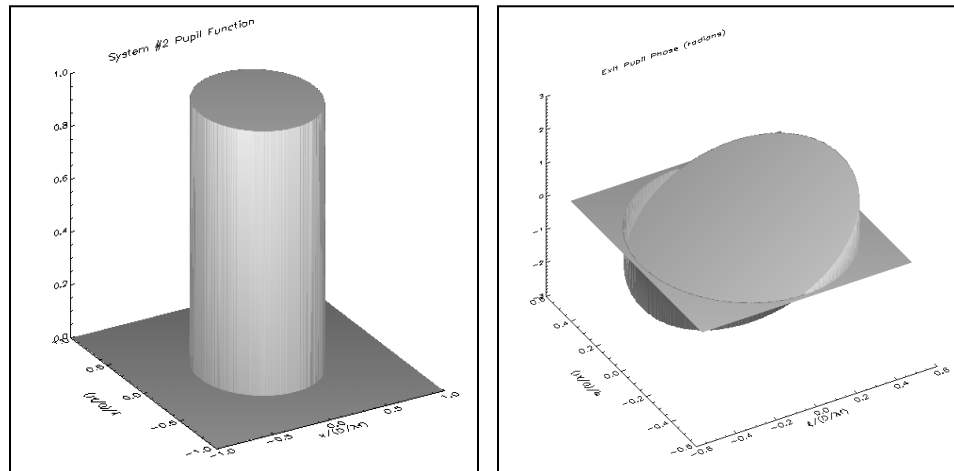
Figure 37: Filled aperture with 0.10 waves rms tilt error.
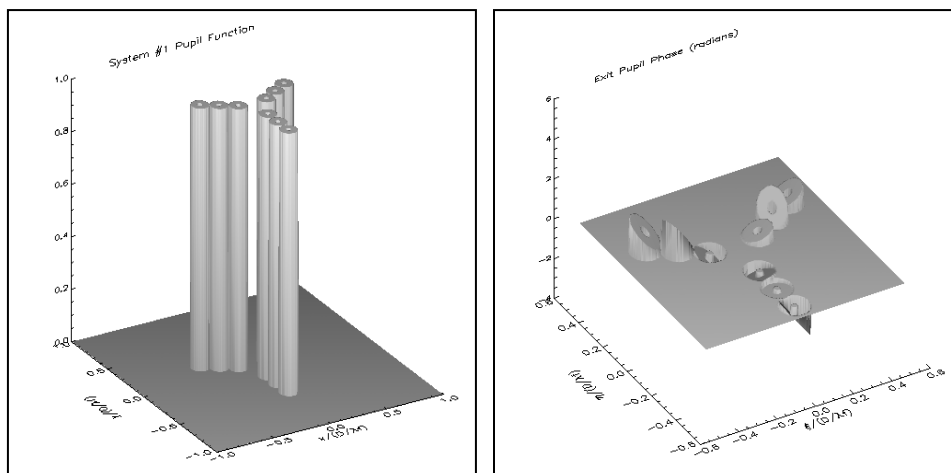
Figure 38: Sparse aperture with 0.10 waves rms random piston, tip/tilt error.

4.6.2 Aperture OTF Evaluation

With the spectrally scaled complex pupil function described in the previous section, the key imaging system components required by the governing linear equations in Chapter 3 are the impulse response and associated optical transfer function. Both of these critical optical

system characteristics essentially capture the action of the imaging system on the pristine radiance image, inducing a reduction in modulation or contrast that ultimately degrades image sharpness. Since the proof-of-concept simulation model developed for this research effort employs a Fourier optical approach in the frequency domain, the optical transfer function (OTF) will be addressed first. The impulse response or point spread function that correlates with the assessed transfer function will be discussed in the next section. As indicated earlier, one of the principal components of the system transfer function is the aperture optical transfer function, physically acquired through the complex autocorrelation of the aberrated pupil function addressed in Section 4.6.1. With the phase profile characterization described in the previous section, the complex-valued aperture OTF ultimately captures system aberrations as well as the effects of subaperture phasing errors in the proposed modeling approach.

As indicated in the previous chapter, the aperture OTF is ultimately derived by taking the *complex autocorrelation of the scaled pupil function and normalizing by the area of the exit pupil.* For more complicated pupil geometries, such as those encountered with sparse aperture systems, this mathematical operation can effectively be performed with a digital computer. In such a case, the approach for computing the OTF simply involves the squared magnitude of the Fourier transform of the scaled pupil function (thereby computing the unnormalized incoherent PSF), the inverse Fourier transform, and normalization by the area of the pupil (or its Fourier transform evaluated at zero frequency). The sequence of mathematical operations required to compute the aperture OTF appears in Figure 39. As observed in the figure, there are two principal routes that can be pursued to derive the OTF expression of interest. Depending on the complexity of the problem, one can either evaluate a closed-form autocorrelation of the scaled pupil function or use the Fourier transform to initially derive an expression for the point spread function (PSF). As indicated above, the latter tends to facilitate analyses of complicated aperture geometries, as observed in the sparse aperture arena. Consequently, the proof-of-concept simulation capability pursued in this research involves the Fourier transform path depicted in Figure 39, with the point spread function acquired as an interim step.
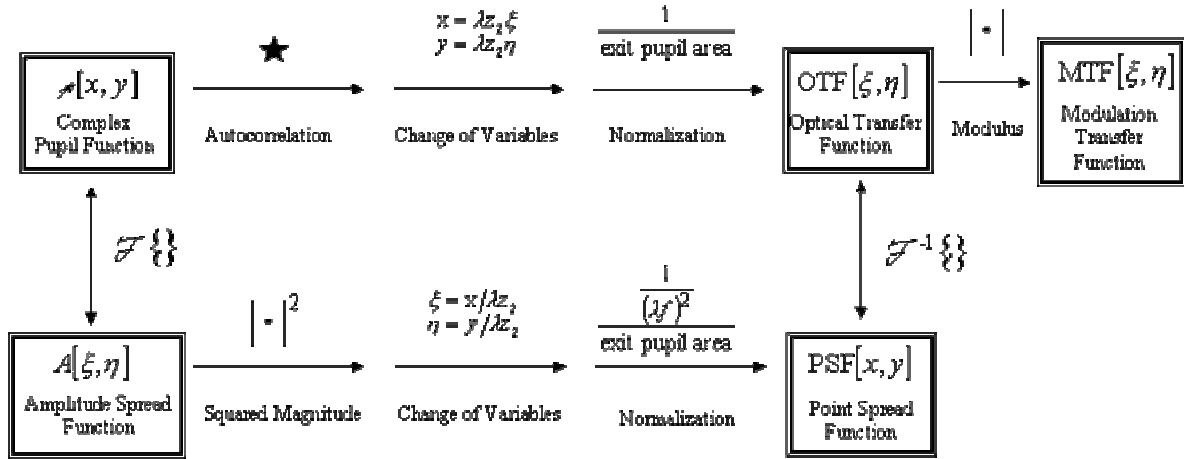
Figure 39: Computation of the aperture OTF for complex pupils.

Given the methodology described above, aperture transfer functions can be developed for both diffraction-limited and aberrated cases on a wavelength-by-wavelength basis. Based on output from the proof-of-concept model, Figure 40 depicts the normalized MTF associated with filled circular and tri-arm sparse aperture configurations. In Figure 40(a), one will observe a surface plot of the classic CTRI-function MTF supported by a diffraction-limited circular aperture. In Figure 40(b), the well-established star-like character of the MTF associated with a diffraction-limited nine-aperture tri-arm system is apparent. Finally, one can see the destructive nature of 0.20 waves rms of piston, tip/tilt error in the aberrated MTF profile for the tri-arm sparse aperture system in Figure 40(a).

| (a) Filled | (b) Tri-arm | (c) Tri-arm (aberrated) |
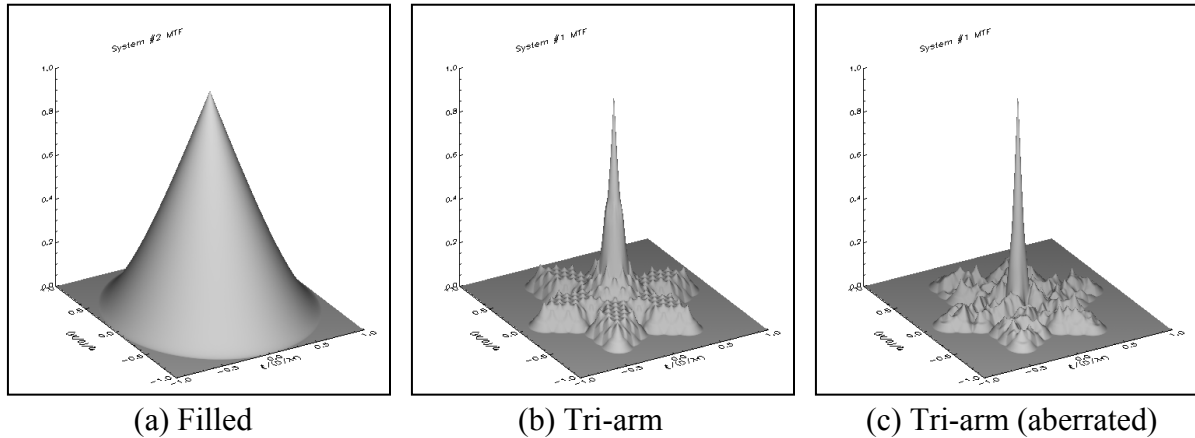
Figure 40: Comparison of filled versus tri-arm sparse aperture MTF
(Aberrated MTF: 0.20 waves rms of piston, tip/tilt error).

In addition to the two-dimensional images and three-dimensional surface plots demonstrated above, one can also plot slices of the individual transfer functions for evaluative purposes. To that end, Figure 41 plots the cardinal ξ– and η–plane axes for the transfer functions depicted above. From this figure, it is apparent that the sparse aperture system (in blue and black) has significantly reduced modulation relative to its filled circular counterpart (in red), an attribute manifested by most sparse aperture configurations. In addition, the very deleterious effect of aberrations at the level of 0.20 waves rms is also readily apparent, as the aberrated tri-arm MTF (in black) shows even greater loss of modulation, as well as significant new peaks and valleys, relative to a diffraction-limited case (in blue). In fact, 0.20 waves rms tends to reduce the modulation to the point that serious nulls are introduced in the spatial frequency coverage of the MTF. This unique nature of the sparse aperture transfer function introduces interesting image quality effects, especially when the spectral scaling of the complex pupil involved in the aperture autocorrelation is considered.
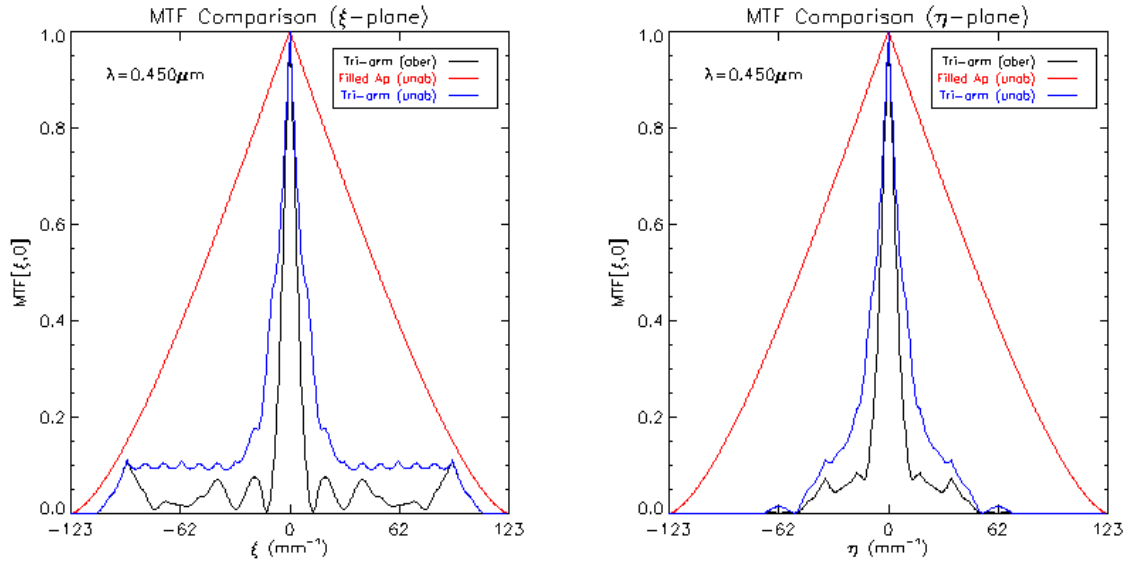
Figure 41: Comparison of filled versus tri-arm sparse aperture MTF
(Aberrated MTF: 0.20 waves rms of piston, tip/tilt error).

From a spectral perspective, the wavelength associated with the detected radiation has two principal means for influencing the overall character of the complex aperture OTF. First, the wavelength essentially scales the pupil function diameter associated with the aperture autocorrelation. As a result of this spectral consideration, the OTF region of support as

defined by the optical cutoff ($D/\lambda f$) exhibits a size dependency that is inversely proportional to wavelength, with the result that shorter wavelengths produce larger regions of support in the spatial frequency plane (i.e., produce higher optical cutoff frequencies and better overall resolution). The second primary mechanism of influence for the wavelength of the incident photons involves the phase term associated with an aberrated complex-valued aperture. The impact of spectral diversity on this aspect of the complex pupil autocorrelation is far less intuitive than the previously described region of support influence. As seen in equations 74 and 75, the phase associated with a complex pupil is also inversely proportional to wavelength, implying the amplitude of the phase will exhibit a spectrally dependent scaling prior to undergoing the complex autocorrelation operation required to derive the aperture OTF. Therefore, the aperture transfer function will exhibit two primary spectral dependencies, with the phase amplitude consideration having dramatic implications for a sparse aperture configuration due to subaperture phasing issues.

When the complex, randomly distributed phase profile associated with an aberrated sparse aperture is additionally considered, the overall implication of the spectrally weighted phase amplitude becomes difficult to ascertain without use of a digital model. Figure 42 displays empirically the impact of wavelength on the pupil phase profile and associated modulation transfer function for a nine-aperture tri-arm system with 0.25 waves rms of piston, tip/tilt error. As described previously, this rms wavefront error was derived by computing the standard deviation of the OPD errors and converting to waves at the mean wavelength considered in this example. On the top row of this figure, one will observe that the amplitudes of individual normalized subaperture phase profiles become reduced as the wavelength changes from 0.44 to 0.80 μm. This reduction in phase amplitude correlates with reduced aberration strength at longer wavelengths, which can be seen in the MTF images on the bottom row of the figure where there are fewer nulls and generally higher modulation amplitude at longer wavelengths (compare, for instance the two plots at 0.44 to 0.80 μm). In addition to this not-so-subtle aberration effect on the transfer function, one can also observe the obvious alteration in the overall region of support as the wavelength is varied. From that perspective, the shorter wavelengths support higher spatial frequency coverage (i.e., better resolution) than that associated with longer wavelengths, which of course is highly intuitive.

In addition to providing insight into phenomenology, these sample products from the proof-of-concept code demonstrate some of the utility of the model in evaluating the spectral issues associated with optical systems in a context that has not been sufficiently explored in the past.

| (a) 0.435 μm | (b) 0.619 μm | (c) 0.801 μm |
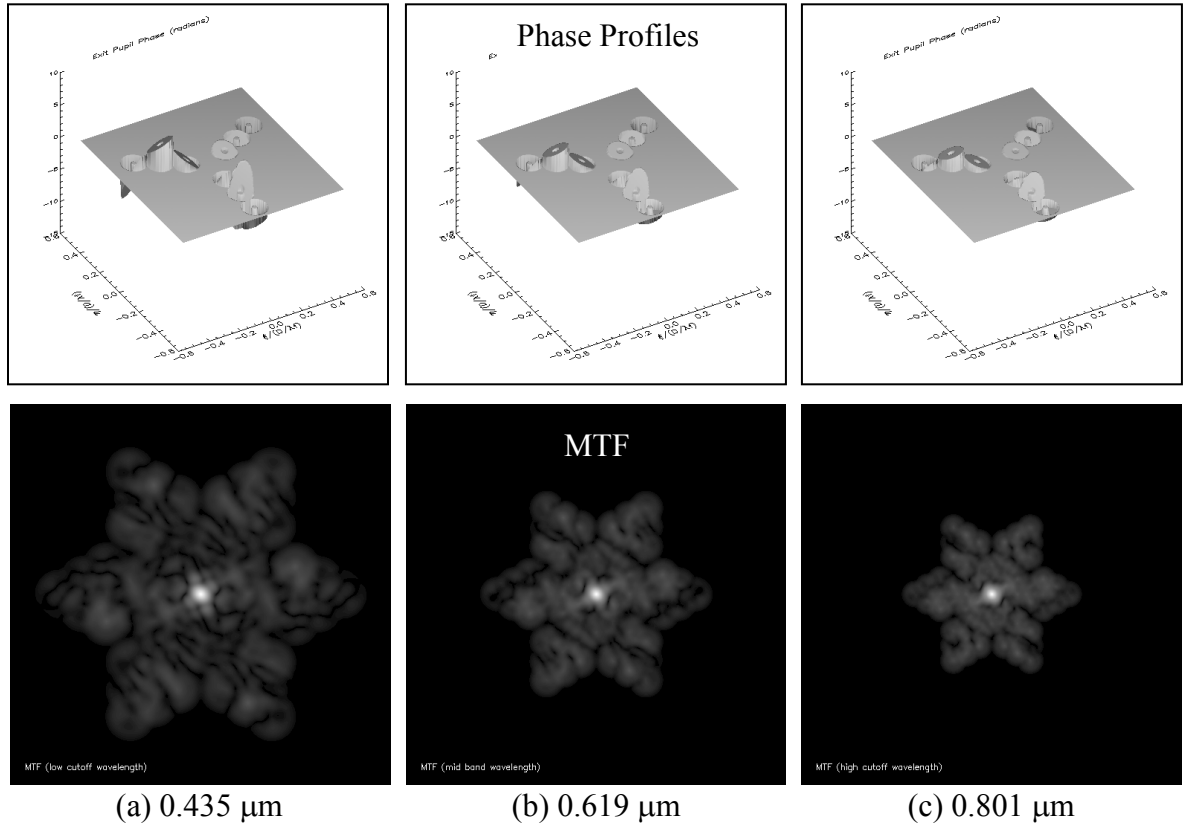
Figure 42: Variation of phase profile and aperture MTF with wavelength
with 0.25 waves rms of piston, tip/tilt error.

4.6.3 Aperture PSF Evaluation

As indicated earlier, a natural by-product of the aperture transfer function calculation illustrated in Figure 39 is the generation of the point spread function (PSF) or impulse response associated with the aperture. Although not specifically used with the engineering model to develop image predictions, the computed point spread functions are output for insight and evaluative purposes. As discussed at length previously, the actual image simulations are performed through a Fourier optics approach utilizing the optical transfer function instead. The aperture PSF can be instructive, however, as it provides a spatial

domain characterization of the action of the imaging system on the incident object radiance field. As a consequence, one can generally acquire greater intuitive feel for the nature of an imaging system by exploring the PSF as an indication of how a point source in the object will be degraded in the image plane.

| (a) Filled | (b) Tri-arm | (c) Tri-arm (aberrated) |
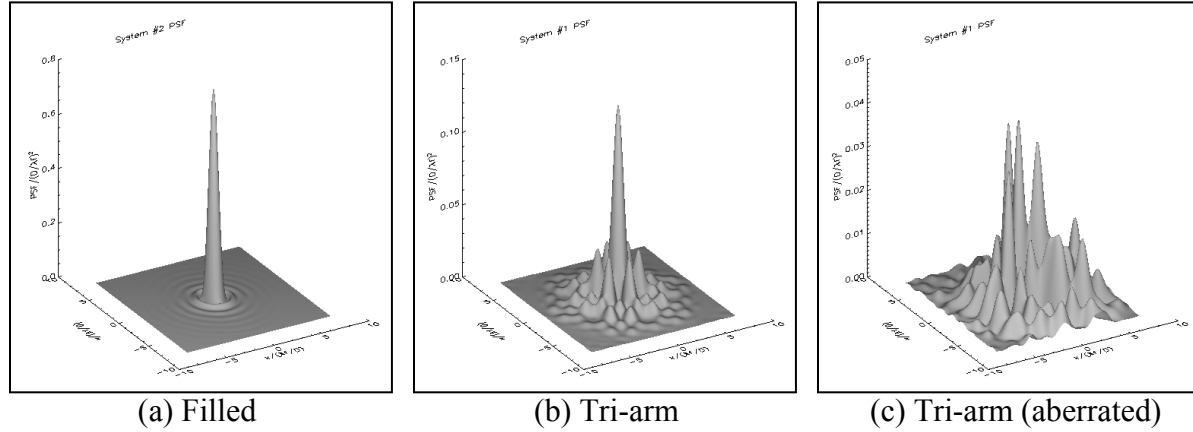
Figure 43: Comparison of filled versus tri-arm sparse aperture PSF
(Aberrated MTF: 0.20 waves rms of piston, tip/tilt error).

To that end, Figure 43 provides surface plots of the aperture PSF that correlate with each aperture MTF in Figure 40. Accordingly, in Figure 43(a) the filled circular aperture exhibits the classic Airy pattern or squared SOMB-function PSF that correlates with the CTRI-function MTF in Figure 40(a). For the diffraction-limited tri-arm sparse aperture configuration, the star-like MTF structure in Figure 40(b) corresponds to a PSF in Figure 43(b) that has considerable reduction in the central lobe peak amplitude and increased energy in the "wings" relative to the circular filled impulse response. This PSF character naturally leads to object points that are considerably blurred from the baseline image sharpness established by the filled aperture. Finally, the impact of 0.20 waves rms of piston, tip/tilt error is displayed in Figure 43(c) for the tri-arm configuration, where multiple peak lobes and significantly increased "wing" power now arise in the observed PSF. This will ultimately produce detected imagery that exhibits even poorer image sharpness. Based on these exemplar diagrams, it is clear that the nature of the PSF provides good intuition into how the correlated OTF will impact overall detected image quality.

4.6.4 System OTF Evaluation

Given a "pristine" object spectral radiance field that is appropriately sampled optically (including focal plane scale), the next step in the modeling approach outlined in Figure 22 is incorporation of system OTF effects. The system transfer function captures the physical imaging processes that result in reduced modulation, contrast or sharpness in the radiance image. Previous sections have detailed how the complex pupil function is developed and used to formulate the aperture OTF, including the appropriate spectral scaling rules. The final system transfer function must then be generated to include effects beyond the optical configuration, including those due to atmosphere, image motion and the focal plane detector. To ultimately include these effects in the proof-of-concept simulation model, standard Fourier optical techniques were utilized to apply the cascaded system OTF to the frequency spectrum of the detected object radiance image acquired through DIRSIG or the resampled airborne imagery. For the engineering model, expressions for the following system OTF components detailed in Chapter 3 were ultimately incorporated: complex aperture OTF (i.e. complex autocorrelation of the exit pupil), detector aperture MTF, smear (linear motion) MTF, jitter (random motion) MTF and atmospheric turbulence MTF. Obviously, the complex-valued aperture OTF captures the deleterious effect of system aberrations and/or subaperture phasing errors as described previously. Therefore, the approach pursued in this research effort effectively captures most of the principal imaging system attributes that ultimately impact final image quality.

Although all the transfer function components enumerated above certainly contribute to the overall detected image quality, the effects of the various mechanisms on the image quality are different. The stratification in impact can be observed in figures 44 and 45, where slices of the individual system transfer function components have been plotted for sample filled circular and tri-arm sparse aperture configurations. The imaging parameters that were investigated in these two figures are consistent with the nominal scenario appearing in Table 2, including aberrations on the order of 0.10 waves rms, 0.5-pixel linear smear, 0.25-pixel random jitter, and Nyquist or better optical sampling. Both figures clearly indicate that the dominant contributor to the total system transfer function (in black) entails the aperture OTF or complex autocorrelation of the pupil (in dashed blue). In previous discussion, it has been

shown that the aperture OTF also exhibits the prominent spectral character associated with the total system transfer function. As a consequence, although all the OTF components mentioned above are available in the proof-of-concept modeling capability, it is possible to perform a more focused investigation on the impact of the aperture OTF alone on restored image quality. This observation provides most of the rationale behind the attention given to the nature of the aperture OTF in earlier sections.

The baseline approach pursued in this research effort also entailed a more direct implementation of the physics associated with equation 37, thereby avoiding the spectrally averaged, polychromatic MTF implementation in equation 99 that marginalizes potential spectral effects. For comparative purposes, the spectrally averaged OTF approach was implemented as well, providing the opportunity to explore the value and/or impact of the increased spectral fidelity associated with the more rigorous baseline implementation. Additional discussion, sample simulations and final results comparing these two system OTF options will be provided in the sections to follow. With an object scene representing the spectral radiance reaching the entrance pupil of the imaging system, the developed model implementation involves direct application of the computed, spectrally variant system OTF to each wavelength-specific object scene in the spectral "data cube." After the application of noise, these detected signal spectral planes (including the effects of OTF) are numerically integrated across the modeled passband of interest, with appropriate scaling factors to acquire an estimate of the detected electrons count for each pixel in the scene. Consistent with the governing equations in the previous chapter, this detected signal is subsequently quantized into digital counts to provide the final estimate of the detected image for the optical configuration under investigation. Some additional discussion will be provided on the approach associated with the post-OTF system model in the sections that follow.
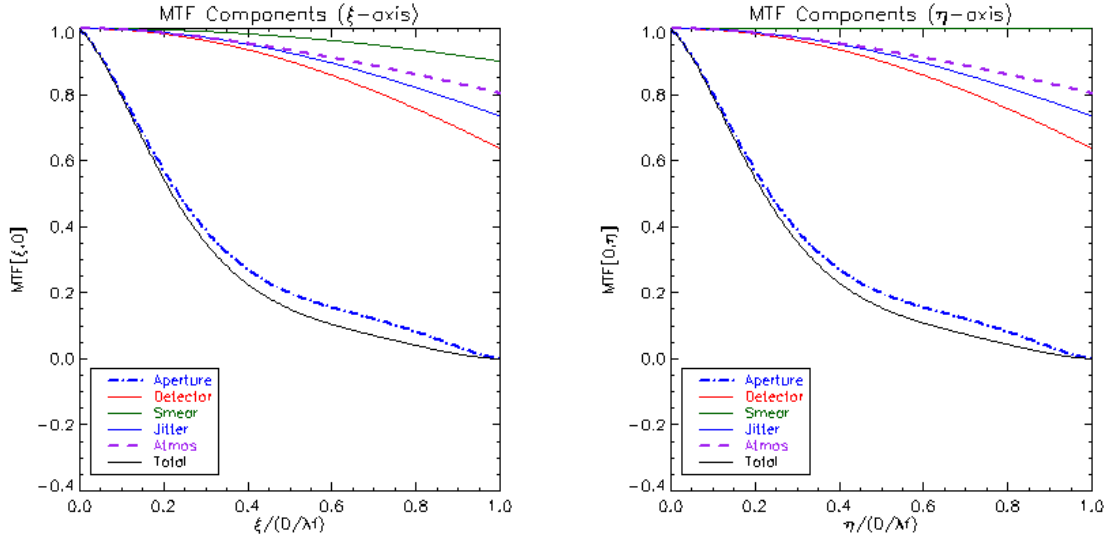
Figure 44: System MTF for a filled aperture
with 0.10 waves rms of defocus error.
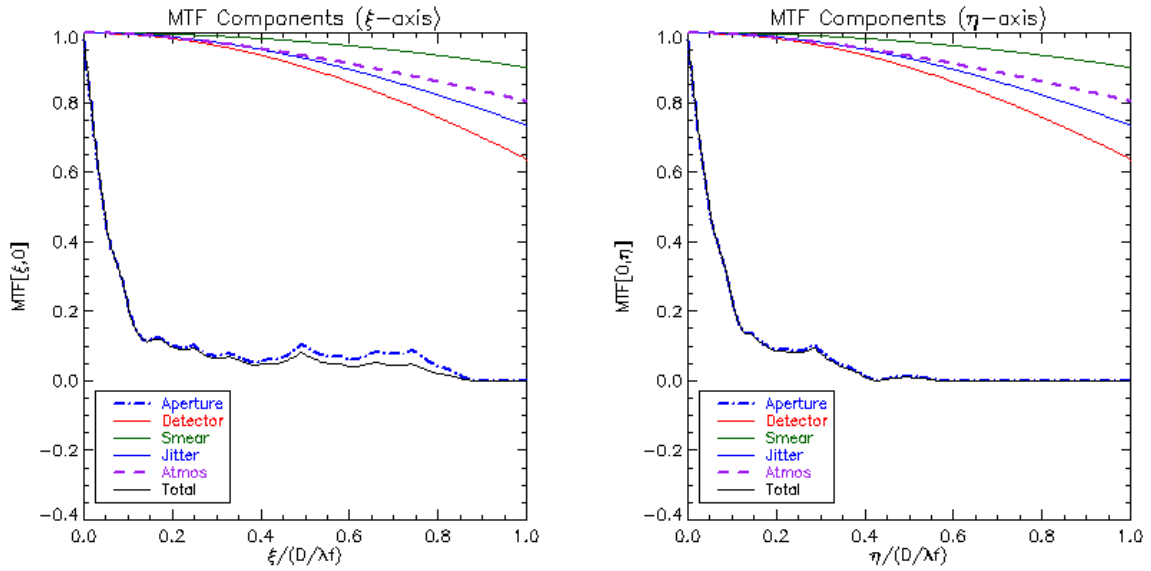
Figure 45: System MTF for a tri-arm sparse aperture
with 0.10 waves rms of piston, tip/tilt error.

Simulation parameters in figures 44 and 45:

Optical Sampling: $Q = \dfrac{\lambda f}{pD} = 2.0$; Wavelength: 0.65 μm; $F\#$: 18.0; Smear: $0.5p$; Jitter: $0.25p$

4.7 Quasi-Monochromatic Signal

As an interim product of the simulation process, one acquires a quasi-monochromatic prediction of the detected "image" at each wavelength. The spectral interval between these quasi-monochromatic realizations is essentially driven by the spectral resolution associated with the airborne or synthetically derived object data utilized within the simulation. Ultimately, these monochromatic radiance maps undergo numerical integration to develop an estimate of the total signal across the passband. However, they also can be instructive in highlighting the spectral character of the collection on a wavelength-by-wavelength basis, enabling one to perform comparative analyses between spectral content. For instance, the degraded image scene (including the effects of system OTF and noise) for one monochromatic wavelength (perhaps 0.4 μm) can be quantitatively compared to another (0.45 μm for example) with all the correct spectrally diverse differences in the collection physics captured between them.

Given quasi-monochromatic predictions that span the spectral passband under investigation, one can evaluate the quality associated with each spectral plane as an approximation to what features may be observed in the broadband polychromatic quality. Of course, one must be cautious with any absolute conclusions drawn based on the monochromatic predictions alone, as the integration process across a detector passband tends to have an averaging effect over any observed monochromatic signal content. As a consequence, the spectral effects that are observed in the monochromatic predictions have a tendency to be over-accentuated relative to the spectrally averaged signal content that is ultimately detected and restored across a broadband region of the electromagnetic spectrum. Nonetheless, it must be recognized that the monochromatic spectral features are physically present in the integrated signal at some level and therefore provide excellent guideposts for identifying the source of observed spectral quality issues in the captured imagery.

This pre-cursor quasi-monochromatic analyses becomes particularly powerful when one begins to study the post-processed Wiener filter restorations, as physical insight can be gained into the implications of "mis-boosting" the spatial frequency content at certain frequencies on a spectrally variant basis. Obviously, if one could individually restore each

spectral plane, this mismatch between the level of restoration "boost" and the actual detected degradation in the spatial frequency content would be minimized. However, such an exercise would not be a realistic reflection of the collection physics, as ultimately each quasi-monochromatic spectral plane is boosted with a single transfer function constituent in a broadband application. There are many options for identifying the transfer function within the Wiener filter, but the two most obvious choices involve (1) the system OTF associated with the central collection wavelength and (2) a spectrally averaged system OTF generated through a weighted sum of monochromatic transfer functions across the detector passband. Regardless of the selected choice, however, individual monochromatic spectral planes will exhibit various levels of mis-boost, since the single system OTF actually utilized in the restoration will inevitably not be identical to the one responsible for degrading the original spectral object in the first place. As a consequence, initial investigations into the monochromatic nature of the sparse aperture imagery were conducted with the proof-of-concept simulation tool to gain insight into the implications of this restoration mis-boost captured through the additional spectral fidelity in the modeling process. In response to this objective, restorations that entailed both central-wavelength and spectrally averaged system transfer function constituents were explored.

As examples of the types of quasi-monochromatic products that were investigated, Figure 46 illustrates the degradation of an RGB spectral object through the Fourier optics approach to acquire monochromatic predictions for (b) filled circular and (c-d) tri-arm sparse aperture systems. As anticipated, the figure demonstrates the remarkable loss in sharpness that occurs due to the reduced modulation exhibited by a sparse aperture system OTF relative to its filled aperture counterpart. In addition, the presence of considerable wavefront error (0.20 waves rms in this case) leads to further loss in image detail, as observed by comparing the unaberrated and aberrated imagery predictions in Figure 46(c) and (d), respectively. Closer investigation of scene content will also uncover the spectral physics, where quality clearly scales with wavelength but also manifests an interesting balance for the aberrated case, where the loss of resolution as wavelength increases is partially offset by differences in aberration strength. In the end, it is the restored imagery that provides the ultimate indication of the impact of spectral artifacts, and monochromatic predictions certainly provide no exception to

this observation. The general nature of the image restorations pursued in this research effort will be described in additional detail in Section 4.10. In the interest of keeping the results as an integrated whole, specific examples acquired from this quasi-monochromatic simulation process (including a variety of restoration implementations) are reserved for future discussion in the chapter to follow.

(a) Original Object   (b) Unaberrated Filled Aperture

(c) Unaberrated Tri-arm Aperture   (d) Aberrated Tri-arm (0.20 waves rms)
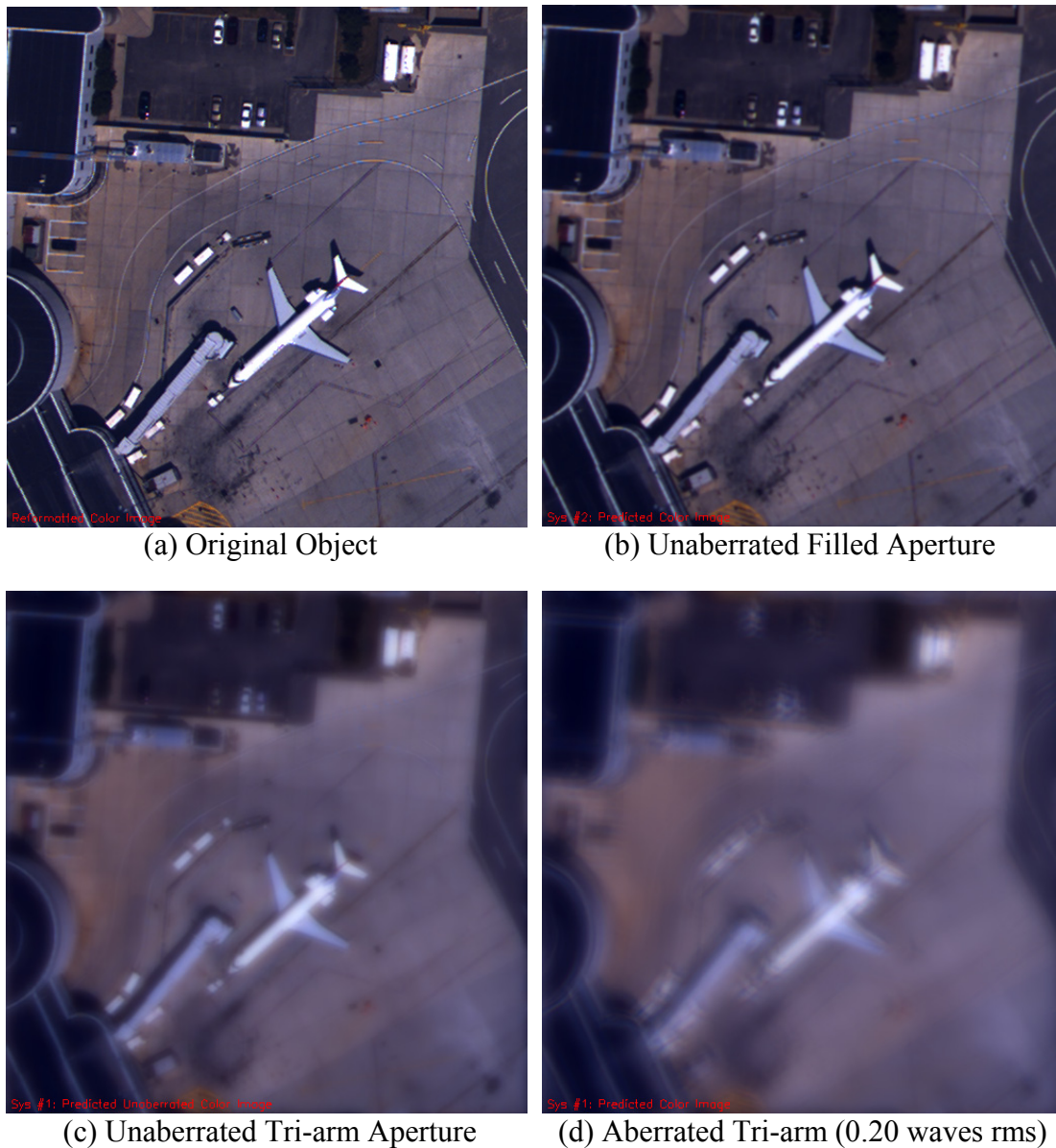
Figure 46: Quasi-monochromatic detected imagery predictions
(prior to restoration).

4.8 Integrated Detected Signal

As indicated in Figure 22, the proof-of-concept simulation predicts the integrated detected signal across the passband of interest. To accomplish this objective, a unique numerical integration methodology utilizing matrix math operations within IDL^{TM} was developed to avoid the implementation of software loops. This integration process ultimately performs the numerical calculation captured in equations 35 and 37. In addition to the object scene spectral radiance and system OTF or PSF, other key spectrally dependent system parameters captured in the integration process include the quantum efficiency and optical transmittance. With these fundamental imaging system and object scene characteristics, one can derive an appropriate estimate of the detected image scene at the focal plane for the optical configuration under investigation.

The simulation code developed for this dissertation allows one to introduce any spectrally variant function for the detector quantum efficiency and optical system transmittance through an ASCII lookup table. Based on the user-generated file, an interpolation occurs within the code to align the functional form of the expressions associated with each constituent of the numerical integration at common wavelengths. For the purposes of this investigation, which entails a nominal visible panchromatic scenario, a spectral response curve consistent with a silicon detector and Indium Tin-Oxide (ITO) gates was selected to represent the quantum efficiency. In addition, an arbitrarily-selected optical transmittance curve founded in principal on data acquired from the Hubble Optical Telescope Assembly (OTA) was developed for the research investigations documented in this dissertation. See Figure 47 for representative plots of these system parameters as a function of wavelength. As indicated, the choice of quantum efficiency and optical transmittance curves was somewhat arbitrary but certainly representative of a potential remote sensing platform implementation. One, of course, could pursue any system representation for these values and not significantly change the conclusions that will be drawn in a subsequent chapter regarding the results acquired from this research effort.
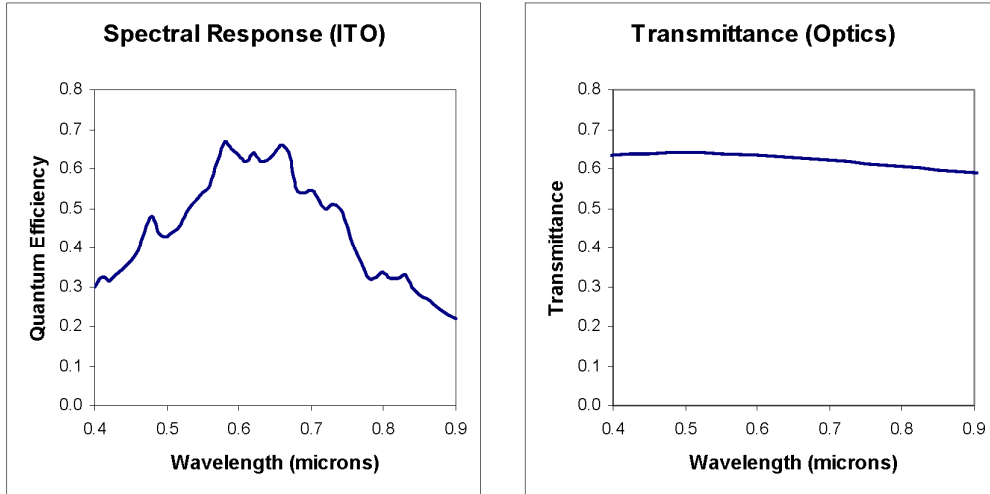
Figure 47: Sample variation of system response and
optical transmittance with wavelength.

Given a radiometrically accurate object scene and the imaging system characteristics detailed
previously, the numerical methodology described above produces predictions of the
integrated signal that will be detected by the prescribed imaging system. These simulations
can be accomplished for both the spectral radiometric, polychromatic physics
implementation as well as the spectrally averaged approach that utilizes a resampled, gray-
scale object image. Providing samples of potential simulation products, Figure 48 compares
the detected panchromatic imagery acquired from circular filled and tri-arm sparse aperture
system configurations given a polychromatic input object. For comparative purposes, the
color object image was converted in Figure 48(a) to a gray-scale equivalent object through an
appropriate spectral-weighting process.

As with the quasi-monochromatic RGB simulations in Figure 46, the integrated
panchromatic imagery exhibits the anticipated quality trends. In Figure 48(b), for instance,
the Nyquist-sampled filled aperture demonstrates only a slight degradation in image quality
from the original object scene. In addition, the unaberrated sparse aperture system in Figure
48(c) exhibits significant reduction in image sharpness due to the differences in OTF
modulation observed in diagrams such as Figure 41. This image blurring effect due to
system OTF modulation is further exacerbated in Figure 48(d) for the aberrated sparse
aperture system with 0.20 waves rms of piston, tip/tilt error. Clearly, optical aberrations

142

and/or subaperture dephasing (as is modeled in this scenario) can have a dramatic impact on the detected image quality. As a result, these diagrams clearly highlight the need to restore sparse aperture detected imagery in order to recover image quality commensurate with the filled aperture case. One should also note that these simulations involve the integrated spectral signal across the detector passband without the inclusion of system noise, which will be addressed in the subsequent section.

<div align="center">

(a) Gray-Scale Object   (b) Unaberrated Filled Aperture
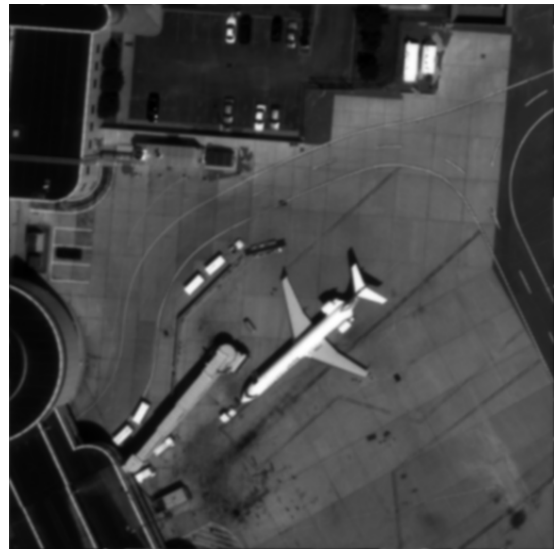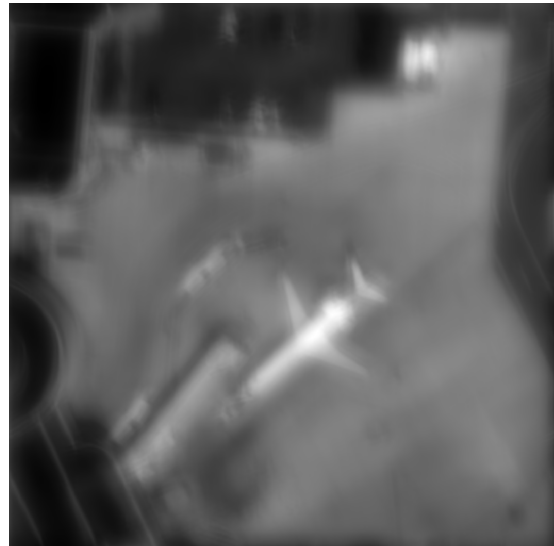
(c) Unaberrated Tri-arm Aperture   (d) Aberrated Tri-arm (0.20 waves rms)

Figure 48: Integrated panchromatic detected signal predictions
(noiseless and prior to restoration).

</div>

4.9 System Noise Evaluation

With an appropriate modeling estimate acquired for the detected broadband signal (including the effects of system OTF and phase errors), the next step in the linear systems model outlined in Figure 22 is the inclusion of system noise. In general, the noise implementation will be consistent with the theoretical development pursued in Section 3.14, assuming that it can be appropriately modeled as a statistically independent white noise source with zero mean and whose variance is driven by the characteristics of the system and collection under review. With detailed system design information, one could address all noise sources considered in the theory section, including photon, quantization, dark current, signal chain and readout constituents. However, since this research was focused principally on overall phenomenology and system sensitivity, the major noise contributors were emphasized, especially those with significant spectral impact.

As a consequence, the detailed model for total system noise specified in equation 102 was simplified to include three principal components: total photon (shot) noise, dark current offset, and total read noise (including all noise effects that tend to be characterized through a constant bias in rms electrons). In addition, for modest to high signal-to-noise ratios, it is reasonable to model physical Poisson processes (such as those typically observed with shot and dark current noise) by Gaussian distributions. These simplifying simulation assumptions ultimately lead to the total system noise equation:

$$n[x,y,\lambda] \cong \sqrt{f_{\mathrm{obj}}[x,y,\lambda] * \mathscr{A}[x,y,\lambda]}\, n_1[x,y] + \sigma_{\mathrm{dc}}(T_{\mathrm{int}}) n_2[x,y] + \sigma_{\mathrm{read}} n_3[x,y] \tag{145}$$

where the shot, dark current and read noise terms appear consecutively and $n_i[x,y]$ represent zero-mean, unit-variance Gaussian noise distributions. Of course, this assumption begins to break down as the SNR deteriorates under low spectral radiance imaging conditions. For this reason, an alternative Poisson model has also been included in the proof-of-concept simulation tool if the investigator chooses to enable it for the appropriate noise terms. In the expression above, the effects of read, electronics and quantization noise are effectively captured through a single constant "read" noise term. In addition, the identified system noise model clearly indicates that shot noise exhibits the primary source of spectral dependence

144

amongst the individual noise terms. Finally, one should note that equation 145 provides a simplified analytical expression for the total system noise intended to illustrate the underlying physical nature of the principal noise constituents. In implementation, the noise model is actually developed in electron space, with the radiance component contributing to shot noise converted to detected electrons to allow summation with the other noise terms.

The noise model implementation is accomplished in the spatial domain after the original spectral radiance image has been optically sampled by the imaging system, blurred by the total system OTF, and integrated to form a composite target signal image. To support this modeling capability, IDL^{TM} engineering software was developed to incorporate these system noise effects into the detected imagery prediction (i.e., prior to any digital post-processing or restoration). Since the airborne spectral imagery should exhibit a degree of radiometric accuracy and DIRSIG has the inherent capability to perform high fidelity spectral radiometric calculations for the synthetically derived object scenes, the proposed modeling effort can accommodate spectrally structured noise (e.g., spectral variation in shot noise due to differences in the number of collected photons at various wavelengths). For the baseline visible panchromatic scenarios pursued in this research activity, spectrally structured noise is not necessarily an important phenomenon to address given the integrated nature of the detected signal. However, the implementation is clearly founded on the ability to address this noise effect, and it would be warranted for future multispectral application studies to explore its implications on overall spectral quality.

One should note that the current implementation does not specifically address spectrally correlated noise, although inclusion of such a noise component is not strictly prohibited. For instance, one could pursue a fairly standard technique utilizing principal component (PC) analysis in conjunction with routine statistical approaches to identify correlated noise distributions external to the modeling capability. Exhibiting the correct statistical correlation properties desired on a wavelength-by-wavelength basis, these distributions could then be treated as an additive source in accordance with the current noise implementation. Spectrally correlated noise is certainly a visible effect in most multi/hyperspectral imagery data sets and consequently represents a research thrust that would be of interest in the future. For the

nominal panchromatic scenarios emphasized here, this level of detail was deemed unnecessary to address the general sparse aperture phenomenology issues of interest.

Figures 49 and 50 provide samples of the noise model implementation and compare the total system noise associated with a typical sparse aperture system collection versus that for a filled circular aperture with commensurate image quality. To achieve the latter, the integration time for the sparse aperture system was increased by an inverse factor of F_{fill}^3 in accordance with the theoretical development. Given that scenario and 11-bit quantization, Figure 49 displays plots of the string of random noise counts applied to a 512x512 detected image scene for (a) a sparse aperture system with detection SNR of 273.7 and (b) a circular filled aperture with SNR equal to 33.7. From these data, it is readily apparent that the sparse aperture system must significantly overcollect photons in order to achieve comparable image quality, resulting in higher total noise count, better SNR (recall more photons are being collected), and significantly longer integration times. For the same scenario, Figure 50 provides histograms of the total system noise associated with each system, clearly indicating the zero-mean Gaussian nature of the noise at these SNR levels. In addition to illustrating the overall nature of the system noise for this scenario, these plots also provide confidence the noise model specified in equation 145 was implemented properly.

For further illustration of the noise model approach, Figure 51 provides a series of predictions of sparse aperture imagery with various levels of noise. As expected, increased noise leads to perceptible reduction in the detected image quality. Obviously, one would expect this to be the case for the restored set of imagery derived from these samples, a concept which will be introduced in the next section and pursued in further depth in the final results discussed in the chapter to follow.
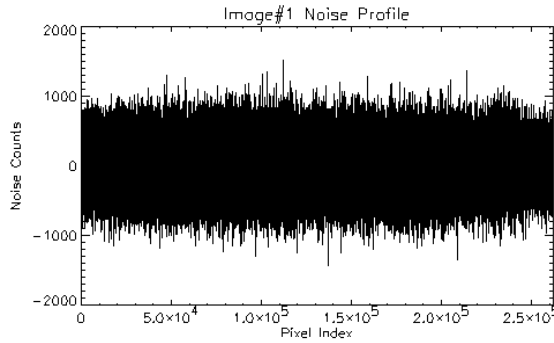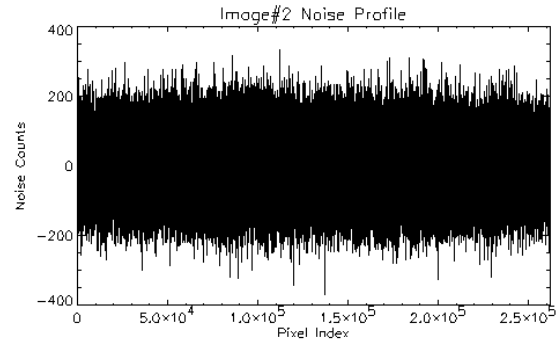
(a) Sparse Aperture (SNR = 273.7) (b) Filled Aperture (SNR = 33.7)

Figure 49: Sample white, Gaussian noise profiles.
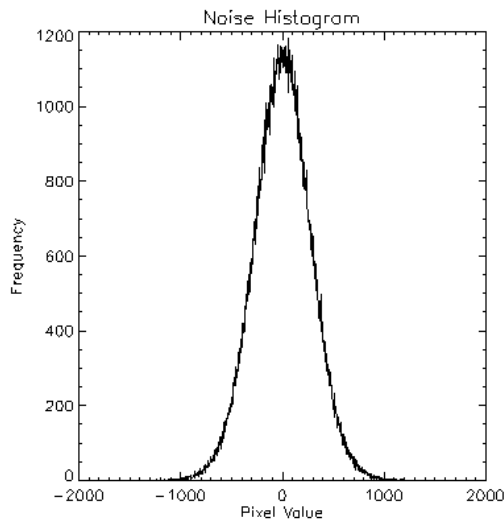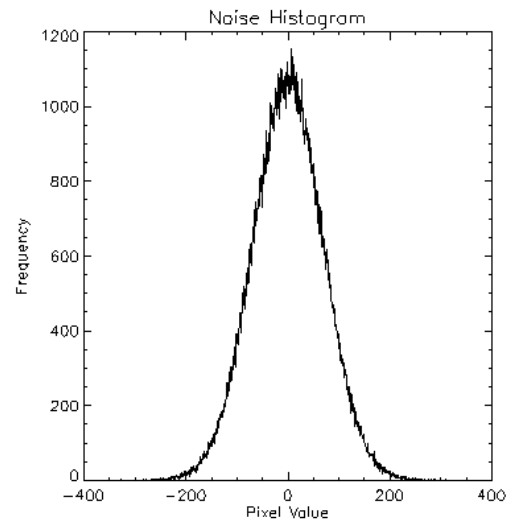
(a) Sparse Aperture (SNR = 273.7) (b) Filled Aperture (SNR = 33.7)

Figure 50: Sample white, Gaussian noise histograms.

(a) No Noise   (b) SNR = 273.7

(c) SNR = 70.9   (d) SNR = 37.8
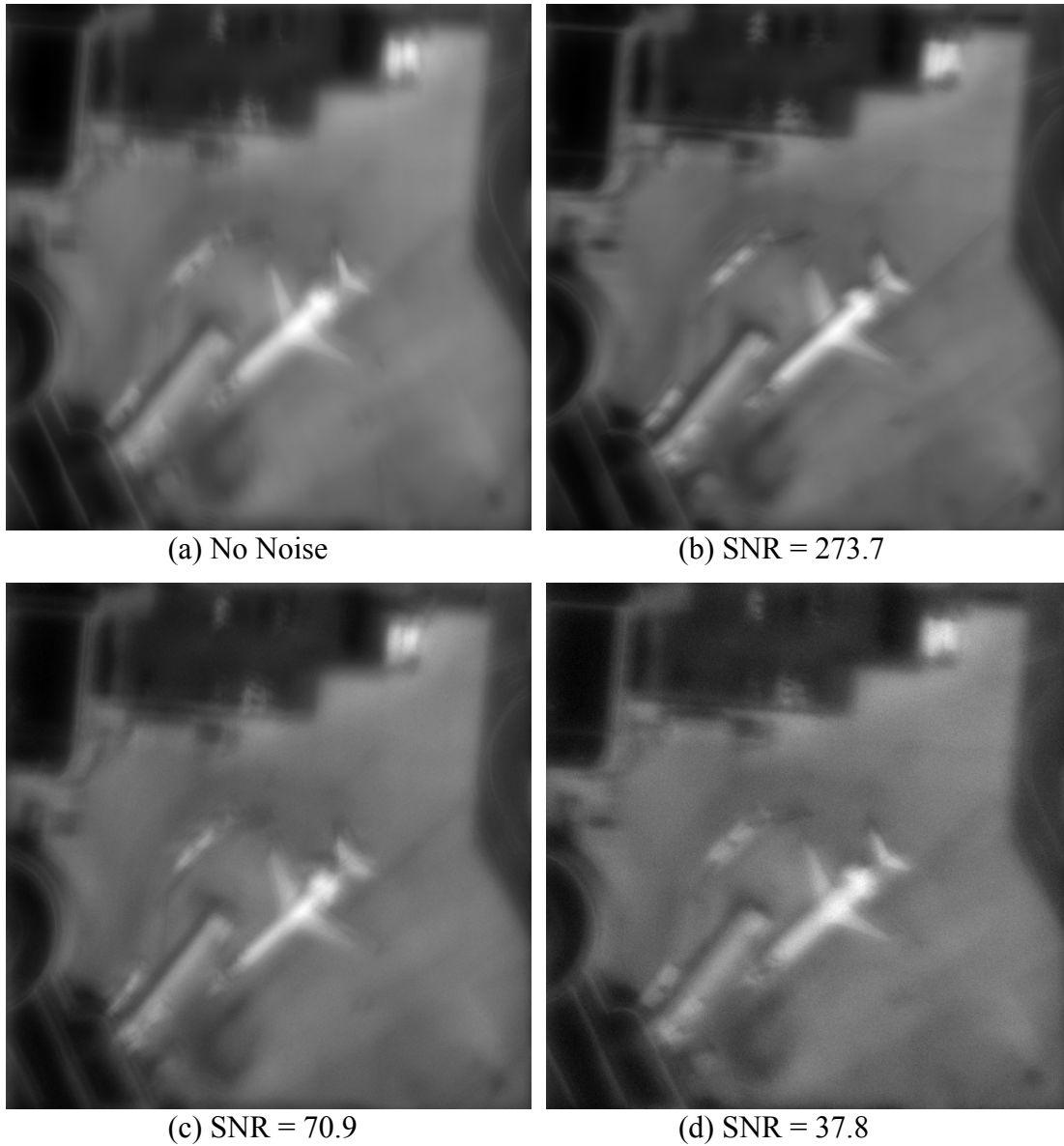
Figure 51: Variation of sparse aperture integrated panchromatic detected imagery predictions with signal-to-noise ratio (prior to restoration).

4.10 Image Restoration

Although originally characterized as goal-oriented research effort, the last step (image restoration) was deemed to be critical for understanding the end-to-end image quality associated with sparse aperture systems, including implications of the spectral fidelity introduced into the modeling process. Based on the degraded output imagery that is ultimately acquired from these imaging platforms (e.g., Figure 51), it is essential that high-

quality post-processing techniques are implemented to reconstruct the imagery without excessively boosting the noise. To meet this objective, several different Wiener filter restoration variants consistent with the general algorithmic development contained in Section 3.15 were implemented in the model. Similar to the detected image prediction, all image restoration algorithms were implemented within the IDL^{TM} software environment.

The restoration algorithms pursued in this research were based on the standard approach of a conventional frequency-domain Wiener filter. Slight variations in the general implementation approach were essentially based on assumptions of system transfer function, noise power spectrum, and object power spectrum knowledge. These three parameters provided various levers for performing sensitivity studies within the overall Wiener filter construct. Given the *a priori* knowledge available through the simulation process, the baseline Wiener filter approach relied upon complete knowledge of the optical transfer function and noise-to-object power spectrum ratio. As such, this filter implementation theoretically represents a near-optimal restoration solution, as the degrading effects of the imaging system (including aberrations), the noise power spectrum, and object signal spectrum are assumed to be perfectly known.

A number of different variants of the baseline restoration approach were pursued. The primary alternative version assumed that the noise-to-object power spectrum ratio was unknown, which is much more consistent with a real-world collection scenario. In the latter implementation, one must manually select the power spectrum ratio and rerun the restoration until acceptable image quality is achieved. Although time consuming, this approach has been frequently pursued by the photo-interpretation community for similar image quality exercises. Since the author has no access to that level of expertise, results of this implementation likely depart considerably from the optimal but are instructive from the perspective of providing insight into the impacts of collection unknowns. The key realism issue for this Wiener filter variant is the remaining assumption that the complex system transfer function and system aberrations (by extension) are perfectly known. To address this problem, additional restorations were performed based on top-level variations in the knowledge of the exit pupil phase, thereby modeling the impact of lack of knowledge of

OPD or wavefront errors during a given collection scenario. There are an infinite number of possible departures in wavefront knowledge that one could explore, so this exercise only represented an initial incursion into the general area.

Obviously, the trade space associated with a given modeling scenario is fairly wide open even for the few identified restoration filter variables, not to mention the possible imaging system parameters that can be adjusted. As a result, a limited number of restorations were actually performed during this investigation to place bounds on the nature of the quality performance envelope. To that end, one must remember that the objective of this research effort was not to perform an exhaustive sensitivity study of various sparse aperture collection parameters. It was specifically focused on developing a feasible proof-of-concept model and exploring the trade space to determine if such a sensitivity investigation was worthy of additional study. In its basic form, the conventional Wiener filter implementation provided a key mechanism for addressing the overall system quality expected from various sparse aperture system configurations. As such, this relatively simple but mathematically elegant restoration filter enabled the critical assessment of quality implications arising from the enhanced spectral fidelity included in the proof-of-concept model developed for this dissertation. Without this goal-level research pursuit, that evaluation would not have been remotely possible.

With the baseline Wiener filter restoration methodology described above, one is able to compare different aperture configurations, as shown in figures 52 and 53 for filled circular and tri-arm sparse aperture systems. These two figures contain simulation products from the implemented proof-of-concept model, including (a) the original spectral radiance object image, (b) a spectrally weighted panchromatic depiction of the object, (c) the detected image for the prescribed aperture configuration, and (d) the restored image acquired through Wiener filtering. The scenario pursued in both figures was consistent with the details enumerated in Table 2, with the sparse aperture configuration experiencing a 0.20 waves rms piston, tip/tilt error at the mean wavelength of 0.55 μm. The exit pupil associated with the sparse aperture was a nine-subaperture tri-arm configuration with abutting optics (i.e., fill factor of 0.173). For comparison, the filled circular aperture in this example was diffraction limited and

Nyquist sampled. The system noise associated with these simulations was previously plotted in Figure 50. In the development of the noise profiles, the integration time for the sparse aperture system was increased relative to the filled aperture dwell time by the cube of the inverse fill factor. As a result, the detected imagery examples in figures 52 and 53 are representative of the type of predictions studied at length in this research.

The restorations in these figures were performed assuming perfect phase error and system OTF knowledge, as well as utilizing the exact noise-to-object power spectrum ratio that degraded the original object in the first place. Since the noise and object power spectra are known *a priori* through the modeling process, one can develop a single ratio expression (based on the integrated signal and noise content) that varies with spatial frequency to form the ideal Wiener filter. As a consequence, the restorations that appear in figures 52(d) and 53(d) are near-optimal, especially given the excellent detection SNR associated with them. Despite this fact, one sees that the sparse aperture prediction (although exhibiting very good quality) is not quite equivalent to its filled aperture counterpart. There are a number of contributing factors for this physical phenomenon, not the least of which is the need to physically oversize the encircled diameter of the sparse aperture to achieve commensurate resolution. Upon careful examination, one will also observe that noise is boosted and correlated through application of the Wiener filter restoration, an artifact that is particularly noticeable for the sparse aperture case. This is a direct result of the increased boost required for the Wiener filter to restore the significantly demodulated system OTF associated with that collection system. Accordingly, figures 52 and 53 provide excellent examples of the nature of the products that can be acquired and evaluated through use of the engineering model developed for this effort. Considerably more detail for individual scenarios and collection apertures will appear in the discussion on results in the chapter to follow.

(a) Original Object

(b) Gray-scale Object

(c) Detected Imagery

(d) Restored Imagery

Figure 52: Restored panchromatic imagery predictions (filled aperture).
Fill Factor: 1.000; Wavefront Error: 0.0 waves rms; SNR: 33.7

(a) Original Object

(b) Gray-scale Object

(c) Detected Imagery

(d) Restored Imagery

Figure 53: Restored panchromatic imagery predictions (tri-arm sparse aperture).
Fill Factor: 0.173; Wavefront Error: 0.20 waves rms; SNR: 273.3

4.11 Gray-World Comparison

The simulations appearing in figures 52 and 53 were developed with the enhanced spectral modeling fidelity targeted by this research effort (i.e., assuming a polychromatic world with a spectrally diverse object radiance field as input). In an attempt to quantify the value of this enhanced modeling effort, a software routine was developed to implement the traditional gray-world modeling approach, where a resampled panchromatic gray-scale image is utilized as input into the simulation process. In past investigations, the latter approach has almost exclusively been used to quantify the predicted image quality that can be achieved from conventional and sparse aperture systems alike. As alluded to in previous discussion, there is some concern whether such a modeling approach is entirely appropriate for sparse aperture systems given their unique aperture transfer function character. Consequently, the implementation of the gray-world modeling assumption should provide a comparative yardstick by which to measure the spectral implications of the enhanced model, the primary thrust of this research endeavor.

The gray-world implementation closely parallels the more rigorous polychromatic model, with the principal differences associated with the spectral fidelity of the latter's object scene, optical phase/path difference errors, system optical transfer function, image noise, and rigorous formulation of the signal integration represented by equation 8. Correctly capturing the spectral physics for these imaging components in the higher fidelity implementation was not a trivial exercise, and considerable modeling effort was expended to implement a spectral radiometric model that satisfactorily incorporated them. Fortunately, the implementation of the gray-world approximation was greatly facilitated by the basic foundation laid by the more complex polychromatic simulation capability. Given a spectral radiance "data cube" for the object scene, a reasonably straight-forward implementation of the numerical integration discussed in Section 4.8 was developed without use of a degrading transfer function to form a gray-scale object image. In addition, the means to compute a spectrally averaged system OTF from the individual quasi-monochromatic transfer functions with wavelengths spanning the detector passband of interest were put in place in accordance with equation 101. The single realization of the system transfer function generated through this technique can be directly applied in a Fourier optics schema to the spectrally integrated object scene to acquire

154

a prediction of the spatially-variant detected image. Through this process, one effectively arrives at a reasonable implementation of the traditional gray-world model consistent with equation 42.

With the methodologies described above, several exemplar runs were performed to demonstrate the type of comparative analyses enabled by this modeling capability, as well as introduce the nature of the quality effects observed during restoration with the two model types. Once again, considerably more simulation results, analysis and discussion will be provided in the next chapter. For the purpose of illustration, figures 54 and 55 provide side-by-side comparisons of the restored imagery acquired from the two simulation models for a tri-arm sparse aperture system configuration with 0.20 waves and 0.25 waves rms of wavefront error, respectively. In (a) and (c) of these figures, one observes the restored image quality associated with the higher spectral fidelity, polychromatic-world model implementation. Conversely, the restored imagery products acquired through use of the gray-world model approximation appear in (b) and (d) of these figures. In a given figure, both model examples entail simulation of aperture configurations with the same overall aberrated phase profile and very good detection SNR (on the order of 273). In addition, the depicted restorations rely upon the "optimal" Wiener filter description pursued in previous exercises in the discussion above. With those considerations, the principal differences observed between the restorations should be attributable to the level of spectral fidelity incorporated into the individual models. Accordingly, these figures provide some initial evidence of the implications associated with addressing the spectral effects in a sparse aperture system investigation with additional rigor than is typically pursued.

(a) Restored Imagery
Polychromatic World

(b) Restored Imagery
Gray World

(c) Magnified Region of (a)
Polychromatic World

(d) Magnified Region of (b)
Gray World

Figure 54: Comparison of restored panchromatic imagery predictions
(Wavefront Error: 0.20 waves rms, SNR: 273.7).

(a) Restored Imagery
Polychromatic World

(b) Restored Imagery
Gray World

(c) Magnified Region of (a)
Polychromatic World

(d) Magnified Region of (b)
Gray World

Figure 55: Comparison of restored panchromatic imagery predictions
(Wavefront Error: 0.25 waves rms, SNR: 273.2).

In figures 54 and 55, one generally observes a noticeable difference in the image quality associated with the polychromatic-world simulations on the left side relative to the gray-world predictions on the right. For instance, the polychromatic overview images on the top row of the figures appear to exhibit image structure, artifacts and rippling on a level of magnitude that detectably exceeds their gray-world counterparts. Many of these enhanced artifacts in the polychromatic simulations coincide with image structure and edges that manifest some spectral character in the original spectral radiance object. As a primary example of this observation, the edge of the terminal building seen in Figure 54(a) and (c) exhibits an inadvertent spectral signature in the object scene, a yellow-blue striping artifact due to interpolation errors in the original WASP airborne collection (see the RGB object image in Figure 53). Interestingly, this clearly defined spectral content in the object introduced an artifact site in the restored imagery where increased, nonuniform edge ripple can be observed for the 0.20 waves rms wavefront error case. The magnitude of this edge ripple effect in Figure 54(c) considerably outweighs the more benign adjacency effect due to edge overshoot apparent in Figure 54(d). As a result, the inclusion of enhanced spectral fidelity has clearly resulted in quality implications that were not physically captured by the gray-world model for the sparse aperture system with 0.20 waves rms of wavefront error. Upon closer inspection, similar degraded quality effects can also be observed between the different colored automobiles in the parking lot. Obviously, these vehicles represent rich diversity in spatial frequency and spectral scene content. This combination of scene attributes is ripe for the introduction of spectral artifacts, as will be seen in the detailed results that appear in the next chapter.

The observed artifact effects discussed above become even more apparent and destructive for the 0.25 waves rms wavefront error scenario depicted in Figure 55. The spectral and frequency content of the parked automobiles in this simulation give rise to significant artifacting and rippling for the polychromatic model, as witnessed in Figure 55(a) and (c) of that figure. The degrading effect of these artifacts is not, however, replicated in the gray-world model results in Figure 55(b) and (d). In addition, the overall level of deleterious quality effects arising in the enhanced spectral simulation has increased across the entire image plane at large for this scenario. From these figures, it is apparent that the higher

158

spectral fidelity model captures a quality effect for these optical configurations that has not been adequately accommodated by the traditional gray-world model. The physical phenomenon that gives rise to this spectral artifacting effect will be discussed at greater length in the next chapter. One should note the appearance of spectral artifacts observed in these examples has occurred for dephased or aberrated sparse aperture configurations with relatively high rms wavefront error. There is, of course, interest in attempting to bound the onset of occurrence for this unique spectral artifacting, with some fundamental understanding of the interplay between rms wavefront error, fill factor and signal-to-noise. In addition, although the artifacts are clearly visible in the imagery, some sort of numerical quantification in the context of meaningful quality metrics is also of immense interest to this research effort. To that end, certain image quality metrics have been proposed for use in this research effort and will be described in the next section.

4.12 Data Analysis Metrics

Precision measurement of image quality through quantifiable metrics has effectively eluded the imagery community for many decades. This can in large part be attributed to the psychophysical nature of the human observer responsible for assessing the overall quality of an imagery product. To address this age-old problem, the photo-interpretation community introduced the concept of image interpretability and developed a quality yardstick referred to as the National Imagery Interpretability Rating Scale (NIIRS). This 0-to-9 scale essentially categorizes images into certain "quality bins" based on the level of interpretable detail present in them (higher NIIRS corresponds to improved interpretability). Significant time and effort has been dedicated to conducting so-called NIIRS studies of image quality given various samples of imagery products under different scenarios (e.g., ground sample distance, illumination conditions, signal-to-noise, scene content, post-processing, etc.). The assessment of NIIRS to imagery products typically involves a statistical, psychophysical evaluation performed by trained photo-interpreters. Such an exercise was clearly beyond the scope and capability of the resources available to this research effort.

Over the years, however, an analytical formulation for NIIRS prediction has emerged in what is affectionately called an image quality equation (IQE). In response to general IQE

development, it has been shown through numerous investigations and reported by Leachtenauer (1997) that interpretability (or NIIRS) typically varies with specific operational parameters, as observed in the following general-purpose expression:

$$\text{NIIRS} = a - b \log_{10} \text{GSD}_{\text{GM}} + c \log_{10} \text{RER}_{\text{GM}} - dH_{\text{GM}} - e\left(G_{rms} / \text{SNR}\right) \tag{146}$$

where GSD_{GM} is the geometric mean ground sample distance, RER_{GM} is the geometric mean relative edge response, H_{GM} is the geometric mean overshoot due to post-processed edge sharpening, G_{rms} is the noise gain due to sharpening, SNR is the signal-to-noise ratio, and a-e are appropriate constants for the imaging system and scene content under investigation. From this IQE expression, it is apparent that interpretability entails the complex interaction of a number of parameters. This is further complicated by the fact that the NIIRS dependency expressed above generally varies with both scene content and imaging system configuration. However, based on the general form of equation 146, it seems reasonable to explore the individual constituents of the overall interpretability expression as a means for quantifying the image quality associated with a given collection scenario. With that premise, the relative edge response (RER), noise gain (G_{rms}), and signal-to-noise ratio (SNR) parameters constituted the principal metrics for assessing the quality associated with a particular simulation product in this research effort. The general nature of these physical quantities will be discussed in additional detail in the following sections.

4.12.1 Signal-to-Noise Ratio

Many different expressions have been proposed in the literature for quantifying the signal-to-noise ratio (SNR) for a given collection scenario. Of course, all of the SNR conventions have entailed an appropriate ratio of signal amplitude to noise level. The principal difference between them has generally been associated with their definition of the individual constituents in the ratio (i.e., how to define target signal and image noise). Relying upon a relatively standard convention frequently cited in the literature, this research effort essentially defined SNR as consisting of the ratio of mean target signal to the standard deviation in the image noise level:

$$\text{SNR} = \frac{m_{signal}}{\sigma_{noise}} \tag{147}$$

where m_{signal} is the mean signal level and σ_{noise} is the standard deviation of the noise. This SNR metric is derived from the detected imagery products acquired through the proof-of-concept simulation model, from which the mean signal level from the original object spectral radiance field and the standard deviation in the applied statistically independent noise profile are known a-priori. For comparative purposes, the engineering code also computes an alternative image-based SNR metric founded on the ratio of the variance in the detected image signal counts to the variance in the additive noise counts. As discussed by Lim (1990) and Schowengerdt (1997), these parameters lead to another fairly common variance-based expression that assumes the following form:

$$\text{SNR}_{var} = \frac{\sigma^2_{signal}}{\sigma^2_{noise}} \tag{148}$$

The general relation identified above provides some additional insight over the standard expression in equation 147, since it represents a relative measure of signal-to-noise "power." As is common practice with power expressions, the image-based SNR formulation introduced above can be re-expressed in decibels (dB) as follows:

$$\text{SNR}_{var} = 10\log_{10}\left(\text{SNR}_{var}\right) = 10\log_{10}\left(\frac{\sigma^2_{signal}}{\sigma^2_{noise}}\right) \tag{149}$$

to form a more traditional power ratio figure of merit. As a matter of choice, all the SNR metrics developed in the above expressions are available to the investigator within the proof-of-concept simulation capability. For consistency, one will find that this dissertation relies almost exclusively upon equation 147 to specify the SNR associated with a given simulation product or scenario.

4.12.2 Relative Edge Response

As documented by Leachtenauer (1997), the next quality metric used in this research was normalized relative edge response (RER), which is directly related to the perceived sharpness of an image. As such, RER is a very fundamental quantifier of overall image quality or interpretability. Support for this observation is provided by the NIIRS expression in equation 146, where a combination of the leading coefficient amplitudes and the logarithmic nature of the terms lead to the **GSD** and **RER** as the dominant drivers in determining image interpretability. Most metrics that quantify optical resolution typically capture the nature of the system impulse response or transfer function in some manner. Consistent with this statement, the RER parameter is based upon the total system optical transfer function, including the effects of image post-processing. Since the RER is ultimately derived from the post-restoration system optical transfer function, it is useful to explicitly state the form of the equivalent system transfer function $\mathscr{H}_{\text{restore}}[\xi,\eta]$ of the restored imagery:

$$\mathscr{H}_{\text{restore}}[\xi,\eta] = W_{\text{wiener}}[\xi,\eta]\mathscr{H}[\xi,\eta] = \frac{|\mathscr{H}[\xi,\eta]|^2}{|\mathscr{H}[\xi,\eta]|^2 + \dfrac{S_{\text{n}}[\xi,\eta]}{S_{\text{f}}[\xi,\eta]}} \qquad (150)$$

where $W_{\text{wiener}}[\xi,\eta]$ is the frequency-domain Wiener filter, $\mathscr{H}[\xi,\eta]$ is the imaging system optical transfer function (prior to restoration), $S_{\text{n}}[\xi,\eta]$ is the noise power spectrum, and $S_{\text{f}}[\xi,\eta]$ is the power spectrum associated with the object scene. This post-processed transfer function is the primary component of the derived relative edge response.

To first order, the RER essentially represents the slope of the normalized edge response of the optical system, which measures the degradation of the system on a STEP-function input. In one dimension, the edge response along a cardinal axis is:

$$\text{ER}_{\text{x}}(x) = 0.5 + \frac{1}{\pi}\int_{0}^{\infty}\frac{|\mathscr{H}_{\text{restore}}[\xi,0]|}{\xi}\text{SIN}[2\pi\xi x]d\xi$$

$$\text{ER}_{\text{y}}(y) = 0.5 + \frac{1}{\pi}\int_{0}^{\infty}\frac{|\mathscr{H}_{\text{restore}}[0,\eta]|}{\eta}\text{SIN}[2\pi\eta y]d\eta \qquad (151)$$

162

where [x,y] are the relative positions of the response from the actual horizontal edge of a detector pixel and [ξ,η] are the spatial frequencies measured in cycles per unit length sampled by the detector. Similar quantities can be computed for each cardinal axis along which the system OTF exhibits unique symmetry. This could be important in the case of sparse aperture systems that are not symmetric. For convenience, one can rearrange the terms in these expressions to introduce a SINC function and develop general-purpose expressions for the system edge response along the x- and y-axes:

$$
\mathrm{ER}_x(x) = 0.5 + \int_0^\infty 2x \left| \mathscr{H}_{\text{restore}}[\xi,0] \right| \mathrm{SINC}[2\xi x] d\xi
$$

$$
\mathrm{ER}_y(y) = 0.5 + \int_0^\infty 2y \left| \mathscr{H}_{\text{restore}}[0,\eta] \right| \mathrm{SINC}[2\eta y] d\eta
$$

(152)

where the metric has been computed along those axes for the purposes of illustration. These axial metrics also are used as figures of merit for conventional aperture systems, which tend to exhibit some symmetry that enables use of a geometric mean RER.

Samples of the imaging system edge response for two different aperture configurations appear in figures 56 and 57. For instance, Figure 56 illustrates the character of the system edge response for a Nyquist-sampled filled circular aperture under the nominal imaging scenario specified in Table 2. Similarly, Figure 57 provides examples of edge response curves for an aberrated tri-arm sparse aperture configuration under similar imaging conditions. In these figures, the red plot indicates the edge response that would be observed prior to any applied restoration (i.e., it represents the detected edge response). On the other hand, the blue plot identifies the post-restoration edge response that is utilized in a typical RER calculation. In both figures, it is readily apparent that the applied Wiener filter restoration significantly improves the sharpness of the edge, thereby resulting in better overall image quality for these particular scenarios. Conversely, one will also note that the Wiener filter introduces some overshoot (manifested by the peaks and valleys on either side of the restored edge) that ultimately induces a small amount of ripple that tends to reduce perceived quality. Past psychophysical studies have shown, however, that the human

observer can tolerate a certain level of this deleterious effect if it is accompanied by an appropriate amount of image sharpening. In addition, the human visual system actually prefers a certain amount of this so-called adjacency effect over no overshoot whatsoever. With this background, the sample edge response curves provided below certainly appeared to the untrained observer to fall into the category of improved image quality. In a separate verification exercise, several processed edge images were empirically measured to confirm the accuracy of the theoretical implementation of the edge response metric depicted in the figures. Within the interpolation error associated with physically measuring 0.5-pixel with sampled image data, the results acquired with theory and measurement appeared to be statistically comparable.

Another interesting observation that surfaces with regard to the sparse aperture case in Figure 57 is the seriously blurred nature of the edge, clearly defining the need to apply a restoration technique that sharpens the edge to a level commensurate with the filled aperture product. As observed in the restored edge response curve (in blue), the selected Wiener filter succeeds in accomplishing that objective, although the asymmetry associated with the sparse aperture system transfer function is clearly evident in the differences in the restored edges along the two cardinal axes. These data provide a clear indication that the RER derived for a sparse aperture system must consider the implications of different edge response characteristics along various angular cuts of the spatial plane. Based on the general discussion above, it is also clear that the quantitative RER metric (which is based on the edge response characteristics displayed below) captures the qualitative character of the simulations shown previously, providing evidence that it represents an appropriate metric for the task at hand. Although by no means exhaustive, this metric will certainly help quantify the overall image quality observed in given image simulation products.

(a) x-axis   (b) y-axis
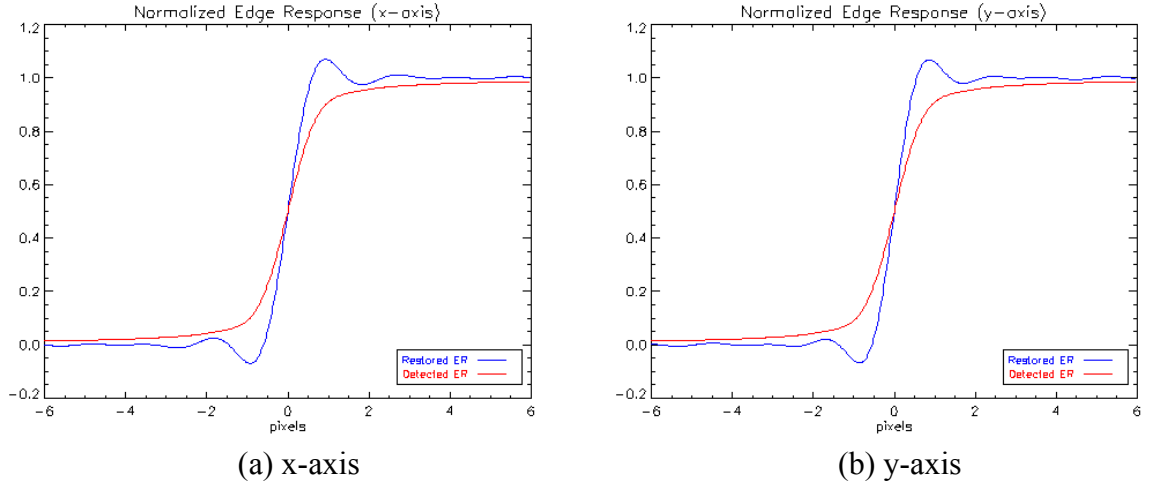
Figure 56: Sample edge responses before and after restoration (filled aperture).

(a) x-axis   (b) y-axis
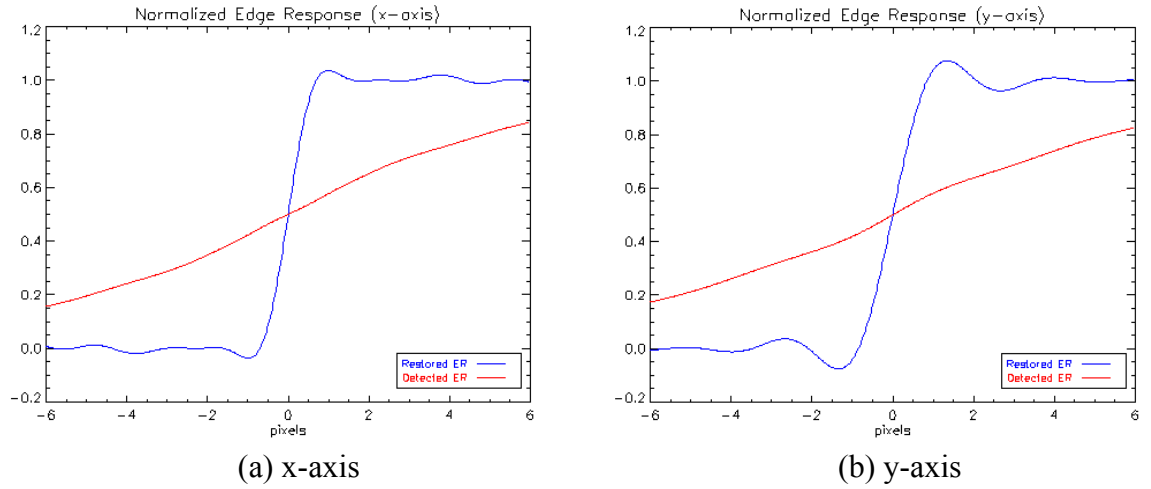
Figure 57: Sample edge responses before and after restoration (sparse aperture).

The desired RER metric is determined to be the slope of the edge response measured between two points located 0.5 pixel on either side of a physical edge. With this convention, the RER in the *x*-dimension would assume the general form:

$$\mathrm{RER}_x = \mathrm{ER}_x\left(x = 0.5\right) - \mathrm{ER}_x\left(x = -0.5\right)$$
$$= 2\int_0^\infty \left|\mathscr{H}_{\mathrm{restore}}\left[\xi,0\right]\right|\mathrm{SINC}\left[\xi\right]d\xi \tag{153}$$

which is acquired through the appropriate substitution from equation 152 and subsequent reduction of the resulting expression. In a similar fashion, one can derive the following equation for the RER in the *y*-dimension:

$$
\begin{aligned}
\mathrm{RER}_y &= \mathrm{ER}_y\left(y = 0.5\right) - \mathrm{ER}_y\left(y = -0.5\right) \\
&= 2\int_0^\infty \left|\mathscr{H}_{\mathrm{restore}}[0,\eta]\right| \mathrm{SINC}[\eta]\, d\eta
\end{aligned}
\tag{154}
$$

As alluded to previously, the two RER expressions are functions of the post-restoration system transfer function. Therefore, the relative edge response clearly represents a good indictor of the restored optical resolution associated with a particular image. Given the RER expressions along the cardinal axes of the spatial plane (i.e., along the horizontal and vertical orientations), one would traditionally compute the geometric mean according to the relationship:

$$
\mathrm{RER}_{\mathrm{GM}} = \left[\mathrm{RER}_x \mathrm{RER}_y\right]^{1/2}
\tag{155}
$$

and use this average RER metric to help quantify the optical quality for most conventional imaging systems. As discussed above, one must be cautious in blindly applying the derived geometric mean RER to sparse aperture systems due to the unique cutoff frequency structure exhibited by these systems. Given the transfer function asymmetry that frequently arises with sparse aperture systems (especially in the presence of aberrations), one may have to rely upon an effective RER computed over the OTF area of support for these unique imaging systems, depending upon the conditions of the collection.

Recognizing the unique asymmetry present in sparse aperture systems, Fienup (2004) proposed an area-based effective RER$_{\mathrm{area}}$ which averages the RER calculation over all angular cuts through the system transfer function. The rationale given for reporting an arithmetic mean RER metric was that it could jointly handle the unique structure associated with sparse aperture transfer functions (both diffraction-limited and aberrated), as well as converge reasonably closely to the traditional geometric mean when the optical resolution along the *x*- and *y*-cardinal axes was similar. Based on this thought process, Fienup

developed the following analytical expression for an area-weighted RER representing the arithmetic mean of individual RER calculations:

$$\text{RER}_{\text{area}} = \frac{1}{N}\left\{1 + \frac{1}{\pi}\sum_{\substack{\xi=-\frac{M}{2}\\\xi\neq 0}}^{\frac{M}{2}-1}\sum_{\substack{\eta=-\frac{N}{2}\\\eta\neq 0}}^{\frac{N}{2}-1}\frac{1}{\left(\xi^2+\eta^2\right)^{\frac{1}{2}}}\text{SINC}\left[\frac{\left(\xi^2+\eta^2\right)^{\frac{1}{2}}}{N}\right]\text{Re}\{\mathcal{H}_{\text{restore}}[\xi,\eta]\}\right\} \qquad (156)$$

where $\text{Re}\{\cdot\}$ represents the real part of the operand and N is the number of samples in the digital Fourier transform in the ξ- and η-directions, respectively. Fienup indicates that this expression is valid when the imaging system is Nyquist sampled or better, which is generally the case for the exercises pursued in this dissertation.

During the course of this research, several different RER implementations were investigated on an anecdotal basis. The latter included the simple geometric mean RER_{GM}, the arithmetic mean RER_{area} analytical expression proposed by Fienup, and a discrete arithmetic mean RER_{eff} generated through the average of ~100 angular cuts through the optical transfer function. This exercise consistently appeared to show that all three potential RER metrics provided similar results to within an accuracy of ≤5% of each other for the range of optical configurations studied in this research effort, even under aberrated/dephased subaperture conditions. Based on these investigations, it is likely that the multiple effects of the spectral averaging that occurs during signal integration, the serious demodulation that occurs when a sparse aperture system experience aberrations, and the area weighting that occurs through the arithmetic mean RER calculation specified in equation 156 results in an effective cutoff frequency that does not manifest as much asymmetry as one might surmise. As a consequence, one could potentially contend that the arithmetic and geometric mean RER metrics both have some merit for quantifying this key optical parameter, even for aberrated sparse aperture systems. For comparative purposes, both the geometric mean and Fienup's arithmetic mean formulation are output by the proof-of-concept simulation model for the investigator's use.

4.12.3 Noise Gain

As stated previously, sparse aperture systems typically exhibit a demodulated optical transfer function that requires some post-processing technique to restore image quality. That characteristic of these unique imaging systems was certainly highlighted by the simulated imagery in Figure 53(c) and (d), as well as many other exemplar model products that appear throughout this chapter. In the process of sharpening edge feature structure within degraded imagery, these restoration filters tend to amplify the image noise σ_{noise} as well, producing an effect referred to as **noise gain**. This noise amplification can be captured in the measured signal-to-noise ratio by multiplying the standard deviation of the noise by the noise gain G_{rms}. Given an MxN spatial domain sharpening kernel, which for purposes of this research was a Wiener filter, the noise gain is traditionally computed via the following general relation:

$$G_{rms} = \frac{\left[\sum_{x=-\frac{M}{2}}^{\frac{M}{2}-1} \sum_{y=-\frac{N}{2}}^{\frac{N}{2}-1} \left| w_{wiener}[x,y] \right|^2 \right]^{\frac{1}{2}}}{\sum_{x=-\frac{M}{2}}^{\frac{M}{2}-1} \sum_{y=-\frac{N}{2}}^{\frac{N}{2}-1} w_{wiener}[x,y]} \tag{157}$$

where $w_{wiener}[x,y]$ is a spatial domain representation of the Fourier domain Wiener filter $W_{wiener}[\xi,\eta]$ actually implemented in the engineering model. Accordingly, the sharpening filter identified in this noise gain expression is essentially the inverse Fourier transform of the applied Wiener filter:

$$w_{wiener} = \mathscr{F}^{-1}\left\{ W_{wiener}[\xi,\eta] \right\} \tag{158}$$

Through the application of linear mathematics, one can recast the general noise gain expression stated in equation 157 into a form that entails the explicitly known Fourier domain filter utilized in the modeling algorithms. Accordingly, after some manipulation one can demonstrate that the noise gain may also be represented by the following formulation:

$$G_{rms} = \frac{\left[\sum_{\xi=-\frac{M}{2}}^{\frac{M}{2}-1} \sum_{\eta=-\frac{M}{2}}^{\frac{M}{2}-1} |W_{wiener}[\xi,\eta]|^2\right]^{\frac{1}{2}}}{MW_{wiener}[0,0]} = \left[\frac{1}{M^2} \sum_{\xi=-\frac{M}{2}}^{\frac{M}{2}-1} \sum_{\eta=-\frac{M}{2}}^{\frac{M}{2}-1} |W_{wiener}[\xi,\eta]|^2\right]^{\frac{1}{2}} \qquad (159)$$

This expression was ultimately utilized in the proof-of-concept modeling capability to quantify the noise gain term. To first order, its implementation was separately verified through empirical measurement of the apparent noise gain in a uniform shadow region of a processed image. As indicated in the discussion regarding figures 52 and 53, the Wiener restoration process pursued in this dissertation has a tendency to correlate the image noise in addition to amplifying it. As observed in figures 54 and 55, this noise correlation can have a dramatic negative impact on the overall quality or interpretability of the imaged scene. Unfortunately, although the noise gain expression developed above captures the effect of noise amplification apparent in a restored image, the simultaneously occurring noise correlation is a phenomenon that will not be adequately quantified by the metric. Equally unfortunate, there is no other known metric that appears to be available to address this correlation effect, short of a full-fledged NIIRS evaluation by trained observers.

4.12.4 Normalized rms Error

The final evaluation metric that will be introduced for use in quantifying observed image quality effects is the normalized root-mean-square error (***nrmse***). This is a very straight-forward metric that can be useful when a-priori knowledge is available on a "truth" image, or the pristine object scene in this case. Since the simulation developed for this dissertation requires the object scene as input in order to produce the final simulated image product, truth data is readily available to determine exactly how the restored image varies from the original object from the perspective of image-wide statistics (i.e., on an rms basis). With the supported foundation to compute this metric, the *nrmse* is evaluated according to the following expression:

$$nrmse = \left[\frac{\sum\limits_{x=-\frac{M}{2}}^{\frac{M}{2}-1} \sum\limits_{y=-\frac{N}{2}}^{\frac{N}{2}-1} \left| \hat{f}_{obj}[x,y] - f_{obj}[x,y] \right|^2}{\sum\limits_{x=-\frac{M}{2}}^{\frac{M}{2}-1} \sum\limits_{y=-\frac{N}{2}}^{\frac{N}{2}-1} \left| f_{obj}[x,y] \right|^2} \right]^{\frac{1}{2}} \qquad (160)$$

where $f_{obj}[x,y]$ is a spectrally weighted average of the original object scene scaled to focal plane counts and $\hat{f}_{obj}[x,y]$ typically represents the restored digital imagery in counts. Of course, one can also replace the restored image array term in the expression above with the focal plane digital image array to acquire a quantitative figure of merit on how the detected image (prior to restoration) varies from the original object scene. Obviously, the principal drawback in utilizing a statistical measure like *nrmse* is that it captures quality differences globally across the image. As a result, some of the local quality effects observed in the figures above, including artifacting, may be glossed over in the image-wide statistics (especially from an absolute amplitude perspective). Accordingly, it will be important for one to draw conclusions about the quality implications of certain model scenarios based on use of all the quantitative metrics introduced above in conjunction with critical visual inspection of the results.

Chapter 5

Results

Given the general approach introduced previously, this chapter details specific results acquired from the proof-of-concept sparse aperture system modeling capability developed in support of this research effort. It also provides summaries of the top-level system trade studies that were performed in an attempt to characterize unique quality issues associated with sparse aperture configurations. In general, the emphasis of the following discussion is to demonstrate application of the basic modeling theory in an attempt to deduce whether sparse aperture systems have inherent spectral issues that must be addressed in order to make them practical alternatives for future collection systems. To that end, Section 5.1 below provides a discussion on the general nature of the optical transfer function for the principal configuration explored in this dissertation, the nine-subaperture tri-arm sparse aperture system. As a precursor to the final panchromatic model discussion, Section 5.2 discusses interim quasi-monochromatic simulation results that were acquired early in the research. This is followed up in Section 5.3 with the actual integrated panchromatic signal analyses performed with the full-fidelity polychromatic model implementation discussed in Chapter 3. The model results summarized in this section effectively demonstrate satisfaction of the one remaining dissertation requirement enumerated in Chapter 2, implementation of a proof-of-concept modeling construct to evaluate spectral issues in general sparse aperture systems.

With that foundation established, Section 5.4 subsequently compares and contrasts the dissertation results from the polychromatic model with those acquired from a more traditional gray-world model. The latter was developed in response to the need to better address the value of the enhanced spectral fidelity in the modeling process in terms of the quality implications. Section 5.5 discusses use of different constituent terms in the Wiener filter implementation, an offshoot of the investigations that were performed in the image restoration arena to confirm that observed effects were induced by the spectral physics and not the specific nature of the filter design. Finally, Section 5.6 briefly describes some analysis excursions that were performed over the course of this research effort to demonstrate

the integrity and/or utility of the overall computer model. In this final section, bullet summaries are provided for such analyses as filtering under different noise conditions, changing the integration time associated with a given collection, varying system optical phase knowledge in the restoration process, and comparing the quality effects of subaperture dephasing versus the existence of classic optical aberrations. As a final note, one is referred to the Appendix for summaries of alternative panchromatic simulation results acquired from optical pupils other than the nominal tri-arm system, including the Golay-6, annulus, and phased-petal aperture configurations.

5.1 Transfer Function Character

As discussed in Chapter 3, the general linear systems model implemented in this research effort has several key components for predicting the nature of the imagery detected by a given optical configuration. From an imaging system perspective, one of the principal components that influence the character of detected imagery is obviously the complex-valued system transfer function. This critical piece in the overall imaging process has unique character for sparse aperture systems due to the interaction between subapertures that arise from the auto-correlation of the pupil function. This phenomenon has been discussed at some length previously. However, it becomes an even more dramatic effect when individual subapertures are dephased or aberrated, as a distinct structured character is induced on the aperture transfer function. This can be observed in the various transfer function diagrams in figures 58 through 60, which depict the aperture MTF for a tri-arm sparse aperture configuration with a fill factor of 0.173 subjected to various levels of aberration. In all three figures, a random phase profile has been applied across the exit pupil to simulate piston, tip/tilt in the regime from 0.10 to 0.25 waves rms of wavefront error. For comparative purposes, the diffraction-limited character of the aperture MTF appears in (a) of each figure.

The following series of diagrams provide excellent insight into the overall character of a sparse aperture transfer function in the presence of aberrations. In Figure 58, for instance, top-view "images" of the minimum wavelength MTF are depicted as a function of aberration strength. In reviewing these diagrams, one will note that the most prominent effect of increased wavefront error is the introduction of more zeroes (represented by the black region

in the interior of the MTF) in the spatial frequency coverage. Closer observation will additionally highlight the fact that the amplitude associated with individual spatial frequencies has also diminished. This character in the MTF obviously translates into more degradation in the detected imagery as the wavefront error increase across the collection aperture. The question that remains outstanding and will be addressed in subsequent sections is whether the restored imagery associated with these wavefront errors is deemed of acceptable quality. A final remark that should be made with regard to the figure below is that it depicts the MTF character for a single wavelength. Longer wavelengths in the detection passband will exhibit shorter optical cutoff frequencies (i.e., have reduced coverage in the spatial frequency plane) and reduced amplitude in the observed rms wavefront error (due to wavelength scaling of the optical path differences). As a consequence, the aperture MTF for alternative collection wavelengths will support image modulation that is fundamentally different as a function of spatial frequency than that observed in Figure 58. This mismatch in image modulation will be the source of a spectrally induced quality effect that will receive extensive coverage in the discussion to follow.

As an alternate illustration of the unique character of aberrated sparse aperture transfer functions, Figure 59 displays three-dimensional topographic views of the same functions depicted in Figure 58. This particular view provides considerably more insight into the destructive nature of aberrations since the reduced modulation as a function of increased wavefront error is readily apparent. This figure also highlights the extremely oscillatory nature of the aberrated sparse aperture transfer function, as significant structure in the context of peaks and valleys within the mid- to high-frequency range. Once again, one is reminded that these transfer function plots represent a single wavelength, and alterative spectra within the collection passband will exhibit vastly different structure as a function of spatial frequency. This phenomenon can be observed in the two-dimensional MTF plots in Figure 60, which depict slices through the spatial-frequency surface plots appearing in Figure 59 and incorporate transfer function data for two additional collection wavelengths. As indicated previously, one can again observe that increased wavefront error has the tendency to reduce the modulation and ultimately introduce more nulls in the spatial-frequency plane. This will unquestionably have a deleterious effect on the detected image quality.
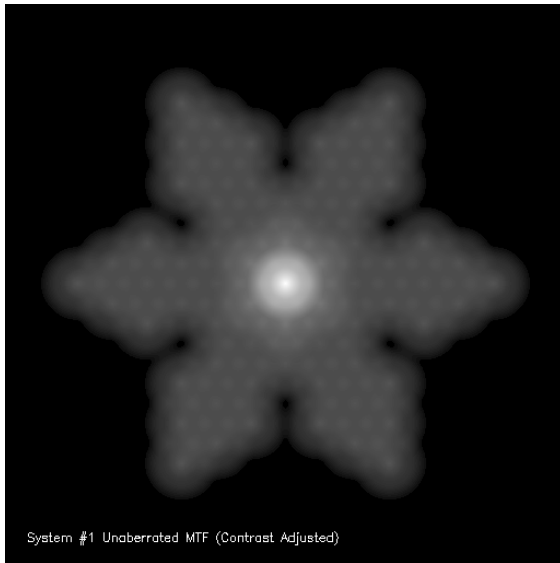
(a) diffraction limited
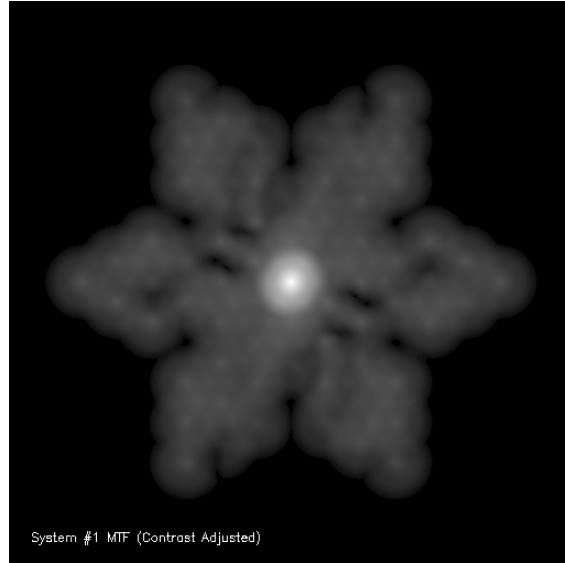
(b) 0.10 waves rms piston, tip/tilt
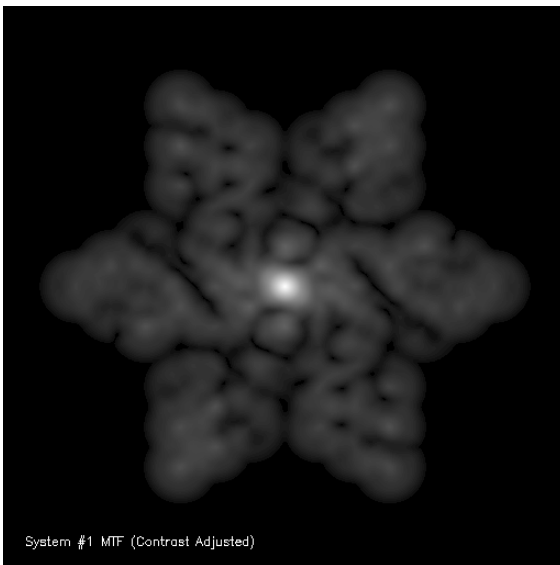
(c) 0.20 waves rms piston, tip/tilt

(d) 0.25 waves rms piston, tip/tilt

Figure 58: Effect of various levels of rms wavefront error on a
tri-arm sparse aperture modulation transfer function.

(a) diffraction limited

(b) 0.10 waves rms piston, tip/tilt

(c) 0.20 waves rms piston, tip/tilt

(d) 0.25 waves rms piston, tip/tilt

Figure 59: Effect of various levels of rms wavefront error on a
tri-arm sparse aperture modulation transfer function.

In addition to the relatively intuitive effect of reduced modulation, one will observe that
increased wavefront error in sparse aperture systems also creates a rapidly varying oscillation
in the modulation that changes significantly with wavelength. This attribute of sparse
aperture transfer functions tends to be unique among optical systems and ultimately gives
rise to a mismatch between the system modulation manifested by individual wavelengths. In
Figure 60, one can readily see this relative mismatch between the imaging system modulation

175

for different wavelengths at given spatial frequencies. In addition, the so-called mismatch is exacerbated as the rms wavefront error increases from zero in the diffraction-limited case to 0.25 waves rms in the most aberrated scenario depicted in the figure. As alluded to above, there are regions in the spatial frequency plane where the minimum collection wavelength exhibits a valley in the transfer function at a location where the maximum supports a peak in modulation, and vice versa. One can easily anticipate that this relative mismatch between wavelength-dependent transfer functions is present throughout the spectrum of possible collection wavelengths. The reason this relative mismatch is deemed to be so problematic is that the final integrated signal composed of this spectral content must be restored through use of a single filter. Accordingly, one cannot possibly design a restoration filter that properly boosts the frequency spectra of the object scene associated with each wavelength in a near-optimal manner. Inevitably, at certain spatial frequencies the selected filter will overboost the modulation associated with given object spectral content and underboost that associated with others. As a consequence, an object scene that exhibits strong spectral and spatial-frequency content is highly likely to suffer the effects of this mis-boost, thereby resulting in a spectrally induced quality effect. The nature of this quality effects will be explored in more detail in the sections which follow.

To demonstrate the relative uniqueness of the conjectured effect, Figure 61 provides a comparison of the spectral character of the transfer function for (a) an aberrated tri-arm sparse aperture and (b) a diffraction-limited filled circular aperture configuration. As observed in this figure, the sparse aperture exhibits the classic oscillatory, spectral mismatch described previously, while its filled counterpart displays a smoothly varying, monotonically decreasing transfer function. As a result of the latter, a restoration filter that is applied in the filled aperture case will produce a smoothly varying mismatch that largely becomes undetectable in the final reconstruction. There are no sharp discontinuities in the spatial-frequency coverage that could give rise to rapid, oscillatory mis-boost at certain frequencies that the human eye can readily detect. In addition, the relatively high modulation exhibited by the original imaging system implies that the actual magnitude of the boost required for restoration is not significant, ensuring that any existent mis-boost is not excessively amplified. As will be seen later, however, even highly aberrated filled aperture systems will

not manifest the spectrally induced quality effects that will become apparent in the sparse aperture case. In this aberrated case, even though the filled transfer function becomes highly demodulated and exhibits some oscillatory character, it still remains relatively smoothly varying relative to its sparse aperture counterpart. Therefore, the rapidly varying, oscillatory nature of sparse aperture transfer functions must be the principle contributor for inducing the effect which will be introduced in the next two sections.
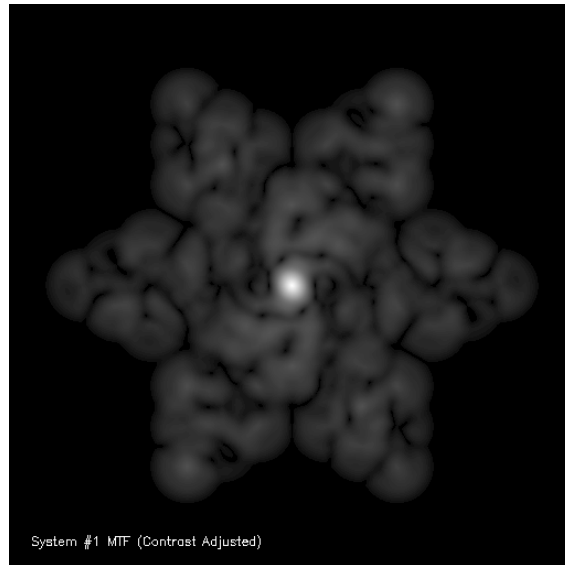

(a) diffraction limited

(b) 0.10 waves rms piston, tip/tilt

(c) 0.20 waves rms piston, tip/tilt

(d) 0.25 waves rms piston, tip/tilt
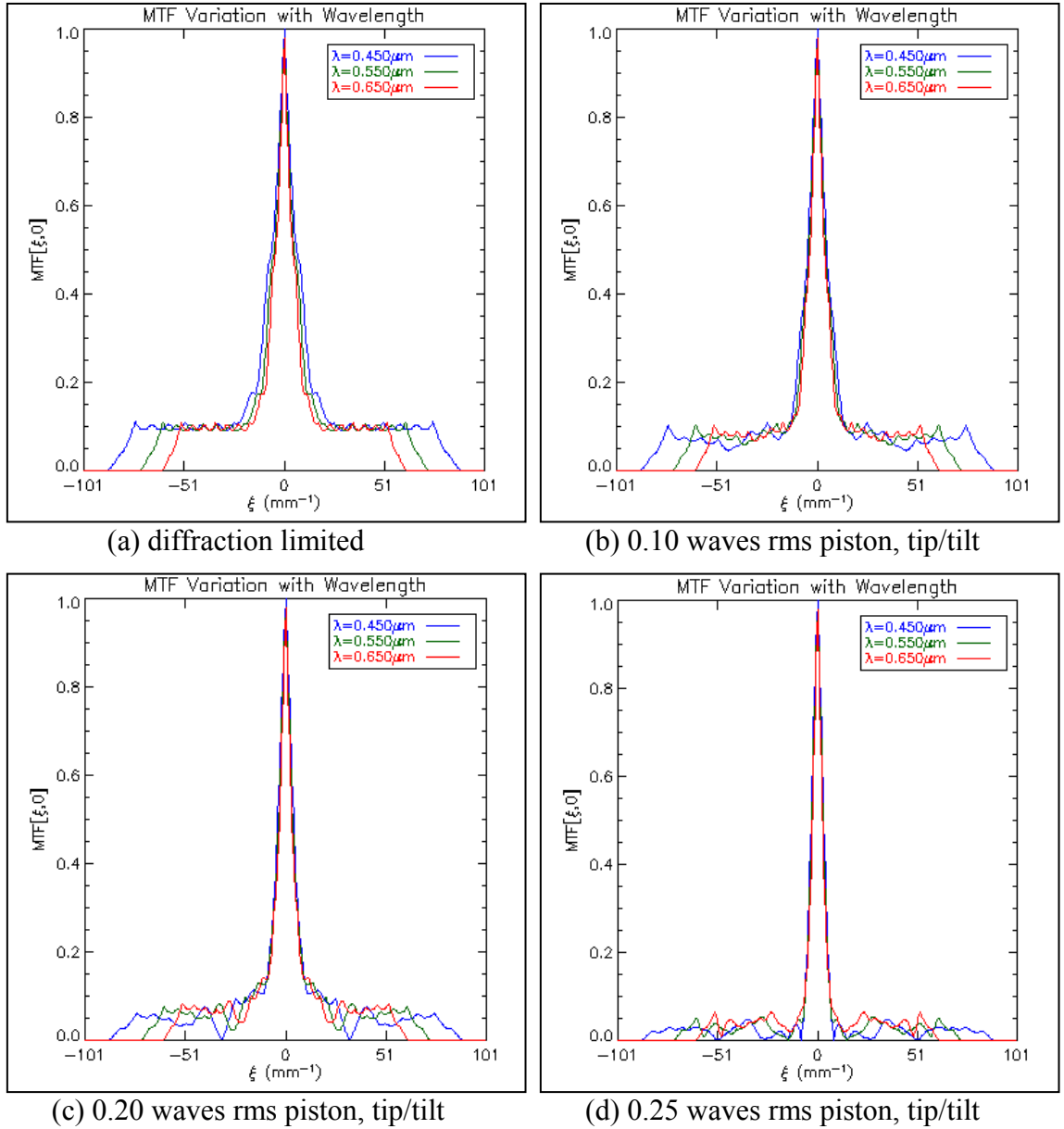
Figure 60: Effect of various levels of rms wavefront error on
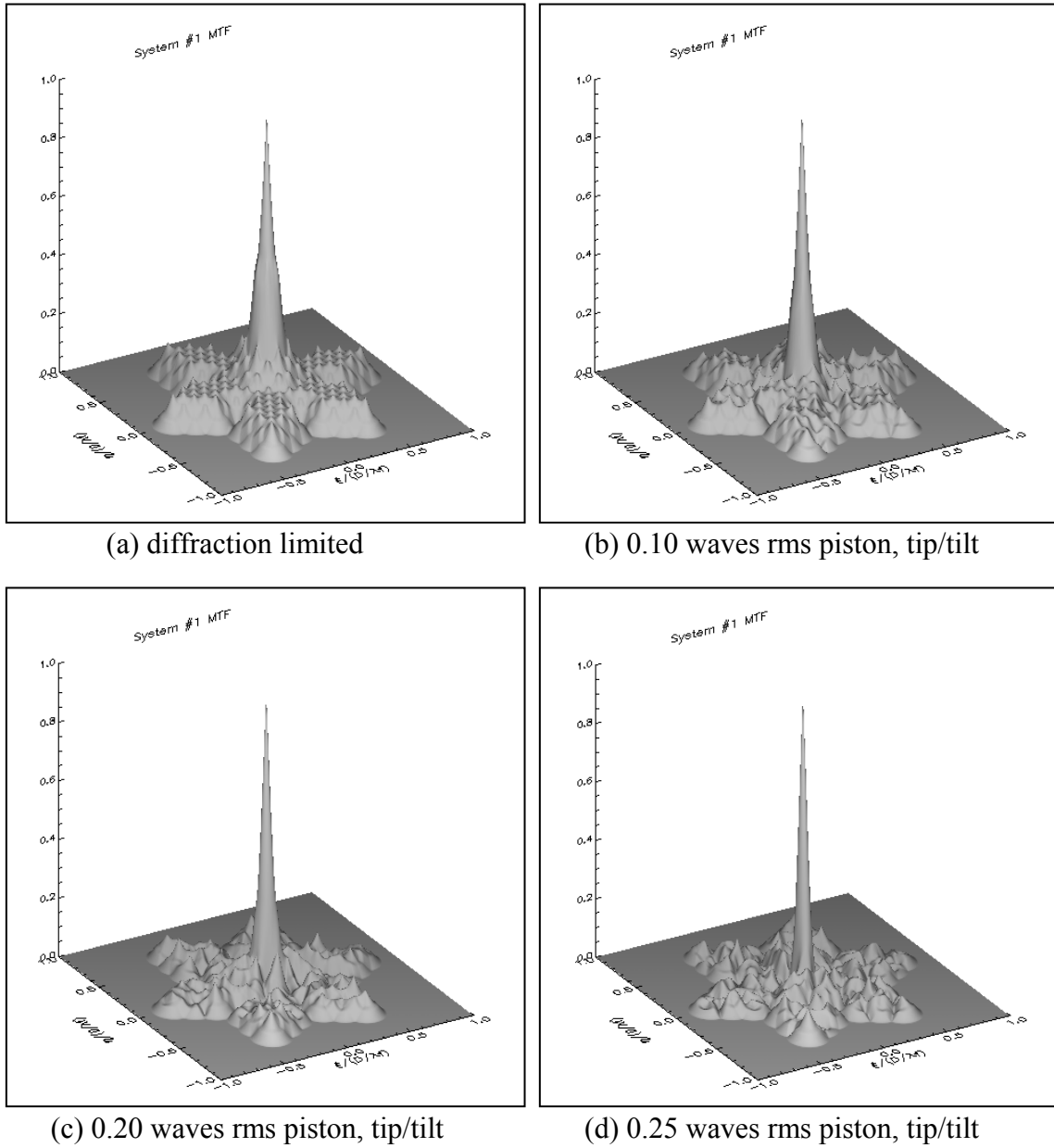tri-arm sparse aperture spectral transfer functions.

(a) Tri-arm Sparse Aperture
0.24 waves rms piston, tip/tilt

(b) Filled Circular Aperture
diffraction limited
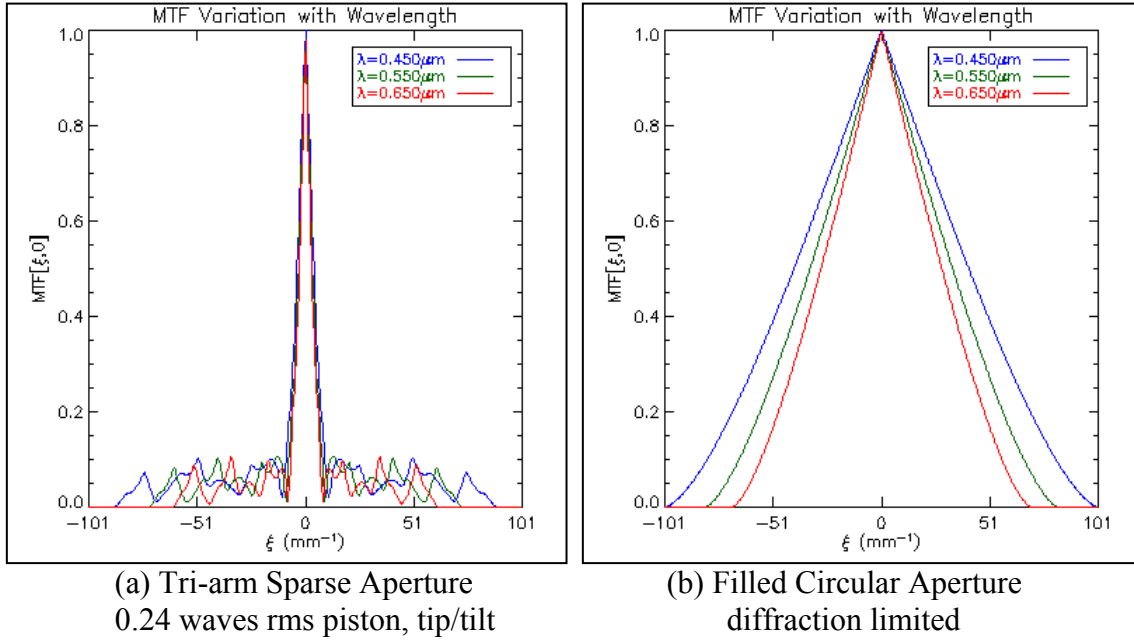
Figure 61: Comparison between the spectral transfer functions
of an aberrated tri-arm sparse aperture and a
diffraction-limited filled circular aperture.

All of the plots described above entail incoherent but quasi-monochromatic realizations of the aperture transfer function. Ultimately, these monochromatic transfer functions modulate a polychromatic object scene at given wavelengths and the resulting signal photons are subsequently "integrated" through the action of the detection device. This integrated signal represents what is actually detected by the imaging system and essentially constitutes a spectral averaging of the monochromatic effects described above. This process is rigorously performed within the enhanced spectral fidelity model generated for this research effort, so the true polychromatic character of the detected signal is adequately captured. The conventional gray-world model, on the other hand, develops a so-called spectrally averaged "polychromatic" OTF from the individual monochromatic transfer functions prior to their application to a resampled gray-scale object scene. In this manner, the gray-world model does capture some of the spectral averaging character that ultimately occurs with the transfer function through the integration process in the detector. As an example of what the detection

178

process does to the "effective" transfer function over the collection passband, one should observe the series of diagrams in figures 62 through 65. In Figure 62, a typical tri-arm sparse aperture system has been configured with a random piston, tip/tilt phase profile that represents a wavefront error of 0.24 waves rms. Given this aperture configuration, figures 63 and 64 provide illustrations of the monochromatic MTF at the minimum collection wavelength as well as the spectrally averaged, effective MTF across the detection passband. As observed in these figures, the spectrally averaged MTF represents a "radially-smoothed" version of the individual monochromatic transfer functions, with reduced overall modulation relative to shorter wavelengths and less overall nulling across the spatial frequency domain (alternate wavelengths effectively "fill in" the zeroes associated with other wavelengths). This averaging process does represent a real-world effect due to the photon integration that occurs in the detection sensor. Consequently, the spectrally averaged transfer functions do have a physical basis in actual imaging conditions and represent a good single approximation of the action of imaging system on the incident spectral radiance profile or object scene.

(a) Two-Dimensional Distribution   (b) Three-Dimensional Surface
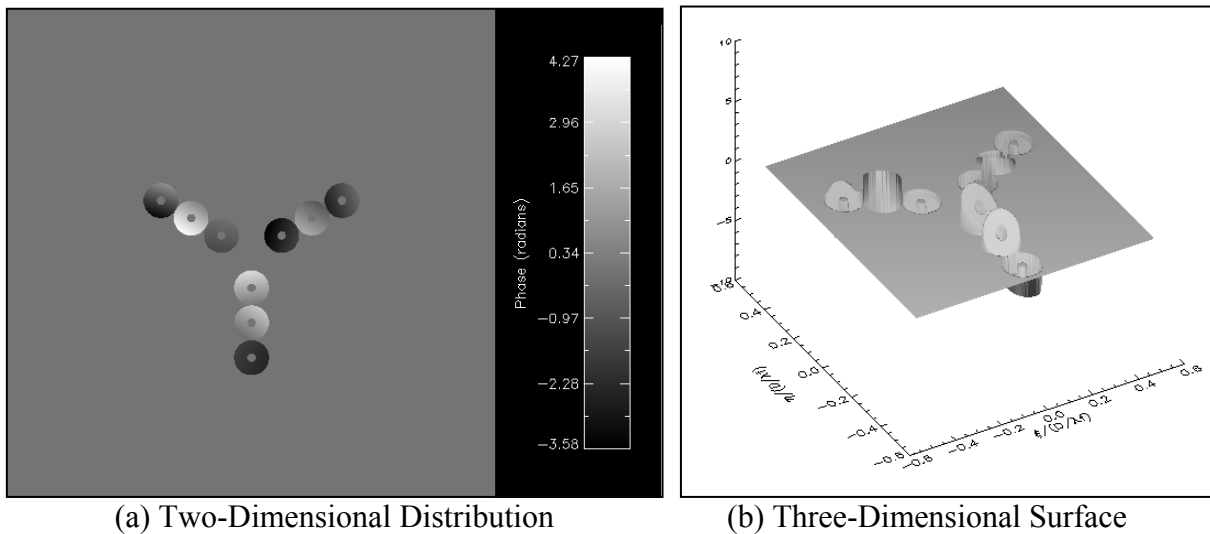
Figure 62: Random phase profile for the central wavelength of an aberrated
tri-arm sparse aperture (0.24 waves rms piston, tip/tilt error).
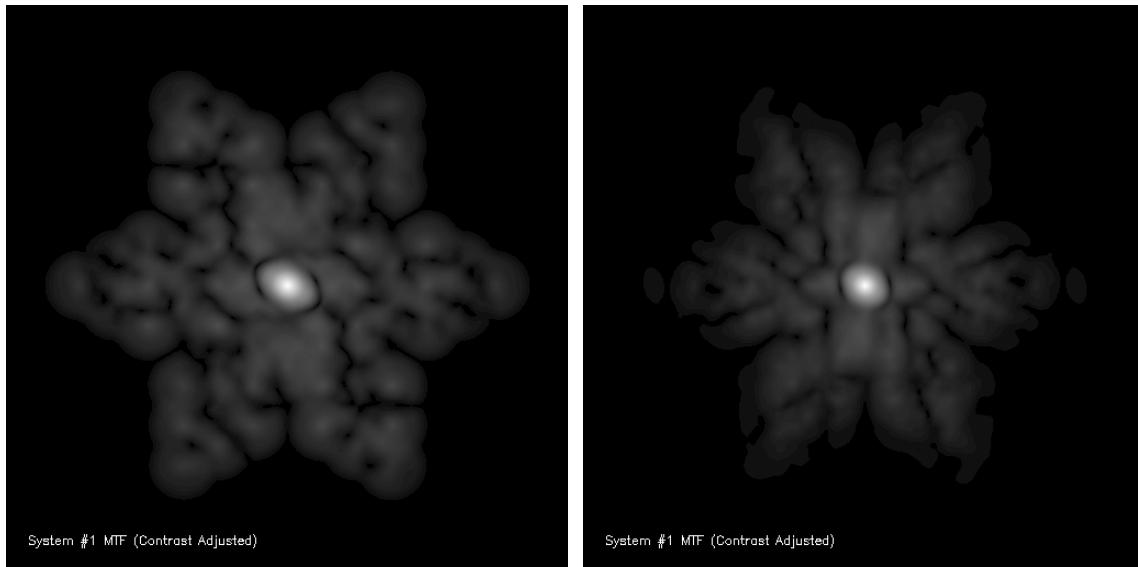
(a) Monochromatic (0.45 μm)   (b) Spectrally Averaged

Figure 63: Comparison between quasi-monochromatic and spectrally weighted
"polychromatic" transfer functions for an aberrated tri-arm
sparse aperture system (0.24 waves rms piston, tip/tilt error).
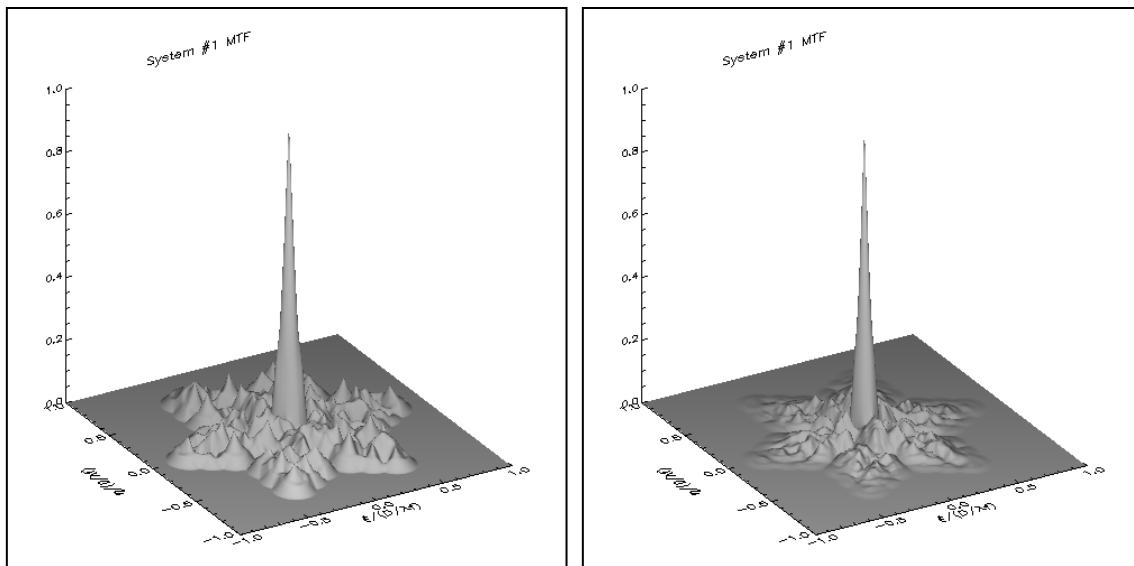
(a) Monochromatic (0.45 μm)   (b) Spectrally Averaged

Figure 64: Comparison between quasi-monochromatic and spectrally weighted
"polychromatic" transfer functions for an aberrated tri-arm
sparse aperture system (0.24 waves rms piston, tip/tilt error).

180

(a) Tri-arm Sparse Aperture
0.24 waves rms piston, tip/tilt

(b) Filled Circular Aperture
diffraction limited
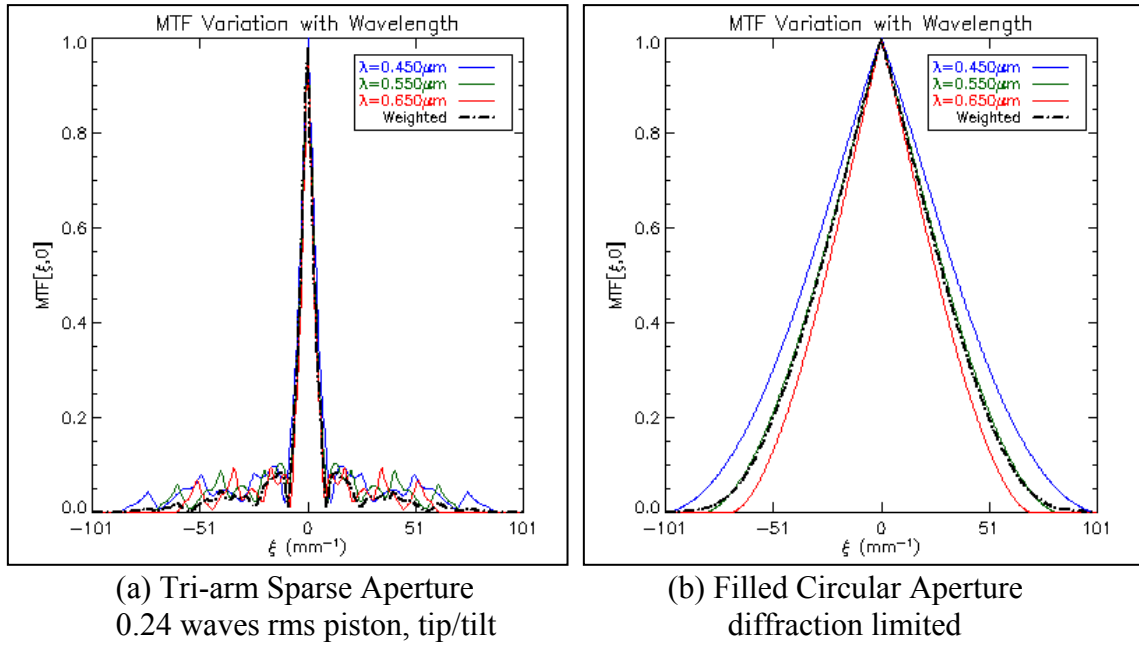
Figure 65: Comparison between quasi-monochromatic and spectrally weighted
system transfer functions for an aberrated tri-arm sparse aperture
and a diffraction-limited filled circular aperture.

Figure 65 provides an illustration of how the spectrally averaged MTF compares with individual transfer functions at discrete wavelengths. In both diagrams, the spectrally averaged MTF appears as a black dotted line and is plotted relative to red (0.65 μm), green (0.55 μm) and blue (0.45 μm) monochromatic transfer functions. In Figure 65(a), one observes that the radial smoothing in the spectrally averaged transfer function mitigates some of the oscillatory character associated with the aberrated tri-arm system MTF at discrete wavelengths. As this is a real-world effect, one would anticipate that a quasi-monochromatic prediction of sparse aperture system quality would typically result in more significant image structure in restored products and generally overstate the nature of any spectrally induced quality effects. The single realization of the spectrally averaged MTF also highlights the fact that use of it alone in a polychromatic simulation fails to adequately capture the true spectral modulation one would anticipate with aberrated sparse aperture systems. In Figure 65(b), one sees that the spectrally averaged MTF for the filled circular aperture case is once again smoothly varying and monotonically decreasing. Such character is entirely consistent with the previous quasi-monochromatic discussion, so the real-world averaging effect of the

181

detector only confirms the contention that conventional apertures exhibit transfer functions that are conducive to restoration of spectrally variant scene content. In addition, it is interesting to note that the spectrally averaged MTF for the filled aperture is more or less consistent with the central wavelength monochromatic transfer function. That is certainly not the case for the sparse aperture system. As a result, this diagram highlights why use of the central wavelength monochromatic OTF represents a good approximation for conventional aperture systems but is likely to be highly suspect for sparse aperture configurations. To that end, one should avoid using monochromatic predictions of sparse aperture image quality as an absolute measure of restored quality. One will observe that such predictions have been included in the next section of this dissertation to gain insight into the physical processes that ultimately feed the final integrated signal products, not as an absolute quantification of the derived image quality one should expect for these systems.

Although a gray-world model should provide reasonable approximations of the image quality **prior to restoration**, the figures above indicate there may be issues with such an approach in the restored imagery under certain combinations of polychromatic scene content and wavefront error amplitude. The problem with the gray-world implementation resides with the fact that spectral content is not modulated prior to the integration process. With conventional systems that do not exhibit serious oscillatory character as a function of spatial frequency, this drawback has not been of significant consequence in the past. With the unique, rapidly oscillating character of sparse aperture systems under certain levels of aberration, however, this approximation does not adequately capture the nature of the collection physics. As a result, any strong spectral content in the object will not be appropriately modulated prior to its contribution to the integrated signal content. For instance, the edge of a red automobile will not be blurred according to the appropriate red system transfer function but by some spectrally averaged OTF instead. As a consequence of this effect, the red automobile signal content will not exhibit the modulation mismatch highlighted in the discussion above and the applied restoration filter will not have the occasion to amplify it. The bottom line of this discussion is that the gray-world model would ultimately fail to account for any spectrally induced artifacting or structured rippling in the restored imagery due to the afore-mentioned spectral modulation mismatch. The enhanced spectral fidelity model, on the other hand,

should capture the nature of this quality effect. Of course, if the object is spectrally flat (i.e., more or less "gray" from a spectral perspective), no spectral artifacting would be induced by the optical transfer function character described above and the gray-world model approximation should more than adequately capture the detected image quality. On the other hand, if the object scene does manifest rich spectral and spatial frequency content, one would expect under aberrated conditions on the levels introduced above that the gray-world model will break down and not sufficiently represent the final restored imagery product. This premise will be tested in the results presented in subsequent sections.

5.2 Quasi-Monochromatic Simulation

Prior to the development of a full-fledged broadband simulation model, an interim capability was developed to evaluate the quasi-monochromatic optical performance of sparse aperture systems. This interim capability was enabled as a direct result of the implemented modeling approach, since each monochromatic spectral plane must be derived before an integrated signal can be estimated. It turned out to be fortuitous that the quasi-monochromatic analysis also lends insight into the physical nature of the final detected signal, as it provides evidence of how each spectral line is impacted by the detection and restoration process. As stated earlier, however, one must be cautious in using the monochromatic results as an absolute measure of the final predicted quality from sparse aperture imaging systems.

To support the quasi-monochromatic analysis, a WASP-derived polychromatic object scene containing a parking lot filled with various colored automobiles at different separations and orientations was selected. As such, the chosen scene demonstrates excellent spectral and spatial frequency content to explore the effects of the unique transfer function character discussed above. The ground sample distance (GSD) associated with this object is approximately 7-inches, and the airborne collection obviously entails three spectral bands with ~100 nm bandwidth. Accordingly, the selected object exhibits good spatial resolution and relatively poor spectral resolution. At this juncture, the latter was much less a concern than the former as this interim monochromatic analysis effort was focused on isolated wavelengths in any event. As a consequence, the WASP scene afforded excellent RGB digital imagery that could be formed into illustrative color composites during the simulation

process to highlight the sparse aperture effects on individual spectra. This can be observed in the quasi-monochromatic imagery simulation products contained in the series of figures which follow.

One should also recall that the Bayer pattern color filter array associated with the WASP source imagery had been interpolated to form individual RGB arrays prior to resampling within the sparse aperture simulation model. Therefore, any source imagery artifacts that surfaced as a result of the interpolation process were considered to represent spectral-radiometric truth for the purposes of this study. With this experimental design, any additional color artifacting observed in the restored imagery relative to the source "truth" data could be attributed directly to the inherent nature of the sparse aperture configuration vice a filter array interpolation phenomenon. On the other hand, this approach also eliminated the opportunity to address potential color filter array implications that may be unique to a sparse aperture collection system. If such an implementation were ultimately envisioned for a sparse aperture imaging system, that area would be worthy of additional investigation in the future.

For the quasi-monochromatic analysis, the baseline nine-subaperture tri-arm sparse aperture system with obscured optics was evaluated. The ratio (s/d) of the separation distance between individual subapertures to the subaperture diameter was unity (i.e., the subapertures were abutting). A Gaussian-distributed zero-mean, unit-variance phase profile was applied across the array of subapertures to simulate random piston, tip/tilt. This was accomplished for a number of different wavefront errors, spanning from 0.10 waves to 0.25 waves rms at the mean wavelength. The objective of the selected range of subaperture dephasing was to capture (or at least bound) the point at which the anticipated spectral artifacting due to the transfer function character described above demonstrated initial incidence and ultimately became destructive to the information content in the imagery. The next series of diagrams will step through the results acquired through this quasi-monochromatic analysis for wavefront errors of 0.10, 0.20 and 0.25 waves rms of piston, tip/tilt for the baseline sparse aperture configuration. For comparison, results acquired from a filled circular aperture with 0.20 waves rms of defocus will subsequently follow.

184

The first quasi-monochromatic simulation to be addressed in this dissertation entails 0.10 waves rms of piston, tip/tilt wavefront error. Numerous iterations have been performed over the course of this research effort at this nominal wavefront error value. For the purposes of illustration, results from one of these simulation runs have been included in the figures below. In Figure 66, for instance, one will observe a typical random phase profile applied to a tri-arm sparse aperture system to simulate 0.10 waves rms of piston, tip/tilt. As indicated in the previous chapter, the diagram on the left side of the figure depicts a two-dimensional "image" of the phase distribution, with greater than background intensity correlating with positive phase and lesser corresponding to negative phase amplitude. An intensity bar has been included in Figure 66(a) to earmark the specific amplitudes represented in the diagram. To aid in its interpretation, Figure 66(b) provides a three-dimensional surface plot of the same phase profile. As one would surmise, these data show that the random phase profile associated with 0.10 waves rms error does not generally exhibit significant overall amplitude (generally less than $\pi/2$) but the relative variation across the pupil can be fairly considerable. One would anticipate that such a profile would have some effect on the optical transfer function and degrade the quality associated with the detected imagery.

One should also note that the phase profile depicted in Figure 66 is specifically for the central wavelength of the collection passband. In the monochromatic simulations, as with the integrated signal predictions to follow, the physical path length differences are assumed to be the same as a function of wavelength while the optical phase errors associated with these path lengths vary appropriately with wavelength. In the model implementation, this is accomplished by adjusting the polynomial (e.g., Zernike) coefficients associated with the central wavelength to target a certain level of rms wavefront error with given aberration constituents. This forms the basis for a phase profile at the central wavelength that can subsequently be scaled to form phase error profiles at other wavelengths. As a consequence, the phase profiles at alternative wavelengths exhibit similar overall form but are scaled spatially and in amplitude to accommodate the desired spectral physics. The principal difference between the monochromatic and integrated signal predictions is that the single wavelength results tend to accentuate the effect of spectral structure in the transfer function

while the integrated band simulations exhibit a natural spectral-weighting effect. In both cases, however, the optical phase errors demonstrate the appropriate variance (amplitude and region of support) due to wavelength considerations.

(a) Two-Dimensional Distribution　　　　(b) Three-Dimensional Surface
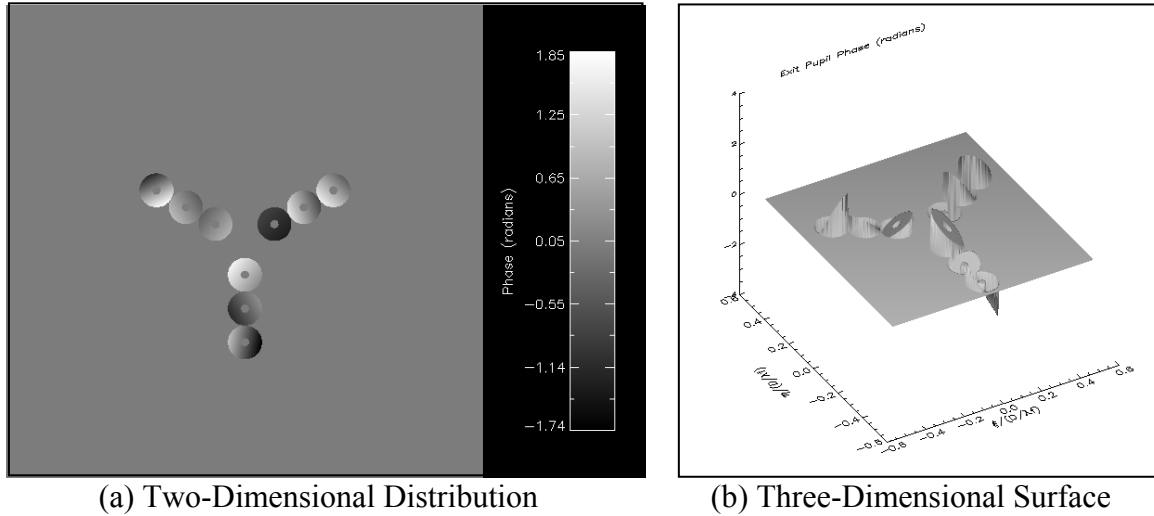
Figure 66: Random phase profile for the central wavelength of an aberrated tri-arm sparse aperture (0.10 waves rms piston, tip/tilt error).

Based on this phase profile, the aperture transfer function derived from the autocorrelation of the exit pupil manifests the character observed in Figure 67(a). From this diagram, it is apparent that even 0.10 waves rms of wavefront error is noticeably destructive to the modulation transfer function, as the modulation has been reduced to the point of introducing nulls at certain spatial frequencies. The implications of this transfer function on the imaged scene can be witnessed through comparison of Figure 67(b) and (c), which contain the original object scene derived from the WASP imagery and the quasi-monochromatic simulation of the detected image at the three central wavelengths associated with the original WASP sensor spectral bands, respectively. Finally, Figure 67(d) displays the Wiener filter restoration of the individual monochromatic detected image planes in an RGB color composite image. In order to "simulate" the effect of restoration filter mis-boost due to the spectrally dependent modulation mismatch described in the previous section for a broadband detection scenario, a single Wiener filter implementation was applied to each individual monochromatic simulation. In other words, the exact same Wiener filter gains were utilized for each quasi-monochromatic restoration. To some degree, this is precisely what occurs to

186

each "spectral line" when a broadband detected signal is boosted by a selected restoration filter. The signal spectrum associated with individual wavelengths experiences a boost that inevitably will be mismatched from the optimal gains, as only a single filter realization can be applied to the integrated broadband signal.

(a) Aberrated MTF

(b) Original Object

(c) Detected RGB Image

(d) Restored RGB Image
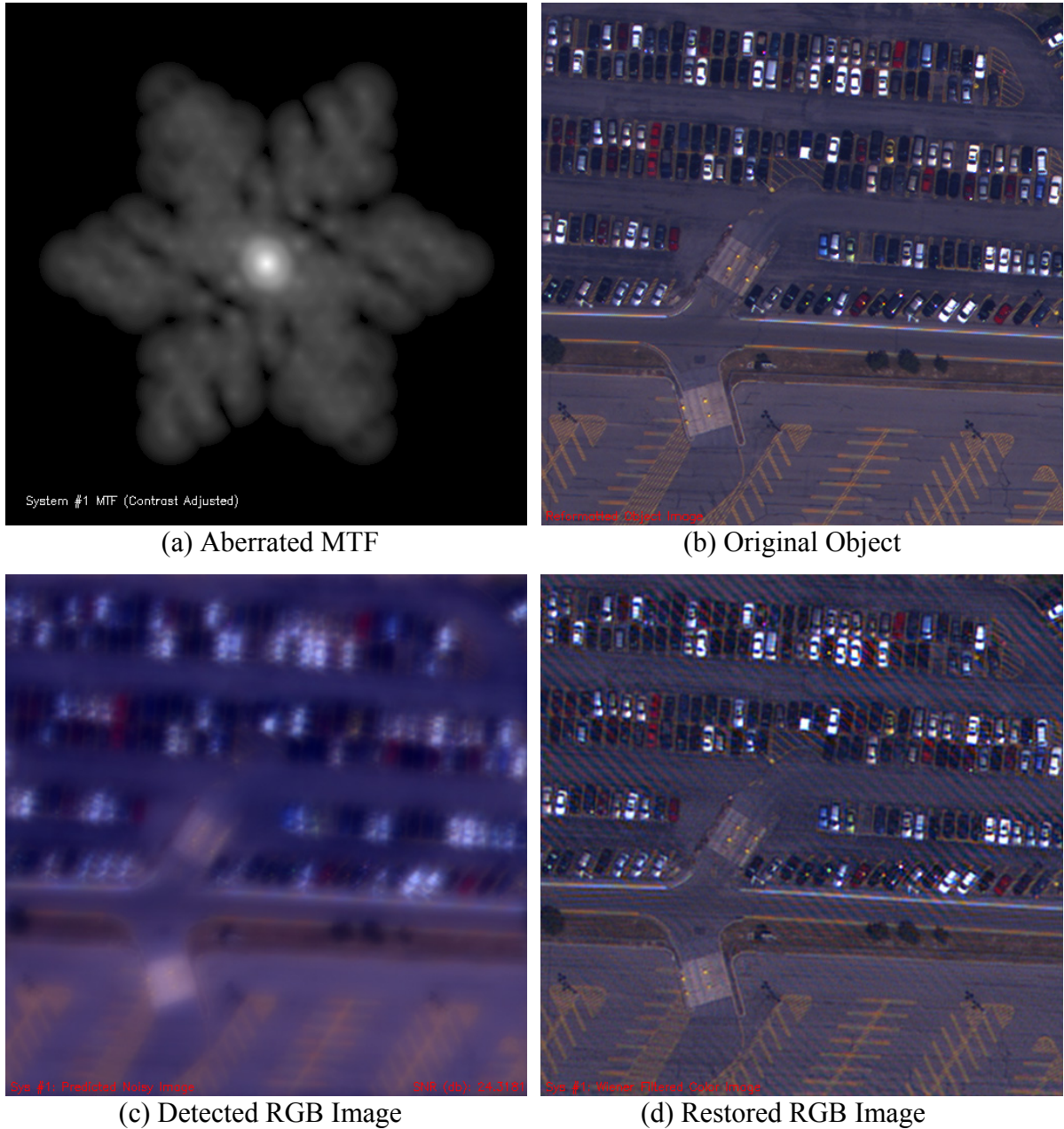
Figure 67: Quasi-monochromatic simulation of an aberrated tri-arm sparse aperture with central wavelength OTF restoration (0.10 waves rms piston, tip/tilt error).

In this particular exercise, the optical transfer function associated with the central wavelength was actually utilized to develop the required Wiener filter. In addition, the exact system transfer function responsible for the original degradation in the detected imagery was also used to derive the Wiener filter. Accordingly, one is essentially assuming in this example that the in-situ phase errors are precisely known at the central wavelength during the collection, so they may be utilized to construct the "perfect" transfer function for use in the applied post-detection reconstruction filter. Of course, this constitutes a reasonably significant assumption and future investigation on phase knowledge sensitivity will clearly illustrate that any lack of knowledge of the OPD errors that exist in sparse aperture systems rapidly leads to unacceptable image quality (see Section 5.6.3). Therefore, it is essential that techniques are explored to ensure highly accurate measurements of the phase errors present during a collection can be acquired for use in post-processing.

With the restoration assumptions stated above, one can clearly identify regions in Figure 67(d) where the mis-boost of spectral content leads to prominent red and blue color artifacts in the restored RGB image (recall that the green plane experiences near-optimal restoration through the central wavelength OTF). This occurs in the quasi-monochromatic imagery predictions for what is generally considered a benign level of 0.10 waves rms of wavefront error. Of course, these monochromatic simulations are likely to represent the extreme level of the anticipated spectral artifacts, as the integration process that occurs in real-world sensors tends to average out individual effects at given wavelengths. Despite this detection averaging phenomenon, there is clearly a spectral effect that is induced by the unique character of the sparse aperture system OTF which will ultimately be captured in the broadband signal. The question remains as to what level the induced spectral effect actually manifests itself in the panchromatic imagery. This will be explored in further detail through the integrated panchromatic signal results summarized in Section 5.3.

Based on Figure 65, one may conjecture that use of a spectrally averaged transfer function in the Wiener filter construction may ultimately produce superior restorations, as on the average the magnitude of the modulation mismatch between various spectra tends to be greatly reduced relative to that which occurs through selection of a single monochromatic OTF for

188

the restoration filter. In other words, use of the spectrally weighted OTF in the restoration filter tends to average out the relative mismatch across all wavelengths in the detection passband, while the monochromatic OTF precisely captures one wavelength and demonstrates the full modulation mismatch with all other colors. To explore this possibility, the quasi-monochromatic restoration process was accomplished again through use of a spectrally weighted OTF in the Wiener filter, enabling the comparison between the two approaches that appears in Figure 68. This side-by-side comparison would seem on the surface to confirm that the conjecture was correct for this particular case, as the spectrally averaged OTF resulted in a monochromatic restoration in Figure 68(b) that exhibits far fewer artifacts than the central-wavelength OTF restoration displayed in Figure 68(a). It should be noted, however, that this comparison only represents a single case and the observed rippling artifact due to spectrally variant modulation mismatch is still apparent in the imagery.

(a) Central OTF Restoration   (b) Weighted OTF Restoration

Figure 68: Comparison of two different restorations of quasi-monochromatic imagery products for an aberrated tri-arm sparse aperture (0.10 waves rms piston, tip/tilt error).

To investigate the effect of alternative levels of aberration, numerous model iterations were performed at different rms wavefront errors. Figure 69 displays a representative random phase profile for the nominal tri-arm system with 0.20 waves rms of piston, tip/tilt error. Relative to the previous example, one will observe that the amplitude of the phase errors is

considerably higher (greater than π in some circumstances) for this level of wavefront error. Given these phase errors, one acquires the aperture MTF displayed in Figure 70(a) through the autocorrelation of the complex pupil function. As seen in the previous section, the modulation has been significantly reduced at this rms wavefront error, ultimately giving rise to more zeroes in the spatial frequency coverage of the transfer function. Clearly, this reduction in modulation leads to significantly degraded imagery at the focal plane, as evidenced by the monochromatic color composite in Figure 70(c). As before, the central wavelength OTF was utilized in the Wiener filter to simulate the restoration process across a broad detection band. For this wavefront error case (0.20 waves rms), Figure 70(d) shows that the quasi-monochromatic restoration again results in the generation of deleterious image structure or artifacts, but on a much more significant level. Clearly, the modulation mismatch between the various spectra is considerably amplified by the selected Wiener filter design at this level of aberration. For comparison, the original object scene is included in Figure 70(b), from which one acquires a sense for the potential loss in interpretability due to this spectrally induced effect.

(a) Two-Dimensional Distribution   (b) Three-Dimensional Surface

Figure 69: Random phase profile for the central wavelength of an aberrated
tri-arm sparse aperture (0.20 waves rms piston, tip/tilt error).

(a) Aberrated MTF

(b) Original Object

(c) Detected RGB Image

(d) Restored RGB Image

Figure 70: Quasi-monochromatic simulation of an aberrated tri-arm sparse aperture with central wavelength OTF restoration (0.20 waves rms piston, tip/tilt error).

As with the previous example, the Wiener restoration was performed a second time with a filter design that included a spectrally averaged system transfer function. The result of this spectrally averaged OTF restoration process appears in Figure 71(b), which is compared to the original central wavelength OTF restoration in Figure 71(a). Unlike the preceding 0.10 waves rms wavefront error case, this particular example appears to suggest that the spectrally

averaged OTF actually generates more objectionable artifacting than its counterpart. Obviously, the spatial frequency content of the original scene is of such a nature that this particular weighted OTF realization actually amplifies the modulation mismatch in the restoration filter to a greater degree than the central wavelength OTF. Numerous other iterations with the quasi-monochromatic simulation seemed to indicate there was a fair amount of variability in the results, depending on the overall character of the system transfer function. Accordingly, it is unclear on the basis of the monochromatic analysis alone which filter type tends to be more optimal from the standpoint of minimizing the spectrally variant modulation mismatch. That notwithstanding, however, it is reasonably clear from Figure 71 that once aberrations reach levels on the order of 0.20 waves rms error, significant artifacting arises to a degree that will inevitably manifest itself in the integrated signal content, regardless of the restoration filter design applied.

(a) Central OTF Restoration   (b) Weighted OTF Restoration
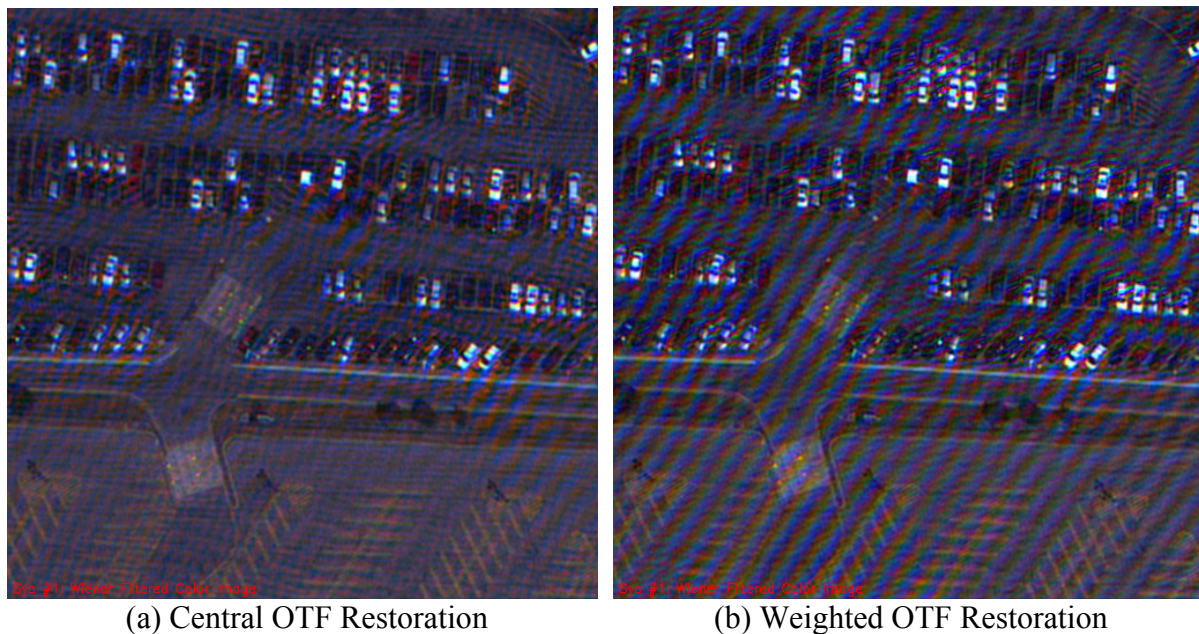
Figure 71: Comparison of two different restorations of quasi-monochromatic imagery products for an aberrated tri-arm sparse aperture (0.20 waves rms piston, tip/tilt error).

As a final example of the quasi-monochromatic simulations performed for sparse aperture systems, a quarter-wave (i.e., 0.25 waves rms) error was induced on the tri-arm system configuration explored in the previous results. A typical random phase profile for 0.25 waves rms of piston, tip/tilt error is displayed in Figure 72, which intuitively shows a phase

distribution with higher amplitude and greater variability than its predecessors. This phase profile subsequently results in the amplitude MTF depicted in Figure 73(a). In this diagram, one observes once again the reduced modulation and increased nulling that have been described previously for the moderately aberrated quarter-wave case. As expected, this degraded transfer function character results in a detected image in Figure 73(c) that has significantly less sharpness than the preceding scenarios. Naturally, the loss of spatial frequency content due to the amplitude of the wavefront errors ultimately leads to a degraded restoration as well. This can be observed in the central OTF Wiener restoration depicted in Figure 73(d), which also displays significantly more artifacting due to the modulation mismatch phenomenon discussed previously. At 0.25 waves rms of wavefront error, the nature of the modulation mismatch across the various wavelengths in the detection passband is of a magnitude that dramatically impacts the interpretability of the image. This becomes readily apparent when one compares the restored sparse aperture image with the original polychromatic object in Figure 73(b). One should again be reminded that these monochromatic simulations tend to accentuate the nature of the observed effect, as the averaging process involved in signal detection will partially mitigate some of its character. Despite that fact, it is reasonably clear that the spectrally induced artifacts in Figure 73(d) are of such a magnitude that they will appear in the integrated panchromatic signal as well.

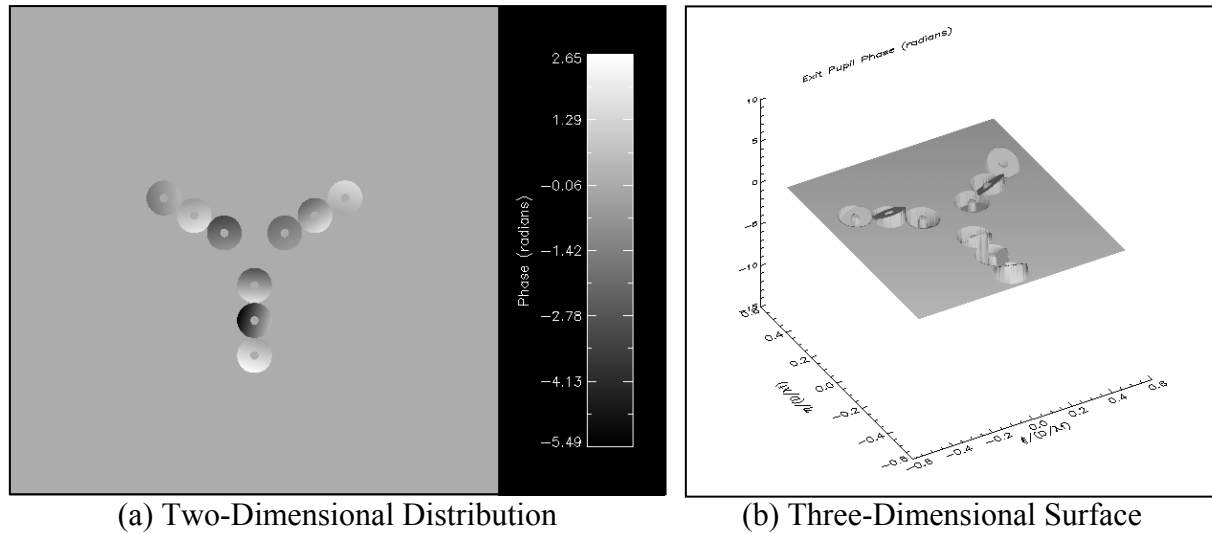| (a) Two-Dimensional Distribution | (b) Three-Dimensional Surface |
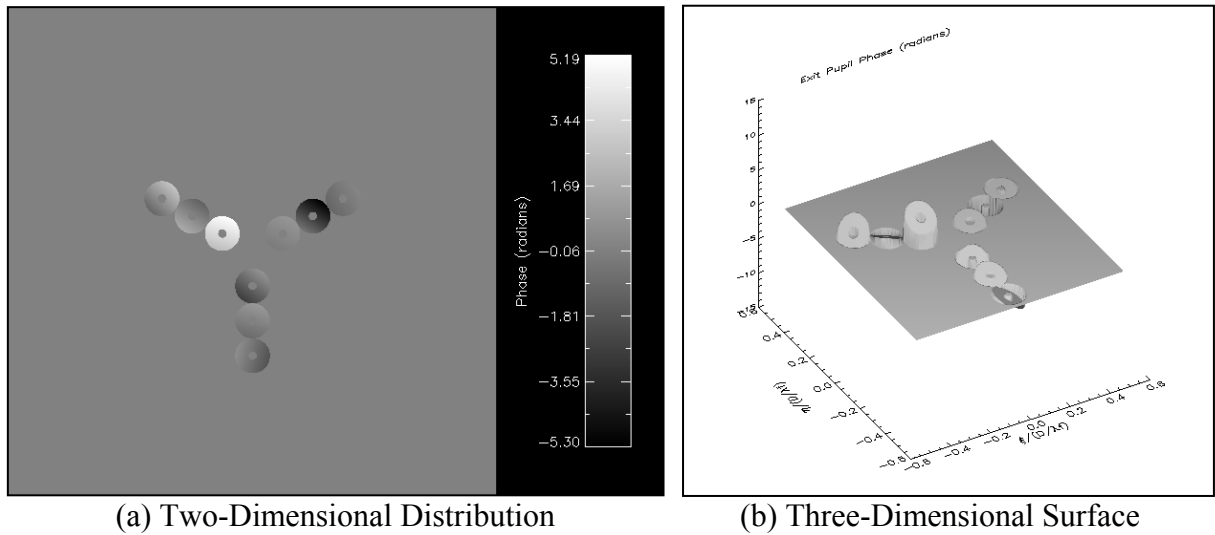
Figure 72: Random phase profile for the central wavelength of an aberrated
tri-arm sparse aperture (0.25 waves rms piston, tip/tilt error).
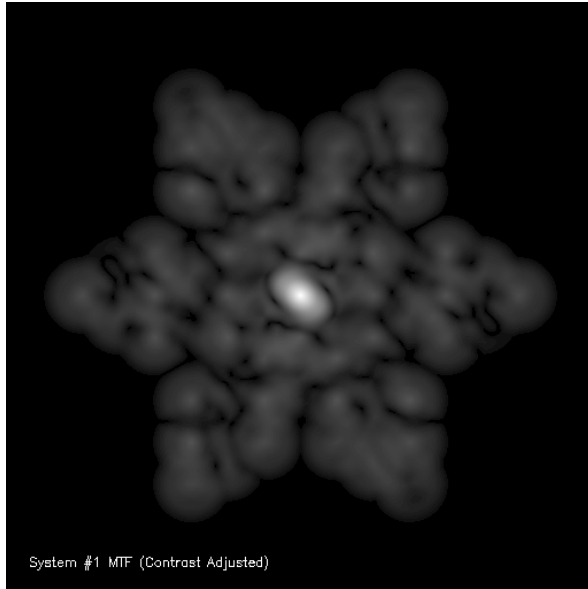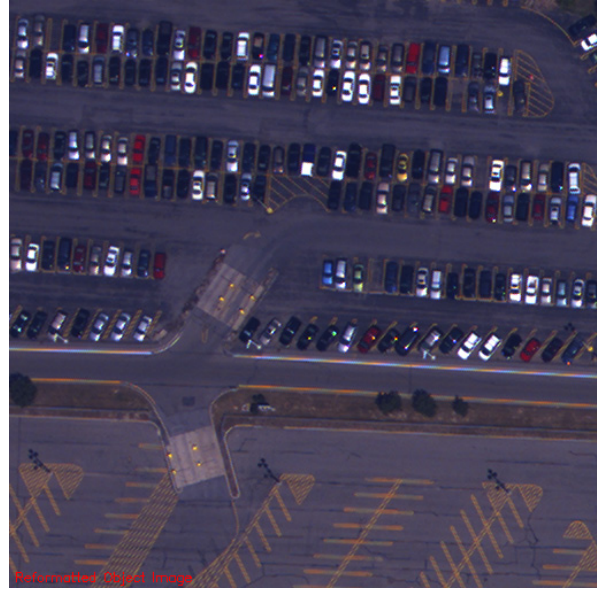
(a) Aberrated MTF

(b) Original Object

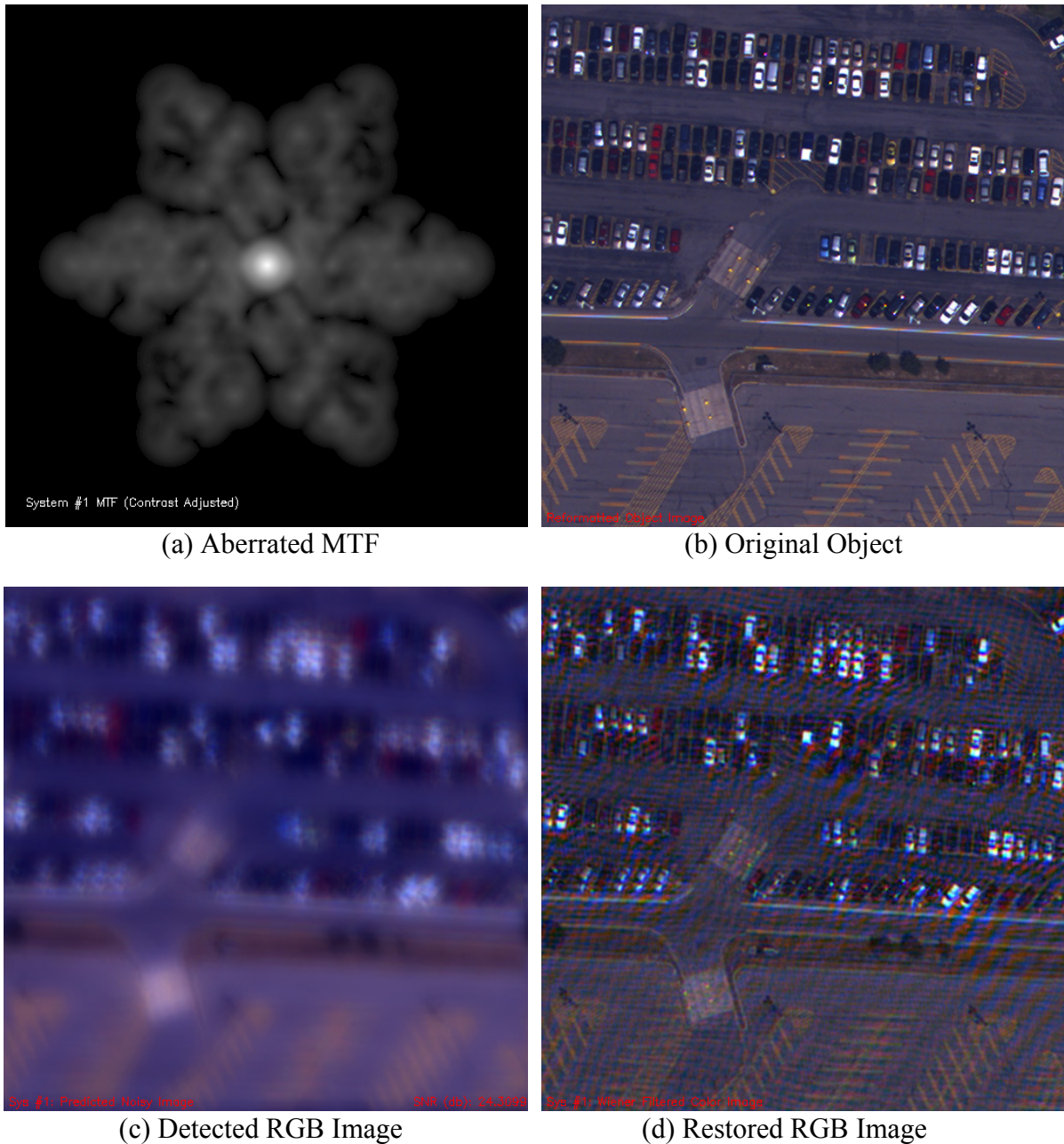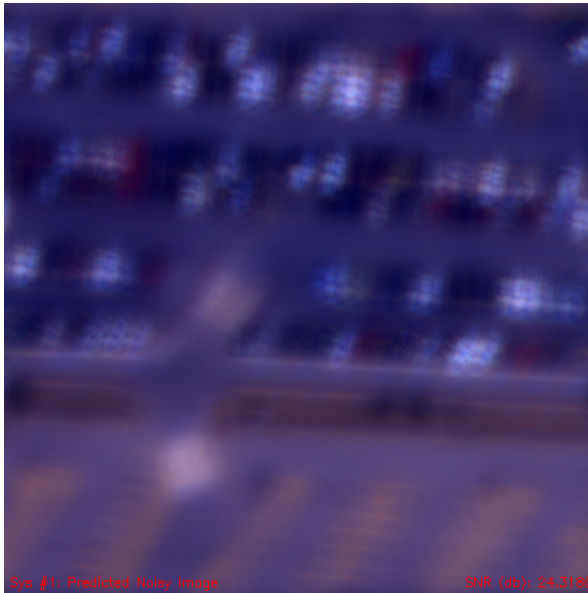(c) Detected RGB Image
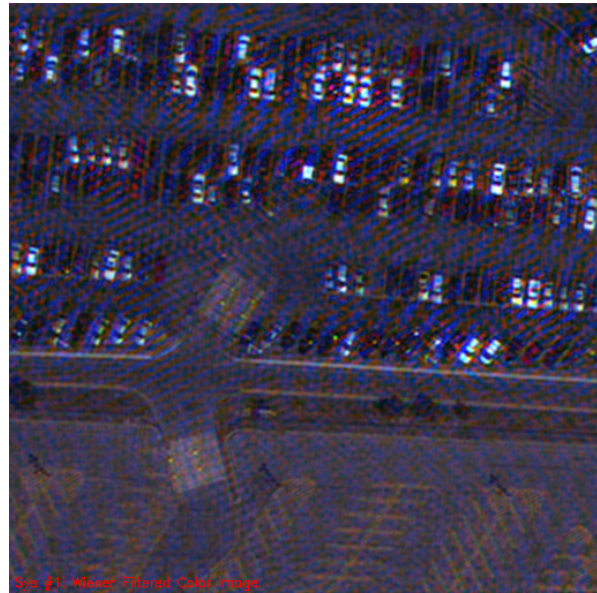
(d) Restored RGB Image

Figure 73: Quasi-monochromatic simulation of an aberrated tri-arm sparse aperture with central wavelength OTF restoration (0.25 waves rms piston, tip/tilt error).

As with previous monochromatic exercises, the initial Weiner restoration which appears in Figure 73 utilized the central wavelength system OTF in the filter design. Once again, a single restoration filter was applied to each monochromatic image to simulate a broadband application. To test the theory that an averaged OTF may marginalize the modulation mismatch that stimulates artifacting, the spectrally weighted transfer function was also

194

included in a subsequent restoration of the sparse aperture imagery. For this particular monochromatic wavefront error case, all the attempted Wiener filter restoration designs induced a considerable amount of spectral artifacts. This observation can be confirmed by comparing Figure 74(a), which contains the restoration achieved with the central wavelength OTF, with Figure 74(b), which displays the result from the spectrally weighted OTF. Clearly, both quasi-monochromatic restoration products entail significant artifacting on levels that dramatically impact overall image quality.

<div align="center">(a) Central OTF Restoration   (b) Weighted OTF Restoration</div>
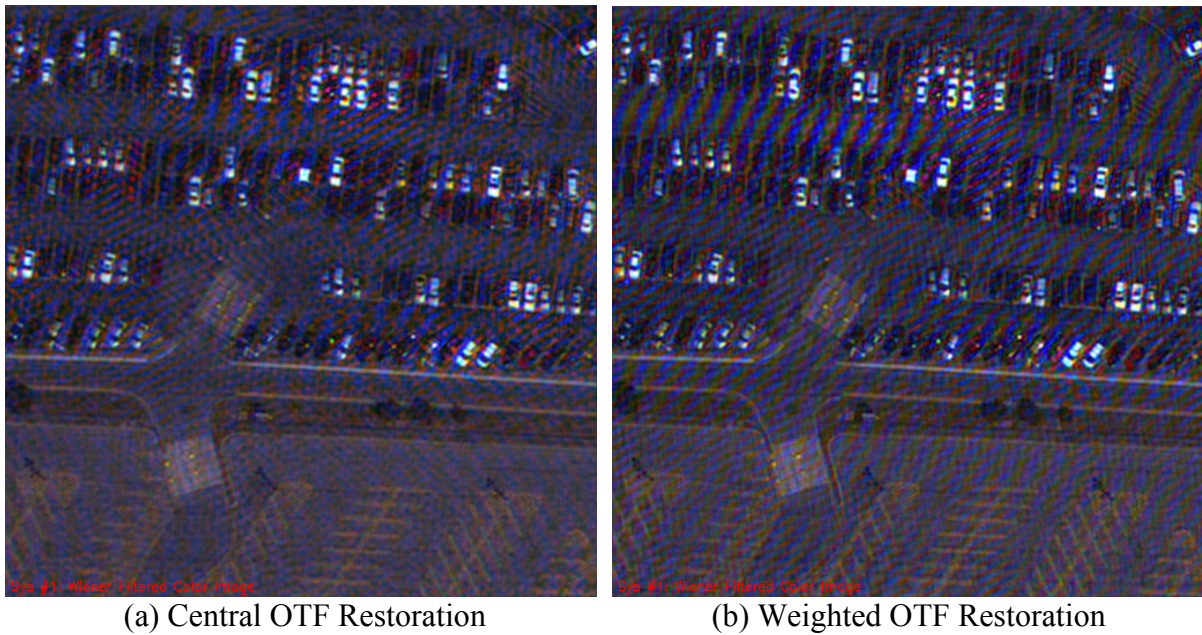
Figure 74: Comparison of two different restorations of quasi-monochromatic imagery products for an aberrated tri-arm sparse aperture (0.25 waves rms piston, tip/tilt error).

To gain a better appreciation of the nature of the spectral artifacts induced by the modulation mismatch identified in the previous section, one should compare the series of images in Figure 75. Within this figure, a small image chip has been removed from the previous monochromatic restorations and magnified to a level where individual automobile features can be ascertained. All of the original rms wavefront error cases are represented in the figure, along with the original object for comparison. As observed in the figure, the incidence of the spectrally induced quality effect described previously appears to occur for wavefront errors as low as 0.10 waves rms for the monochromatic simulation case. It remains to be seen if the averaging effect of real-world sensors over the detection passband

will largely mitigate the artifacts observed at that level. In any event, it should be noted that at least the constituent signal content at discrete wavelengths will manifest some structured character due to the modulation mismatch. Obviously, as the rms wavefront error increases in magnitude, the nature of the spectral artifacting becomes more deleterious. Eventually, the spectral artifacts reach a point where information content is effectively destroyed, which appears to be somewhere between 0.20 and 0.25 waves rms for the monochromatic case.

| (a) Original Object | (b) 0.10 waves rms piston, tip/tilt error |

| (c) 0.20 waves rms piston, tip/tilt error | (d) 0.25 waves rms piston, tip/tilt error |
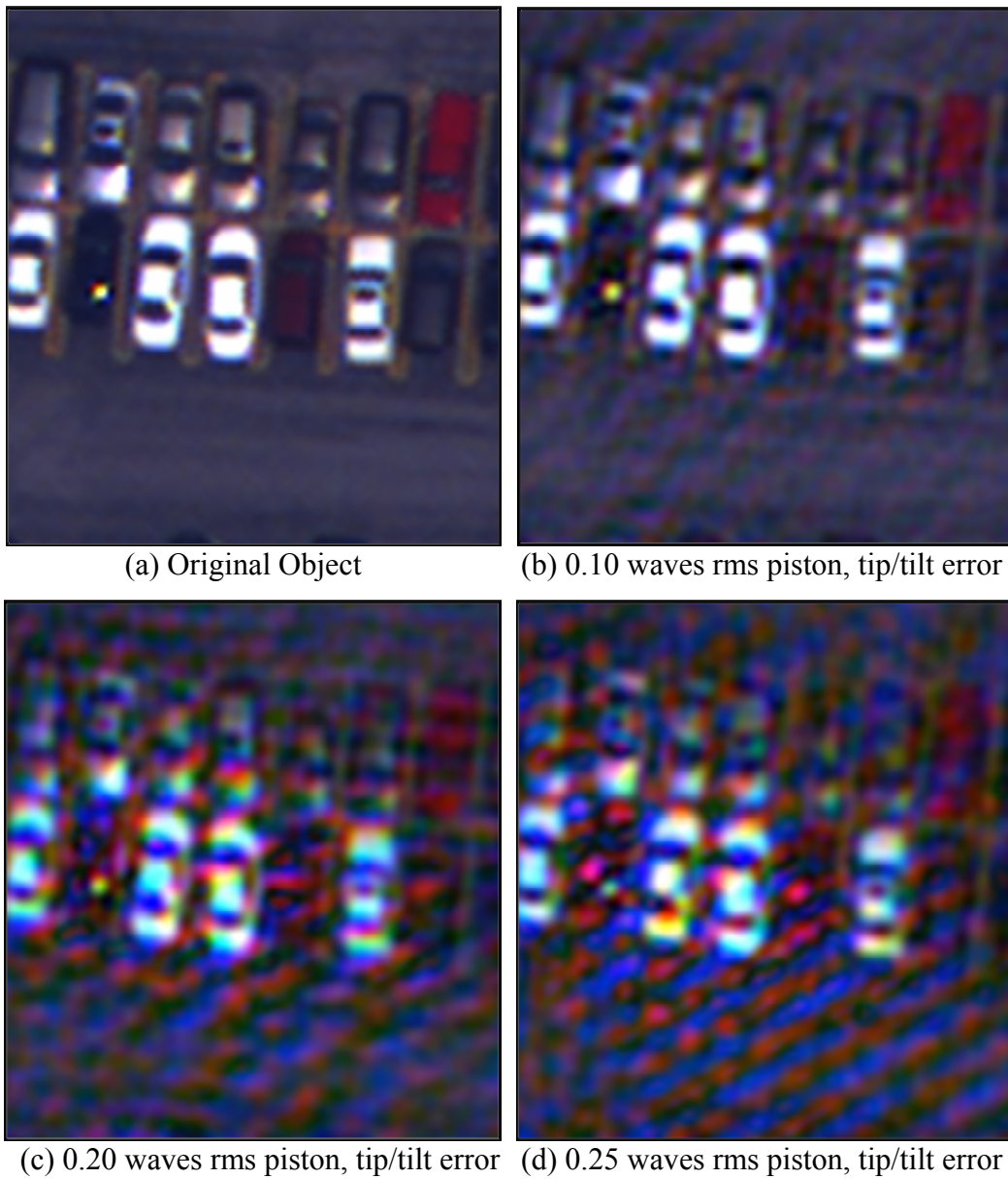
Figure 75: Quasi-monochromatic simulation of an aberrated tri-arm sparse aperture with central wavelength OTF restoration (magnified region of previous images).

To ensure that the spectrally induced quality effects observed in the previous examples for an aberrated sparse aperture system were not the result of the digital model implementation, a similar exercise was performed for an aberrated filled circular aperture. Based on the character of the transfer function, one would not anticipate the kind of quality implications with the filled aperture that surfaced with its sparse aperture counterpart. In addition, plenty of actual imagery data is available from real-world sensors to indicate that such spectral artifacting is not a typical feature of the collection obtained from conventional imaging systems. Once again, this contention is based strictly from an inherent optical configuration perspective, ignoring the effects of interpolation artifacts due to the potential use of a color filter array. Obviously, with the latter implementation to collect spectral data, most of the optical systems under consideration would exhibit various degrees of artifacting, a phenomenon not specifically addressed by this research effort as a unique sparse aperture issue. In light of this discussion, one should expect that the physics-based model developed for this research effort provides an adequate enough representation of the imaging process that any observed effects are not manufactured by the digital implementation. To demonstrate that fact, a large defocus error (0.20 waves rms) was applied to a filled circular aperture to determine whether the spectrally induced effect could be generated for conventional apertures in the quasi-monochromatic case. Figure 76 displays the nature of the quadratic phase error that leads to 0.20 waves rms of defocus. As observed in the figure, this constitutes a fairly severe level of aberration for the filled circular aperture.

(a) Two-Dimensional Distribution   (b) Three-Dimensional Surface
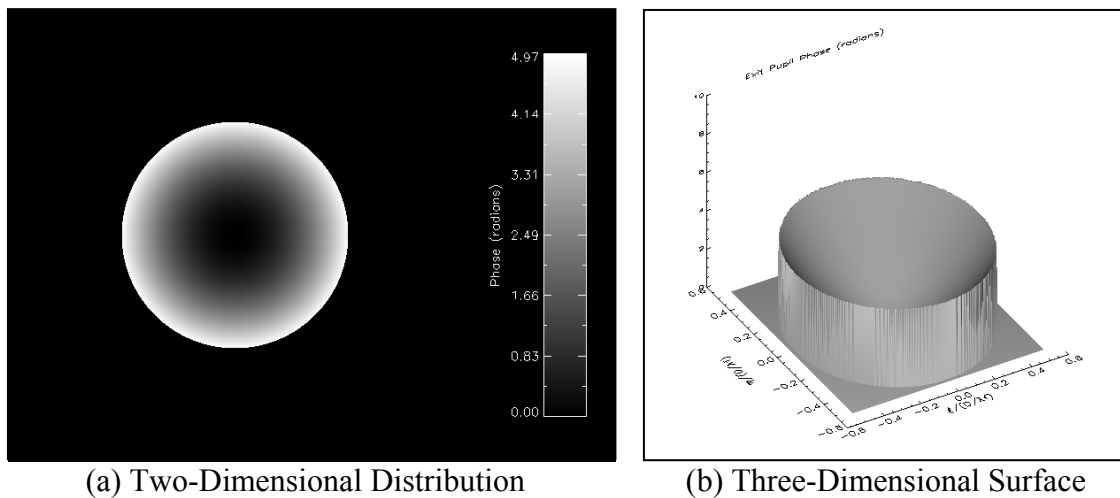
Figure 76: Phase profile for the central wavelength of an aberrated
filled circular aperture (0.20 waves rms defocus).

197
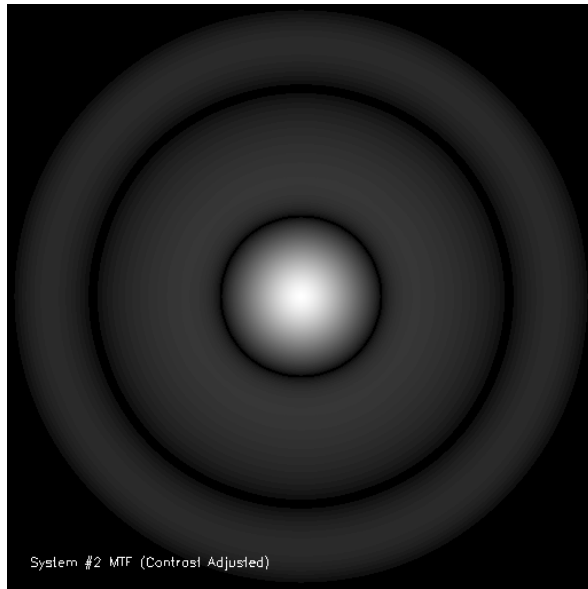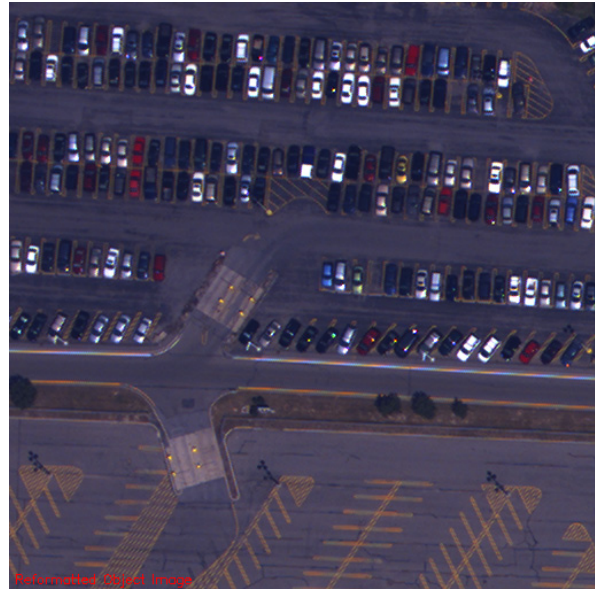
(a) Aberrated MTF

(b) Original Object
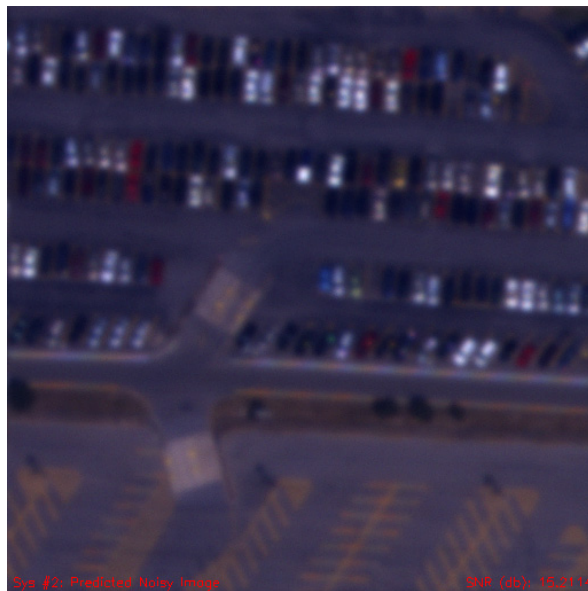
(c) Detected RGB Image
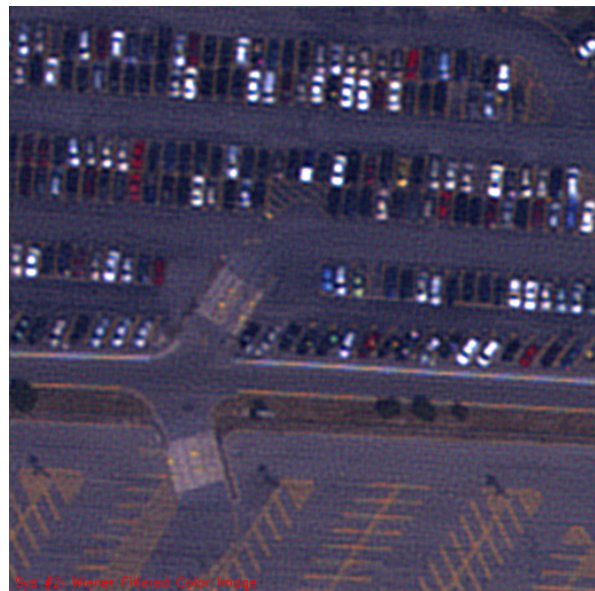
(d) Restored RGB Image

Figure 77: Quasi-monochromatic simulation of an aberrated filled circular aperture with central wavelength OTF restoration (0.20 waves rms defocus).

Based on the phase profile identified in Figure 76, the filled circular aperture exhibits an aperture MTF as depicted in Figure 77(a). From this diagram, it is apparent that the filled transfer function has undergone a considerable amount of demodulation due to the system defocus, ultimately leading to the introduction of several null regions in its spatial frequency coverage. The degraded nature of this defocused aperture MTF subsequently results in a

seriously blurred image at the focal plane, as observed in Figure 77(c). As hoped for in this exercise, the detected image is modulated to a level that is comparable with the degraded image predictions for the sparse aperture case. When an appropriate Wiener filter is applied to the detected image, the restored product in Figure 77(d) exhibits none of the spectral artifacting observed in the previous sparse aperture examples. There is certainly a fair amount of color noise amplification and correlation due to the application of the restoration filter, but there is no image structure or rippling effect from scene edges that was so readily apparent in the sparse aperture case entailing 0.20 waves rms of wavefront error. This result is entirely consistent with the theoretical discussion provided in the previous section on transfer function character and is certainly borne out in real-world imagery data. Therefore, one should have some confidence that the quality effect observed with sparse aperture systems in this quasi-monochromatic analysis is likely a physically viable effect and not a digital artifact of the proof-of-concept model. Obviously, the next essential step is to evaluate the character of the integrated signal to determine if the artifacts observed in the monochromatic cases are still present following the averaging effect of a broadband sensor.

5.3 Integrated Panchromatic Simulation

This section addresses the results acquired from the proof-of-concept model for the nominal broadband panchromatic detection scenario introduced in Chapter 4. Once again, the runs involve the WASP-derived polychromatic object scene containing the parked automobiles explored in the previous section. In fact, for comparative purposes, the first series of simulations following the restoration filter design discussion contain integrated, broadband simulations of the same scenarios that were depicted in the quasi-monochromatic analysis presented above. As before, a random piston, tip/tilt phase error profile that varied with wavelength was derived for the nominal tri-arm sparse aperture system configuration introduced in the previous section. For the comparative runs, these phase distributions were identical to those displayed in Section 5.2. In subsequent model iterations provided later in this section, alternative phase profiles were explored to demonstrate the variability in quality that can be achieved for a given rms wavefront error value. From this discussion, it will become apparent that specifying rms wavefront error is not necessarily a clear indicator of derived image quality.

Based on the quasi-monochromatic results, it was somewhat ambiguous whether the optical transfer function associated with the central wavelength provided better or worse restoration capability compared to a spectrally averaged realization. Obviously, the key to this general question lies in its ability to restore the broadband signal, so a quick sensitivity study was performed to explore differences between the two options. Within this trade study, the noise-to-object power spectrum ratio within the Wiener filter was precisely known, eliminating it as a potential source of uncertainty between the two restoration options. In addition, all phase errors were assumed to be perfectly known in the construction of the individual restoration filters. Figures 78 and 79 provide several exemplar Wiener restorations of the two filter techniques for 0.10 and 0.25 waves rms of wavefront error, respectively. As discussed previously, these wavefront error metrics constitute rms values at the mean wavelength of the spectral passband. The diagrams in (a) provide examples of the restoration utilizing the central wavelength OTF, while those in (b) display reconstructions acquired through use of a spectrally averaged transfer function. The restorations contained in these figures are very representative of the general set acquired during this trade study.

Visually, it is obvious from looking at these figures that the spectrally averaged OTF results in superior image restorations. This observation is also borne out in the metric data as well, as the *nrmse* values reported under the figure captions indicate a demonstrable improvement for the spectrally averaged case over the central wavelength option, given similar values of relative edge response (RER) and rms noise gain (G_{rms}). Unlike the simulation results acquired through the monochromatic analyses, the vast majority of broadband simulation runs indicated better restoration was achievable when a spectrally averaged OTF was utilized to construct the Wiener filter. Accordingly, unless otherwise stated, the majority of the remaining restorations contained in this dissertation involve use of a spectrally averaged system OTF in the Wiener filter. It is also interesting to note that the spectrally weighted OTF filter implementation effectively mitigates most of the artifacting or ringing observed previously for the case of 0.10 waves rms of wavefront error but only marginally does so for the scenario involving 0.25 waves rms of error. The general nature and magnitude of these quality effects will be explored in greater detail in the discussion to follow.

(a) Central Wavelength OTF Restoration
nrmse: 0.1130; RER: 0.849; G_{rms}: 13.5

(b) Spectrally Weighted OTF Restoration
nrmse: 0.0742; RER: 0.842; G_{rms}: 17.3

Figure 78: Restored panchromatic images for an aberrated tri-arm sparse aperture with two different reconstructions (0.10 waves rms piston, tip/tilt error).

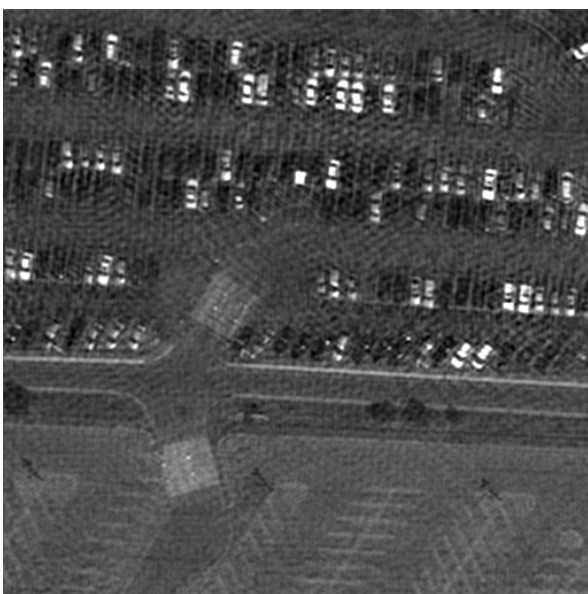
(a) Central Wavelength OTF Restoration
nrmse: 0.1532; RER: 0.804; G_{rms}: 18.2

(b) Spectrally Weighted OTF Restoration
nrmse: 0.1125; RER: 0.777; G_{rms}: 23.0

Figure 79: Restored panchromatic images for an aberrated tri-arm sparse aperture with two different reconstructions (0.25 waves rms piston, tip/tilt error).

201

With the spectrally averaged OTF utilized as a baseline within the Wiener filter restoration, figures 80 through 82 provide the broadband panchromatic simulations that parallel the quasi-monochromatic analyses for the tri-arm sparse aperture system explored in Section 5.2. These simulation products are followed by the broadband integrated signal prediction for the defocused filled circular aperture in Figure 83. Finally, diffraction-limited filled circular aperture simulation results appear in Figure 84 for the purposes of comparison. In all of these figures, (a) contains a spectrally weighted panchromatic-equivalent object image formed from the original polychromatic object scene through use of the scenario collection parameters. In (b), the figures display the integrated panchromatic signal that is predicted at the focal plane prior to any post-detection restoration. The restoration that is subsequently acquired through use of the spectrally averaged system OTF (assuming perfect phase knowledge) and the known noise-to-object power spectrum ratio in the Wiener filter appears in (c). Finally, the original result acquired from the quasi-monochromatic simulation with a spectrally averaged OTF restoration is shown in an RGB composite image in (d). This series of figures provides ample material for comparative analyses on the various physical attributes observed in the imagery for different system conditions.

In comparing the broadband panchromatic simulations with their monochromatic equivalents, one will note that the integrated signal tends to average out some of the spectrally induced ringing that was observed in Section 5.2. This was an entirely anticipated result based on the theoretical development discussed earlier. Despite the fact that some of the artifacting is mitigated, however, one cannot dispute that fundamental image structure due to the modulation mismatch phenomenon is still present in all of the sparse aperture system restorations. In fact, close examination of the restoration in Figure 80(c) relative to the original object in Figure 80(a) and the monochromatic results in Figure 80(d) indicates that some of the spectrally induced artifacts are present even at 0.10 waves rms of wavefront error. Obviously, once the wavefront error deteriorates to the level of 0.20 to 0.25 waves rms, the spectral artifacting reaches a level at which image interpretability is extensively impacted. This can be observed visually in the restored imagery as well as in the reduction of key quality metrics (e.g., *nrmse* and RER). The spectrally induced ringing seen in this series of imagery examples represents an image feature that has not been observed previously

202

with the more traditional gray-world model approximation. As will become clearer in the gray-world model comparisons in the next section, it is a direct reflection of modeling the spectral character of the optical phase, exit pupil, system transfer function and object scene that induces the artifacting in aberrated sparse aperture restorations. Therefore, it is apparent that enhanced spectral fidelity model can be essential for the evaluation of sparse aperture systems that experience some level of dephasing or aberration.

For comparison, figures 83 and 84 provide panchromatic imagery predictions for two different filled circular aperture systems, one that exhibits a wavefront error of 0.20 waves rms of defocus and one that is diffraction limited (i.e., unaberrated). These simulations are instructive in that they both do not manifest any of the unique artifacting or rippling that appears in the sparse aperture examples. This is consistent with what one encounters in the real world with conventional imaging systems and makes good physical sense based on the smoothly varying character of their system transfer functions. In essence, the degraded OTF associated with a filled circular aperture, even under conditions of severe defocus, does not support the type of sharp discontinuities that lead to modulation mismatch and subsequent mis-boost on the part of the restoration filter.

One will note that the defocused filled aperture produces imagery with significant noise amplification and correlation due to the application of the Wiener filter, ultimately resulting in worse overall image quality from a mean-square error perspective. However, one is reminded that the nature of the exercise performed here was to test under stressing conditions whether the conventional aperture system would "manufacture" artifacts that physically should not be present based on first principles. As a result, the filled system was severely aberrated to the point of introducing spatial-frequency zeroes in the transfer function, but the detector integration time was not increased to account for the loss in modulation. This resulted in a detection SNR that was significantly lower than that encountered with the sparse aperture cases (approximately 33 versus 270) and certainly not enough to offset the loss in modulation in the system OTF due to the induced wavefront errors. As a consequence, the standard noise amplification due to restoration was encountered in a significant way, an effect that could have been marginalized somewhat through improved collection SNR. The

bottom line, however, was that the defocused case did not produce spectrally induced artifacts, demonstrating such a feature to be a unique attribute of moderately aberrated sparse aperture systems.

(a) Spectrally Weighted Object   (b) Detected Panchromatic Image

(c) Restored Panchromatic Image   (d) Restored Monochromatic RGB Image

Restored Image *nrmse*: 0.0716; RER: 0.846; G_{rms}: 17.5; SNR: 270.6

Figure 80: Integrated panchromatic simulation of an aberrated tri-arm sparse aperture with spectrally weighted OTF restoration (0.10 waves rms piston, tip/tilt error).

(a) Spectrally Weighted Object

(b) Detected Panchromatic Image

(c) Restored Panchromatic Image

(d) Restored Monochromatic RGB Image

Restored Image *nrmse*: 0.1079; RER: 0.782; G_{rms}: 22.0; SNR: 269.6

Figure 81: Integrated panchromatic simulation of an aberrated tri-arm sparse aperture with spectrally weighted OTF restoration (0.20 waves rms piston, tip/tilt error).

(a) Spectrally Weighted Object

(b) Detected Panchromatic Image

(c) Restored Panchromatic Image

(d) Restored Monochromatic RGB Image

Restored Image *nrmse*: 0.1125; RER: 0.777; G_{rms}: 23.0; SNR: 270.5

Figure 82: Integrated panchromatic simulation of an aberrated tri-arm sparse aperture with spectrally weighted OTF restoration (0.25 waves rms piston, tip/tilt error).

(a) Spectrally Weighted Object

(b) Detected Panchromatic Image

(c) Restored Panchromatic Image
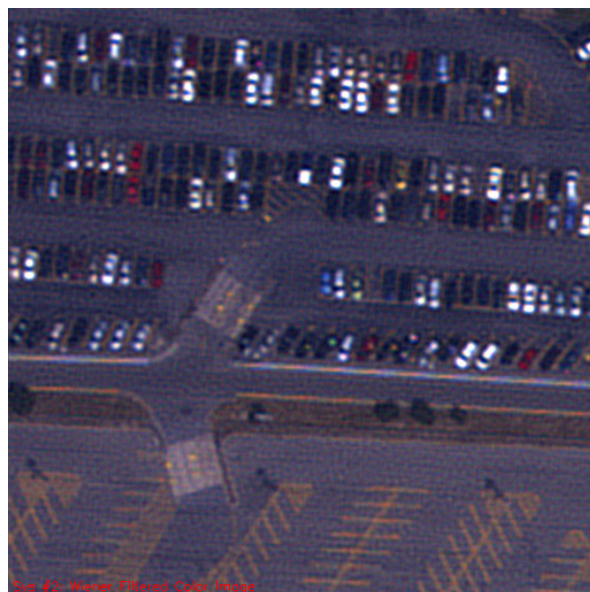
(d) Restored Monochromatic RGB Image

Restored Image *nrmse*: 0.1363; RER: 0.540; G_{rms}: 4.97; SNR: 33.2

Figure 83: Integrated panchromatic simulation of an aberrated filled circular aperture with spectrally weighted OTF restoration (0.20 waves rms defocus).
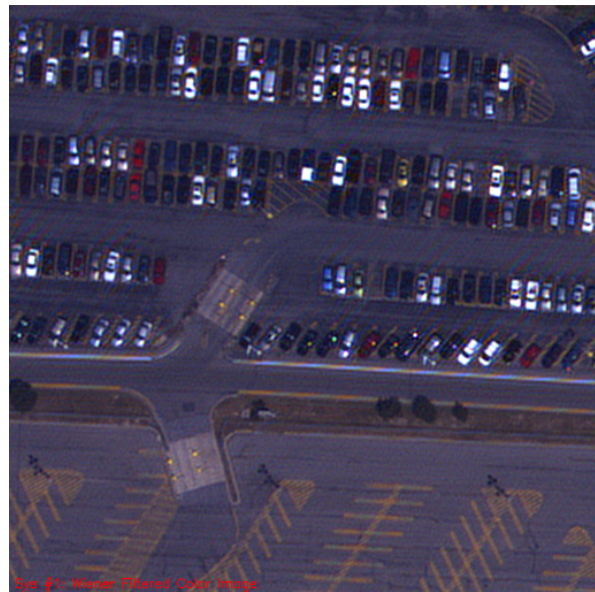
(a) Spectrally Weighted Object

(b) Detected Panchromatic Image

(c) Restored Panchromatic Image

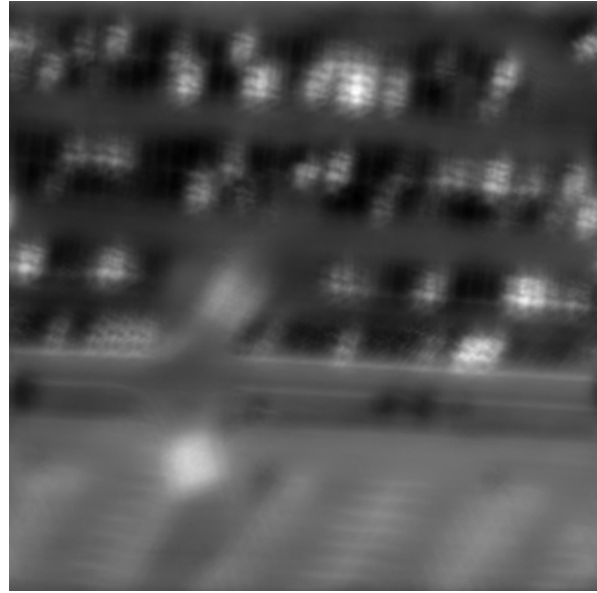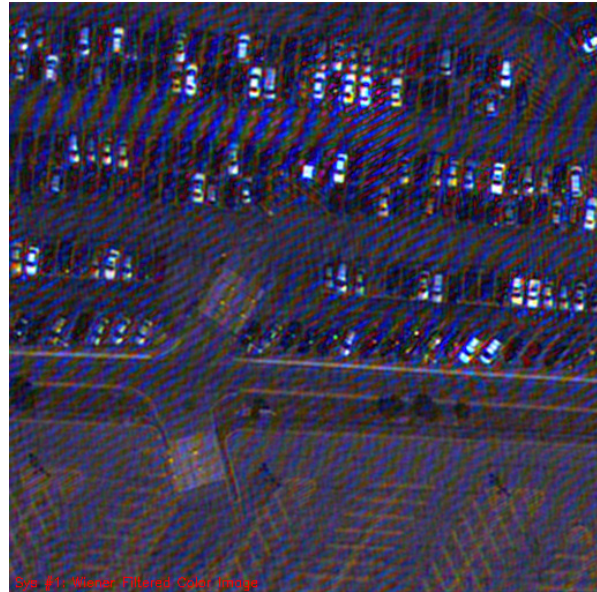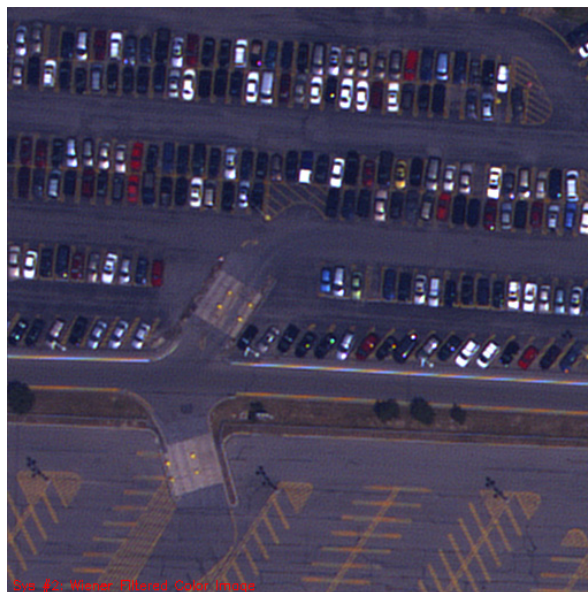(d) Restored Monochromatic RGB Image

Restored Image *nrmse*: 0.0606; RER: 0.926; G_{rms}: 1.99; SNR: 33.1

Figure 84: Integrated panchromatic simulation of a diffraction-limited filled circular aperture with spectrally weighted OTF restoration.

5.4 Polychromatic versus Gray-World Model

As indicated previously, one of the primary objectives of this research effort was to determine the utility of including spectral fidelity in the modeling of sparse aperture imaging systems. To help accomplish that objective, some additional modeling effort was pursued to implement the traditional gray-world approach into the overall simulation architecture. In addition, the original polychromatic object scenes investigated in this dissertation were converted to gray-scale equivalents through an appropriate spectral weighting scheme. These additions subsequently enabled side-by-side comparisons of the imagery products derived from the enhanced spectral model and those from the gray-world approximation. This section details results of various comparison iterations performed to address the value of the full-fledged polychromatic imaging model and ascertain that the previously introduced quality effect was truly the result of the enhanced fidelity spectral physics. To illustrate the nature of the results, several different object scenes exhibiting various spatial and spectral resolutions were selected. As a consequence, this section also provides numerous results to address other modeling issues as well as develop a composite view of the unique sparse aperture image quality issues identified in this research effort.

5.4.1 WASP-Based Object Description

In keeping with previous trends, the first scene to be addressed with the gray-world model will be the WASP-derived scene involving the parked automobiles. Once again, the applied restoration filter makes use of the spectrally averaged OTF (with perfect phase error knowledge) and the known noise-to-object power spectrum ratio. This provides a near-optimal restoration for understanding the "best-achievable" image quality that can potentially be derived under the explored imaging conditions. Obviously, one would anticipate that a reduction in knowledge of the precise imaging conditions will degrade the restored image quality from that presented here. Figure 85 provides a side-by-side comparison of the restored broadband panchromatic imagery from the two models acquired for the tri-arm sparse aperture system with 0.10 waves rms of wavefront error. Specifically, Figure 85(a) depicts the restored imagery acquired through use of the gray-world model and Figure 85(b) displays that produced with the enhanced spectral fidelity model. For this high SNR

scenario, it is apparent that the gray-world and polychromatic-world models produce relatively comparable imagery restorations at 0.10 waves rms of wavefront error.

(a) Gray-World Simulation
nrmse: 0.0676

(b) Polychromatic-World Simulation
nrmse: 0.0716
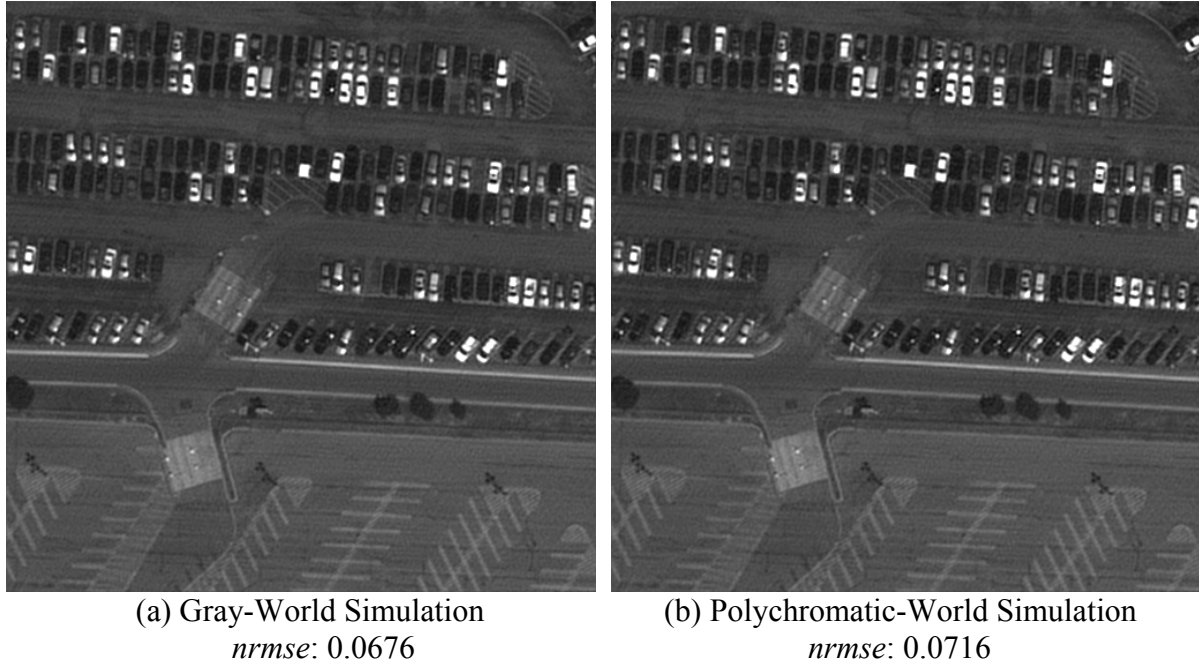
RER: 0.846; G_{rms}: 17.5; SNR: 270.6

Figure 85: Restored imagery comparison between the polychromatic and gray-world models for an aberrated tri-arm sparse aperture (0.10 waves rms piston, tip/tilt error).

There are some detectable differences between the results acquired from these models, which become apparent if one examines the products in softcopy and flickers back and forth between them. Figure 86 displays a magnified region of the two restorations to provide a closer look at differences in perceived small features. As suspected, the differences between the two are subtle but can certainly be detected in the softcopy (of course the hardcopy does not do them justice). For instance, the automobile on the far left side of the three-vehicle image chip seems to have artifacts in the enhanced spectral model restoration in Figure 86(b) that are not apparent in the equivalent gray-world model image in Figure 86(a). It is interesting to note that this particular vehicle is a maroon color in the original object scene, lending credence to the hypothesis that a spectrally induced modulation mismatch is responsible for the artifacting. Similar subtle image structure is visible in the softcopy for other scene content that exhibits some non-gray spectral information. Naturally, the small

variations discussed above result in a difference in the overall mean-level statistics, as evidenced by the 6% difference in *nrmse* computed for this particular case. Therefore, there is a minor quality effect that is just noticeable for sparse aperture systems that are aberrated to the degree studied in this example (0.10 waves rms of wavefront error), one that may be qualitatively insignificant depending on the application under investigation.
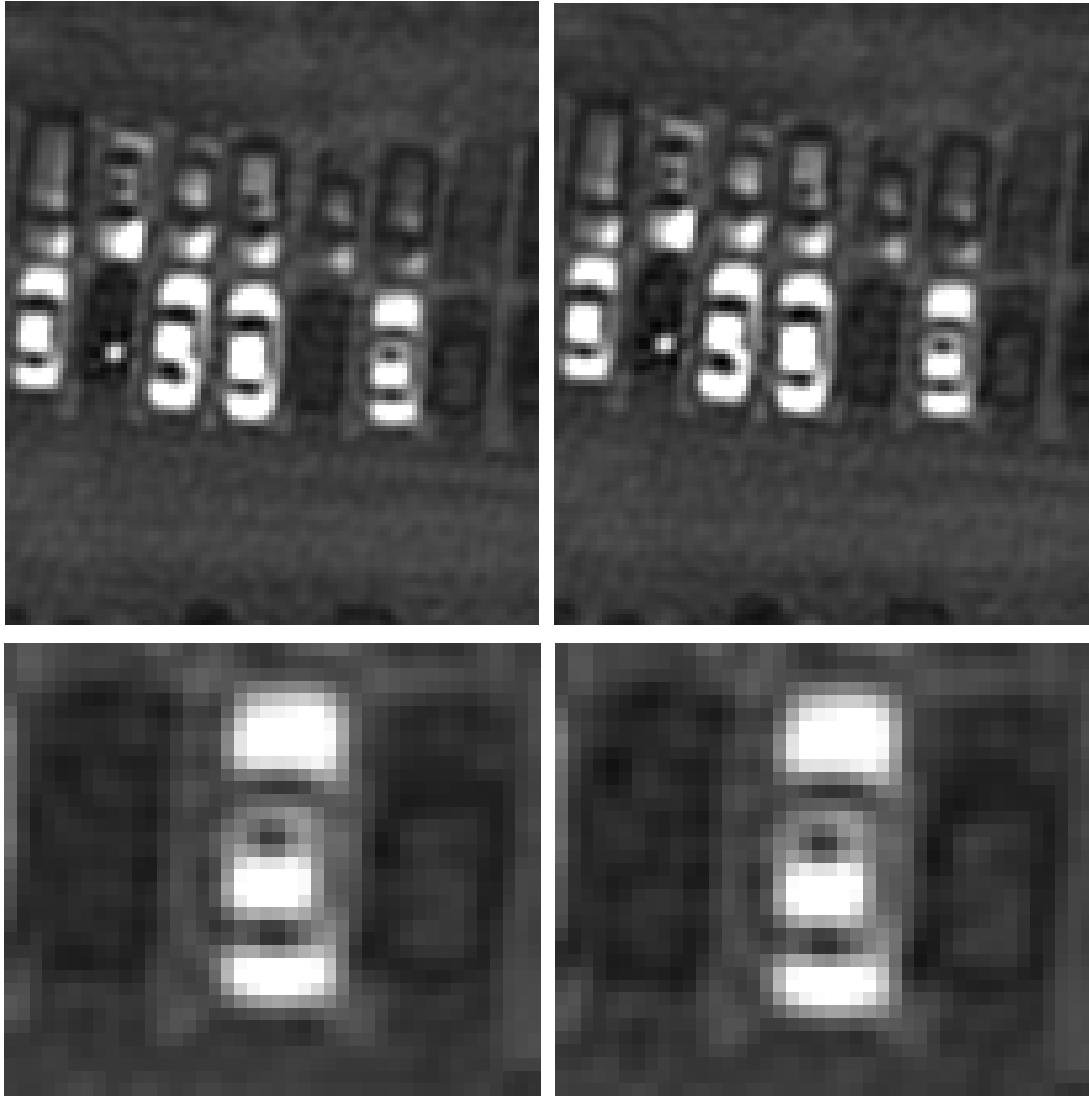
(a) Gray-World Simulation
nrmse: 0.0676

(b) Polychromatic-World Simulation
nrmse: 0.0716

Figure 86: (Magnified) Restored imagery comparison between the polychromatic and gray-world models for an aberrated tri-arm sparse aperture (0.10 waves rms piston, tip/tilt error).

Regardless of the implications of model selection, both simulation approaches appear to substantiate the contention that sparse aperture imaging systems with aberrations on the order of 0.10 waves rms of wavefront error or less have the potential to produce acceptable quality imagery, assuming similar collection conditions and phase knowledge. One is again reminded that this conclusion applies strictly for the broadband VNIR collection application under investigation given the rms wavefront error convention described in Section 4.6.1. Deviations away from collection knowledge assumptions have been cursorily explored in this effort and seem to imply there is some margin for error as real-world effects are included in the analysis. At this juncture, however, these expanded results are very anecdotal in nature and additional sensitivity trades are certainly warranted in the area. Another interesting observation can be made as a result of the restoration quality achieved with the sparse aperture system with 0.10 waves rms of piston, tip/tilt error at the mean wavelength of the spectral passband. Since this level of rms wavefront error typically correlates with a certain amount of frequency-domain nulling, this conclusion also seems to indicate that a certain level of nulls (or zeroes) in the spatial frequency plane may be tolerable.

To demonstrate that the results acquired in this original example were statistically representative of the image quality one should expect for an aberrated system with approximately 0.10 waves rms of wavefront error, a series of simulations were performed with comparable aberration levels. As before, both the gray-world model approximation and the enhanced spectral fidelity model were exercised in this investigation. Figures 87 through 90 provide some examples of the variation observed for the family of aberration cases run at 0.10 waves rms of wavefront error. In these figures, the gray-world model restorations appear in (a) and the polychromatic-world imagery are displayed in (b). Once again, just noticeable differences can be observed between the two model approaches when a flicker test is applied to the softcopy products. In general, the nature of the observed differences is subtle enough that one may choose to ignore them for this particular level of aberrations. From a statistical perspective, however, it would be difficult to refute that an effect is definitely present, as the *nrmse* data for this set of restoration examples exhibit a 6-9% difference between the two models. In all cases, the enhanced model demonstrates slightly worse image quality, highlighting the presence of the spectrally induced artifacting effect.

212

Clearly, moderately aberrated sparse aperture imaging systems manifest a unique spectral character that is not adequately captured in the traditional gray-world modeling approach.

(a) Gray-World Simulation
nrmse: 0.0678; RER: 0.848; G_{rms}: 17.1

(b) Polychromatic-World Simulation
nrmse: 0.0732; RER: 0.848; G_{rms}: 17.1

Figure 87: Iteration #1: Restored imagery comparison between the polychromatic and gray-world models for an aberrated tri-arm sparse aperture (0.101 waves rms piston, tip/tilt error).

(a) Gray-World Simulation
nrmse: 0.0671; RER: 0.853; G_{rms}: 17.4

(b) Polychromatic-World Simulation
nrmse: 0.0713; RER: 0.853; G_{rms}: 17.4

Figure 88: Iteration #2: Restored imagery comparison between the polychromatic and gray-world models for an aberrated tri-arm sparse aperture (0.105 waves rms piston, tip/tilt error).

(a) Gray-World Simulation
nrmse: 0.0702; RER: 0.842; G_{rms}: 17.8

(b) Polychromatic-World Simulation
nrmse: 0.0763; RER: 0.842; G_{rms}: 17.8

Figure 89: Iteration #3: Restored imagery comparison between the polychromatic and gray-world models for an aberrated tri-arm sparse aperture (0.107 waves rms piston, tip/tilt error).

(a) Gray-World Simulation
nrmse: 0.0683; RER: 0.844; G_{rms}: 19.3

(b) Polychromatic-World Simulation
nrmse: 0.0738; RER: 0.844; G_{rms}: 19.3

Figure 90: Iteration #4: Restored imagery comparison between the polychromatic and gray-world models for an aberrated tri-arm sparse aperture (0.109 waves rms piston, tip/tilt error).

To explore how the observed artifacting effect scales with aberration level, a series of simulations were performed with the tri-arm sparse aperture system under the influence of 0.25 waves rms of piston, tip/tilt error. One will recall that this level of aberrations induced a considerable amount of image structure in the integrated panchromatic restoration acquired through the enhanced spectral fidelity model. The restoration result acquired for the same tri-arm system through use of the equivalent gray-world modeling approximation appears in Figure 91(a). Comparison of that restoration with the original polychromatic-world model result in Figure 91(b) clearly shows that the observed artifacting is indeed the result of the enhanced spectral fidelity. As seen in the figure, the level of artifacting within the gray-world restoration is nowhere near commensurate with the deleterious level observed in the polychromatic-world case. In fact, the *nrmse* associated with the enhanced spectral fidelity model is ~33% greater than that observed with the gray-world model for this particular case. Obviously, failing to capture the spectral physics in the modeling process has a dramatic impact on the perceived image quality associated with this aberrated sparse aperture system.

(a) Gray-World Simulation   (b) Polychromatic-World Simulation
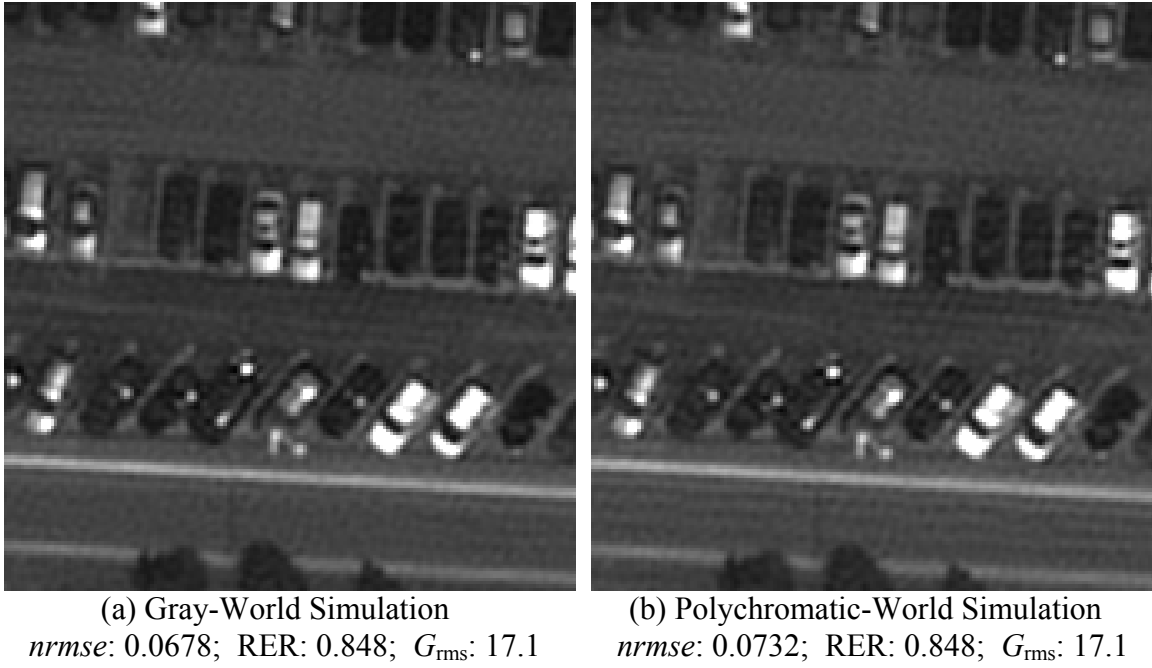*nrmse*: 0.0847   *nrmse*: 0.1125

RER: 0.777; G_{rms}: 23.0; SNR: 270.5

Figure 91: Restored imagery comparison between the polychromatic and gray-world models for an aberrated tri-arm sparse aperture (0.25 waves rms piston, tip/tilt error).
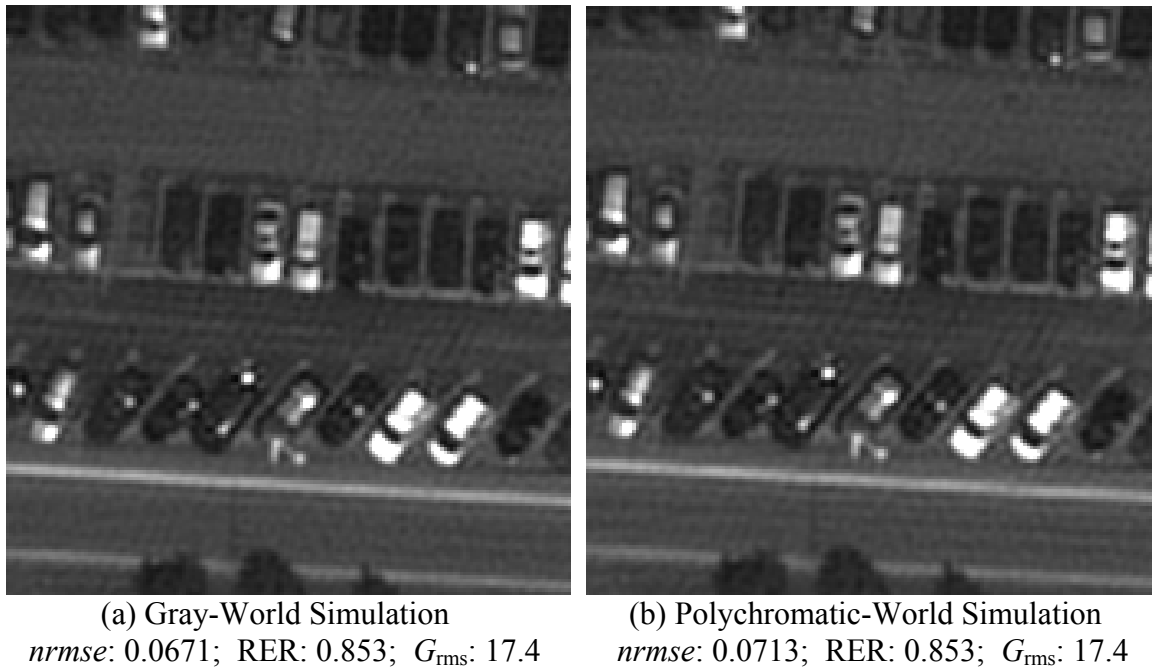
With perfect phase and noise-to-object power spectrum knowledge, the gray-world model predicts one can achieve fairly good image restoration, even under 0.25 waves rms of wavefront error. In fact, the *nrmse* associated with the gray-world model restoration is only ~18% greater than the polychromatic case involving 0.10 waves rms of phase error. By comparison, the enhanced spectral model restoration for quarter-wave aberrations exhibits an *nrmse* that is ~57% worse than the same model predicts for 0.10 waves rms of wavefront error. These differences clearly highlight the importance of including some of the enhanced spectral capability pursued in this research effort when modeling sparse aperture imaging systems with moderate-to-high optical aberrations and/or subaperture dephasing.

This observation is further confirmed through examination of the magnified regions of the two restorations appearing in Figure 92. For example, Figure 92(b) displays the destructive nature of the spectrally induced artifacts that appear in the polychromatic-world simulation. As observed in the final restoration product, the artifacting and ringing that occur in the enhanced spectral model result in considerable loss of information content. As a typical example of this phenomenon, the maroon-colored automobile highlighted previously on the far left side of the three-vehicle image chip has almost been completely obliterated by the artifacts. In contrast to the polychromatic model, the restoration acquired through the gray-world model in Figure 92(a) is relatively free of the type of artifacting observed in its counterpart. Obviously, one does see the standard correlated noise amplification and edge ringing that naturally occur as a result of the unique general character of the sparse aperture system OTF and its restoration through use of a conventional Wiener filter. Completely absent, however, from this restoration is the excessive artifacting and ringing that appear to be the direct result of spectrally variant modulation mismatch in the system transfer function captured in the enhanced system model. Accordingly, the gray-world model appears to break down for sparse aperture imaging systems with aberrations on the order of quarter-wave rms.

(a) Gray-World Simulation
nrmse: 0.0847

(b) Polychromatic-World Simulation
nrmse: 0.1125

Figure 92: (Magnified) Restored imagery comparison between the polychromatic and gray-world models for an aberrated tri-arm sparse aperture (0.25 waves rms piston, tip/tilt error).

As with the scenario entailing 0.10 waves rms of wavefront error, numerous iterations of the proof-of-concept model were performed to ensure these results were statistically representative of the restoration quality one should expect for 0.25 waves rms of wavefront error. Once again, both the gray-world and enhanced spectral fidelity models were investigated in this study. Figures 93 through 95 provide samples of the variation observed for the family of aberration cases run in this exercise (i.e., for 0.25 waves rms of wavefront error). Within these figures, the gray-world model restorations again appear in (a) and the

restored polychromatic-world imagery are shown in (b). Much like the preceding example, all of the polychromatic restorations exhibit more image structure or degradation. In fact, the spectrally induced artifacting and ringing in the enhanced model is so significant that overall image interpretability is visually impacted for these restorations. By comparison, the structured image quality effect noted in the polychromatic case does not appear to be evident in any of the gray-world equivalents found in this series of figures. In general, one does not even require a softcopy flicker test to ascertain the significant differences that exist between the two models (even in hardcopy). Naturally, these differences are confirmed quantitatively by the *nrmse* statistics reported below restorations, as the difference in this quality metric between the two models appears to be in the range of 24-32%. As a result, this exercise again confirms that aberrated sparse aperture systems exhibit a unique spectral character that induces deleterious quality artifacts which are not adequately captured by the gray-world modeling approach. In fact, for the case of a system aberrated by up to 0.25 waves rms of wavefront error, the missed spectral physics can ultimately lead to a completely different prediction of perceived image quality.

(a) Gray-World Simulation
nrmse: 0.0901; RER: 0.730; G_{rms}: 24.3

(b) Polychromatic-World Simulation
nrmse: 0.1116; RER: 0.730; G_{rms}: 24.3

Figure 93: Iteration #1: Restored imagery comparison between the polychromatic and gray-world models for an aberrated tri-arm sparse aperture (0.245 waves rms piston, tip/tilt error).

(a) Gray-World Simulation
nrmse: 0.0862; RER: 0.757; G_{rms}: 24.7

(b) Polychromatic-World Simulation
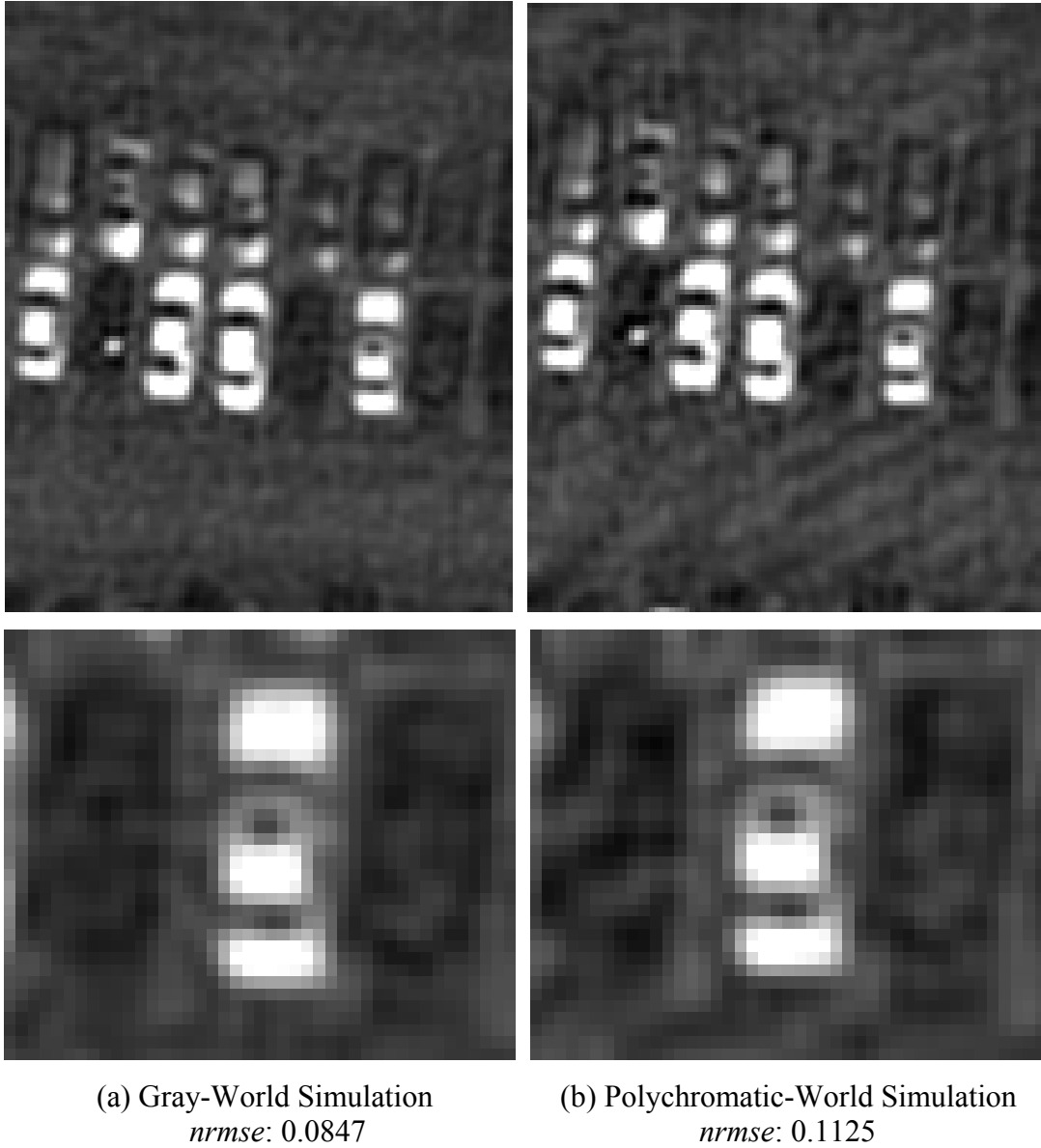*nrmse*: 0.1110; RER: 0.757; G_{rms}: 24.7

Figure 94: Iteration #2: Restored imagery comparison between the polychromatic and gray-world models for an aberrated tri-arm sparse aperture (0.246 waves rms piston, tip/tilt error).

(a) Gray-World Simulation
nrmse: 0.0916; RER: 0.733; G_{rms}: 26.1

(b) Polychromatic-World Simulation
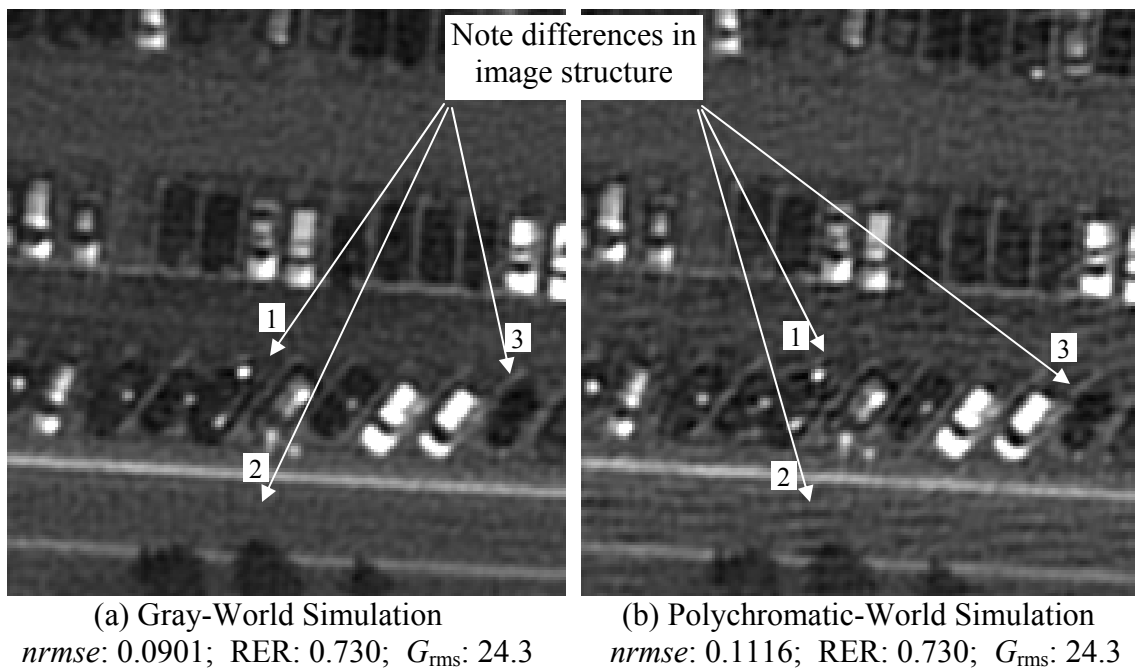*nrmse*: 0.1209; RER: 0.733; G_{rms}: 26.1

Figure 95: Iteration #3: Restored imagery comparison between the polychromatic and gray-world models for an aberrated tri-arm sparse aperture (0.252 waves rms piston, tip/tilt error).

5.4.2 HyMap-Based Object Description

The restoration results in the previous examples highlighted a unique spectrally induced quality effect that appeared to become more problematic as the imaging system exhibited increased levels of aberration. One will recall that these simulations entailed a polychromatic object scene derived from the three-band WASP digital airborne camera. As such, the original object displayed superb spatial sampling but less than optimal spectral resolution. To investigate how enhanced spectral resolution in the derivation of the integrated broadband signal impacts the nature of the spectral artifacts that surfaced for the moderately aberrated sparse aperture case, several polychromatic scenes from HyMap digital airborne data were captured in the simulation process.

For the panchromatic scenarios of interest to this dissertation, the HyMap sensor provides 33 reflective hyperspectral bands from 435-905 nm with ~15 nm bandwidths. This provides reasonably good spectral fidelity for the type of modeling performed in conjunction with this research effort. Unfortunately, the ground sample distance (GSD) associated with this data is relatively poor, with the observed ~10-ft GSD far below the 1.5 ft sampling desired in the nominal collection scenario. As a consequence, the following series of modeling iterations exhibits good spectral resolution but less than desirable spatial sampling. To avoid any uncertainty introduced into the modeling process by aliasing, the imaging system design was modified to ensure Nyquist sampling or better for these particular simulation cases. Despite the spatial resolution limitations described above, it is still a worthwhile exercise to evaluate other spectrally diverse object scenes to confirm the general nature of the spectrally induced quality effect conjectured through the system OTF character and observed in the WASP-derived simulation data.

An overhead view of the port of Mobile, AL was selected for the initial HyMap-based series of sparse aperture system predictions. Figure 96(a) displays the original polychromatic object scene, which clearly demonstrates excellent spatial frequency content and nominal spectral content from a remote sensing perspective. It should be noted that the scene is far less challenging from the standpoint of the spectral and spatial-frequency content observed in the WASP-derived scene. As before, the Wiener filter applied in these restorations uses the

spectrally averaged OTF (with perfect phase error knowledge) and the known noise-to-object power spectrum ratio. The rationale behind this selection has been discussed previously. In Figure 96(b), a spectrally weighted panchromatic version of the original polychromatic object scene has been developed for the purposes of comparison. As was done in the previous series of examples, individual restorations were accomplished through use of both the gray-world approximation and the enhanced spectral fidelity model. The bottom row of the figure provides a comparison of the restored broadband panchromatic imagery from the two models acquired for the tri-arm sparse aperture system with 0.10 waves rms of wavefront error. In specific, Figure 96(c) contains the restoration acquired with the gray-world model, and Figure 96(d) depicts the restored imagery generated by the polychromatic model. For this high SNR scenario, the gray-world and polychromatic-world models appear to produce similar restorations for aberrations on the order of 0.10 waves rms of wavefront error.

Once again, there are some differences between the restoration results acquired from the two simulation models, but a softcopy flicker test is required to observe the subtle variations. In this example, the mean-level statistics are a clear indicator of how minor those differences truly are, as only a ~4% difference in *nrmse* exists between them. Of course, the slightly poorer quality is exhibited by the enhanced spectral fidelity restoration, seemingly pointing to the likely possibility that the conjectured modulation mismatch observed with previous simulations is again being manifested for this particular example, albeit at an extremely low level. Closer examination of the two restorations in Figure 97 does little to highlight any detectable changes in the perceived quality. Therefore, although there is a minor but statistically significant difference between the two restorations, one has to conclude that the gray-world model provides a reasonable approximation of the anticipated restored image quality for this sparse aperture imaging scenario involving 0.10 waves rms of wavefront error. As was the case before, both simulation approaches also support the conclusion that a sparse aperture system can theoretically suffer up to 0.10 waves rms of piston, tip/tilt error and still produce good quality imagery under the collection assumptions pursued in this research investigation.
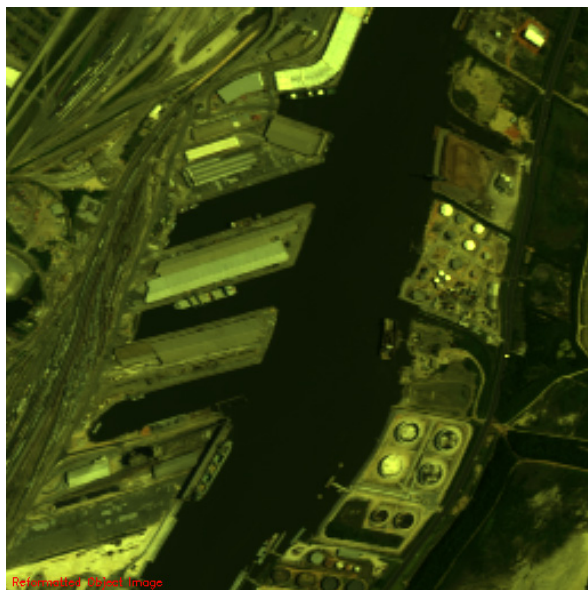
(a) Original Object

(b) Spectrally Weighted Object

(c) Gray-World Simulation
nrmse: 0.0634

(d) Polychromatic-World Simulation
nrmse: 0.0662

RER: 0.662; G_{rms}: 17.9; SNR: 276.2

Figure 96: Integrated panchromatic simulation of an aberrated tri-arm sparse aperture with spectrally weighted OTF restoration (0.10 waves rms piston, tip/tilt error).

(a) Gray-World Simulation
nrmse: 0.0634

(b) Polychromatic-World Simulation
nrmse: 0.0662
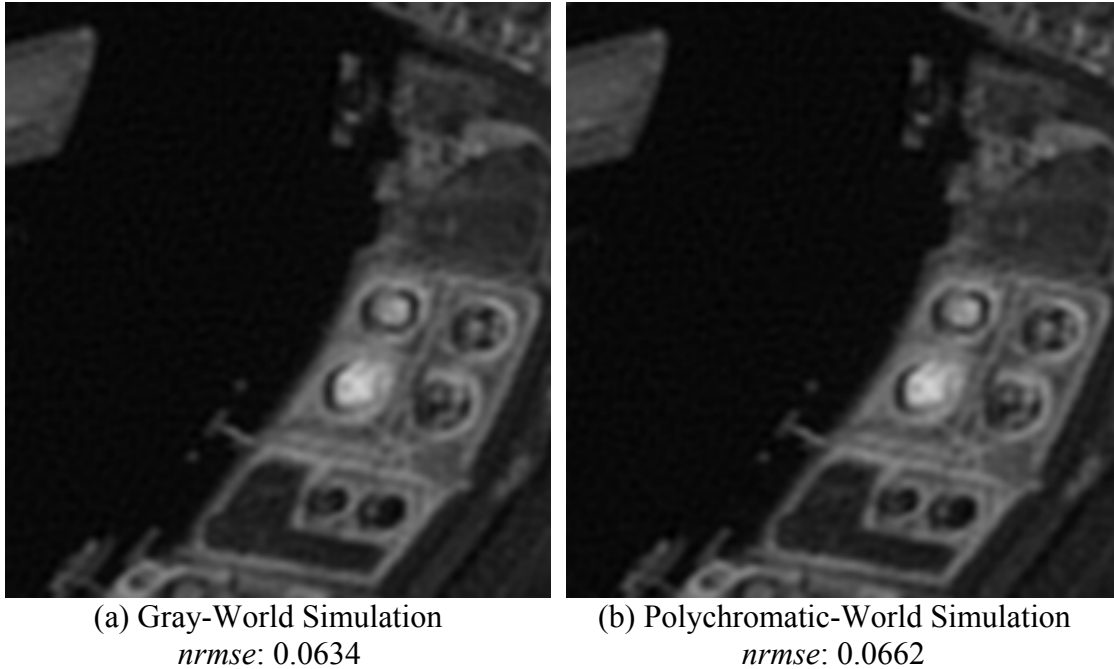
Figure 97: (Magnified) Integrated panchromatic simulation of an aberrated tri-arm sparse aperture with spectrally weighted OTF restoration (0.10 waves rms piston, tip/tilt error).

To explore whether increased rms wavefront error promotes the kind of spectral artifacting observed in the WASP-derived scenes, a series of HyMap-based investigations were performed with an aberrated tri-arm sparse aperture system exhibiting 0.25 waves rms of wavefront error. The restoration results acquired through this study for the HyMap-based harbor scene can be found in figures 98 through 101. Within this set of diagrams, Figure 99 depicts a magnified region of the restoration found in Figure 98, and similarly Figure 101 displays an enlarged image chip from Figure 100. For comparison within individual figures, the restorations from the gray-world model are depicted in (a) and those acquired through use of the spectral model appear in (b).

At this level of aberration, it becomes apparent both visually and in the metric data that the spectrally induced artifacts again surface for the polychromatic-world model. Although noise amplification and some ringing are also apparent in the gray-world model restoration, the perceived level of that image structure is significantly below that witnessed in the polychromatic model products. It is clear that the majority of the latter is the product of the Wiener filter restoration in conjunction with the general character of the aberrated sparse

223

aperture system transfer function, not the result of any spectral modulation mismatch that the gray-world model is technically unable to support. The level of artifacting or ringing in the restored imagery from the enhanced model is significant enough to be observed in the hardcopy and is only accentuated through a softcopy flicker test between the two model results. For these examples, the statistical metrics also capture the significant variation between the two model results, as the computed *nrmse* difference is in the range of 25-28%. Such a difference is a clear indicator that there are physical processes captured in the polychromatic-world simulation that are not adequately addressed through the equivalent gray-world approximation.

As with the previously derived results, these HyMap-based restorations with increased spectral resolution seem to confirm that a spectrally induced artifact mechanism is supported by the unique structure of sparse aperture imaging system transfer functions. This is an encouraging result as it appears that the addition of spectral planes in the derivation of the integrated broadband signal does not average out the effect. In other words, the spectral content of the remotely sensed scenes investigated in this effort does not appear to exhibit features that would be accentuated to the point of inducing artifacts as a result of insufficient spectral sampling. To test this theory, an additional Hymap-derived scene and a higher spectral-resolution DIRSIG object will be explored in the discussion to follow. Based on the results acquired through this series of investigations and those conducted earlier, it appears that the artifacting mechanism is not triggered extensively until the wavefront error is considerably worse than 0.10 waves rms. At 0.25 waves rms of wavefront error, the spectrally induced quality effect is severe enough that image interpretability is considerably impacted. To capture the nature of this phenomenon, however, one must implement an enhanced spectral fidelity model, as the traditional gray-world approach does not address the spectral mechanism that is responsible for inducing the deleterious image artifacts observed in this dissertation.

(a) Gray-World Simulation
nrmse: 0.0850

(b) Polychromatic-World Simulation
nrmse: 0.1063

RER: 0.549; G_{rms}: 23.0; SNR: 270.7

Figure 98: Iteration #1: Panchromatic simulation of an aberrated tri-arm sparse aperture with spectrally weighted OTF restoration (0.25 waves rms piston, tip/tilt error).

(a) Gray-World Simulation
nrmse: 0.0850

(b) Polychromatic-World Simulation
nrmse: 0.1063

Figure 99: Iteration #1 (Magnified): Panchromatic simulation of an aberrated tri-arm sparse aperture with spectrally weighted OTF restoration (0.25 waves rms piston, tip/tilt error).

(a) Gray-World Simulation
nrmse: 0.0841

(b) Polychromatic-World Simulation
nrmse: 0.1074

RER: 0.553; G_{rms}: 24.3; SNR: 275.8

Figure 100: Iteration #2: Panchromatic simulation of an aberrated tri-arm sparse aperture with spectrally weighted OTF restoration (0.25 waves rms piston, tip/tilt error).

(a) Gray-World Simulation
nrmse: 0.0841

(b) Polychromatic-World Simulation
nrmse: 0.1074

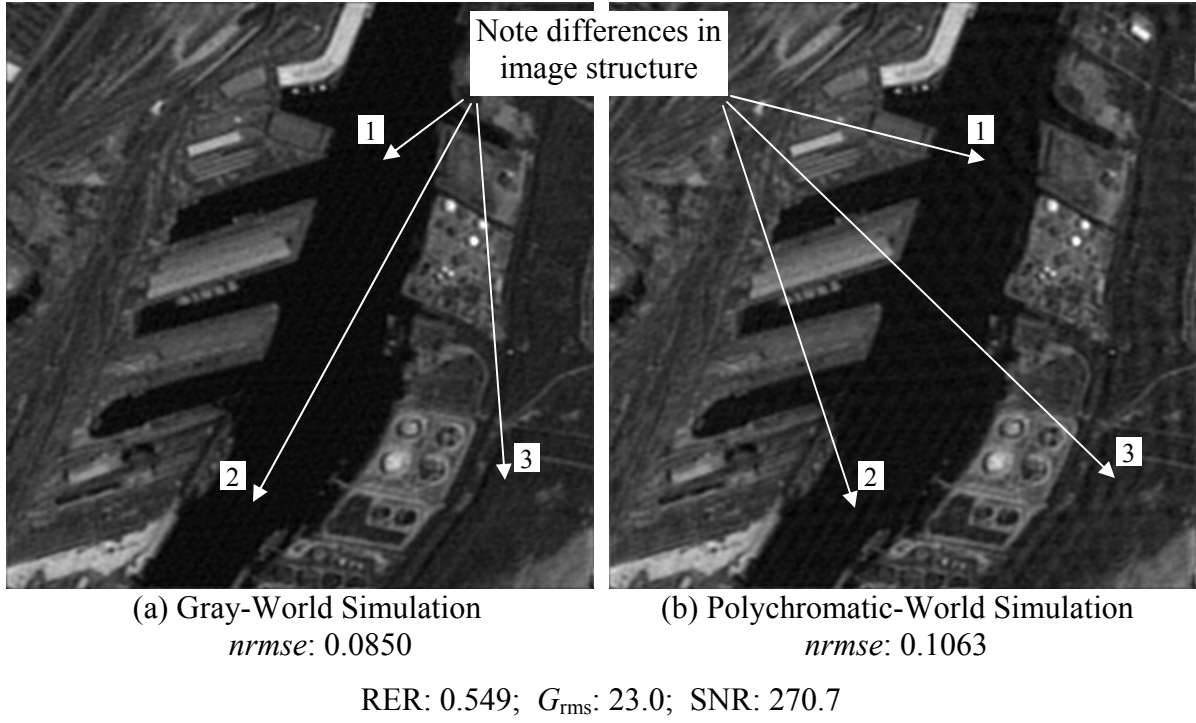Figure 101: Iteration #2 (Magnified): Panchromatic simulation of an aberrated tri-arm sparse aperture with spectrally weighted OTF restoration (0.25 waves rms piston, tip/tilt error).
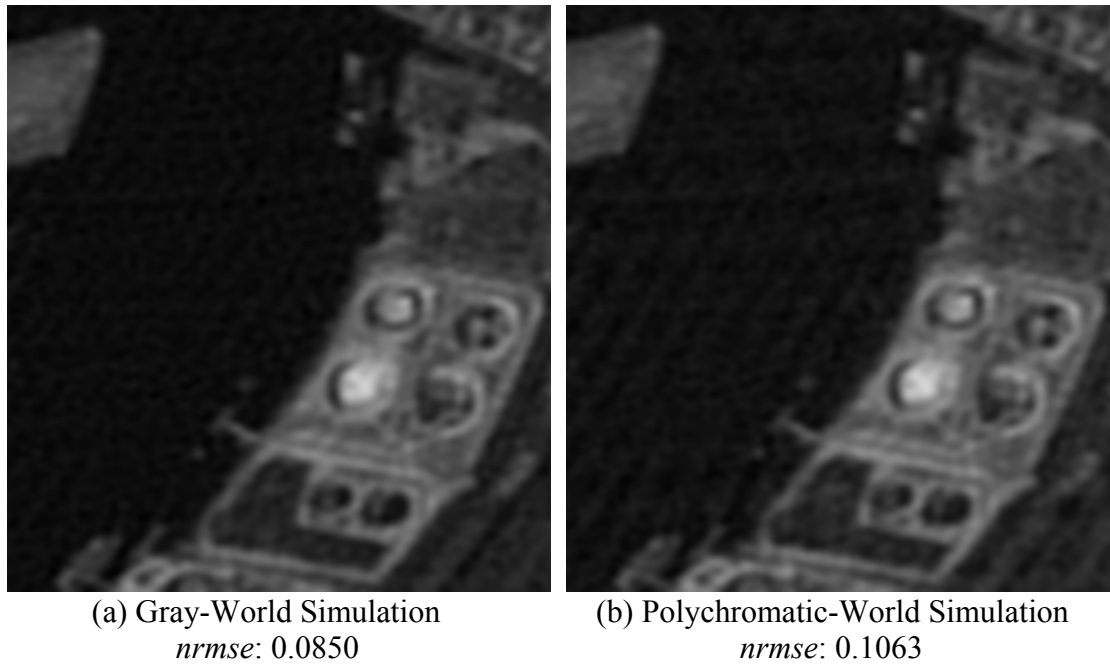
226

As alluded to above, numerous iterations have been performed with various object scenes and optical phase distributions to ensure the nature of the reported results are consistent with the norm. To that end, the restoration results from a different HyMap-based polychromatic object scene will be discussed next. As before, the new polychromatic object scene exhibits spatial sampling of ~10-ft GSD and spectral resolution on the order of ~15 nm. Figure 102 contains a series of imagery products acquired for the tri-arm sparse aperture system with 0.10 waves rms of piston, tip/tilt error at the mean wavelength. Figure 102(a) displays the original color object, which clearly contains urban/suburban scene content including a highway interchange as a prominent central feature. In Figure 102(b), a spectrally weighted panchromatic object has been formed from the original hyperspectral data cube to provide a means for comparison between the two imaging models under investigation. Finally, Figure 102(c) depicts the restoration results from the gray-world model, and Figure 102(d) displays the restored imagery from the polychromatic model.

Figure 103 shows a magnified region of the restored imagery in Figure 102 to allow a closer examination of their quality. Based on these figures, it is clear that only marginal visual differences exist between the predictions acquired through the gray-world model and those from the enhanced spectral capability for this level of aberration. As previously observed for 0.10 waves rms of wavefront error, one can perform a softcopy flicker test between the two different imagery restorations and detect noticeable differences. However, given the GSD associated with the scene, it is difficult to ascertain whether the quality effects observed in the softcopy imagery impact feature interpretability for the untrained observer. Despite the apparent minor nature of the difference in overall visual appearance, the statistical data portrays a slightly different story, with an *nrmse* difference of ~21% exhibited between the gray-world and polychromatic models. Based on this metric data, it is apparent there are some spectral effects captured in the enhanced model on a level not observed previously for 0.10 waves rms of wavefront error. This particular scene clearly exhibits significant mid-spatial frequency content as a function of wavelength that accentuates the effect of the spectral mis-boost in the Wiener filter restoration. One will see shortly that this effect becomes very prominent in the restoration quality associated with this particular overhead scene as the aberration levels increase.

(a) Original Object

(b) Spectrally Weighted Object

(c) Gray-World Simulation
nrmse: 0.0557

(d) Polychromatic-World Simulation
nrmse: 0.0674

RER: 0.629; G_{rms}: 12.8; SNR: 269.0

Figure 102: Integrated panchromatic simulation of an aberrated tri-arm sparse aperture
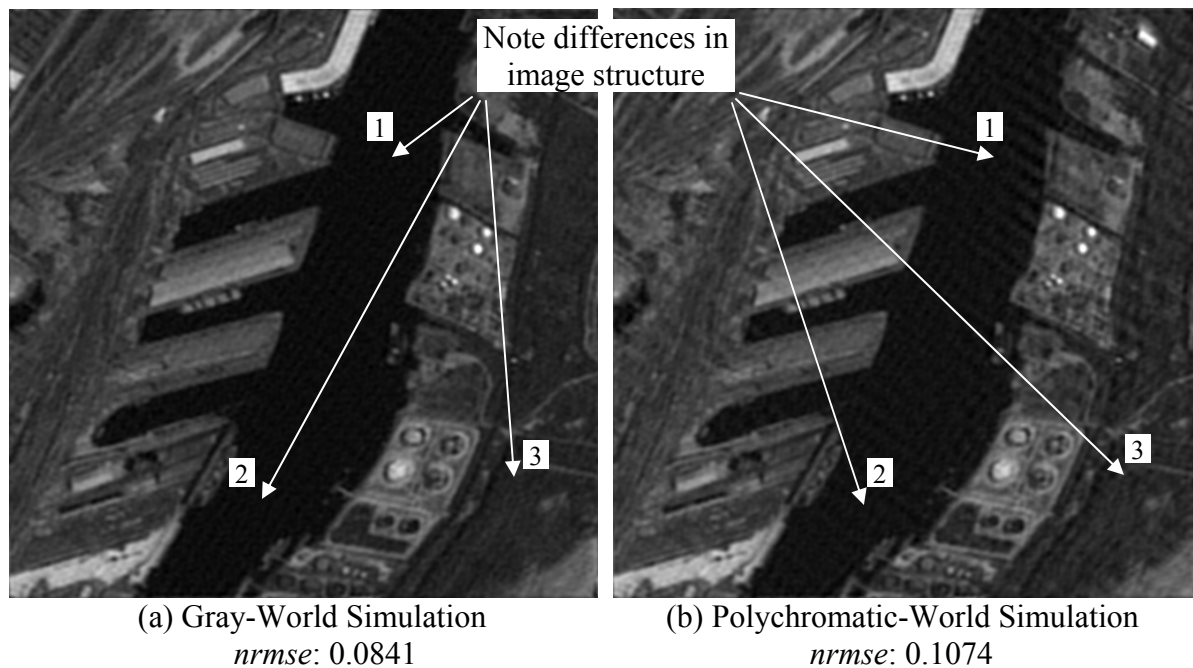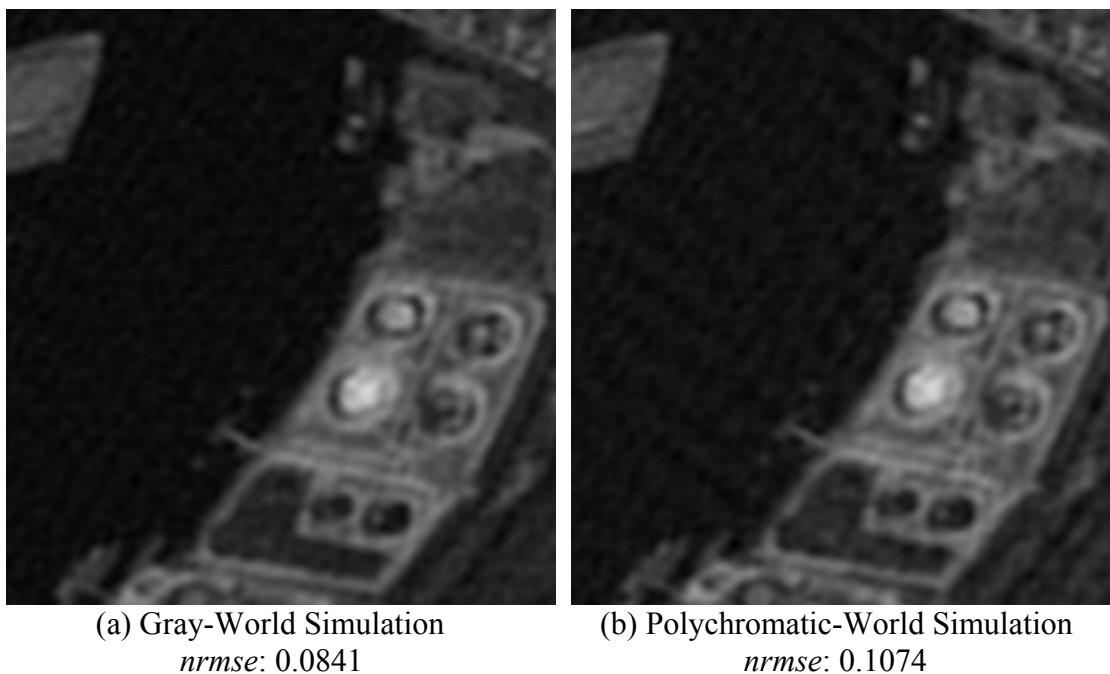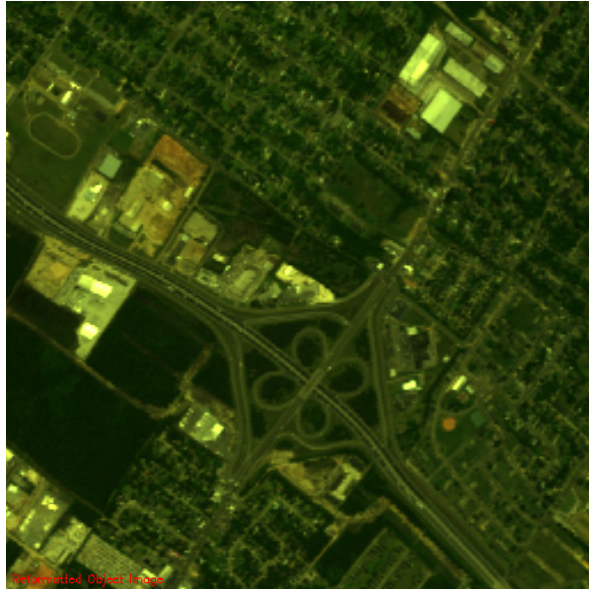with spectrally weighted OTF restoration (0.10 waves rms piston, tip/tilt error).

(a) Gray-World Simulation
nrmse: 0.0557

(b) Polychromatic-World Simulation
nrmse: 0.0674
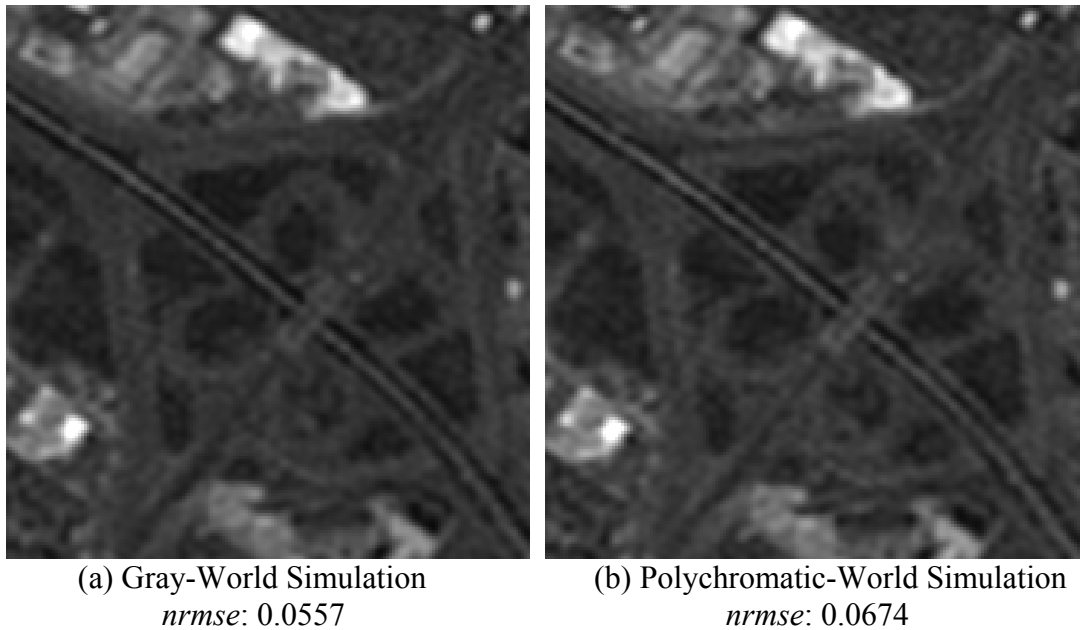
Figure 103: (Magnified) Integrated panchromatic simulation of an aberrated tri-arm sparse aperture with spectrally weighted OTF restoration (0.10 waves rms piston, tip/tilt error).

As in previous exercises, the polychromatic object scene identified in Figure 102 was utilized in additional simulations involving a tri-arm sparse aperture system with 0.25 waves rms of wavefront error and fill factor of 0.173. A sample of the restoration results acquired through this investigation for the two modeling capabilities of interest appear in figures 104 and 105. As forecasted by the *nrmse* data from the previous example, the enhanced spectral fidelity model provides a restoration that is beset by significant artifacting for this level of aberration. In fact, the ringing within the restored imagery associated with this model is so extensive that information content is visibly lost, leading to a serious reduction in image interpretability even at ~10-ft GSD. Once again, the comparable gray-world model does not manifest any of this image structure, pointing to the hypothesis that they must be spectrally induced. Multiple iterations were performed at the level of 0.25 waves rms of piston, tip/tilt for this HyMap-derived object scene, and all appeared to generate similar results that were in family with those presented in figures 104 and 105. For this particular case, the two scenes exhibit an approximate 89% difference in computed *nrmse* from the original gray-scale object, confirming quantitatively the nature of the destructive artifacting that arises in the spectral model. Based on these results, one can conclude that inclusion of spectral physics in the simulation process is clearly essential for particular collection conditions.

(a) Gray-World Simulation
nrmse: 0.0743

(b) Polychromatic-World Simulation
nrmse: 0.1402

RER: 0.515; G_{rms}: 24.1; SNR: 265.1

Figure 104: Integrated panchromatic simulation of an aberrated tri-arm sparse aperture with spectrally weighted OTF restoration (0.25 waves rms piston, tip/tilt error).

(a) Gray-World Simulation
nrmse: 0.0743

(b) Polychromatic-World Simulation
nrmse: 0.1402

Figure 105: (Magnified) Integrated panchromatic simulation of an aberrated tri-arm sparse aperture with spectrally weighted OTF restoration (0.25 waves rms piston, tip/tilt error).
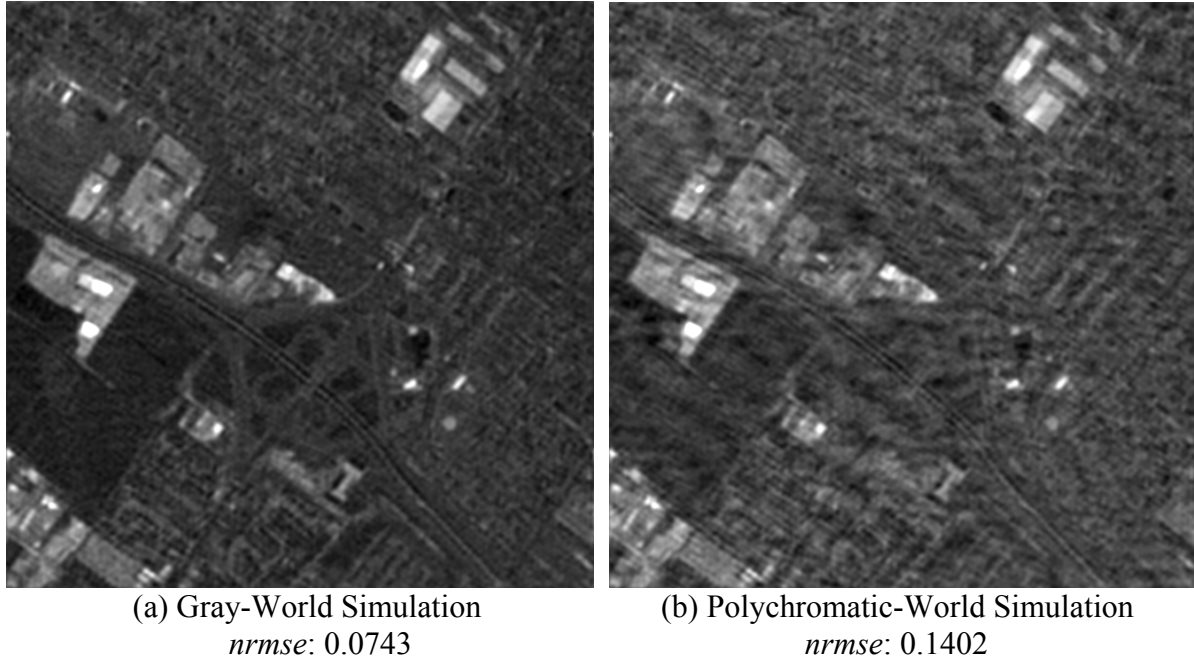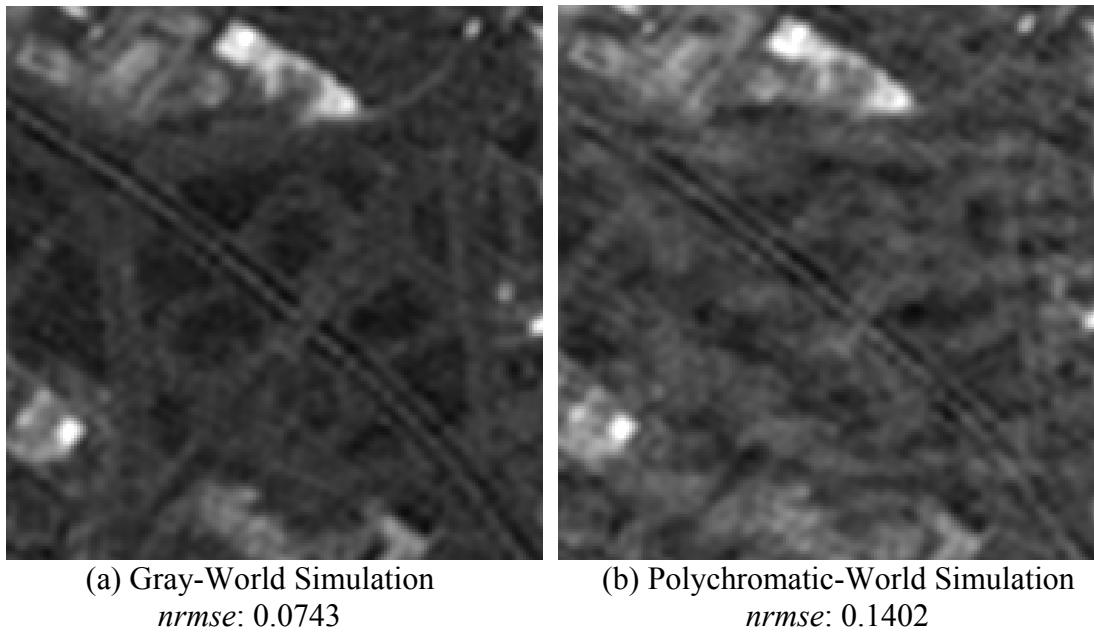
Based on these examples, it is clear that capturing some of the spectral character of the collection can be extremely important in certain sparse aperture imaging scenarios, especially those entailing moderate-to-high aberration levels and significant mid-spatial frequency content that varies as a function of wavelength. The HyMap-derived exercises provide key insight into how dependent the observed quality effect is on scene content, as well as the relative distribution of phase error across the exit pupil. As a consequence, one must be very cautious in simply specifying rms wavefront error to quantify sparse aperture system performance, as enormous variability in restored image quality can be observed for a given level of aberration.

5.4.3 DIRSIG-Based Object Description

With the reporting of the airborne-derived scene results now complete, the final polychromatic object to receive attention in this dissertation is a scene that was synthetically generated through use of DIRSIG. As discussed previously, DIRSIG affords the unique opportunity to systematically adjust the spatial and spectral resolution for a given scenario according to the principal investigator's objectives. With a complex scene of the Rochester, NY metropolitan area already constructed, there was considerable leverage available for performing a high-resolution, spectrally accurate simulation with a realistic synthetic scene. Additionally, through the flexibility of the DIRSIG model, the spatially variant spectral radiance at the entrance pupil could be computed at the desired 18-in GSD at spectral intervals of 5 nm with considerable radiometric accuracy. Unfortunately, due to constraints in the spectral content of the underlying texture map (the digital airborne data responsible for creating it only provided reflectance data in the visible part of the spectrum), realistic imagery could only be acquired across a detection bandwidth of 400-700 nm. Therefore, the simulations in the following examples exhibit excellent spatial and spectral resolution, but suffer some limitations in detection bandwidth and unique model-based attributes. As a consequence, the DIRSIG-based simulations which follow provide another essential piece of the composite picture on the value of the enhanced spectral modeling of sparse aperture systems but should not be considered exclusively without regard to the previously derived results.

As with the previous analyses, the first scenario to be addressed with the DIRSIG scene entails an aberrated tri-arm sparse aperture system with 0.10 waves rms of piston, tip/tilt error at the mean wavelength and a fill factor of 0.173. The original polychromatic object scene (composed of 61 bands at 5 nm spectral resolution) appears in Figure 106(a). From this diagram, it is apparent that the selected suburban scene is relatively "flat" from a spectral perspective, with many neutral earth tones, foliage and field spectra represented in the scene content. In addition, all the reflectance data associated with the scene are essentially Lambertian diffuse, so there is no physical specularity apparent in the simulated scene addressed through this investigation. Finally and perhaps most importantly, the detection bandwidth associated with the scene is considerably reduced (by a 3:5 ratio) from that utilized in previous examples. As a consequence of these features, the scene constitutes a far less severe case than explored previously since the observed spectral variation is relatively narrow. With these caveats in mind, Figure 106(c) and (d) provide the image restorations for the gray-world and polychromatic models, respectively. For comparison, a spectrally weighted equivalent panchromatic object image has been included in Figure 106(b).

As was encountered in the previous exercises, the restorations associated with 0.10 waves rms of wavefront error show very subtle differences between the two simulation models. Even in the magnified region of the restorations depicted in Figure 107, the nature of these differences cannot be easily discerned in the hardcopy. Interestingly, the *nrmse* data do indicate there is a statistical difference of ~4% between the two restorations, comparable to the level of degradation observed in the previous examples. Once again, the enhanced spectral fidelity model appears to capture a deleterious effect that is not present in the gray-world model restoration. These results are entirely consistent with what was observed in previous simulations of the tri-arm sparse aperture system aberrated at 0.10 waves rms error. Therefore, with increased spectral resolution, the DIRSIG restoration results again seem to confirm that the conjectured spectrally induced quality effect is present in aberrated sparse aperture systems, but at a low enough level that interpretability is not impacted at 0.10 waves rms of wavefront error. As a consequence of the relatively low amplitude of the effect at this aberration level, both models produce visually similar restoration products that imply

232

acceptable quality can be acquired with a sparse aperture system under the conditions and assumptions pursued in this investigation.

(a) Original Object	(b) Spectrally Weighted Object
(c) Gray-World Simulation	(d) Polychromatic-World Simulation
nrmse: 0.0634	*nrmse*: 0.0659
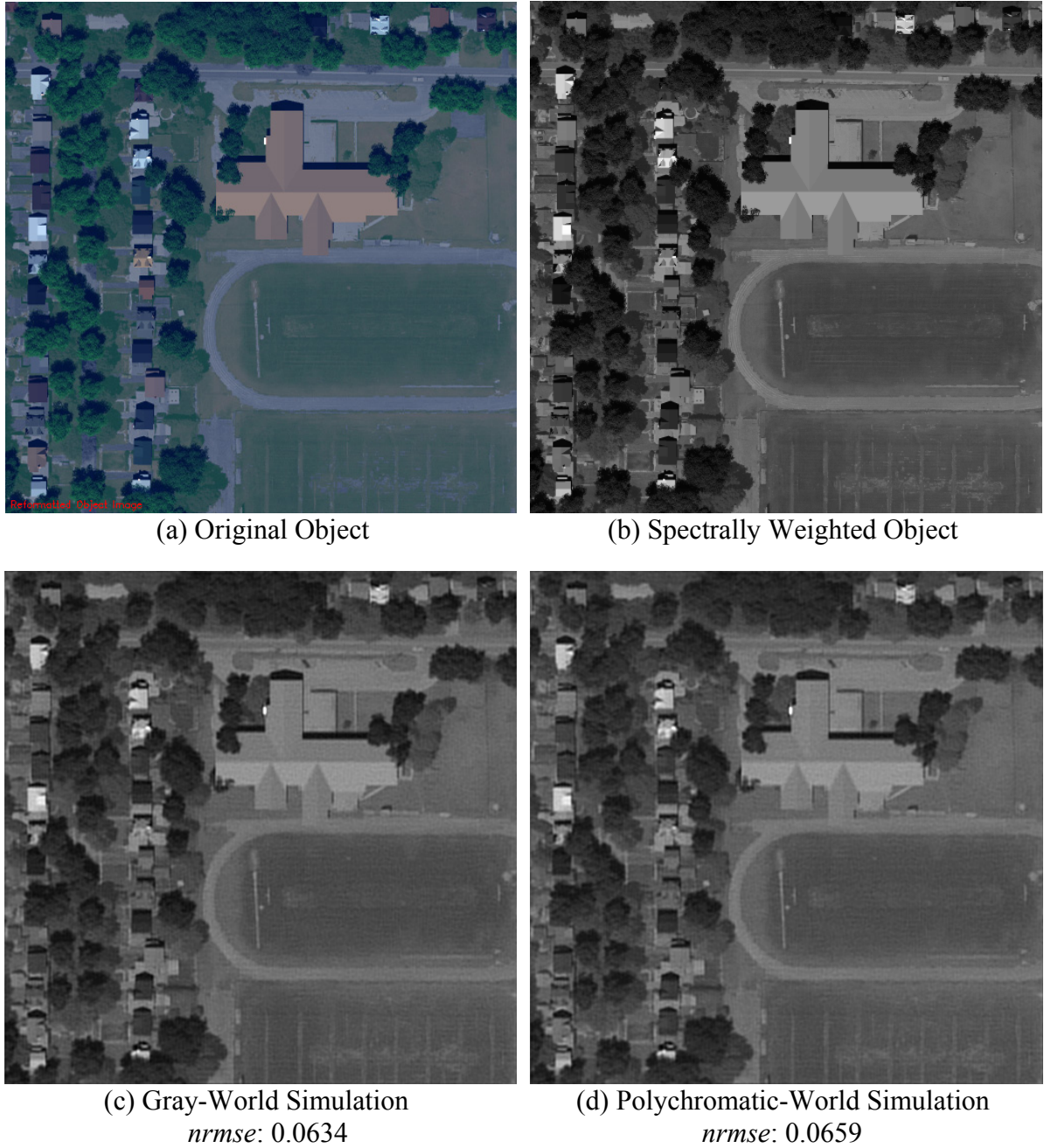
RER: 0.740; G_{rms}: 13.7; SNR: 279.2

Figure 106: Integrated panchromatic simulation of an aberrated tri-arm sparse aperture with spectrally weighted OTF restoration (0.10 waves rms piston, tip/tilt error).

(a) Gray-World Simulation   (b) Polychromatic-World Simulation
nrmse: 0.0634   *nrmse*: 0.0659

Figure 107: (Magnified) Integrated panchromatic simulation of an aberrated tri-arm sparse aperture with spectrally weighted OTF restoration (0.10 waves rms piston, tip/tilt error).

In parallel structure with previous investigations, the obvious next step is to evaluate a DIRSIG-derived object scene with a sparse aperture system that is aberrated by 0.25 waves rms of piston, tip/tilt error. With the object scene content provided through DIRSIG, numerous iterations were performed with this level of aberration applied to the nominal 0.173 fill factor tri-arm imaging system. The principal difference between the various iterations was the random seed used to distribute the optical phase across subapertures. The results depicted in figures 108 through 115 are representative of the set of runs that were executed for this particular evaluation. In this series of diagrams, a leader-follower relationship exists whereby the full restoration is sequentially followed by a magnified region of that image. From these results, it is readily apparent that the spectral model again captures an artifacting or ringing effect that is not present in the equivalent gray-world model restorations. Despite the reduced detection bandwidth associated with these predictions, the spectrally induced effect is very prominent and has a serious deleterious impact on the visual quality of the restored imagery. In addition, the unique effect appears to be statistically significant in the mean-level image quality metrics, as the difference in the computed *nrmse*

between the two model approaches is generally on the order of ~13-21%, with outliers as large as 42% also observed.

(a) Gray-World Simulation
nrmse: 0.0780

(b) Polychromatic-World Simulation
nrmse: 0.0915

RER: 0.582; G_{rms} : 18.1; SNR: 279.4

Figure 108: Iteration #1: Panchromatic simulation of an aberrated tri-arm sparse aperture with spectrally weighted OTF restoration (0.25 waves rms piston, tip/tilt error).
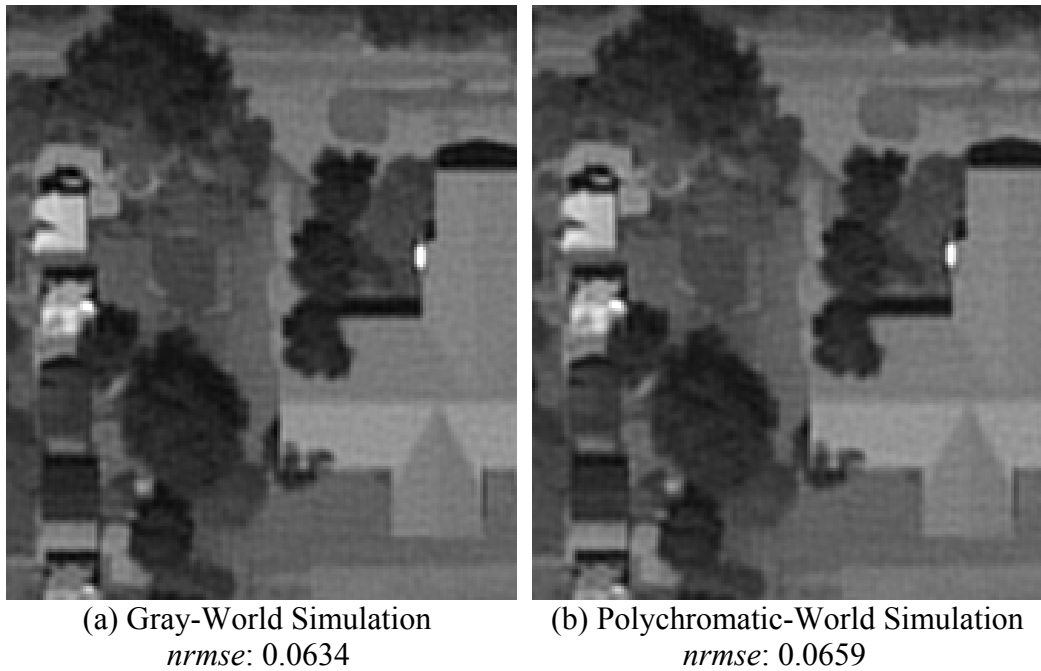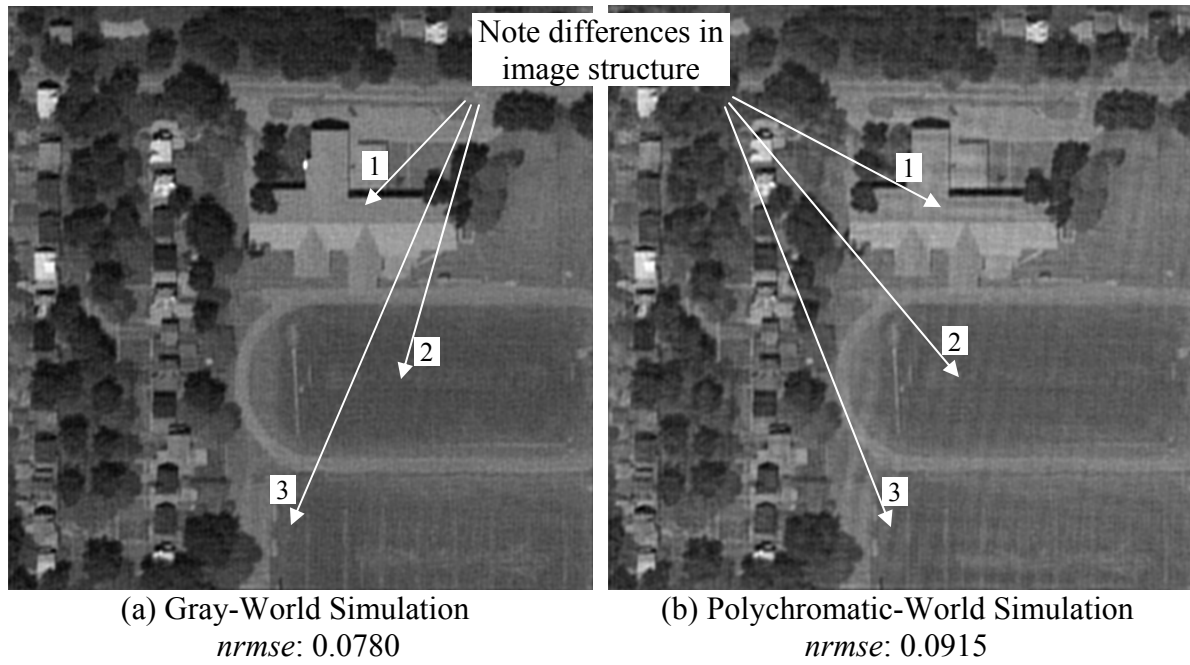

(a) Gray-World Simulation
nrmse: 0.0780

(b) Polychromatic Simulation
nrmse: 0.0915
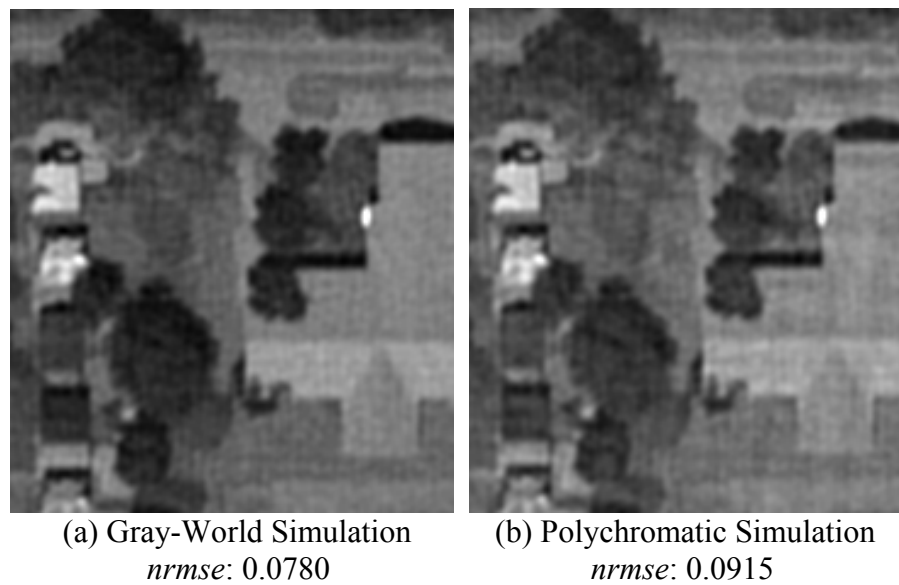
Figure 109: Iteration #1 (Magnified): Panchromatic simulation of an aberrated tri-arm sparse aperture with spectrally weighted OTF restoration (0.25 waves rms piston, tip/tilt error).

(a) Gray-World Simulation
nrmse: 0.0961

(b) Polychromatic-World Simulation
nrmse: 0.1089

RER: 0.614; G_{rms}: 20.1; SNR: 240.4

Figure 110: Iteration #2: Panchromatic simulation of an aberrated tri-arm sparse aperture with spectrally weighted OTF restoration (0.25 waves rms piston, tip/tilt error).
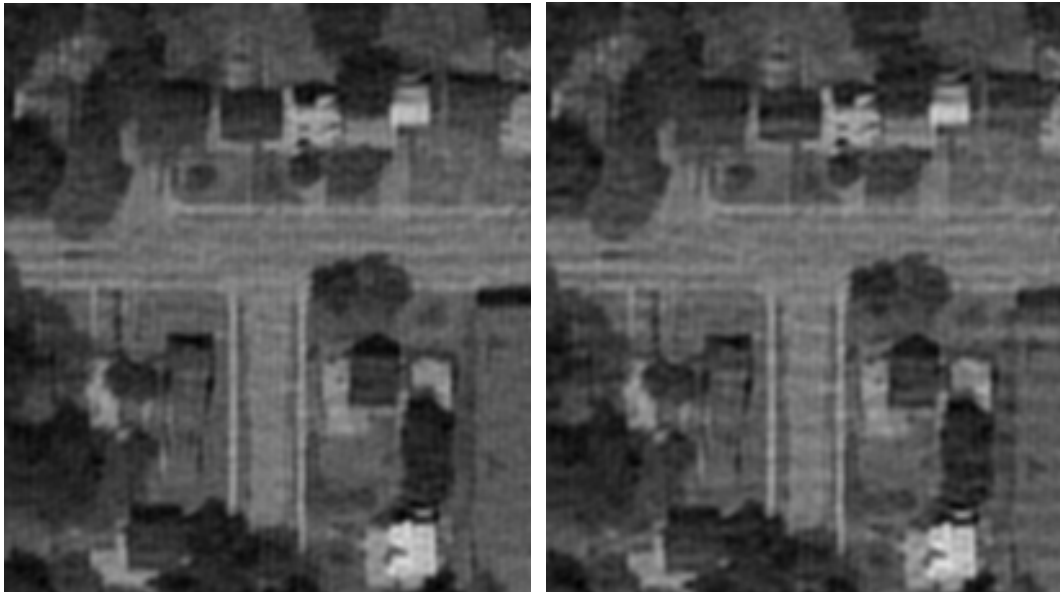
(a) Gray-World Simulation
nrmse: 0.0961

(b) Polychromatic Simulation
nrmse: 0.1089

Figure 111: Iteration #2 (Magnified): Panchromatic simulation of an aberrated tri-arm sparse aperture with spectrally weighted OTF restoration (0.25 waves rms piston, tip/tilt error).

(a) Gray-World Simulation
nrmse: 0.0877

(b) Polychromatic-World Simulation
nrmse: 0.1057

RER: 0.676; G_{rms}: 20.6; SNR: 273.2

Figure 112: Iteration #3: Panchromatic simulation of an aberrated tri-arm sparse aperture with spectrally weighted OTF restoration (0.25 waves rms piston, tip/tilt error).
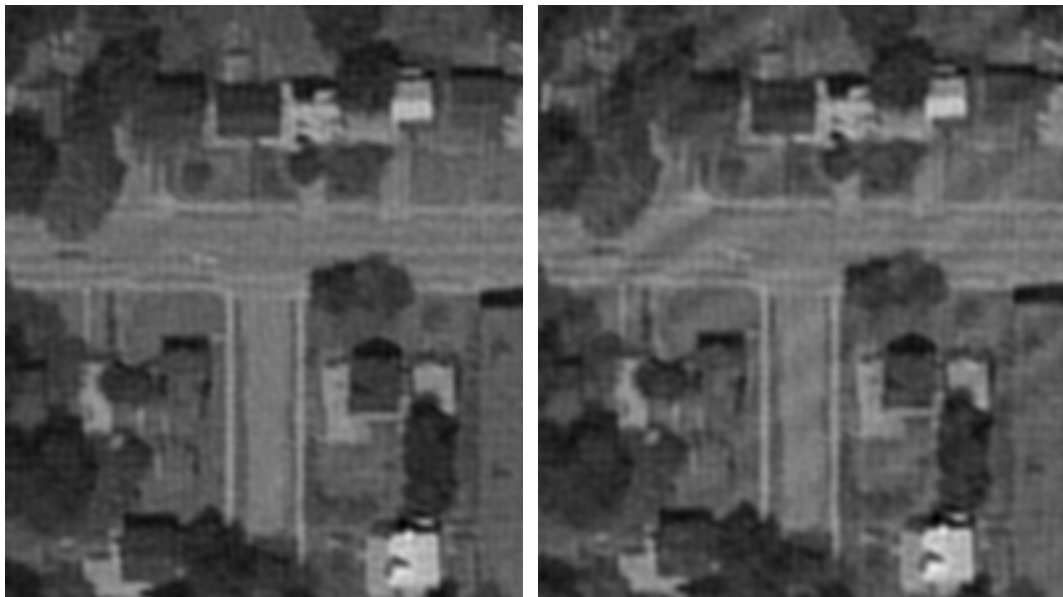
(a) Gray-World Simulation
nrmse: 0.0877

(b) Polychromatic Simulation
nrmse: 0.1057

Figure 113: Iteration #3 (Magnified): Panchromatic simulation of an aberrated tri-arm sparse aperture with spectrally weighted OTF restoration (0.25 waves rms piston, tip/tilt error).

(a) Gray-World Simulation
nrmse: 0.0933

(b) Polychromatic-World Simulation
nrmse: 0.1324

RER: 0.621; G_{rms}: 24.5; SNR: 274.0

Figure 114: Iteration #4: Panchromatic simulation of an aberrated tri-arm sparse aperture with spectrally weighted OTF restoration (0.25 waves rms piston, tip/tilt error).

(a) Gray-World Simulation
nrmse: 0.0933

(b) Polychromatic Simulation
nrmse: 0.1324

Figure 115: Iteration #4 (Magnified): Panchromatic simulation of an aberrated tri-arm sparse aperture with spectrally weighted OTF restoration (0.25 waves rms piston, tip/tilt error).
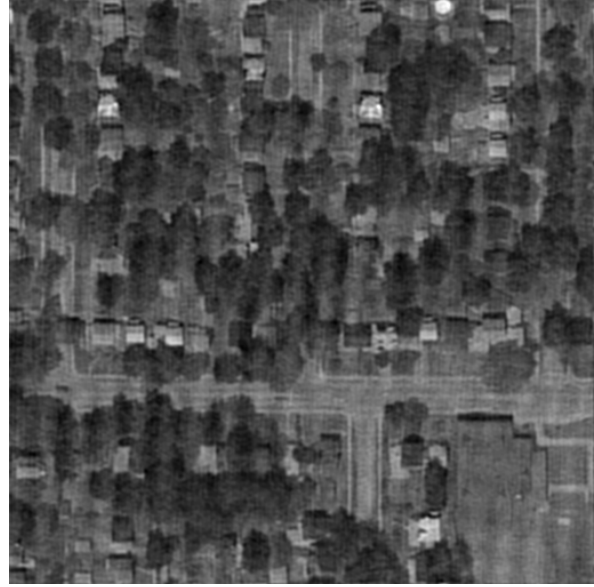
Although certainly within family, the restorations achieved with the spectral model appear to exhibit a minor reduction in the relative magnitude of the observed artifacting effect relative to some of the previous results. The most obvious contributor to this reduction is the relatively neutral spectral character of the object scene. As observed above, the scene consists of a fair amount of natural content that does not show significant spectral variation across the investigated passband. Future sensitivity studies should be performed with a scene that demonstrates greater diversity in spectral and spatial-frequency content to explore this premise. Another significant issue that undoubtedly contributes to the reduced nature of the effect is the narrower detection bandwidth (300 nm versus 500 nm) associated with these particular simulations. As introduced previously, the observed artifacting effect is largely the result of modulation mismatch across the detection passband. As the passband becomes narrower, the opportunity for spatial frequency mismatch that can be accentuated through application of the Wiener filter is significantly reduced, ultimately leading to much less mis-boost and associated artifact generation. Despite the apparent reduction in the impact of the observed artifacting effect, it is still a primary attribute of the image quality at this aberration level (0.25 waves rms) and is not adequately captured by the gray-world model. The fact that the quality effect still exists despite the mitigating factors introduced above demonstrates it is an issue with which one must deal when analyzing moderately aberrated sparse aperture systems with low fill factors. Thus, the results acquired with higher spectral resolution (5 nm intervals) again confirm the existence of unique quality issues for aberrated sparse aperture imaging systems, demonstrating once again the need to incorporate enhanced spectral fidelity into the modeling process when addressing this kind of optical system.

5.5 Alternative Wiener Filter Options

Even within the context of a traditional Wiener-Helstrom filter, there are a multitude of possible restoration filter options that could be pursued to reconstruct degraded imagery acquired from sparse aperture imaging systems. Some of the potential filter alternatives have been previously introduced in this dissertation. Since the implemented model approach derives the degrading system transfer function, the physical image noise spectrum, and the exact spatial object description; all of the essential components are available to develop an optimal filter design. This "optimal" filter with perfect system transfer function knowledge

and *a priori* knowledge of the noise-to-object power spectrum has been used extensively within the various system trades as the baseline restoration methodology. Obviously, one could perform sensitivity trades on the relative collection uncertainty to gain insight into the effect of real-world conditions on restored image quality. Although some trades on system uncertainty were performed in concert with this research, they were rather preliminary in nature so the bulk of this problem is left for future investigation. This section will, however, document some of the more extensive comparative work that was accomplished for selection of the individual components within the classic Wiener filter construct.

To that end, Figure 116 illustrates integrated panchromatic restoration products acquired for a moderately aberrated tri-arm sparse aperture system with fill factor of 0.173. All of these restorations were developed through use of the enhanced spectral model and various options for the individual Wiener filter constituents (i.e., system transfer function and noise-to-object power spectrum ratio). For the purposes of comparison, a spectrally weighted panchromatic object image formed from the original polychromatic scene appears in Figure 116(a). As seen in this diagram, the object scene utilized in this investigation is derived from the WASP airborne imagery. In Figure 116(b), one observes the image restoration generated with the perfect central wavelength OTF and exact noise-to-object power spectrum present in the modeled panchromatic signal. As noted in Section 5.3, this selection of Wiener filter design leads to considerable amplification of the modulation mismatch in the spectral transfer function, inducing a significant amount of artifacting and ringing in the derived imagery. In agreement with this visual quality assessment, one will also note that this restoration option correlates with the worst statistical errors of the filters represented in the figure, as manifested by the relatively poor *nrmse* of 0.1532.

As observed in Figure 116(c), one finds that slightly better restoration quality can be achieved for the central wavelength OTF restoration if some uncertainty is prescribed in the noise-to-object power spectrum ratio. In this part of the exercise, that key ratio was assumed to be unknown and treated as a constant to be adjusted for derivation of "optimal" quality. Such a process is not unlike what is accomplished for real-world imagery restorations, although the latter are usually performed by trained photo-analysis professionals. For the

240

central wavelength OTF restoration, use of a constant for the power spectrum ratio seems to result in imagery with reduced sharpness but also reduced amplitude in the perceived level of artifacting. In effect, the uncertainty in the power spectrum ratio induces an averaging mechanism in the restoration that helps to mitigate some of the artifacts observed in the imagery. Statistically, this smoothing effect in the image restoration results in ~8% improvement in the computed *nrmse* for this particular example. Although this phenomenon is consistently observed in central wavelength OTF restorations, it is not the case that is typically experienced with restorations utilizing spectrally weighted transfer functions. In the latter case, uncertainty in the power spectrum ratio generally results in poorer restoration quality than use of the exact ratio in the Wiener filter construction. This will be observed in the subsequent comparative analysis on alternative filter options, where *a priori* knowledge of the power spectrum ratio will clearly be shown to be beneficial for spectrally averaged OTF restorations.

On the other end of the spectrum, one finds in Figure 116(d) the "optimal" restoration filter design with a perfect spectrally averaged system OTF and known noise-to-object power spectrum ratio generates the lowest statistical measure of error, with an observed *nrmse* of 0.1125. Of course, the quality associated with the latter restoration is still very suspect when the wavefront error is on the order of 0.25 waves rms, as one observes the destructive spectral artifacting and overall loss of information content noted previously. The principal point of this trade study, however, is that the spectrally averaged OTF restoration is consistently better than the central wavelength OTF reconstruction, resulting in significantly reduced image quality impact. As noted in earlier sections, it appears use of the spectrally weighted transfer function within the Wiener filter generally minimizes the amplification in modulation mismatch that gives rise to the whole spectral artifacting phenomenon. Consequently, it appears that the spectrally weighted system OTF is the optimal constituent to use within the Wiener filter for this kind of imaging system. The impact of the smoothing effect of unknown noise-to-object power spectrum in conjunction with this "optimal" transfer function will be addressed in the discussion on the next series of restoration examples.

(a) Spectrally Weighted Object
(formed from original color object)
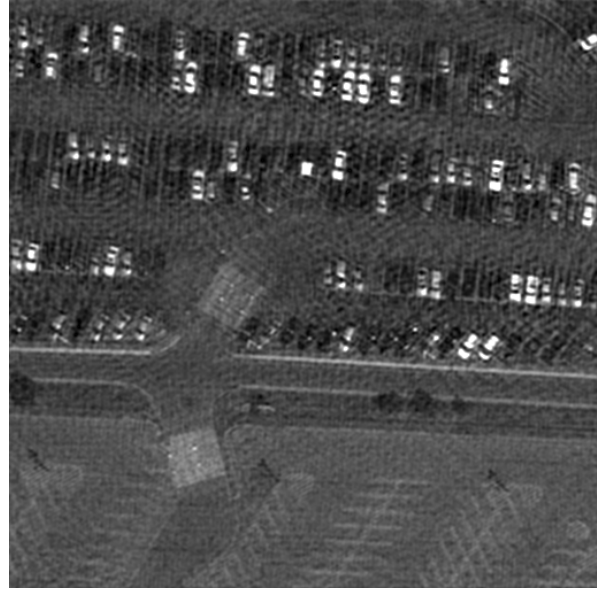
(b) Central OTF Restoration
(*a priori* power spectrum knowledge)
nrmse: 0.1532; RER: 0.804; G_{rms}: 18.2

(c) Central OTF Restoration
(no power spectrum knowledge)
nrmse: 0.1411; RER: 0.836; G_{rms}: 16.9

(d) Spectrally Averaged OTF Restoration
(*a priori* power spectrum knowledge)
nrmse: 0.1125; RER: 0.777; G_{rms}: 23.0

Figure 116: Integrated panchromatic simulation of an aberrated tri-arm sparse aperture
with various restoration filters (0.25 waves rms piston, tip/tilt error).

Continuing with the discussion on alternative restoration filter realizations, Figure 117 provides some comparisons between different gray-world and polychromatic model reconstructions for the aberrated tri-arm sparse aperture system with wavefront error on the order of 0.25 waves rms. All of the restorations in this particular case make use of the "optimal" spectrally averaged system transfer function deduced in the previous study. The comparison that is achieved in this example is the impact of uncertainty in the noise-to-object power spectrum ratio when the "perfect" spectrally weighted OTF is captured in the Wiener filter design. For this exercise, a panchromatic equivalent image of the original HyMap-derived polychromatic scene used to perform the simulations appears in Figure 117(a). For purposes of comparison, the gray-world model restoration result assuming exact system OTF and power spectrum knowledge has been provided in Figure 117(b). One should recall that this simulation fails to adequately capture the spectral character of the scene and system OTF, so the deleterious effect of the spectrally induced ringing is not present in this restoration. The latter quality effect is captured by the restoration displayed in Figure 117(d), the prediction achieved with the enhanced spectral fidelity model assuming perfect OTF and power spectrum ratio knowledge. As observed previously, this restoration exhibits all of the artifacting character introduced in previous sections, seriously degrading the quality of the collected imagery.

To address the impact of noise-to-object power spectrum uncertainty, the restoration in Figure 117(c) again involves the enhanced polychromatic model and perfect phase (i.e., system OTF) knowledge, but treats the power spectrum ratio as a constant that must be tweaked to acquire near-optimal image quality. Such a Wiener filter implementation is fairly common practice within the larger remote sensing community. As observed in this restoration, the difference between the estimated and exact power spectrum ratio introduces a "smoothing" effect that blurs edges within the scene content and reduces the perceived level of the artifacting. Closer examination of this restoration still indicates the existence of the artifacting phenomenon (especially when a softcopy flicker test with the gray-world model result is conducted), so the natural averaging effect of collection uncertainty does not entirely mitigate the effect. In addition, with the reduction in edge response (as manifested by the lower RER for this case), the overall image quality is actually reduced as a consequence of

this unknown system parameter. This result is certainly consistent with one's intuition on the impact of unknowns in the collection and restoration process.

(a) Spectrally Weighted Object
(formed from original color object)

(b) Gray-World Model Restoration
(*a priori* power spectrum knowledge)
nrmse: 0.0692; RER: 0.619; G_{rms}: 30.6

(c) Spectrally Averaged OTF Restoration
(no power spectrum knowledge)
nrmse: 0.1035; RER: 0.546; G_{rms}: 14.7
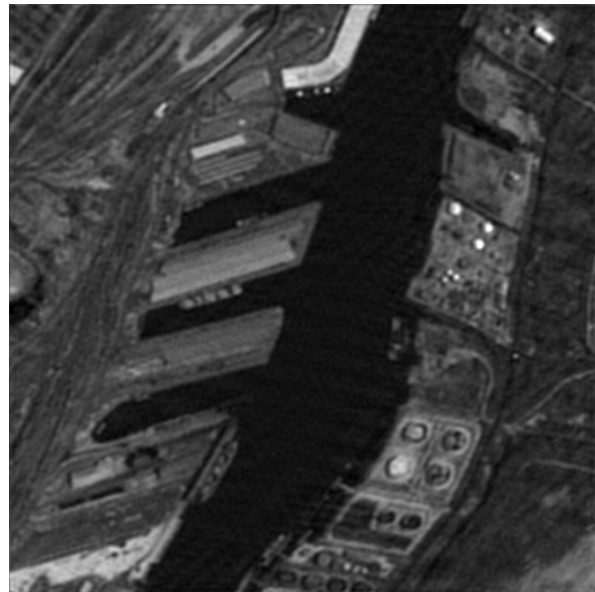
(d) Spectrally Averaged OTF Restoration
(*a priori* power spectrum knowledge)
nrmse: 0.0985; RER: 0.619; G_{rms}: 30.6

Figure 117: Integrated panchromatic simulation of an aberrated tri-arm sparse aperture with various restoration filters (0.25 waves rms piston, tip/tilt error).

The apparent visual degradation in the restoration involving collection uncertainty is confirmed by the metric data, as the computed *nrmse* for this scenario is ~5% worse than the equivalent spectral model restoration with perfect knowledge and ~50% worse than the gray-world model approximation with no unknowns. As this is a real-world effect, the dual impact of spectral artifacting due to amplification of the modulation mismatch in the Wiener filter and reduced sharpness resulting from imperfect restoration due to collection uncertainty can be a significant issue for moderately aberrated sparse aperture imaging systems. Unfortunately, this general character of the collection process for these unique systems has not been adequately addressed by the traditional gray-world model approach in the past. Clearly, depending on the nature of the collection scenario and imaging system characteristics anticipated, one needs to carefully consider the use of enhanced spectral fidelity when evaluating these advanced optical configurations.

5.6 Analysis Excursions

The final section in this chapter documents the results acquired from several analysis excursions performed with the proof-of-concept modeling capability developed for this research effort. These modeling trades are far from exhaustive in nature, but they do provide initial insight into some fundamental principles of the imaging problem as well as unique aspects of sparse aperture imaging systems. The excursions that will be detailed in the discussion below include preliminary analyses of noise level impact on restoration quality, detector integration time versus optical fill factor, impact of no optical phase knowledge on Wiener filtered products, and comparison of various aberration types on overall restored image quality. All of the results presented in this section represent cursory analysis that deserves more attention in future research. They have been included in this dissertation for illustrative purposes to demonstrate some of the capability available within the spectral model developed for this effort.

5.6.1 Filtering Under Different Noise Levels

The first system analysis to be captured in this section illustrates qualitatively through use of derived imagery products the impact of noise on the restoration process. This particular study was performed using the interim quasi-monochromatic capability resident within the

proof-of-concept simulation model. Although the monochromatic results are not necessarily reflective of the final integrated signal for a given collection scenario, the emphasis of this investigation was placed on characterizing the qualitative nature of system noise on restoration quality. As such, the color composites available through the monochromatic analysis provide a unique aid in visualizing spectrally diverse noise and its consequence on sparse aperture image restoration. Consequently, in all the imagery products included in this section, individual monochromatic spectral planes have been combined to form an RGB color composite image for purposes of illustration.

Figure 118 provides a series of diagrams that introduce the nature of the analysis excursion that was performed through this effort. Figure 118(a) displays the two optical configurations that were evaluated in this study, an aberrated tri-arm sparse aperture system with 0.20 waves rms of wavefront error at the mean wavelength and a diffraction-limited filled circular aperture of commensurate physical encircled size. There is absolutely no significance to the arbitrarily selected physical diameter pursued in this exercise. The critical aspect of the evaluation is that the two apertures involve the same encircled diameter. As with previous investigations, the fill factor F_{fill} associated with the sparse aperture imaging system is 0.173. Figure 118(b) depicts the WASP-derived polychromatic object scene that was utilized in the evaluation. This color image provides an excellent benchmark for comparing the quality of restored imagery products under the different image noise conditions pursued in this study. In Figure 118(c) and (e), one observes the degraded tri-arm sparse aperture monochromatic imagery predictions for noiseless (i.e., infinite SNR) and high-SNR scenarios prior to restoration. Based on those detected imagery examples, one acquires the pseudo-inverse and Wiener filter restorations that appear in Figure 118(d) and (f), respectively. In all of these examples, an "optimal" filter has been developed through use of the known system OTF and noise-to-object power spectrum ratio, as appropriate.
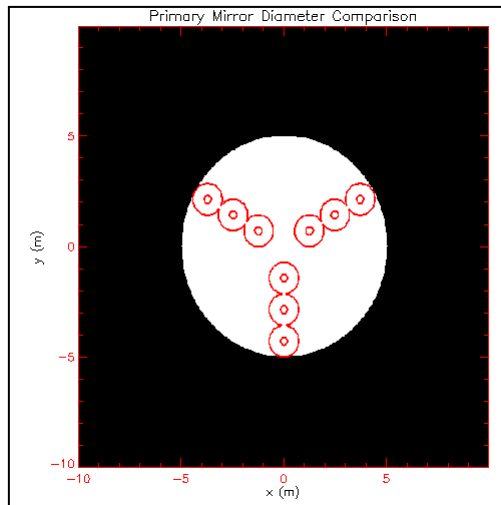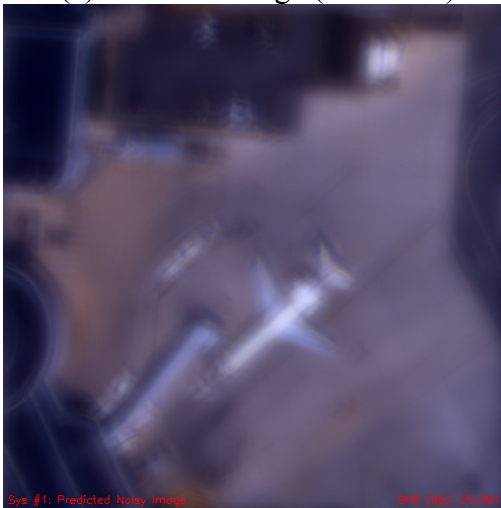
(a) Pupil Configuration

(b) Original Object
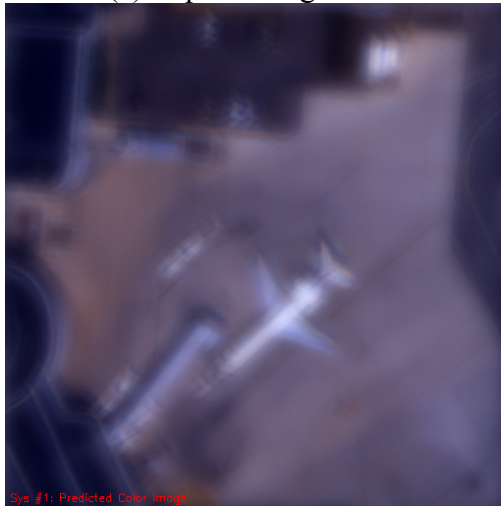
(c) Detected Image (No Noise)

(d) Inverse-Filtered Image

(e) Detected Image (SNR = 337.4)

(f) Wiener-Filtered Image

Figure 118: Comparison of inverse and Wiener filtering results for an aberrated tri-arm sparse aperture (0.20 waves rms piston, tip/tilt).

247

In these examples, the individual monochromatic planes were restored with the exact system OTF that was responsible for the original degradation. As a result, the exercise pursued in this section is fundamentally different from the previous quasi-monochromatic analyses, which utilized the central wavelength OTF to "simulate" the broadband detection scenario. In this case, the quasi-monochromatic model results are utilized to highlight the character of the restoration process under optimal conditions. Given these evaluation conditions, one can subsequently draw conclusions on the optimal nature of the overall restoration process under different noise conditions.

In the noiseless case, for instance, one can theoretically reproduce the exact object through use of an inverse filter given perfect knowledge of the system transfer function. With real-world digital imagery, one can almost accomplish the same result with implementation of a pseudo-inverse filter, as demonstrated by the restoration appearing in Figure 118(d) for the noiseless detection case. Comparison of the imagery in Figure 118(b) and (d) confirms that the original object can effectively be recovered in the absence of any noise and with perfect system OTF knowledge. In a similar manner, the example in Figure 118(f) involving restoration in the presence of low noise demonstrates that the Wiener filter provides near-optimal recovery of the original object when the detection SNR is high (~337 in this case). Certainly, one can detect the presence of a small level of correlated noise in the softcopy representation of Figure 118(f), but the overall quality of the restoration is remarkably close to the original object quality.

To address other noise levels, Figure 119 provides additional examples of the performance of the Wiener filter under "optimal" conditions (i.e., known system OTF and power spectrum ratio). In these simulations, considerable noise has been incorporated into the detection scenario to capture monochromatic predictions in Figure 119(c) and (e) that are more representative of remote sensing applications. Based on these predictions, Figure 119(d) and (f) provide near-optimal Wiener filter restorations of the individual monochromatic image planes for the conditions under evaluation. Similar prediction products for the noiseless case have been provided in Figure 119(a) and (b) to highlight the extent of the degradation that occurs as the result of increased noise power in the detected imagery. As observed in this

imagery, the addition of noise obviously degrades the quality of the final restored product, resulting in the introduction of ringing or artifacting once the noise level begins to compete with the signal at certain spatial frequencies. Although the restored imagery appears to be very good quality, these examples highlight how the introduction of noise impacts quality *for the optimal case.* One must recall that they are not very representative of potential real-world applications, since each color plane is restored individually through absolute knowledge of the collection scenario (including system OTF and noise-to-object power spectrum ratio). It is not difficult to imagine how real-world collection uncertainty can amplify the degradation mechanism introduced here to produce unacceptable image restorations from a quality perspective. Certainly, the results reported in previous sections have provided a good indication of how detrimental the inclusion of real-world collection effects can be on overall image quality.

The final phase of this particular analysis excursion provides a precursor to the investigation that appears in the next section. For the mid-level SNR case, a comparative evaluation was performed with a diffraction-limited filled circular aperture, providing the detected imagery and associated restoration depicted in Figure 120(c) and (d), respectively. For purposes of illustration, the aberrated tri-arm sparse aperture imagery prediction and restoration appear in Figure 120(a) and (b). As noted through comparison of this imagery, the filled circular aperture can achieve restoration quality commensurate with that acquired from the sparse aperture imaging system under considerably less favorable noise conditions. In this particular contrived example, the aberrated sparse aperture system with a fill factor of 0.173 requires ~18 times better detection SNR to achieve image quality on par with the filled aperture. This is obviously a direct reflection of the highly demodulated system transfer function and the low aperture fill factor associated with the sparse aperture configuration explored in this study, consistent with the theoretical development from Fienup (2000) described at length in Chapter 3. Clearly, the proof-of-concept model provides a testament to the relative integrity of the previously derived sparse aperture theory. This point will receive additional attention in the section to follow.

(a) Detected Image (No Noise) (b) Inverse-Filtered Image
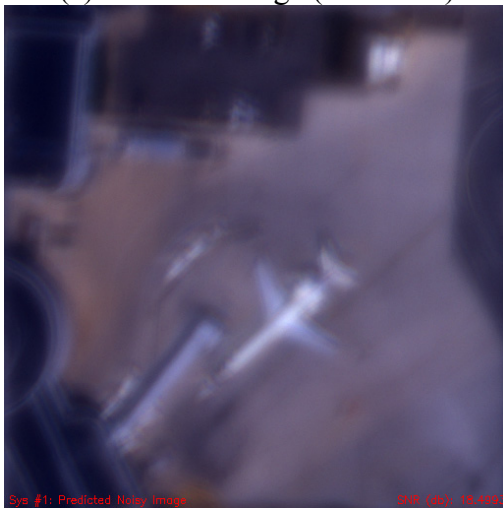
(c) Detected Image (SNR = 70.9) (d) Wiener-Filtered Image (SNR = 70.9)

(e) Detected Image (SNR = 37.8) (f) Wiener-Filtered Image (SNR = 37.8)

Figure 119: Comparison of inverse and Wiener filtering results for an aberrated tri-arm sparse aperture (0.20 waves rms piston, tip/tilt).

Tri-arm sparse aperture system with 0.20 waves rms piston, tip/tilt

(a) Detected Image (SNR = 70.9)   (b) Wiener-Filtered Image (SNR = 70.9)

Diffraction-limited filled circular aperture system
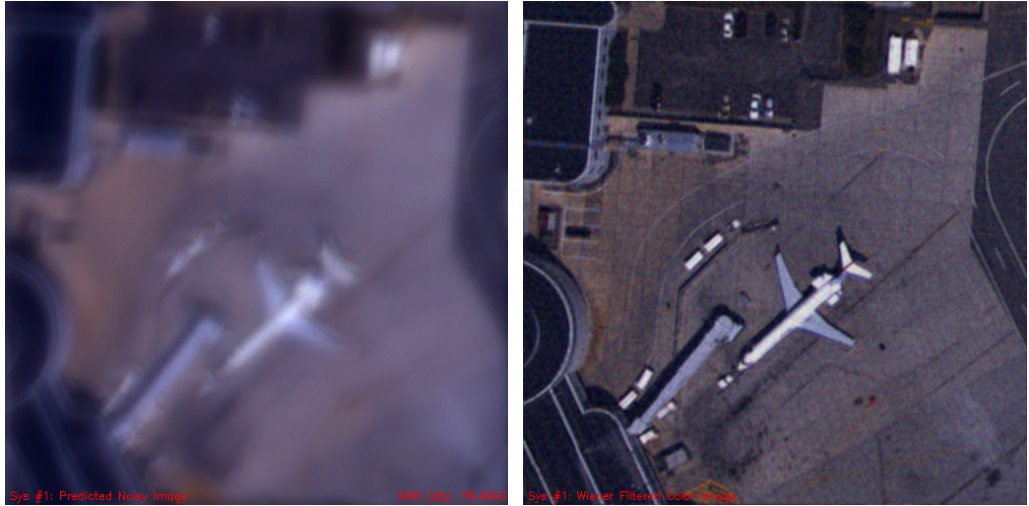

(c) Detected Image (SNR = 3.94)   (d) Wiener-Filtered Image (SNR = 3.94)

Figure 120: Comparison of the Wiener filtering results for an aberrated tri-arm sparse aperture and diffraction-limited circular filled aperture.

5.6.2 Integration Time vs. Fill Factor

As indicted in Section 5.6.1, the proof-of-concept model developed for this research effort can provide evidence to verify the relative accuracy of sparse aperture theory on collection SNR or detector integration time. As discussed in Chapter 3, Fienup (2000) has shown through appropriate analysis that the integration time T_{int} must be increased by a factor larger than that required to just accommodate the loss of photons resulting from the reduced fill factor. At a top-level, his analysis predicts that a general sparse aperture system with a relative plateau in the mid-spatial frequency regime should require an increase in the integration time by the cube of the inverse fill factor, or in other words $T_{int} \propto F_{fill}^{-3}$. Fiete (2002) subsequently showed through detailed system modeling and psychophysical analysis that the integration time typically must increase in proportion to somewhere between F_{fill}^{-2} and F_{fill}^{-3}, depending on the specific aperture configuration under consideration. During this research effort, those figures of merit were qualitatively studied through use of the modeling capability developed for this dissertation.

To highlight the character of the sparse aperture integration time (or equivalent detection SNR) required to achieve comparable quality to a filled aperture system, the quasi-monochromatic capability resident within the model will again be exercised. As before, the rationale behind use of the monochromatic analysis is the fact that RGB color composite images can be generated to highlight the visual effects of interest. Of course, there is nothing fundamental about that choice, and one could easily have accomplished this same exercise utilizing the full-fledged, integrated signal model. Through use of the appropriate monochromatic prediction products, Figure 121 provides color samples of the restorations achieved for (a) a diffraction-limited filled circular aperture and (b) an aberrated tri-arm sparse aperture system when the detector integration time for the latter is only increased by the inverse fill factor (i.e., $T_{int} \propto F_{fill}^{-1}$). For this investigation, the sparse aperture system is aberrated by 0.10 waves rms of piston, tip/tilt (PTT) at the mean wavelength. Under the first scenario, one effectively increases the dwell time associated with the sparse aperture by an amount that only accommodates the reduction in incident photons through the optical pupil. As observed in Figure 121, this increase in integration time is not sufficient to achieve a

252

restoration product that rivals the quality of the equivalent filled aperture image. The differences between the two restorations become very apparent if one performs a softcopy flicker test.

The fact that commensurate quality is not achieved through an integration time proportional to F_{fill}^{-1} is obviously a direct result of the demodulated character of the sparse aperture system transfer function. As a result of the latter, one must effectively over-dwell in order to increase detection SNR and achieve the desired product quality. As a demonstration of Fienup's derived proportionality, Figure 122 depicts the quasi-monochromatic restoration products one acquires when the sparse aperture system integration time abides by the relationship $T_{\text{int}} \propto F_{\text{fill}}^{-3}$. As witnessed in this figure, one does actually achieve a very comparable restoration product when the integration time is increased by the cube of the inverse fill factor, confirming to first order the obvious need to over-dwell in this manner. Based on the work of Fiete, there is little doubt that one could reduce the integration time slightly and still achieve very comparable image quality with the filled aperture. The key point that was emphasized in this investigation, however, is that the integration time associated with a sparse aperture system must be increased considerably longer than that simply required to make up for lost photons. In addition, that increase in dwell time is generally on the order of an inverse fill factor power relationship like F_{fill}^{-3}, entirely consistent with the original first-principles analysis performed by Fienup. The final reinforcement of that point is provided by the sparse aperture image restorations displayed in Figure 123, which clearly highlight the need to over-dwell in order to reduce the level of noise amplification one naturally encounters through the Wiener filtering process and ultimately acquire near-optimal product quality for the collection conditions studied in this exercise.

(a) Filled Circular Aperture Restored Image
σ_{WFE}: diffraction limited; RER: 0.840; G_{rms}: 1.82; SNR: 33.6

(b) Tri-arm Sparse Aperture Restored Image
σ_{WFE}: 0.10 waves rms PTT; RER: 0.501; G_{rms}: 3.75; SNR: 33.3

Figure 121: Comparison between tri-arm and filled aperture images
with the sparse aperture integration time increased to accommodate
lost photons only ($T_{\mathrm{int}} \propto F_{\mathrm{fill}}^{-1}$).

254

(a) Filled Circular Aperture Restored Image
σ_{WFE}: diffraction limited; RER: 0.840; G_{rms}: 1.82; SNR: 33.6

(b) Sparse Aperture Restored Image
σ_{WFE}: 0.10 waves rms PTT; RER: 0.824; G_{rms}: 12.2; SNR: 273.4

Figure 122: Comparison between tri-arm and filled aperture images with the sparse aperture integration time increased to accommodate lost photons and degraded OTF ($T_{\mathrm{int}} \propto F_{\mathrm{fill}}^{-3}$).

255

(a) Integration time: $T_{\text{int}} \propto F_{\text{fill}}^{-1}$

σ_{WFE}: 0.10 waves rms PTT; RER: 0.501; G_{rms}: 3.75; SNR: 33.3

(b) Integration time: $T_{\text{int}} \propto F_{\text{fill}}^{-3}$

σ_{WFE}: 0.10 waves rms PTT; RER: 0.824; G_{rms}: 12.2; SNR: 273.4

Figure 123: Comparison between tri-arm sparse aperture images with varied dwell time to illustrate the need to accommodate both lost photons and degraded OTF.

5.6.3 Phase Knowledge Sensitivity

Many of the modeling scenarios documented in this dissertation used the exact system optical transfer function responsible for the original degradation in construction of the appropriate restoration filter. In this context, one in effect assumes perfect knowledge of the optical phase distribution or character of the associated wavefront error across the exit pupil during the collection period. While certain techniques have been investigated as options for providing information on the nature of the wavefront error present during a given collection, these methodologies are certainly not flawless and one would consequently anticipate some uncertainty in the knowledge of in-situ phase error. To address this concern, several preliminary sensitivity runs were performed with the enhanced spectral fidelity model under various levels of phase uncertainty.

This section highlights the criticality of incorporating knowledge of transfer function phase into the development of the restoration filter. On the opposite end of the spectrum from perfect knowledge, it demonstrates the quality implications of having no knowledge of the wavefront errors during the detection scenario. To that end, several exercises were performed with the tri-arm sparse aperture imaging system at different levels of aberration, assuming both perfect and no knowledge of the optical phase errors across the pupil. One will find examples of these model iterations for 0.10 and 0.25 waves rms of wavefront error in the figures provided in this section. As with previous exercises, the tri-arm sparse aperture imaging system has a fill factor of 0.173. Consistent with the previous discussion on the "optimal" filter, a spectrally averaged system OTF has been developed for all the restorations in this analysis. In addition, for the case of no phase knowledge, the *a priori* diffraction-limited transfer function is used within the Wiener filter design. Finally, to eliminate uncertainty in the noise-to-object power spectrum ratio as a complicating factor, the exact ratio derived from the detected imagery is used in the restoration filter construction. As a result of the latter, the differences that are observed in the restorations will principally be a function of the knowledge in optical phase. Although representative of the extreme cases, the restorations associated with perfect and no phase knowledge are instructive as they bound the range of potential optical performance one may actually encounter operationally.

Figure 124 depicts a typical random piston, tip/tilt phase profile one may experience with an aberration level of 0.10 waves rms at the mean wavelength. Given that distribution of phase, one can derive through the complex autocorrelation of the pupil the aperture MTF that appears in Figure 125. As observed in this figure, the MTF associated with a slightly aberrated sparse aperture imaging system exhibits some demodulation and introduction of minor nulling across the spatial frequency plane. These diagrams illustrate that the case explored in this analysis excursion is completely consistent with the phase profile and transfer function character explored previously for this level of aberration. For the restoration involving perfect knowledge, this exact phase distribution and transfer function are used within the restoration process. For the case involving unknown phase, however, no phase distribution is assumed and the classic diffraction-limited tri-arm transfer function is prescribed within the Wiener filter.

With this problem definition, Figure 126 provides the range of simulation products that were acquired for this particular sensitivity study. For comparative purposes, a panchromatic equivalent object image and the detected imagery prediction (prior to restoration) are displayed in Figure 126(a) and (b), respectively. Figure 126(c) shows the restoration achieved when the optical phase is perfectly accounted for in the Wiener filter, and Figure 126(d) depicts the post-processed imagery when no phase knowledge is incorporated into the reconstruction. Visually, it is readily apparent how critical it is to capture phase in the overall restoration process, as the case involving no phase knowledge manifests significant blurring and loss of image sharpness. This loss in image quality is further emphasized by the metric data, as the computed *nrmse* increases by ~110% as a consequence of not knowing the phase errors contributing to the original degraded imagery. Despite the relatively low level of 0.10 waves rms of wavefront error, the overall interpretability of the restored imagery is dramatically impacted by the failure to accommodate phase in the Wiener filter. As a result, this exercise has definitely highlighted the criticality of including optical phase in the restoration process for even modest levels of aberration and/or subaperture dephasing.

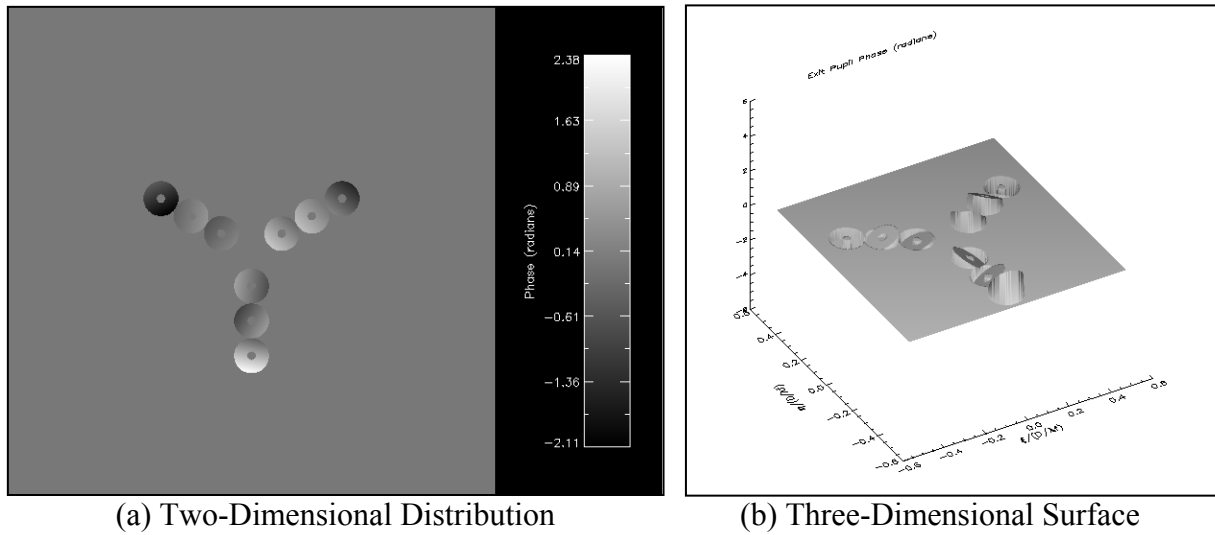(a) Two-Dimensional Distribution   (b) Three-Dimensional Surface

Figure 124: Random phase profile for the central wavelength of an aberrated tri-arm sparse aperture (0.10 waves rms piston, tip/tilt error).

(a) Two-Dimensional Image   (b) Three-Dimensional Surface
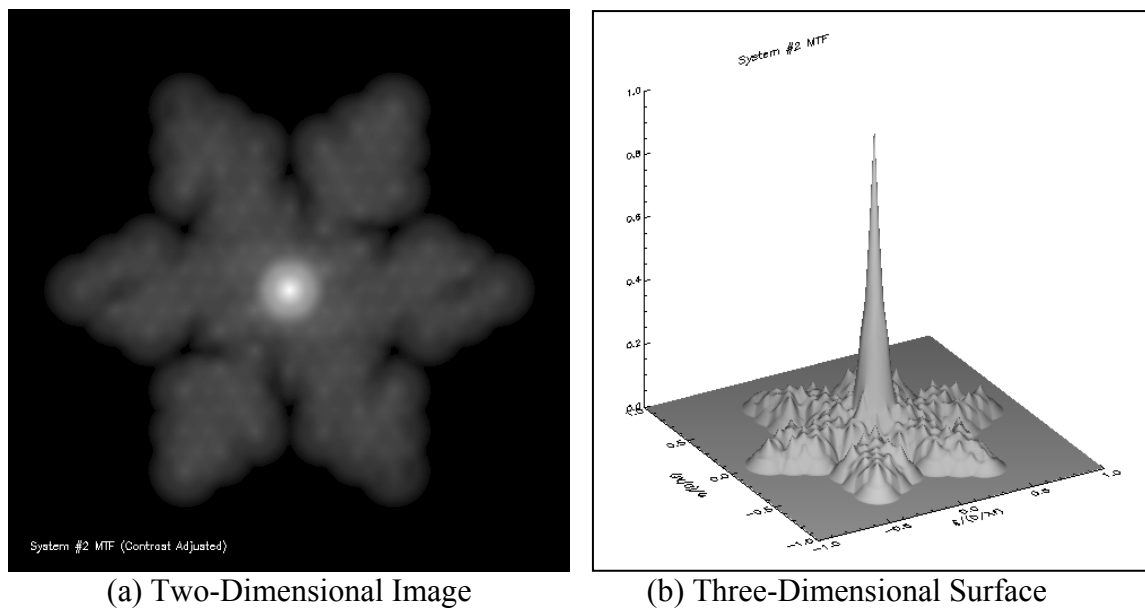
Figure 125: Modulation transfer function for an aberrated tri-arm sparse aperture (0.10 waves rms piston, tip/tilt error).

(a) Spectrally Weighted Object

(b) Detected Panchromatic Image

(c) Restored Panchromatic Image
(perfect phase knowledge)
nrmse: 0.0715

(d) Restored Panchromatic Image
(no phase knowledge)
nrmse: 0.1504

Figure 126: Integrated panchromatic simulation of an aberrated tri-arm sparse aperture with spectrally weighted OTF restoration (0.10 waves rms piston, tip/tilt error).

To explore this issue further, additional iterations were performed with the tri-arm sparse aperture imaging system aberrated by 0.25 waves rms of piston, tip/tilt error at the mean wavelength. Given this level of aberration, a representative optical phase distribution and associated aperture MTF appear in figures 127 and 128, respectively. The character of these key system parameters is entirely consistent with that observed in previous exercises. Once again, the objective of this analysis excursion was to explore the criticality of phase knowledge by performing simulations that capture the phase knowledge and OTF structure perfectly, followed by complete failure to accommodate any phase knowledge whatsoever.

Figure 129 illustrates the different simulation products that were derived for this particular sensitivity study. In this case, the observed implications of not including optical phase in the Wiener filter restoration are severe. As attested to by the restoration depicted in Figure 129(d) for the scenario involving no phase inclusion, complete lack of knowledge in the in-situ wavefront errors is catastrophic when aberrations approach levels of 0.25 waves rms. In this restoration, the failure to accommodate the optical phase has produced a seriously defocused image, illustrating a significant loss of interpretability based on comparison with the panchromatic object in Figure 129(a). In fact, the restored image quality associated with the case entailing no phase knowledge is only marginally better than the original detected imagery depicted in Figure 129(b). In addition, despite the fact that the perfect knowledge scenario in Figure 129(c) exhibits the spectrally induced artifacting effect discussed earlier, it demonstrates considerably better quality than that associated with its counterpart involving no phase knowledge in Figure 129(d). This observation is confirmed by comparison both visually and through use of the mean-level image statistics. With regard to the latter, the *nrmse* metric really highlights the deleterious nature of the lack of phase knowledge in the restoration process as it increases by an impressive 184% (almost a factor of 3)!

Once again, this analysis excursion provides convincing evidence that some level of phase knowledge is absolutely essential in reconstructing highly degraded sparse aperture system imagery. Of course, this cursory analysis only touched upon the extremes of the potential performance envelope. Future research effort should focus on the sensitivity of image quality to a range of optical phase uncertainty that falls in between these extremes, as it is

highly likely that any potential future application in the sparse aperture arena will have some means, albeit imperfect, of ascertaining the levels of wavefront error degradation during the collection. This exercise has certainly demonstrated the criticality of such techniques.

(a) Two-Dimensional Distribution   (b) Three-Dimensional Surface

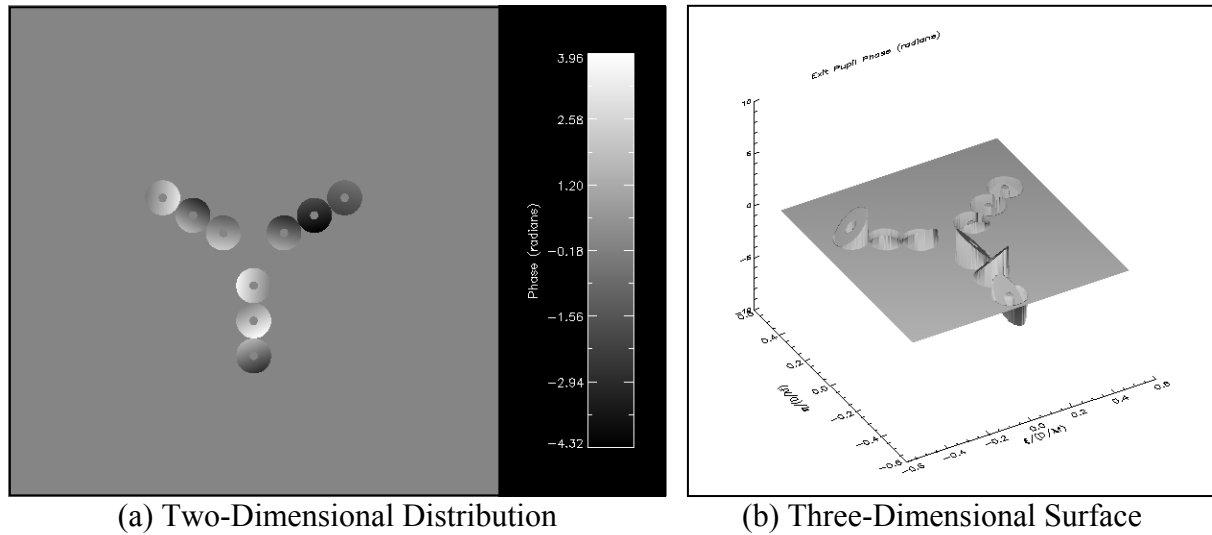Figure 127: Random phase profile for the central wavelength of an aberrated tri-arm sparse aperture (0.25 waves rms piston, tip/tilt error).

(a) Two-Dimensional Image   (b) Three-Dimensional Surface
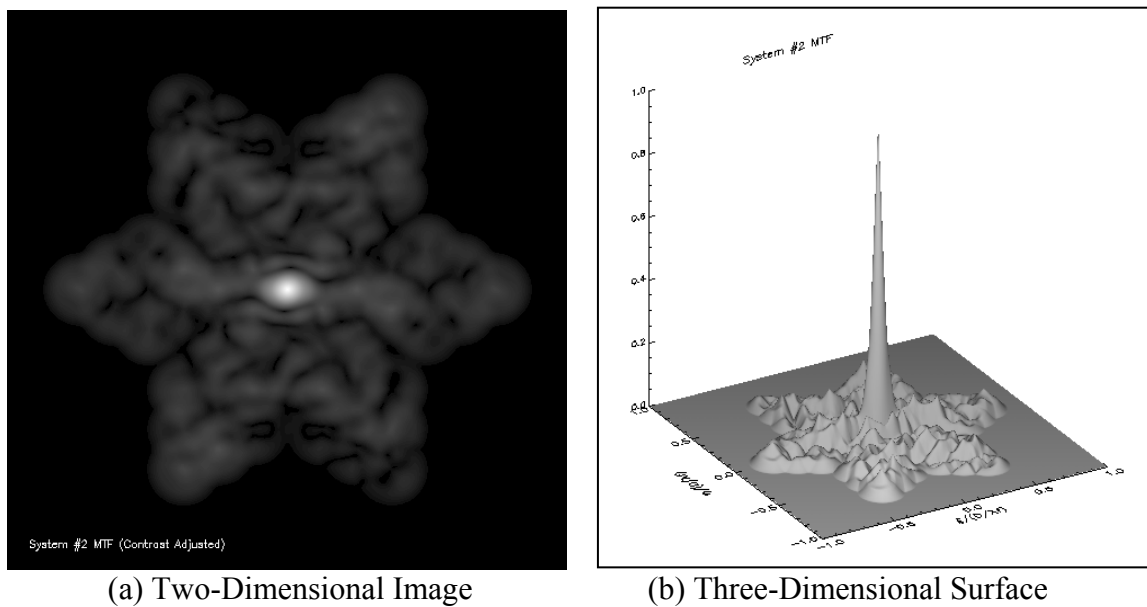
Figure 128: Modulation transfer function for an aberrated tri-arm sparse aperture (0.25 waves rms piston, tip/tilt error).

(a) Spectrally Weighted Object
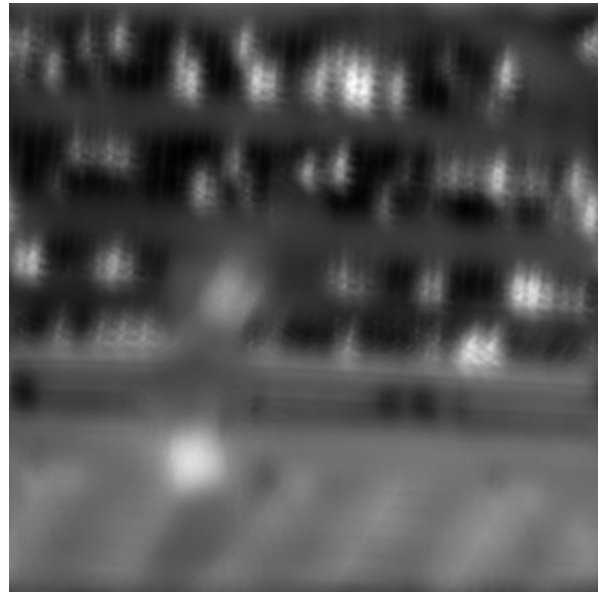
(b) Detected Panchromatic Image

(c) Restored Panchromatic Image
(perfect phase knowledge)
nrmse: 0.1064
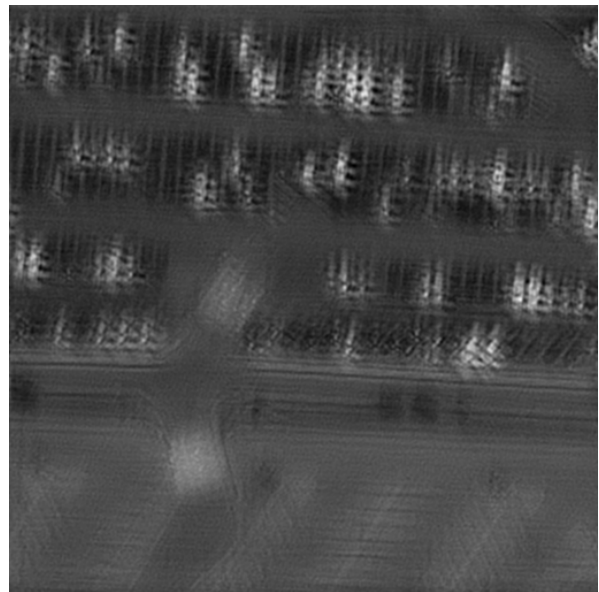
(d) Restored Panchromatic Image
(no phase knowledge)
nrmse: 0.3025

Figure 129: Integrated panchromatic simulation of an aberrated tri-arm sparse aperture
with spectrally weighted OTF restoration (0.25 waves rms piston, tip/tilt error).

5.6.4 Subaperture Dephasing vs. Optical Aberrations

The final analysis excursion that was pursued in the course of this research effort involved an initial investigation of the impact of different types of aberration on the quality of sparse aperture imagery. The objective of this particular trade study was to investigate the character of a typical sparse aperture imaging system under different aberration conditions, comparing the impact of pure piston, tip/tilt errors to a random combination of system focus, third-order Seidel and higher-order aberrations. The general concept behind this analysis focus was to address the sensitivity of restored image quality to typical manufacturing errors (represented by the random distribution of various aberrations) as compared to aberrations experienced due to classic subaperture dephasing issues (i.e., piston, tip/tilt error). The results reproduced in this dissertation for this area have been included to demonstrate the capabilities resident within the proof-of-concept system model. They tend to be anecdotal in nature and consequently deserve considerably more attention in future research endeavor. As a consequence, the output from a representative run will be documented in the discussion to follow but only conclusions of a general overall nature will be drawn. Further detailed development of this potential sensitivity study area is left to a future investigator.

For this exercise, figures 130 through 132 provide different views of typical optical phase distributions for the two scenarios under investigation. In (a), these figures depict a random phase profile consisting of system defocus, spherical, astigmatism, coma, and various higher order errors applied to the nominal tri-arm sparse aperture pupil configuration to simulate the effect of manufacturing error. Conversely, these diagrams display the traditional dephasing mechanisms of piston and tip/tilt in (b). By design, both of these phase profiles represent wavefront errors on the order of 0.10 waves rms at the mean wavelength to enable side-by-side comparison. Based on these phase distributions, one acquires the aperture transfer functions that are displayed in figures 133 and 134. It is interesting to note that for this particular example, the random distribution of manufacturing errors tends to reduce the overall level of the modulation on a relatively uniform basis. On the other hand, the random piston, tip/tilt dephasing error has a greater tendency to lead to focused reduction of the modulation in localized regions, thereby inducing nulls in the spatial frequency coverage. Whether this observed behavior is statistically normal for this exercise is unknown at this

time, although several iterations of the random seed responsible for generating the wavefront error profile produced similar results. Based on this anecdotal evidence, this sensitivity area is obviously ripe for additional investigation in the future.

(a) Random Manufacturing Aberrations   (b) Random Piston, Tip/Tilt

Figure 130: Random phase profile for the central wavelength of an aberrated tri-arm sparse aperture (wavefront error of 0.10 waves rms).

(a) Random Manufacturing Aberrations   (b) Random Piston, Tip/Tilt

Figure 131: Random phase profile for the central wavelength of an aberrated tri-arm sparse aperture (wavefront error of 0.10 waves rms).

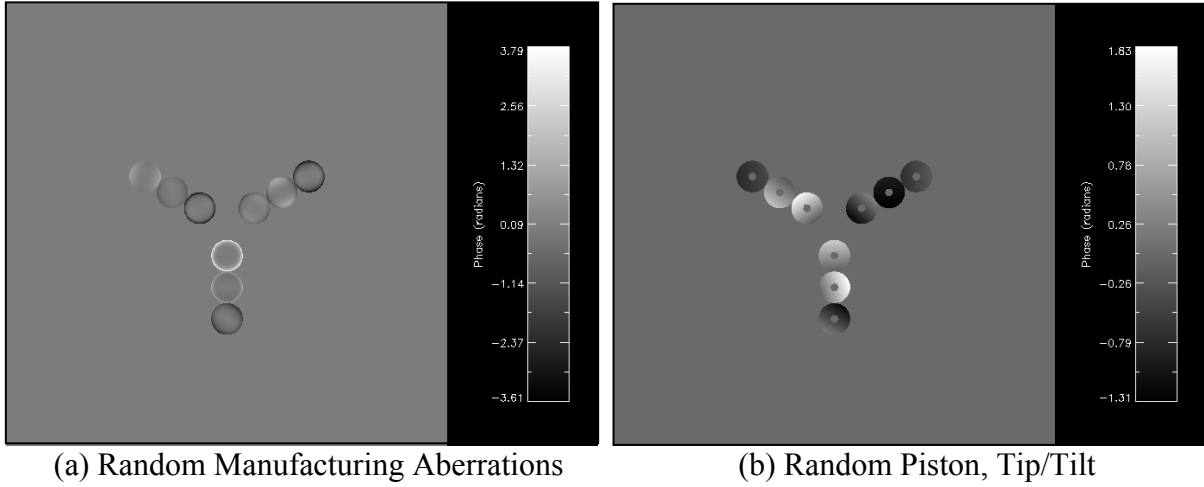(a) Random Manufacturing Aberrations   (b) Random Piston, Tip/Tilt
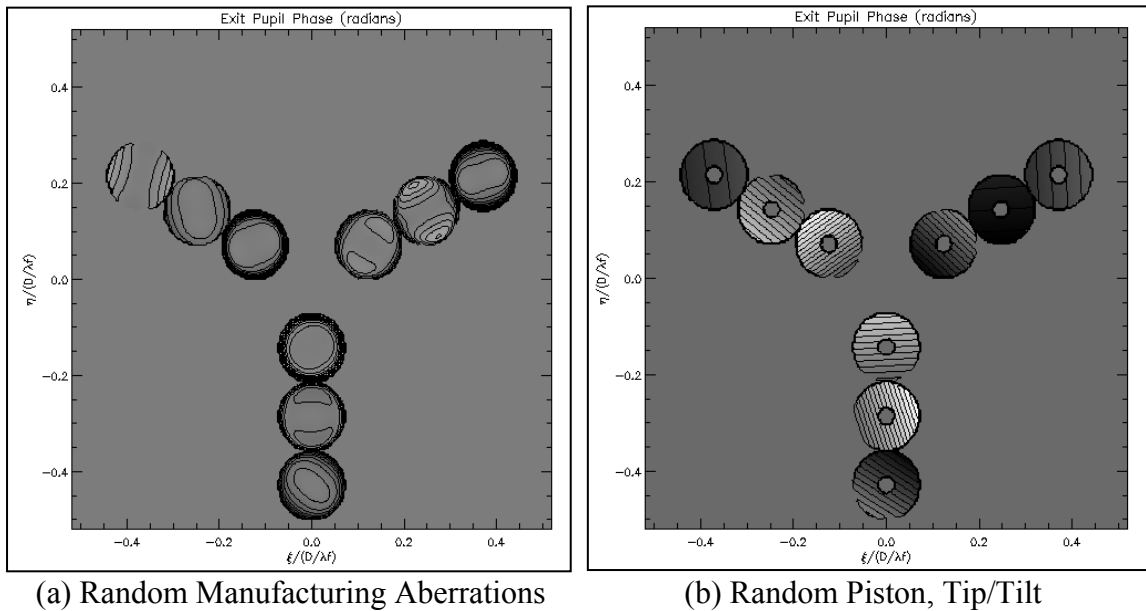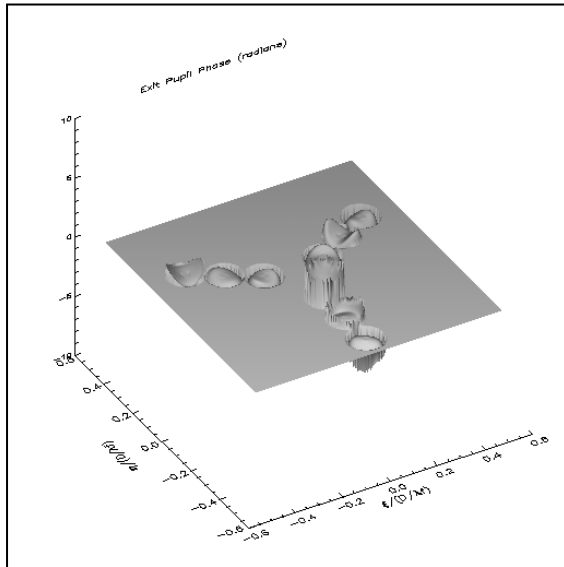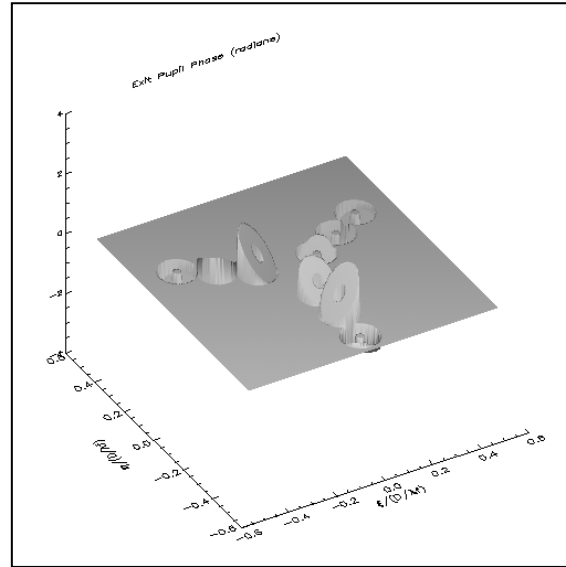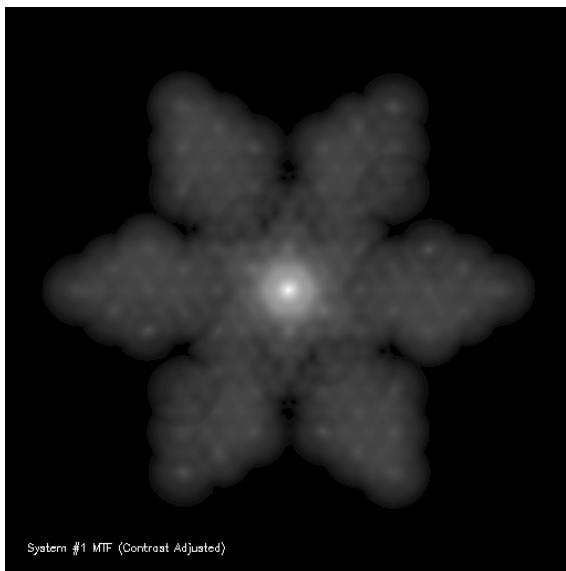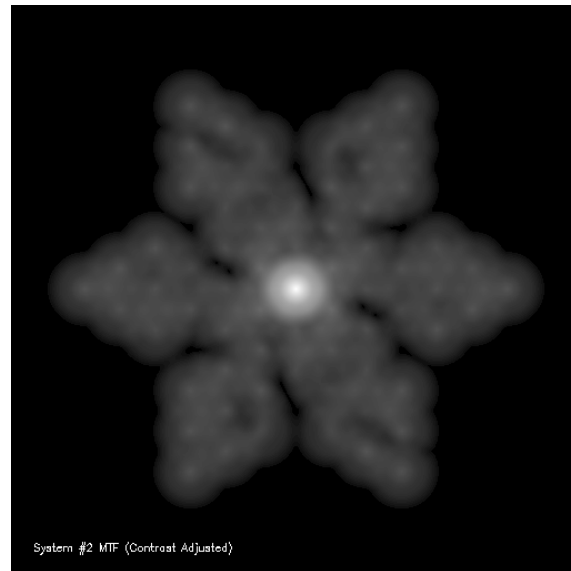
Figure 132: Random phase profile for the central wavelength of an aberrated tri-arm sparse aperture (wavefront error of 0.10 waves rms).

(a) Random Manufacturing Aberrations   (b) Random Piston, Tip/Tilt

Figure 133: Modulation transfer function for an aberrated tri-arm sparse aperture (wavefront error of 0.10 waves rms).

266

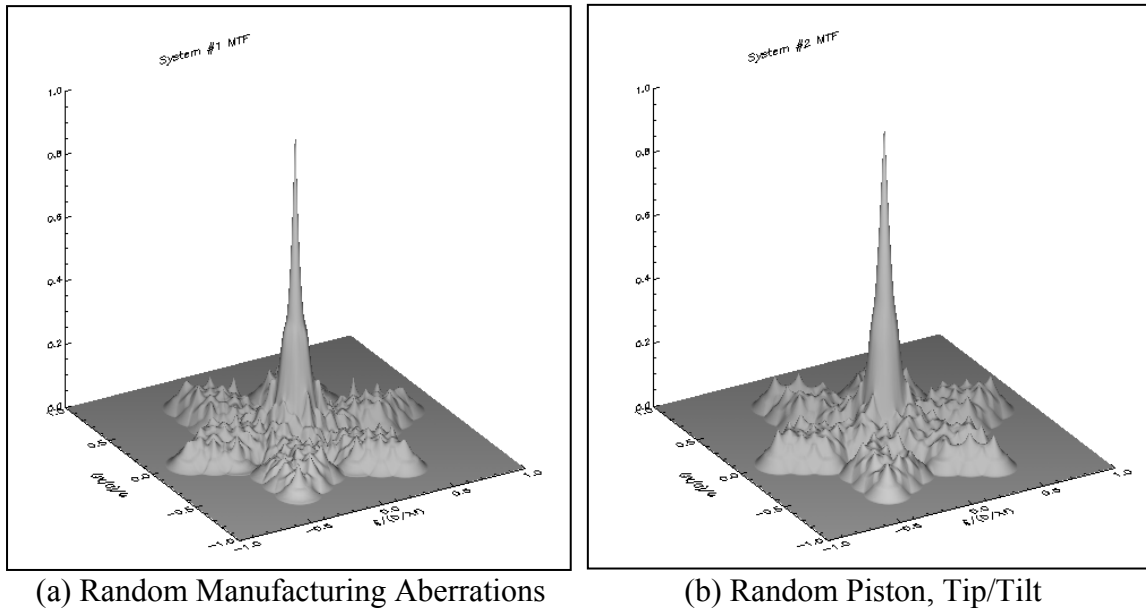| (a) Random Manufacturing Aberrations | (b) Random Piston, Tip/Tilt |

Figure 134: Modulation transfer function for an aberrated tri-arm
sparse aperture (wavefront error of 0.10 waves rms).

Given the phase distributions and associated transfer functions depicted here, the enhanced spectral fidelity model produces restorations of the quality exhibited in Figure 135. At a top level, it appears that the predictions for both phase profiles result in reasonably comparable quality at this level of aberration (i.e., wavefront error of 0.10 waves rms). Even through a softcopy flicker test, the differences between the two restorations appear marginal at best to the untrained observer. Figure 136 provides a magnified region of the full image restorations for the two cases investigated in this study. Although some minor image structure differences can be noted in the softcopy, it would appear to be debatable if there is any detectable difference in interpretability between the two images. Although the quality metrics (*nrmse* and RER) highlight a small variation in quality between the two simulations, one really needs to question whether the observed ~1% difference is truly statistically significant. Based on the anecdotal results presented here, one would have to conclude that the two aberration cases essentially produce imagery of comparable quality. As stated before, however, these preliminary iterations are definitely worthy of further study in the context of a rigorously defined sensitivity trade study. In that vein, the exercise has at least demonstrated that the proof-of-concept modeling capability developed for this research effort has the potential to support such a trade.

267

(a) Restored Panchromatic Image
(manufacturing errors)
nrmse: 0.0733; RER: 0.838; G_{rms}: 17.6

(b) Restored Panchromatic Image
(piston, tip/tilt)
nrmse: 0.0722; RER: 0.853; G_{rms}: 16.8

Figure 135: Integrated panchromatic simulation of an aberrated tri-arm sparse aperture with spectrally weighted OTF restoration (wavefront error of 0.10 waves rms).

(a) Restored Panchromatic Image
(manufacturing errors)
nrmse: 0.0733

(b) Restored Panchromatic Image
(piston, tip/tilt)
nrmse: 0.0722

Figure 136: (Magnified) Integrated panchromatic simulation of an aberrated tri-arm sparse aperture with spectrally weighted OTF restoration (wavefront error of 0.10 waves rms).

Chapter 6

Conclusions

The remote sensing community continues to show growing interest in fielding imaging platforms that strike a balance between extended-duration access, high spatial resolution and spectral diversity. Previous research has indicated that sparse aperture systems may hold the key for enabling missions that exhibit the required optical performance and the desired access time. These systems typically consist of an array of smaller subapertures or optical systems that are phased to synthesize a larger effective collection aperture. Of course, critical technological challenges such as subaperture pupil matching, subaperture phasing over a fraction of a wavelength, and imaging platform stability over the longer integration times associated with these systems must be overcome. If demonstrated as technically viable, however, sparse aperture systems may be able to achieve imaging performance from high-altitude sensor platforms which would otherwise be impractical with monolithic mirror designs due to payload launch and deployment constraints.

Much of the previous research in the sparse aperture arena has focused on trying to quantify the panchromatic optical performance of these configurations, with emphasis on modeling diffraction effects, field effects, aberrations, pupil matching and subaperture phasing. In addition, the systems have typically been modeled assuming a gray-world object scene and utilizing a spectrally weighted system optical transfer function (OTF) to resample airborne overhead gray-scale imagery. This dissertation effort attempted to add to the existing body of knowledge by investigating some of the spectral implications of typical sparse aperture optical configurations through an enhanced spectral fidelity model of the imaging process. To that end, it specifically focused on laying the groundwork for synthetic model-based evaluation of the optical performance of these imaging systems, including the incorporation of spectrally unique effects.

Starting with the basic assumption of a linear systems model, the research effort developed appropriate expressions to depict the first-principles spectral character of the object scene to

be imaged, exit pupil aberrations, the system OTF, and overall image noise in order to derive a prediction of the detected output image from various sparse aperture collection systems. In addition, traditional Wiener-Helstrom filter techniques were explored in this research to restore quality to the highly demodulated imagery predicted for these sparse aperture systems. Given the theoretical development, a proof-of-concept digital model for the end-to-end imaging system was developed to demonstrate application of the theoretical approach and provide a basis for evaluating the unique spectral character of sparse aperture systems. With this modeling capability in place, some cursory system trade studies were performed for nominal sparse aperture collection scenarios of interest. From an overall perspective, this thesis activity entailed a fundamental investigation and demonstration of the first-principles physics required to model the potential spectral implications associated with the sparse aperture system collection of an extended, remotely sensed scene. Specific research findings, limitations and recommendations for future work appear in the sections that follow.

6.1 Findings

Upon review of the primary objectives enumerated in Chapter 2, one will note that the research effort conducted for this dissertation generally exceeded the stated requirements and peripherally addressed a number of the research goals. The requirement to gain an understanding of the unique physical processes involved in imaging scenarios with sparse aperture telescopes was effectively satisfied through integration of the key theoretical concepts in Chapter 3. Establishment of this theoretical foundation then led to the development of the modeling concept described in Chapter 4, satisfying the need to construct a theoretical approach for assessing the optical performance of sparse aperture systems on a spectral basis. Finally, the fundamental requirement for developing and implementing a proof-of-concept imaging model to capture the essential spectral physics associated with overhead sparse aperture collection systems was demonstrated through the results summarized in Chapter 5. From a goal perspective, Chapter 5 also introduced the additional image restoration techniques, gray-world imaging model development, and some of the cursory sensitivity analyses that were explored in concert with this research effort. The latter effort was originally deemed to be goal-oriented but ultimately became desirable as the modeling capability came together and demonstrated its initial utility.

270

Given the imaging system model created for this research effort, several interesting observations can be made on the nature of sparse aperture imaging systems and their predicted image products. First and foremost, the model results seem to indicate that including spectral fidelity introduces a unique quality effect for sparse aperture systems not observed in the past with the traditional gray-world modeling approach. In addition, the spectral artifacts that were observed in the sparse aperture system scenarios were not apparent in the results acquired with conventional filled apertures under similar conditions. Clearly, the distinct spectral character of sparse aperture optical transfer functions, especially in the presence of subaperture dephasing or aberrations, provides a catalyst for introducing spatial structure in the restored imagery. One must, however, physically model the spectral character of the system transfer function and sample a polychromatic object scene in order to induce the observed artifacting effect. As a consequence, the traditional gray-world approach of resampling existing panchromatic imagery and applying a spectrally weighted optical transfer function does not adequately capture the effect. Depending on the severity of existing optical aberrations and the nature of the overall collection scenario under investigation, this can certainly lead to some degree of concern when utilizing a gray-world approximation for moderately aberrated, low fill factor sparse apertures, as attested to by the dramatic differences in the derived results between the polychromatic and gray-world model seen in Chapter 5.

Based on the results acquired through this research, it should be noted that the magnitude of the spectrally induced effect is highly dependent upon a number of system variables, including the amplitude of aberrations in the pupil, the relative distribution of those errors, the overall encircled fill factor of the optical configuration under investigation, and the spectral/spatial frequency content of the imaged scene. The complex interactions between all of these system parameters make it difficult to unequivocally state absolute bounds, but an attempt to generically qualify certain performance regions can be attempted based on the derived results. For instance, one finds that the nature of the spectral effect observed in restored sparse aperture imagery products with the spectral model typically does not constitute a significant impact for 0.10 waves rms of wavefront error at the mean wavelength

of the spectral passband although it was certainly statistically significant in the *nrmse* data.
Given the collection and restoration assumptions pursued in this research effort, this was
even the case for sparse aperture fill factors that would be considered reasonably low (e.g.,
0.173) by most standards. As the optical system becomes more aberrated, however, the
observed spectrally induced artifacts or image structure becomes dramatic, with a major
deleterious effect noted when the system is aberrated by up to 0.25 waves rms of wavefront
error at the mean wavelength of the spectral passband. It is interesting to note that the
equivalent gray-world model frequently predicts acceptable quality can be achieved for this
level of aberrations if the optical phase error is precisely known. Based on these
observations, it may be necessary for future sparse aperture imagery studies to incorporate
enhanced spectral fidelity depending on the nature of the scenario under investigation.

It should be noted that the conclusions drawn above on the impact of various levels of rms
wavefront error apply specifically for the range of collection parameters investigated through
the nominal scenario introduced in Chapter 4. To that end, the findings cited above tend to
be relevant for relatively high-SNR detection scenarios involving an extended object scene, a
VNIR panchromatic passband (0.4-0.8 μm), and a low fill factor sparse aperture collection
system. One would anticipate that the conclusions drawn about rms wavefront error and the
observed spectrally induced quality effect are highly sensitive to the nature of the collection
scenario under investigation. As an example, there is preliminary evidence that suggests the
spectrally induced phenomenon observed in this research becomes less dramatic as detection
SNR is lowered. Intuitively, one can envision that the relative impact of the spatial
frequency boost mismatch that occurs in the Wiener filter restoration at various wavelengths
is attenuated as the noise begins to compete with the signal for highly demodulated transfer
functions (i.e., for moderately high rms wavefront errors and relatively low detection SNR).
One would expect there to be similar sensitivity with the overall width of the detection
passband as well as the relative sparseness of the distributed aperture entrance pupil.
Therefore, this research effort has identified a specific quality effect related to sparse aperture
imaging systems that has not been previously published, but the quantification of the region
over which it is potentially problematic has only been preliminarily addressed. This area

definitely deserves more attention in follow-on research and sensitivity studies, which will be highlighted in the recommendations that appear later in this chapter.

Clearly, lack of phase knowledge (i.e., transfer function errors in the restoration process) as well as limited knowledge of the noise-to-object power spectrum ratio will also have an impact on derived image quality and the nature of the observed spectrally induced quality effect. Unfortunately, this lack of knowledge can potentially work positively or negatively from the standpoint of observed image artifacts, as the frequency mismatch that promotes the effect can either be accentuated or averaged out in the process. Certainly from an overall quality perspective, lack of knowledge will inevitably introduce image blurring so the relative sharpness of the restored imagery will undoubtedly diminish. Based on the unknowns, additional study is certainly warranted in the area of trying to characterize the impact of collection uncertainty on overall image quality. As demonstrated previously, the digital modeling capability is effectively in place to conduct these kinds of system studies in the future.

There are other interesting findings that have surfaced as a consequence of the preliminary modeling results acquired through this research. For instance, it has been suggested in the past that the introduction of nulls (or zeroes) in the spatial frequency coverage of the sparse aperture system transfer function induces unacceptable quality degradations. As evidenced in the results in Chapter 5, however, there are many occasions when a moderately dephased or aberrated sparse aperture pupil manifests nulls in the system OTF yet generates perfectly acceptable restored imagery. Of course, this statement assumes phase errors are well characterized and the detection SNR is high enough to prevent the effective area associated with spatial frequency zeroes from becoming too large. Consequently, assuming aberrations are known to some degree and the detection SNR is adequate, it appears that a certain level of spatial frequency nulling within the transfer function is actually tolerable. Obviously, spatial frequency content will have been lost as a result of this transfer function phenomenon, but the effect appears to be marginalized over an integrated passband if the level of nulling is not too excessive.

With regard to transfer function zeros, it has also been stated that those sites are solely responsible for any spectral artifacting that may appear in restored imagery. Although nulls certainly constitute legitimate sites where artifacts may be induced, it appears reasonably clear from the data results that another physical effect is at play. This becomes apparent in exploring the nature of a severely aberrated filled, circular aperture. In Chapter 5, results were presented for a filled aperture with 0.20 waves rms of defocus error, where the introduction of zeroes in the spatial frequency plane as well as regions of contrast reversal certainly led to degraded imagery product but did not introduce the type of artifacting observed in the sparse aperture cases. Accordingly, it appears that the principal contributor to the structural effects observed in the sparse aperture restorations is actually the mismatch that inevitably occurs between the rapidly oscillatory, spectrally varying character of an aberrated sparse aperture system transfer function and the selected filter design. The latter physical characteristics of the system transfer function result in certain spatial frequencies exhibiting a peak at a given wavelength where another wavelength actually supports a valley. This situation creates regions of mis-boost when a restoration filter is applied, introducing spectral artifacting or rippling in the reconstructed image. Of course, nulls in the spatial frequency plane provide ideal locations where individual spectral lines may exhibit this modulation mismatch with other wavelengths, but they certainly do not appear to constitute the exclusive source of the problem.

The final observation that will be summarized here regards the impact of fill factor on overall restored image quality. Previous studies have shown that image quality generally reduces in relationship to sparse aperture fill factor if the integration time is not increased to accommodate it. These studies have also demonstrated through use of the gray-model approximation that one can typically restore imagery to comparable quality with a filled aperture by increasing the dwell time according to the proportionality $T_{int} \propto F_{fill}^{-3}$. Of course, eventually the fill factor will drop to the point where significant zeroes are introduced into the spatial frequency coverage of the optical transfer function, and restoration to the filled equivalent quality will no longer be feasible regardless of the amount of integration time. Through use of the higher spectral fidelity model, this research effort demonstrated the relative merit of increasing integration time proportional to F_{fill}^{-3} but also identified issues

with achieving comparable quality to a filled aperture in the presence of aberrations. As indicated previously, the spectral character of the sparse aperture system transfer function provides a mechanism for introducing spectral artifacts into restored imagery products that also prevents the achievement of image quality commensurate with a filled aperture. Although statistically apparent in the *nrmse* results, the nature of this spectrally induced quality effect appeared to be mitigated as the fill factor approaches values of 0.50 and largely disappears for fill factors consistent with more conventional apertures. Of course, it would be difficult to classify apertures exhibiting fill factors greater than 0.50 as truly "sparse." For moderately aberrated imaging systems with fill factors below 0.35, however, the effect appeared to be a prominent feature of the restored imagery for the optical configurations explored in this dissertation. Obviously, this research effort did not entail a significant exploration of the overall trade space and further investigation of the dependency of the quality effect on fill factor and optical configuration is certainly merited.

6.2 Limitations

There are certain limitations associated with the imaging system model and derived study results that deserve attention in future research effort. These generally fall into the category of potential model enhancements but also include a final word of caution regarding the conclusions drawn from the trade studies performed for this research. The latter should probably be the first to be addressed. Since the original objective of this research effort was to demonstrate a proof-of-concept modeling capability, the performance studies included in this dissertation were by their very nature somewhat limited in scope. Although numerous iterations were performed and exemplar results representative of the total set of runs were selected to demonstrate certain effects, one still needs to be aware that the wide-open trade space has only truly received cursory exploration through this research. There are many different combinations of object scene content, optical aberrations, signal-to-noise, system fill factor, etc., which should be investigated more thoroughly in a rigorously defined sensitivity study. In addition, although not quite anecdotal in nature, the limited set of runs performed in this effort also warrant additional iterations to confirm they statistically represent the typical performance one would expect for the system parameters identified in the nominal scenario. As a consequence, although the utility of the modeling capability has

been demonstrated and a unique physical attribute identified for moderately aberrated sparse aperture systems, considerably more effort should be expended to characterize the overall quality implications of the observed spectrally induced effect. It should also be noted that all the results in this research dissertation were acquired based on first-principles modeling effort. In the future, one should perform some small-scale experiments with actual imaging hardware involving a distributed, aberrated pupil to confirm the spectrally induced effect can be recreated in real-world imaging instruments.

In the area of model enhancements, there are several attributes of the proof-of-concept imaging model which should be targeted for improvement. The principal limitation associated with the entire modeling effort resides with the implemented governing signal equation and the assumption that these imaging systems can be treated as linear, shift-invariant. Clearly, as soon as one starts to contemplate the possibility of aberrations, the shift-invariance assumption begins to become suspect depending on the nature and magnitude of the errors. For high-resolution systems with low level aberrations, it has been demonstrated in the past that the linear, shift-invariant modeling assumption represents a fairly good approximation to what physically is captured in the imaging process. That is certainly not the case for a highly aberrated optical system however. To handle this situation, the current model should be enhanced to separate the imaged object scene into isolated isoplanatic regions based on incident field angle and apply the linear, shift-invariant approximation across the field on a moving window basis. Through such a construct, the strength and character of aberrations off the optical axis could be adjusted in the designated isoplanatic regions to reflect what actually occurs in real-world imaging scenarios. Some criteria such as rms wavefront error or Strehl ratio could be utilized to ascertain the boundaries of the region over which the imaging system can be approximated as shift-invariant. Obviously, it will be critical that such an implementation enables enough samples to be included in the isoplanatic patches that the discrete Fourier transform produces credible results in the imaging model.

Another significant improvement area that should be targeted in the current modeling capability lies in the software engineering arena. The proof-of-concept imaging model

276

development pursued in this dissertation was never intended to be a robust capability that could be exported to external users in a turn-key operation. The software was developed on a personal computer (PC) utilizing the IDL^{TM} development environment and is truly engineering code by its very nature. As engineering code, the software algorithms were designed to achieve the desired research objectives, not necessarily be the most elegant software implementation. One could certainly accomplish significant enhancements in the area of code optimization, modularity and memory usage. The latter is especially problematic in the current implementation, as the number of large arrays required to handle the incident object radiance hypercube, a spectrally varying complex pupil function, a complex optical transfer function data cube of similar size, a spectrally diverse noise field, interim restoration imagery products, etc., lead to significant memory usage. The memory issues in the current implementation have a tendency to either limit the size of the image that can be investigated or reduce the spectral resolution associated with the integrated signal prediction. Fortunately, the use of IDL^{TM} software has resulted in reasonably good portability across computer platforms, so the digital model can be executed on PC and UNIX machines alike, providing an opportunity to use more capable computing resources to work around some of the optimization and memory limitations. This software portability was in fact demonstrated during the course of this research effort as numerous runs were performed on both IBM PC and Sun UNIX platforms.

In addition to the software issues identified above, the engineering code design currently requires a highly iterative process for investigating certain aberration levels of interest. It would be very useful to explore a more flexible architecture that supported batch file runs and ultimately aimed at incorporating a Monte Carlo implementation for performing a significant number of iterations for a given set of inputs. Since a single rms wavefront error figure of merit can be achieved by a significant number of possible pupil phase profiles and lead to a wide distribution of possible image predictions, a Monte Carlo approach would be very useful for exploring and quantifying the distribution of potential end-products achievable through a given collection scenario. The current implementation also requires some human interaction to execute the imaging scenario of interest. In general, a knowledgeable user is required to turn on/off functionality to perform the desired simulation

and acquire certain modeling results. Some of these limitations could be resolved through better software design practice and some could be handled through introduction of an appropriate Graphical User Interface (GUI). With regard to the latter, a preliminary GUI was constructed early in the course of this research effort and abandoned to focus on the critical algorithm development. It is possible that GUI could be resurrected and enhanced to accommodate some of the human interaction issues described above. Finally, documentation and internal commenting are fairly sparse for the current system model, once again highlighting the need for a trained operator to get the simulation to produce desired results. It would be worthwhile to expend some effort in this area as well if it is envisioned the modeling capability will be used to support future research endeavors.

6.3 Recommendations

One should note that a number of recommendations for model enhancement and system model verification appeared in the previous section. Although only briefly touched upon, a significant requirement in the view of this author is the need to verify the potential existence of the spectrally induced quality effect through experimental evidence acquired with actual imaging hardware. Software models can only capture real-world physical effects to a certain degree and past experience has shown that unanticipated results frequently surface with actual hardware implementation, necessitating revisions to modeling approximations in order to describe what is empirically observed. In addition to those recommendations, there are three prominent areas that deserve further attention based on this research effort and the implemented modeling capability now available for future studies. These include future research pursuit in the areas of sparse aperture system quality trade studies, enhanced image restoration methodologies, and interferometric performance considerations with these unique optical systems. The three general areas enumerated above will be briefly summarized in the following discussion.

6.3.1 Sensitivity Studies

As alluded to in the discussion above, there is a fairly significant need to more thoroughly explore the performance trade space associated with sparse aperture systems to better quantify the nature of the quality effects highlighted in this research effort. To that end, one

should consider utilizing the existing modeling capability to perform a series of sensitivity studies that vary key imaging system parameters to determine their impact on restored image quality. Although there are a considerable number of different trades that could be performed, the obvious candidates for initial exploration should include detection signal-to-noise ratio, aberration type and level, scene content (spatial and spectral), scene contrast, system fill factor, and in-situ exit pupil phase profile knowledge. These parameters received some cursory attention in the limited trade studies performed in conjunction with this dissertation. Based on those results, it appeared the enhanced spectral fidelity model identified certain quality issues that had not been detected in the past through use of a conventional gray-world modeling approximation. As a consequence, there is merit in attempting to better quantify the incidence of those effects to determine when the gray-world model is appropriate for use with sparse aperture systems and when an enhanced spectral model must be exercised to capture the anticipated collection physics.

Based on this research effort, it would appear reasonable to pursue a similar set of sparse aperture optical configurations in future sensitivity studies, as the tri-arm, Golay-6 and annulus represent fairly standard apertures in the literature and provide a good range of possible restoration quality effects. With these sparse aperture systems, the results achieved in this dissertation also indicate the need to further explore subaperture aberrations in the regime between 0.10 and 0.20 waves rms of wavefront error at the mean wavelength. At the former level (0.10 waves rms), it appeared that the spectrally induced quality phenomenon is just initiated for the imaging conditions investigated in this work, with likely not enough impact to cause great concern for most applications of interest. On the other hand, once a sparse aperture system exhibits a wavefront error of 0.20 waves rms, most scenarios seem to lead to artifacting on a level that ultimately impacts the interpretability of the restored imagery. Consequently, the range of possible wavefront error realizations between those two extremes should receive additional attention to ascertain the point at which quality effects become objectionable to the typical observer.

Another system parameter that deserves further study in the context of the proposed sensitivity study is the sparse aperture effective fill factor. In effect, this research effort only

sampled the fill factor parameter space from 0.173 to 1.000 in a preliminary manner. For illustrative purposes, one will find that the dissertation tends to emphasize documenting the single case of 0.173, as all three sparse aperture configurations pursued in this research can support that value. There were additional simulation runs that were performed at alternate fill factors of 0.349 (Golay-6, annulus), 0.500 (annulus), 0.942 (Cassegrain, phased petal), and 1.000 (filled circular). As discussed above, the unique quality effect displayed by aberrated sparse aperture systems was apparent for moderate-to-low fill factors below 0.500. At that point, the nature of the effect became less remarkable and eventually dwindled away for fill factors associated with conventional apertures. Given the apparent sensitivity of the observed spectrally induced effect, it would be a useful exercise to rigorously evaluate different fill factors in the overall trade space.

From the perspective of detected signal level, one should note that the majority of computer runs performed for this research effort involved high signal-to-noise conditions (e.g., an SNR of ~270 in most cases). Although this level provided a good benchmark for evaluating the nature of the observed quality effect and largely eliminated noise as a potential contributor to its generation, many remote sensing scenarios involve SNR conditions that are considerably less favorable. As a consequence, it would be a very worthwhile exercise to perform additional runs under much lower SNR conditions to gain some understanding of how the effect scales with detected signal level. As part of the latter exercise, one should definitely attempt to address low-contrast, low-light imaging conditions to ascertain whether sparse aperture systems exhibit any kind of unique character relative to their conventional counterparts. In this context, it would be extremely useful to pursue some studies that investigated sparse aperture image quality for solar illumination angles less than 15 degrees of elevation. As the conventional MODTRAN atmospheric propagation physics tend to break down below this illumination level, one would have to support this low-light study with empirical measurements utilizing radiometric instruments available within the Center for Imaging Science at RIT. With such measurements, one could perform an appropriate extrapolation of MODTRAN results achieved with given scenarios for illumination angles less than 15 degrees elevation. The resulting low-light spectral radiance levels could subsequently be utilized to ascertain whether sparse aperture systems exhibit unique

character under low detection SNR conditions and perhaps even low contrast target signal with selection of an appropriate object scene.

Finally, it would be of considerable interest to further explore the effects of unknown phase and system transfer function character on the quality of restored imagery products for the trade space proposed above. As stated earlier, most of the simulation performed for this dissertation entailed perfect knowledge of the exit pupil phase profile and the associated optical transfer function acquired through the autocorrelation of the aperture. The rationale for implementing such knowledge in the Wiener filter was interest in achieving an optimum restoration as a baseline. The more unknowns that could be eliminated in the restoration process helped to isolate the potential sources of any observed quality effects. With such a baseline established, it would be useful to investigate how adding certain realism back into the modeling process affects image quality. In that vein, some preliminary studies on phase knowledge were performed with the proof-of-concept system model developed for this dissertation. The results of those study excursions seem to indicate that the spectrally induced effect is still present under condition of phase uncertainty (i.e., it is not averaged out) and can be exacerbated if the transfer function mismatch with the resulting restoration filter boost is increased. As one can obviously detect through the discussion provided here, there are a considerable number of different potential sensitivity studies that could be pursued in greater depth and contribute more expansively to the body of knowledge on sparse aperture systems. From that perspective, the initial modeling capability developed through this research effort has the potential to be a real enabler for future investigations.

6.3.2 Advanced Filter Techniques

Although the general Wiener filtering technique implemented in this dissertation has proven to be very effective in restoring degraded image products, including those predicted from sparse aperture systems, the implementation is only optimum in the sense of image-wide statistics. This is due to the fact that the Wiener filter is derived based on minimizing the *mean* square error between the reconstructed estimate and the original object. As a result, the conventional Wiener filter essentially characterizes an image field as homogeneous, whereby the mean-level characteristics of the signal and noise are assumed not to vary from one part

281

of the image to the other. Of course, real-world imagery typically does exhibit some variation from one local region to the other, from either space-variant imaging system degradation effects such as optical aberrations or scene content-related effects like rapid variations in source intensity. Given the unique OTF structure of aberrated sparse aperture systems, one may also find localized regions in imagery derived from these collectors where objectionable spectral artifacts surface, as observed in a number of the simulations found in Chapter 5. This discussion gives rise to the notion of an *adaptive filter*, where the restoration is adaptively adjusted on a pixel-by-pixel basis according to the local statistics associated with the degraded image under investigation.
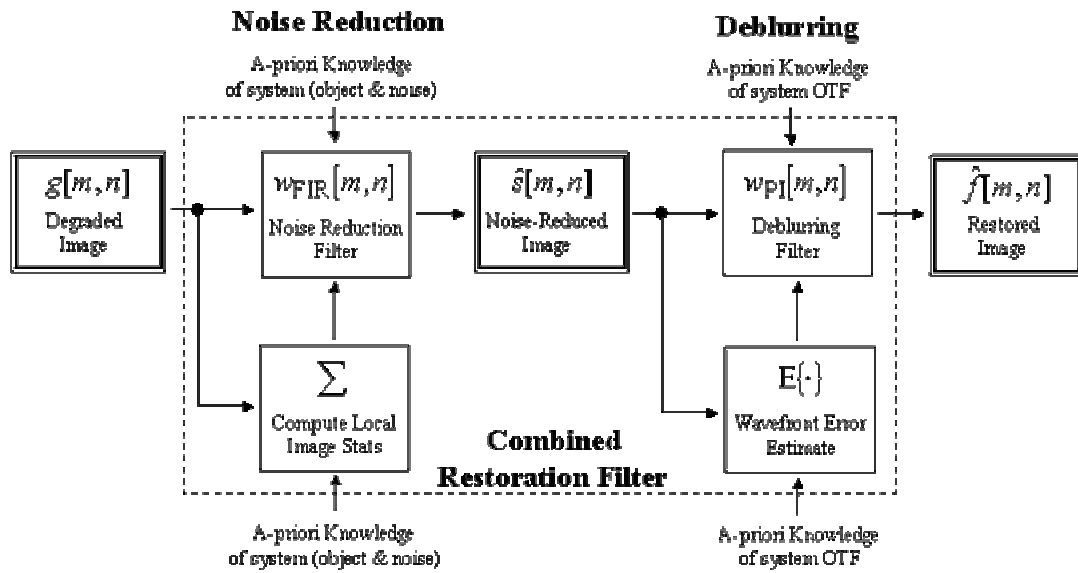
Figure 137: General adaptive filtering image restoration methodology

The concept of locally varying the amount of restoration applied to various regions of an image is generalized by the flowchart in Figure 137. Most adaptive filtering systems follow the basic formulation depicted in this figure, with either a single combined filtering step or a two-step implementation of noise reduction and deblurring procedures. Regardless of the particular implementation of choice, the basic premise behind the filtering operation is essentially the same: to spatially vary the amount of noise reduction and image restoration according to localized statistics within the detected imagery. To accomplish this objective, the adaptive filter typically assumes a different posture depending on the nature of the image

282

content in the local region. If the local neighborhood contains high detail in the scene content, for instance, the signal variance will be much greater than the noise variance (i.e., $\sigma_{obj}^2 >> \sigma_n^2$) and the adaptive filter will attempt to boost the spatial frequency content and preserve the local contrast. As a consequence, detailed localized regions will typically experience a fair amount of sharpening in a good adaptive filter design. On the other hand, in low detail regions of the image such as those exhibiting uniform intensity, the noise will represent the dominant image content (i.e., $\sigma_n^2 >> \sigma_{obj}^2$) and the adaptive filter will significantly attenuate the contrast in an attempt to reduce the objectionable noise resident in the area. In other words, the relative filter gains in low signal content regions will be established in good filter designs at levels that attempt to minimize the amount of noise boost. Once again, one can envision that such filter behavior could be beneficial in scenes that manifest spectral artifacts or anomalies, in addition to variation in noise-to-signal power.

Most adaptive filtering operations rely on what is commonly referred to as a Finite Impulse Response (FIR) filter, which by convention is implemented in the spatial domain through use of the impulse response of the filter. The value of FIR filters tends to be in their reduced computational complexity, as the finite nature of the impulse response allows these filters to be reduced considerably in size and typically be implemented through a block Toeplitz matrix equation for the required convolution operation. Lee (1980), Lim (1990) and Jain (1989) have all proposed various FIR implementations for an adaptive Wiener filter application for conventional imagery products. As their investigations all concluded that image quality could generally be improved through use of such a filter, it seems reasonable to explore a similar implementation for application in the sparse aperture arena.

6.3.3 Interferometric Investigation

Obviously, this dissertation principally focused on modeling and simulation of remote sensing applications, which fundamentally involve imagery collection physics. In the future, however, it would be instructive to address some of the interferometric considerations associated with the sparse aperture optical systems investigated in this effort. In fact, Goodman (1985) has suggested that even evaluating imaging as an interferometric process can be enlightening. Since sparse aperture systems can obviously be operated in both modes,

imaging and interferometry, it makes sense to put some of the theoretical development that appears in Chapter 3 into an interferometric framework and implement an appropriate model to handle system interferometry. To the author's knowledge, such an analytical approach has not been physically explored before in the context of a sparse aperture system *imaging* application.

In order to address imaging as an interferometric process, it would be necessary to introduce some analytical scaffolding to set up the problem definition. The latter include the concepts of a mutual coherence function, mutual intensity, and complex degree of coherence. These interferometric concepts are described in detail by Goodman (1985) in his general statistical optics development. One of the most widely used constructs in interferometry is the mutual coherence function, which in its normalized form is frequently utilized as a relative measure of the spatial and temporal coherence of incident radiation. For instance, if the normalized mutual coherence function is near unity, one finds that the detected radiation is effectively coherent in nature. On the other hand, a normalized mutual coherence function that is very small correlates with an incoherent imaging scenario. In between these two extremes, one finds a virtual "no-man's land" where partial coherence exists on short time scales that may or may not have detectable image quality implications. As such, this fundamental interferometric figure of merit can become a basic building block, in conjunction with the mutual intensity, for analyzing constructive and destructive interference effects in the overall image formation process.

Even in the context of general incoherent remote sensing imaging applications, the coherent phasing issues introduced by sparse aperture systems can potentially introduce short-time scale conditions where quasi-monochromatic conditions of partial coherence actually exist, especially if the collection passband is narrow enough. To address this problem, one must explore the fundamental nature of the coherence time or length of the incident light. For instance, it has been demonstrated that interference fringes may form in white light if the optical path difference between sources is considerably less than the coherence length. This could become especially troublesome as one begins to consider sparse aperture multi- or hyperspectral applications which naturally involve narrower bandwidths. In such a situation,

where one attempts to maintain the phasing of separate subapertures to tolerances on the order of 0.10 waves rms error, one may find the inevitable random misalignments of telescopes through standard tip/tilt or piston mechanisms results in optical path differences that are substantially less than the coherence length. In such a scenario, one can envision an *inadvertent interferometry* physical effect that effectively degrades the overall image quality. It would be the intent of the proposed research effort to pursue the theory behind such a potential inadvertent interferometry scenario and put it into an appropriate mathematical context that enabled comparison with traditional Fourier optical analytical techniques.

In addition to the inadvertent interferometry problem conjectured above, one can also envision taking advantage of partial coherence or interferometric fringes if they could be detected on the focal plane. Although currently only an academic exercise, this concept would entail intentional or *advertent interferometry*, whereby a sparse aperture imaging system could conceivably be intentionally misaligned in order to aid the subaperture phasing process. In this construct, one would make use of detected fringe patterns to draw conclusions on the relative misalignment of individual apertures and eventually provide an aid to realignment efforts. The ultimate objective of this recommended future research effort would be to ring out the conjectured inadvertent and advertent interferometry concepts in additional mathematical detail and actually model the effects with adequate rigor to determine if they represent physically viable constructs.

References

[1] Berk, A.B., L.S. Bernstein, and D.C. Robertson (1989). "MODTRAN: A moderate resolution model for LOWTRAN 7," Tech. Rep. GL-TR-89-0122, Spectral Sciences Inc., Burlington, MA.

[2] Boucher, Richard H. (2000). "Image Quality Issues in Sparse Aperture Systems," Briefing charts, Electrical-Optical Systems Dept., the Aerospace Corp., Los Angeles, CA.

[3] Boucher, Richard H. (2000). "Figures of Merit for Sparse Aperture Systems," Briefing charts, Electrical-Optical Systems Dept., the Aerospace Corp., Los Angeles, CA.

[4] Butts, R.R. (1981). "Effects of piston and tilt errors on the performance of multiple mirror telescopes," *Proc. SPIE* **293**, 85-89.

[5] Easton, Roger L. (2003). "Optical Imaging Systems as Linear Filters," Course notes, Fourier Optics, PhD Lab and Linear Mathematics, Rochester Institute of Technology, Rochester, NY.

[6] Ebbini Emad S. (1998). "Image Restoration," Course notes, Chap 9, Signal and Image Processing, Univ. of Michigan, Ann Arbor, MI.

[7] Fender, Janet S. (1983). "Synthetic apertures: an overview." *Proc. SPIE* **440**, 2-7.

[8] Fender, Janet S. (1986). "Phased array optical systems," *Proc. SPIE* **643**, 122-128.

[9] Fienup, James R. (2000). "MTF and integration time versus fill factor for sparse-aperture imaging systems," *Proc. SPIE* **4091**, 43-47.

[10] Fienup, James R., D. Griffith, L Harrington, A.M. Kowalczyk, J.J. Miller and J.A. Mooney (2002). "Comparison of reconstruction algorithms for images from sparse-aperture systems," *Proc. SPIE* **4792-01**.

[11] Fienup, James R. (2002). "Image Quality Equation for Sparse-Aperture Systems," Briefing charts, consultant to Veridian Systems, Institute of Optics, University of Rochester, Rochester, NY.

[12] Fienup, James R. (2003). "RER Versus Aberrations for Sensitivity Analysis and IQE Generalization," Briefing charts, consultant to Veridian Systems, Institute of Optics, University of Rochester, Rochester, NY.

[13] Fienup, James R. (2004). "Exploration of IQE Generalization," Briefing charts, consultant to General Dynamics Advanced Information Systems, Institute of Optics, University of Rochester, Rochester, NY.

[14] Fiete, Robert D., T.A. Tantalo, J.R Calus, and J.A. Mooney. (2002). "Image quality of sparse-aperture designs for remote sensing." *Optical Engineering* **41** (8), 1957-1969.

[15] Fiete, Robert D. (1999). "Image quality and λFN/p for remote sensing systems," *Optical Engineering* **38**, 1229-1240.

[16] Fiete, Robert D. and T.A. Tantalo (2001). "Comparison of SNR image quality metrics for remote sensing systems," *Optical Engineering* **40**, 574-585.

[17] Gaskill, Jack D. (1978). *Linear Systems, Fourier Transforms, and Optics.* John Wiley & Sons, Inc., New York, NY.

[18] Golay, M.J.E. (1971). "Point arrays having compact, nonredundant autocorrelations," *Journal of the Optical Society of America* **61**, 272-273.

[19] Gonzalez, Rafael C. and R.E. Woods (2002). *Digital Image Processing.* Second Ed. Prentice Hall, Inc., Upper Saddle River, NJ.

[20] Goodman, Joseph W. (1996). *Introduction to Fourier Optics.* Second Edition. McGraw-Hill Companies, Inc., New York, NY.

[21] Goodman Joseph W. (1985). *Statistical Optics.* John Wiley & Sons, Inc., New York, NY.

[22] Hailstone, Richard K. (2002). "Image Microstructure," Course notes, Basic Principles of Imaging Science, Rochester Institute of Technology, Rochester, NY.

[23] Harvey, James E. and R.A. Rockwell (1988). "Performance characteristics of phased array and thinned aperture optical telescopes," *Optical Engineering* **27**, 762-768.

[24] Harvey, James E. and C. Ftaclas (1995). "Field-of-view limitations of phased telescope arrays," *Applied Optics* **34** (25), 5787-5798.

[25] Harvey, James E., A. Kotha, and R.L. Phillips (1995). "Image characteristics in applications utilizing dilute subaperture arrays," *Applied Optics* **34**, 2983-2992.

[26] Harvey, James E., M.J. MacFarlane, J.L. Forgham (1983). "Design and performance of ranging telescopes: monolithic vs. synthetic aperture," *Proc. SPIE* **440**, 56-67.

[27] Hooker, R.B. (1974). *The Effects of Aberrations in Synthetic Aperture Systems.* Ph.D. Dissertation, University of Arizona.

[28] Holst, G.C. (1995). *Electro-optical Imaging System Performance.* SPIE Optical Engineering Press, Bellingham, WA.

[29] Jain, Anil K. (1989). *Fundamentals of Digital Image Processing.* Prentice Hall, Inc., Englewood Cliffs, NJ.

[30] Lampkin, Curt M., G.W. Flint, and M.J. MacFarlane (1988). "Optical and mechanical design aspects of a four-telescope array for combined imaging," *Optical Engineering* **27** (9), 749-754.

[31] Leachtenauer, J. C., W. Malila, J. Irvine, L Colburn and N. Salvaggio (1997). "General Image Quality Equation: GIQE," *Applied Optics* **36**, 8322-8328.

[32] Lee, J.S. (1980). "Digital image enhancement and noise filtering by use of local statistics," *IEEE Trans. Pattern Analysis and Machine Intelligence*, Vol. 2, 165-168.

[33] Lim, Jae S. (1990). *Two-Dimensional Signal and Image Processing.* Prentice Hall PTR, Prentice Hall Inc., Upper Saddle River, NJ.

[34] Lomheim, Terrance S. and E.D. Hernandez-Baquero (2002). "Translation of spectral radiance levels, band choices, and signal-to-noise requirements to focal plane specifications and design constraints," *Proc. SPIE* **4486,** 263-307.

[35] Lomheim, Terrance S. (2002). "Infrared Imaging: Applications and Subsystems, A Systems-Oriented Approach," Short course notes, UCLA, Los Angeles, CA.

[36] Meinel, A.B., M. Meinel, and N. Woolf (1983). "Multiple aperture telescope diffraction images," *Applied Optics and Optical Engineering IX*, R.R. Shannon and J.C. Wyant, eds., pp. 149-201, Academic Press, New York, NY.

[37] Meinel, A.B. (1970). "Aperture Synthesis Using Independent Telescopes," *Applied Optics* **9** (11), 2501-2504.

[38] Palma, G.E., and S.S. Townsend (1983). "Performance and phasing of multiline synthetic apertures," *Proc. SPIE* **440**, 68-76.

[39] Sabatke, Erin M. and J.M. Sasian (2000). "Phase theory for multiple aperture systems," *Proc. SPIE* **4091**, 6-17.

[40] Schott, John R. (1997). *Remote Sensing: the Image Chain Approach.* Oxford University Press, Oxford, NY.

[41] Schott, John R., S. Brown, R. Raqueno, H. Gross, and G. Robinson (1999). "An advanced synthetic image generation model and its application to multi/hyperspectral algorithm development," *Canadian Journal of Remote Sensing* **25(2)**, 99-111.

[42] Schowengerdt, Robert A. (1997). *Remote Sensing, Models and Methods for Image Processing.* Second Edition. Academic Press, New York, NY.

[43] Smith, S.L., J.A. Mooney, T.A. Tantalo, and R.D. Fiete (1999). "Understanding image quality losses due to smear in high-resolution remote sensing imaging systems," *Optical Engineering* **38**, 821-826.

[44] Smith, Warren J. (2000). *Modern Optical Engineering: The Design of Optical Systems.* Third Ed. McGraw-Hill Companies, Inc., New York, NY.

[45] Traub, W.A. (1986). "Combining Beams from Separated Telescopes," *Applied Optics* **25** (4), 528-532.

[46] Weaver, L.D., J.S. Fender, and C.R DeHainaut (1988). "Design Considerations for Multiple Telescope Imaging Arrays," *Optical Engineering* **27** (9), 730-735.

[47] Welford, W.T. (1986). *Aberrations of Optical Systems.* Adam Hilger, Bristol, England.

[48] Wilson, Raymond G. (1995). *Fourier Series and Optical Transform Techniques in Contemporary Optics.* John Wiley & Sons, Inc., New York, NY.

[49] Wyant, James C. and K. Creath (1992). "Basic Wavefront Aberration Theory for Optical Metrology," Chap. 1, *Applied Optics and Optical Engineering*, Vol. XI, Academic Press, Inc.

Appendix

Alternative Optical Configuration Predictions

As alluded to in the main body of this dissertation, numerous simulation iterations were performed during the course of this research effort. For these software runs, various system parameters were varied in an attempt to gain physical insight into the overall character of sparse aperture image quality. Such fundamental parameters as optical configuration, fill factor, aberration level, optical phase distribution, and detection signal-to-noise ratio (SNR) were varied in these system trade studies. For the most part, the restoration results acquired from these alterative simulations were consistent with the conclusions drawn previously with the baseline tri-arm sparse aperture imaging system. In the interest of completeness, the figures in this appendix provide the raw results acquired for some of these alternative configuration simulations. These results should provide the genesis for a more rigorous system trade study of key sparse aperture imaging system parameters in the future.

A.1 Golay-6 Sparse Aperture

This section provides results for the Golay-6 non-redundant array of subapertures with a fill factor F_{fill} of 0.173 and wavefront errors of 0.10 and 0.25 waves rms at the mean wavelength. As with previous tri-arm sparse aperture simulations, the gray-world and polychromatic restorations were accomplished with a traditional Wiener filter, assuming perfect system OTF and noise-to-object power spectrum ratio knowledge. The following figures provide the optical phase profile, the aberrated aperture MTF, and the final restoration products for the specified conditions. One will observe that the results are in family with those acquired for the tri-arm sparse aperture imaging system, with subtle differences appearing in the two simulation models for aberrations on the order of 0.10 waves rms and extensive variation due to spectrally induced artifacting at wavefront errors approaching 0.25 waves rms.
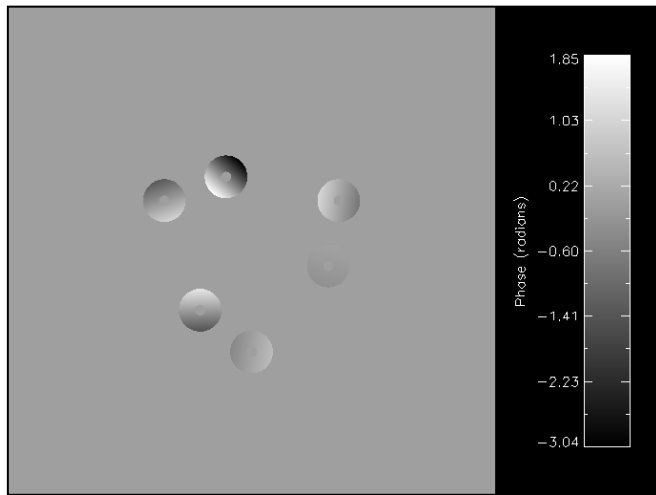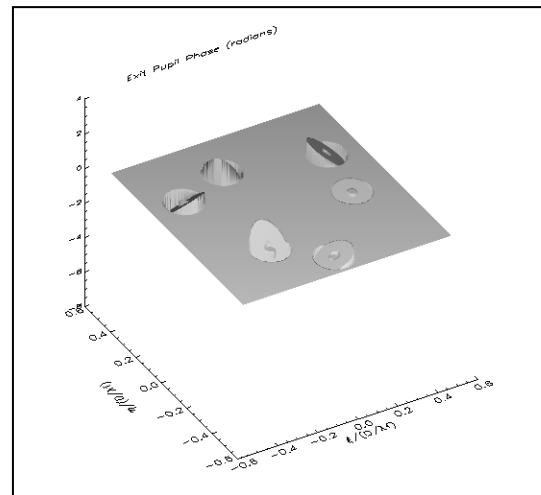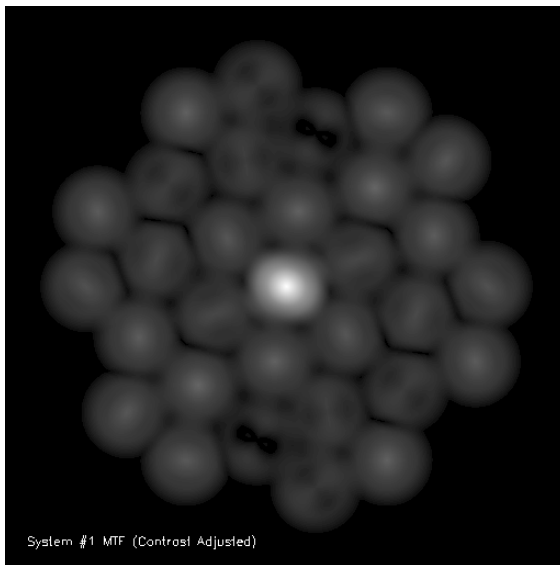
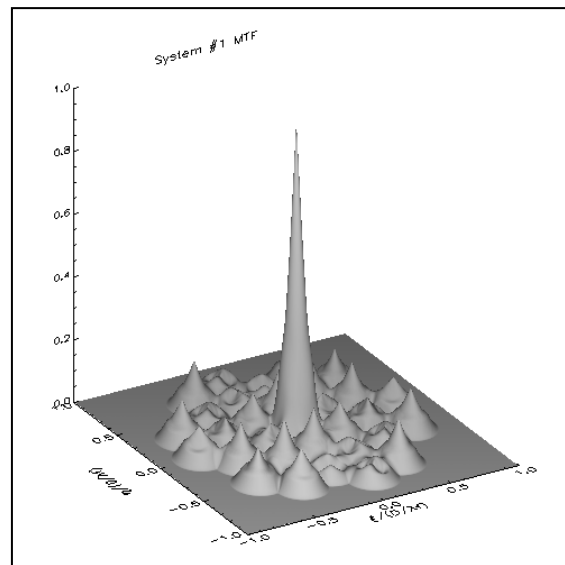(a) Two-Dimensional Distribution   (b) Three-Dimensional Surface

Figure 138: Random phase profile for the central wavelength of an aberrated
Golay-6 sparse aperture (0.10 waves rms piston, tip/tilt error).
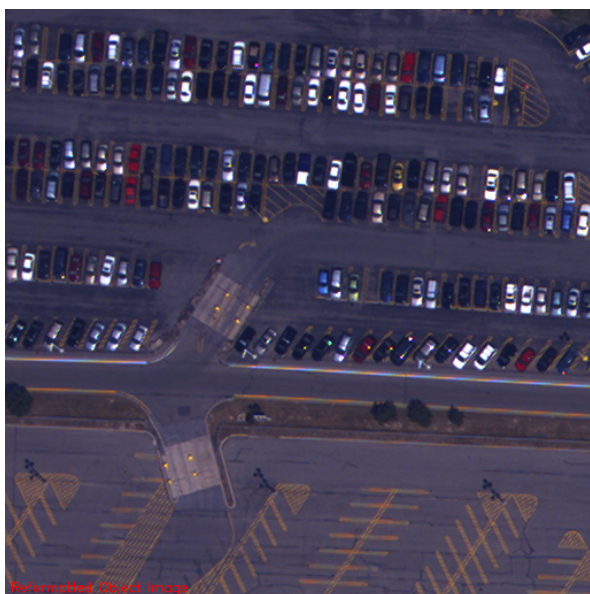

(a) Two-Dimensional Image   (b) Three-Dimensional Surface

Figure 139: Modulation transfer function for an aberrated Golay-6
sparse aperture (0.10 waves rms piston, tip/tilt error).
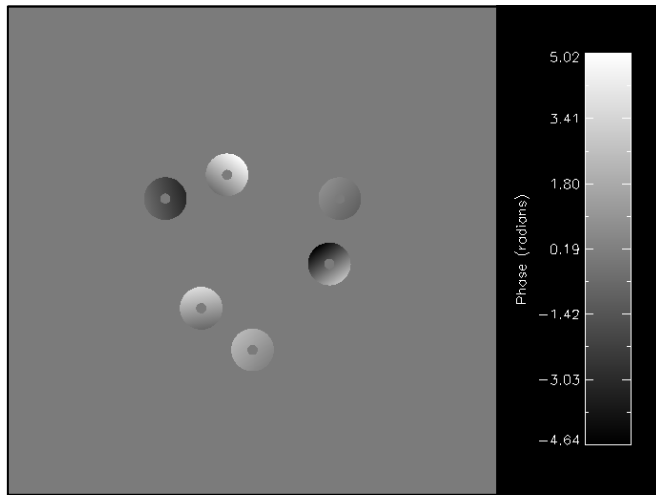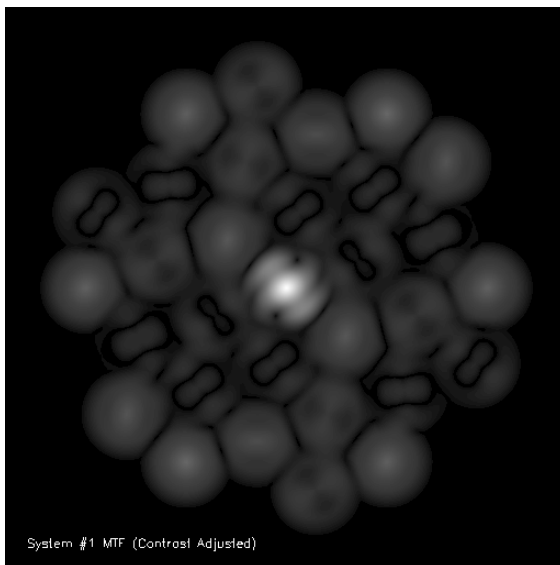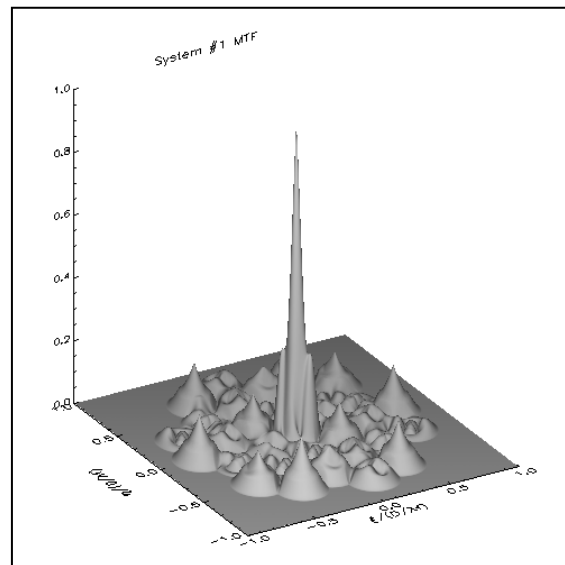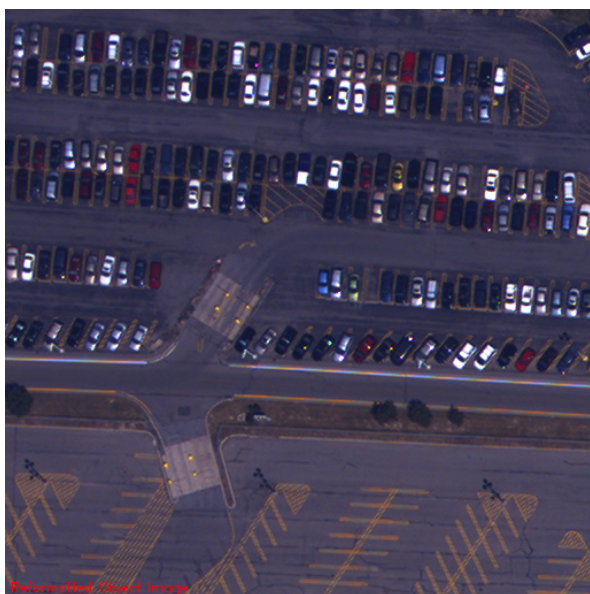
(a) Original Object   (b) Spectrally Weighted Object

(c) Gray-World Simulation   (d) Polychromatic-World Simulation
nrmse: 0.0617   *nrmse*: 0.0674

RER: 0.878; G_{rms}: 17.3; SNR: 271.4

Figure 140: Integrated panchromatic simulation of an aberrated Golay-6 sparse aperture with spectrally weighted OTF restoration (0.10 waves rms piston, tip/tilt error).
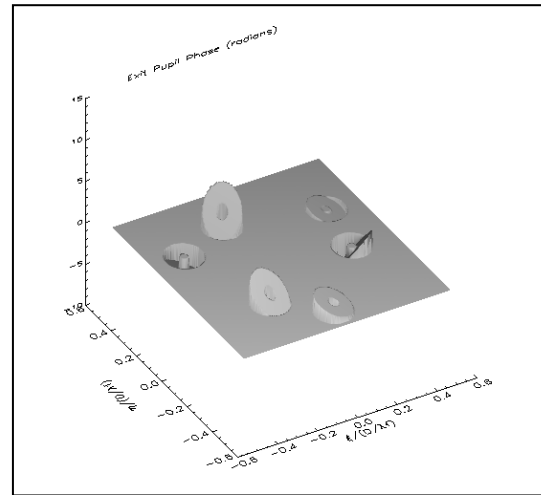
(a) Two-Dimensional Distribution   (b) Three-Dimensional Surface

Figure 141: Random phase profile for the central wavelength of an aberrated
Golay-6 sparse aperture (0.25 waves rms piston, tip/tilt error).

(a) Two-Dimensional Image   (b) Three-Dimensional Surface

Figure 142: Modulation transfer function for an aberrated Golay-6
sparse aperture (0.25 waves rms piston, tip/tilt error).

294

(a) Original Object

(b) Spectrally Weighted Object

(c) Gray-World Simulation
nrmse: 0.0885

(d) Polychromatic-World Simulation
nrmse: 0.1121

RER: 0.770; G_{rms}: 24.8; SNR: 270.2

Figure 143: Integrated panchromatic simulation of an aberrated Golay-6 sparse aperture with spectrally weighted OTF restoration (0.25 waves rms piston, tip/tilt error).

A.2 Annulus Sparse Aperture

This section provides simulation results for a 15-subaperture annulus imaging system design with a fill factor F_{fill} of 0.173 and wavefront errors of 0.10 and 0.25 waves rms at the mean wavelength. As with previous sparse aperture predictions, the gray-world and enhanced spectral model restorations were accomplished with a traditional Wiener filter, assuming perfect system OTF and noise-to-object power spectrum ratio knowledge. The figures in this section provide the optical phase profile, the aberrated aperture MTF, and the final restoration products for the specified conditions. Once again, the results appear to be in family with those acquired for the tri-arm sparse aperture imaging system, with subtle model variation exhibited for wavefront errors on the order of 0.10 waves rms and extensive differences manifested in the polychromatic model at 0.25 waves rms of wavefront error due to the spectral artifacting phenomenon.

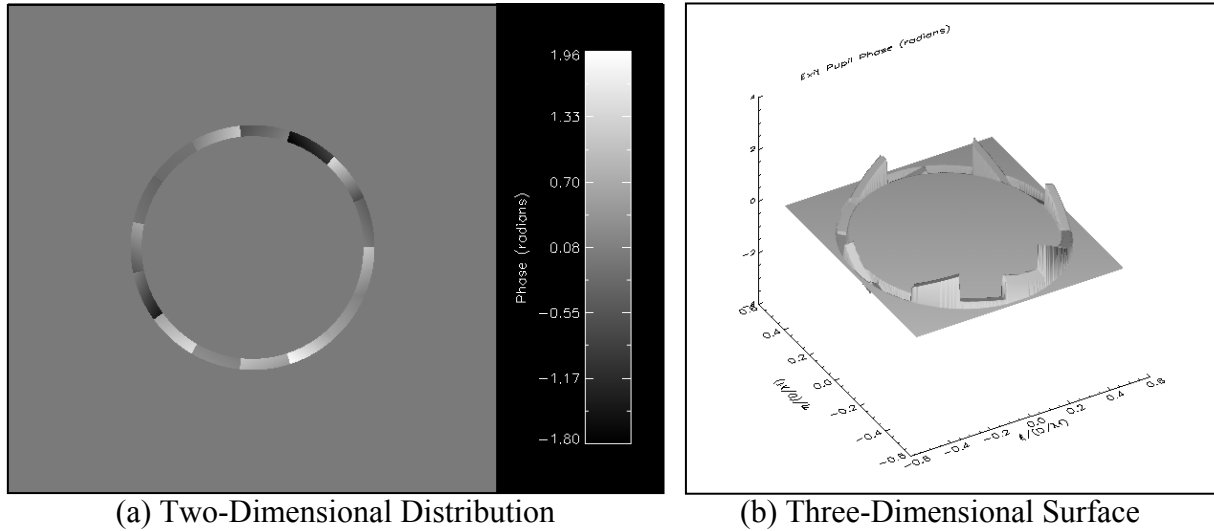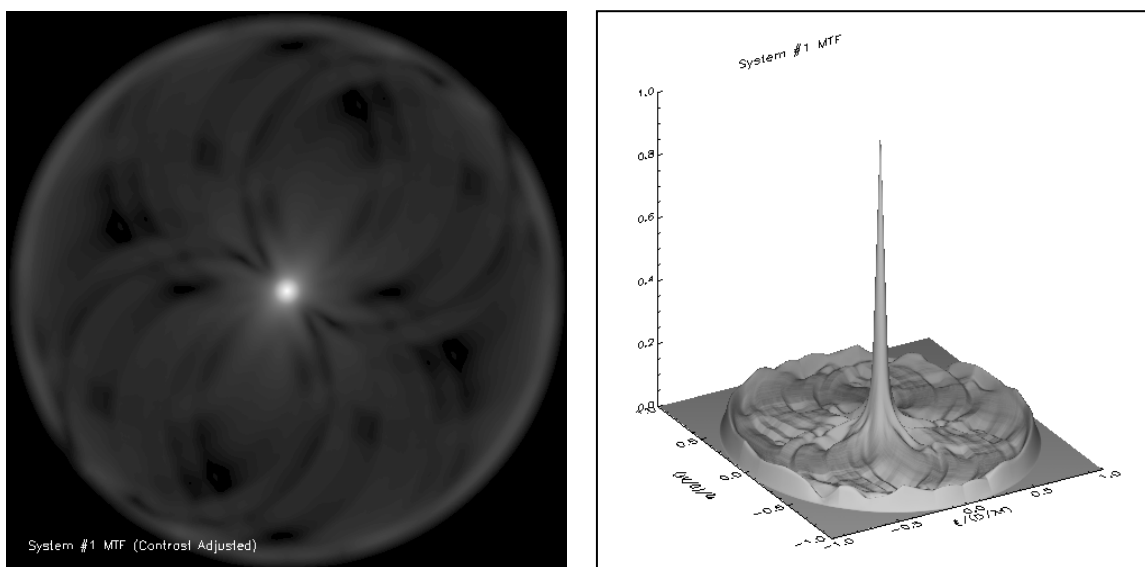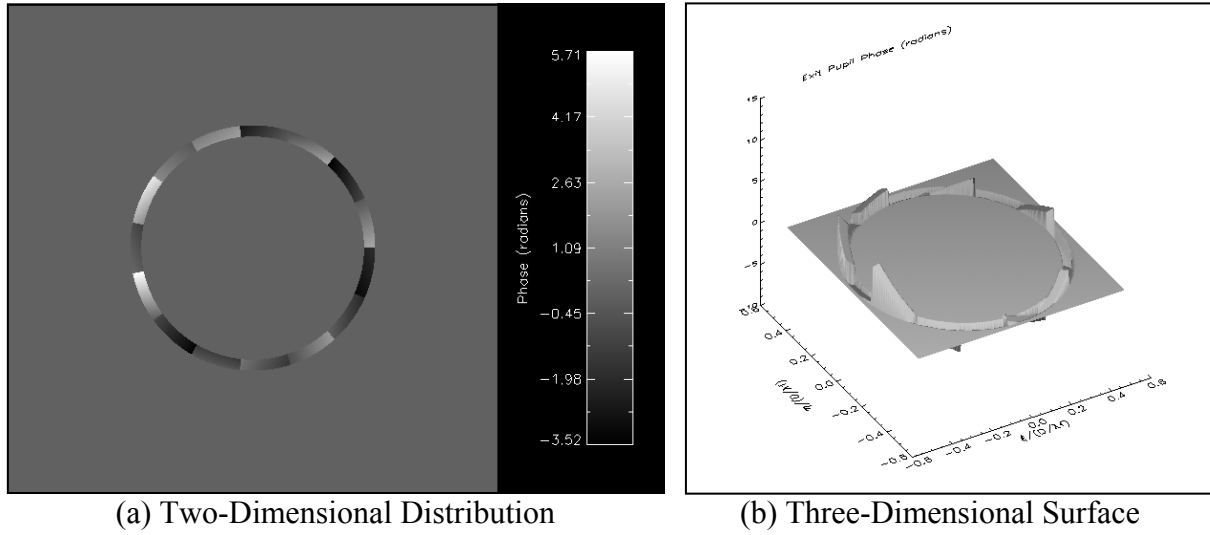(a) Two-Dimensional Distribution   (b) Three-Dimensional Surface

Figure 144: Random phase profile for the central wavelength of an aberrated annulus sparse aperture (0.10 waves rms piston, tip/tilt error).

(a) Two-Dimensional Image 　　　(b) Three-Dimensional Surface

Figure 145: Modulation transfer function for an aberrated annulus
sparse aperture (0.10 waves rms piston, tip/tilt error).

(a) Gray-World Simulation 　　　(b) Polychromatic-World Simulation
nrmse: 0.0646 　　　 *nrmse*: 0.0658

RER: 0.859; G_{rms}: 18.7; SNR: 268.5

Figure 146: Integrated panchromatic simulation of an aberrated annulus sparse aperture
with spectrally weighted OTF restoration (0.10 waves rms piston, tip/tilt error).

(a) Two-Dimensional Distribution   (b) Three-Dimensional Surface

Figure 147: Random phase profile for the central wavelength of an aberrated annulus sparse aperture (0.25 waves rms piston, tip/tilt error).

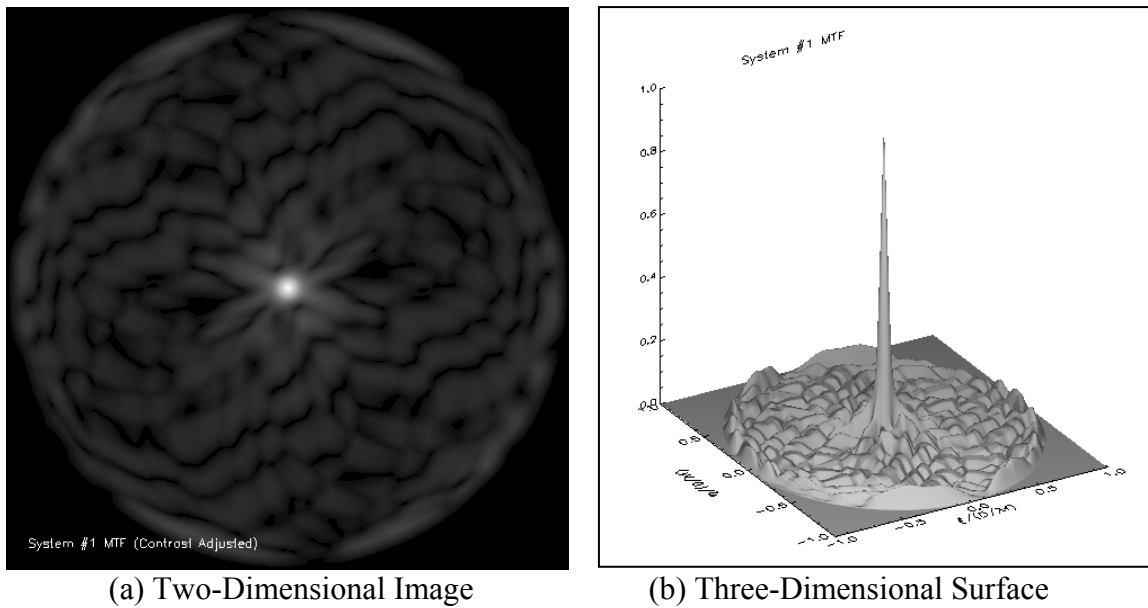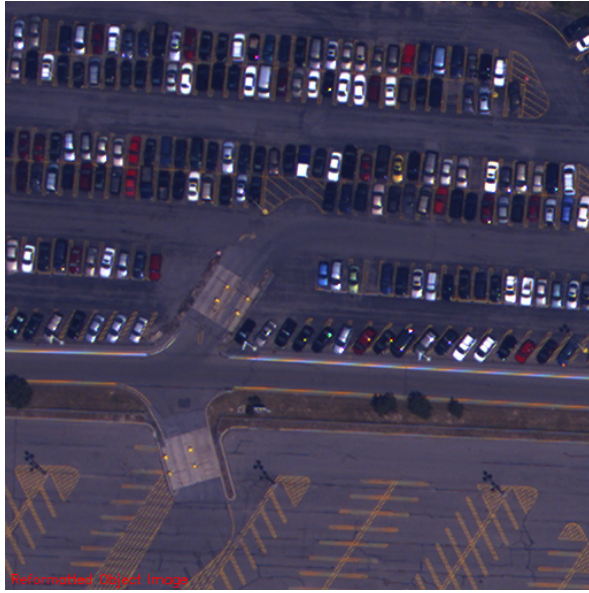(a) Two-Dimensional Image   (b) Three-Dimensional Surface

Figure 148: Modulation transfer function for an aberrated annulus sparse aperture (0.25 waves rms piston, tip/tilt error).

(a) Original Object

(b) Spectrally Weighted Object

(c) Gray-World Simulation
nrmse: 0.0971

(d) Polychromatic-World Simulation
nrmse: 0.1185

RER: 0.712; G_{rms}: 28.7; SNR: 268.6

Figure 149: Integrated panchromatic simulation of an aberrated annulus sparse aperture with spectrally weighted OTF restoration (0.25 waves rms piston, tip/tilt error).

A.3 Phased Petal Aperture

Although technically not a sparse aperture system in the classic sense, formation of a filled aperture through phasing of smaller petals or subapertures certainly lends itself to similar physical processes that were explored in this research effort. As a consequence, an arbitrary phased petal design was developed to explore whether such an optical configuration exhibits any of the unique quality implications manifested by the lower fill factor sparse aperture imaging systems explored in this research. To that end, this section provides simulation results for a phased 36-subaperture filled imaging system configuration with a fill factor F_{fill} of 0.942 and wavefront errors of 0.10 and 0.25 waves rms at the mean wavelength. As with previous predictions, the gray-world and spectral model restorations were accomplished with a traditional Wiener filter, assuming perfect system OTF and noise-to-object power spectrum ratio knowledge.

The following figures provide the optical phase profile, the aberrated aperture MTF, and the final restoration products for the conditions specified above. For this high-fill factor case, there does not appear to be a statistically significant difference between the two model types, seemingly pointing to the conclusion made previously that the spectrally induced quality effect explored in this dissertation is a unique characteristic of low-to-modest fill factor imaging systems. As a final note, one must be cautious in making direct quality comparisons between the aberrated filled aperture results and those acquired for sparse aperture systems under similar conditions, since the scenario depicted here did not adjust the integration time appropriately to accommodate the reduced modulation in the system transfer function. As a consequence, the aberrated phased petal restorations for 0.25 waves rms of wavefront error exhibit detection SNR that is considerably lower than nominal for such levels of aberration. This relatively poor detection SNR was an intentional characteristic of this particular modeling iteration, as a stressing imaging case was desired to ascertain whether spectral artifacts could indeed be generated with a phased petal design.
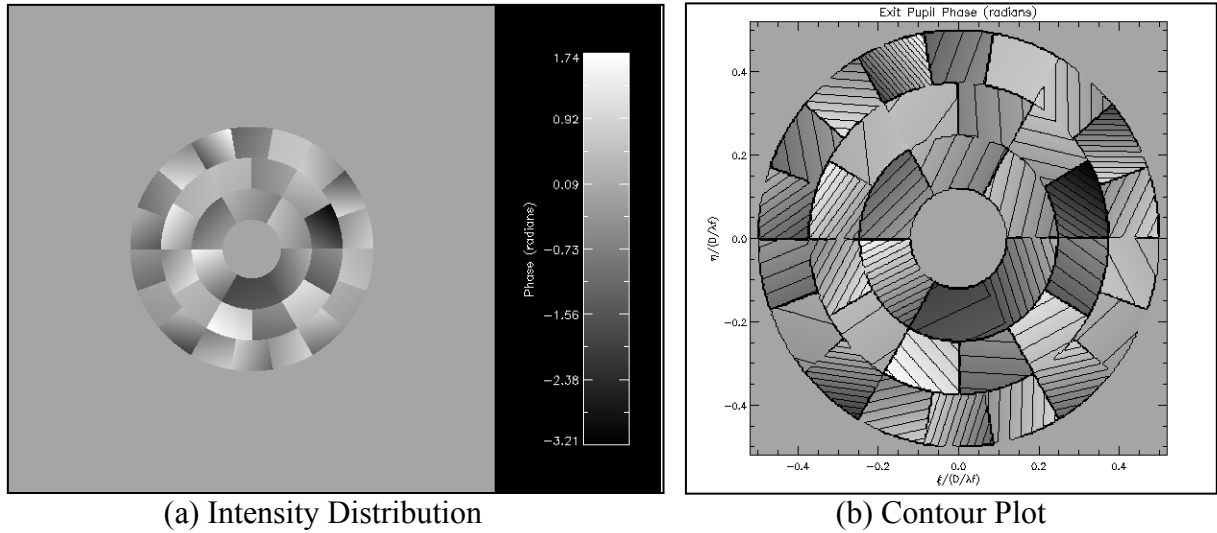
(a) Intensity Distribution

(b) Contour Plot

Figure 150: Random phase profile for the central wavelength of an aberrated
phased petal filled aperture (0.10 waves rms piston, tip/tilt error).

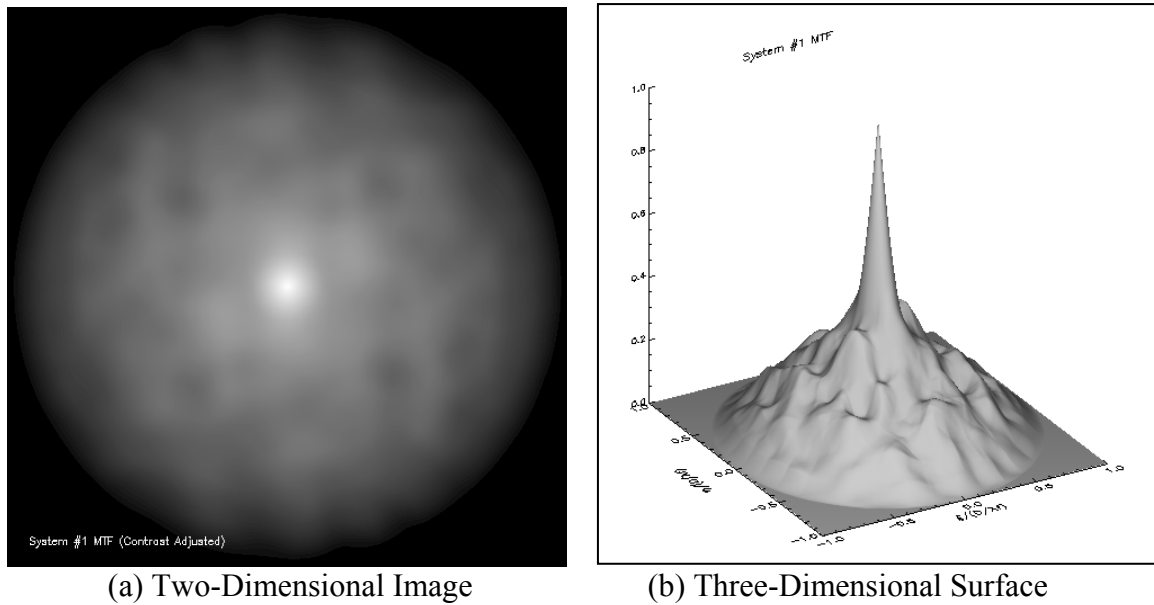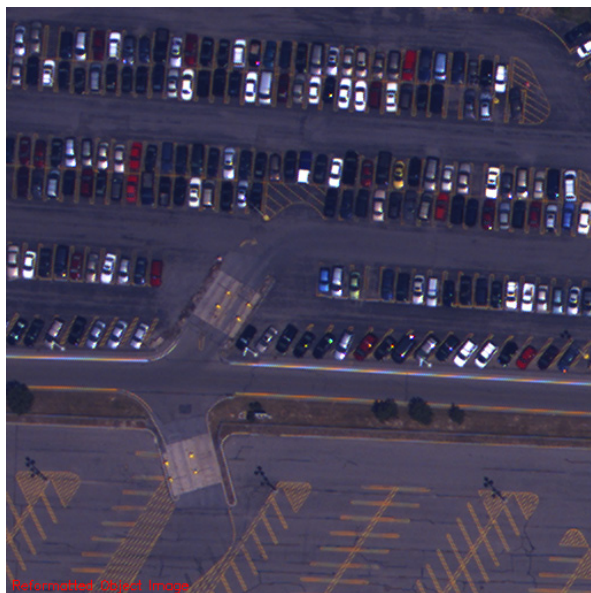(a) Two-Dimensional Image

(b) Three-Dimensional Surface

Figure 151: Modulation transfer function for an aberrated phased petal
filled aperture (0.10 waves rms piston, tip/tilt error).

(a) Original Object

(b) Spectrally Weighted Object

(c) Gray-World Simulation
nrmse: 0.0667

(d) Polychromatic-World Simulation
nrmse: 0.0670

RER: 0.833; G_{rms}: 2.46; SNR: 36.2

Figure 152: Integrated panchromatic simulation of an aberrated phased petal filled aperture with spectrally weighted OTF restoration (0.10 waves rms piston, tip/tilt error).
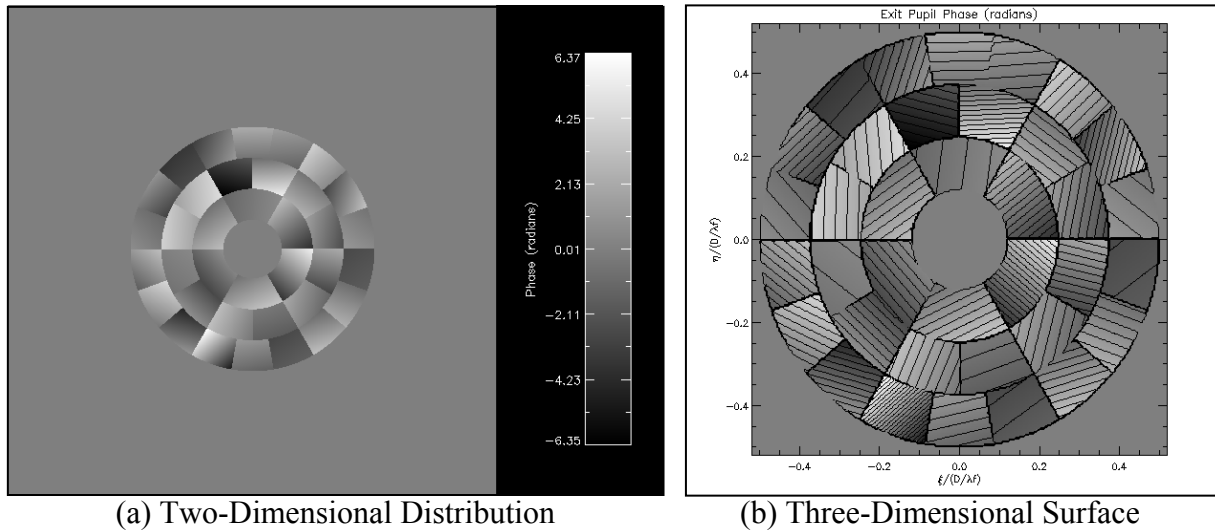
(a) Two-Dimensional Distribution   (b) Three-Dimensional Surface

Figure 153: Random phase profile for the central wavelength of an aberrated
phased petal filled aperture (0.25 waves rms piston, tip/tilt error).

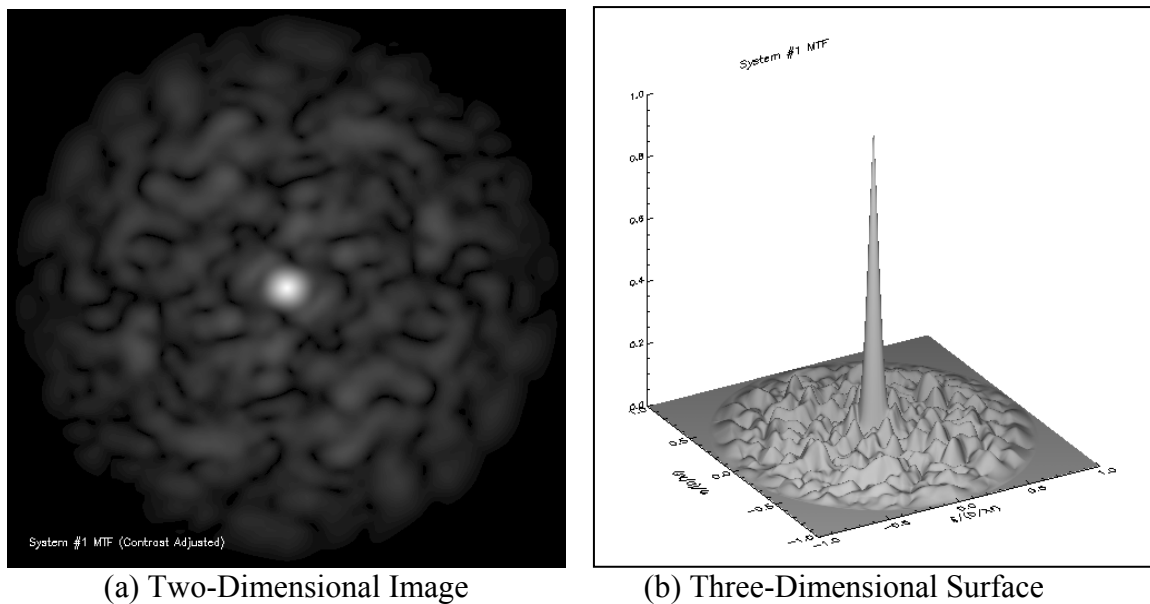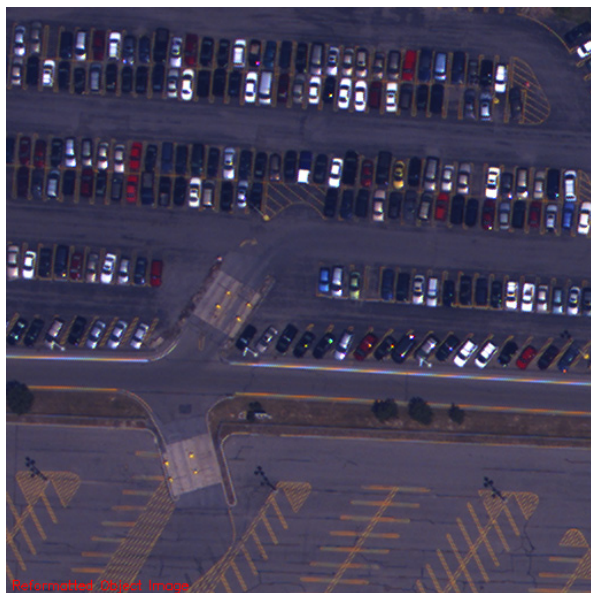(a) Two-Dimensional Image   (b) Three-Dimensional Surface

Figure 154: Modulation transfer function for an aberrated phased petal
filled aperture (0.25 waves rms piston, tip/tilt error).

(a) Original Object

(b) Spectrally Weighted Object

(c) Gray-World Simulation
nrmse: 0.1343

(d) Polychromatic-World Simulation
nrmse: 0.1354

RER: 0.552; G_{rms}: 5.17; SNR: 36.2

Figure 155: Integrated panchromatic simulation of an aberrated phased petal filled aperture with spectrally weighted OTF restoration (0.25 waves rms piston, tip/tilt error).